The Pennsylvania State University
The J. Jeffrey and Ann Marie Fox Graduate School

FROM SILENCE TO SIGNAL: COMPOSING THE SCIENCE OF NEUTRON STAR-BLACK HOLE MERGERS

A Dissertation in
Physics
by
Ish Gupta

Submitted in Partial Fulfillment
of the Requirements
for the Degree of

Doctor of Philosophy

August 2025

The dissertation of Ish Gupta was reviewed and approved by the following:

Bangalore Sathyaprakash
Elsbach Professor of Physics and Professor of Astronomy and Astrophysics
Dissertation Advisor
Chair of Committee

Eugenio Bianchi
Associate Professor of Physics

David Radice
Associate Professor of Physics and Astronomy & Astrophysics

Derek Fox
Associate Professor of Astronomy & Astrophysics

Mauricio Terrones
George A. and Margaret M. Downsbrough Department Head, Evan Pugh University Professor, Professor of Chemistry and Materials Science and Engineering

Abstract

Gravitational-wave (GW) detections have significantly enhanced our understanding of the universe, opening a new observational window onto extreme astrophysical phenomena. The majority of these signals have been from binary black hole mergers, providing unprecedented opportunities to test general relativity in strong gravity and highly dynamic regimes. The groundbreaking observation of the first binary neutron star merger, GW170817, initiated multi-messenger astronomy with GWs, offering insights into heavy-element production through r-process nucleosynthesis and constraining the nuclear equation of state. Neutron star–black hole (NSBH) binaries, consisting of a neutron star orbiting a black hole, further expand this multi-messenger potential. In addition, the pronounced mass asymmetry in NSBH systems activates higher-order harmonics in the GW signal, significantly enhancing the estimation of binary parameters compared to more symmetric binary systems. This dissertation demonstrates how these unique characteristics position NSBH mergers as critical sources for multi-messenger astronomy, inferring astrophysical properties and cosmological parameters.

We first evaluate the detectability and parameter estimation precision of NSBH mergers, highlighting how improvements in detector sensitivity and network configurations will enable unprecedented measurements of the properties of these compact binaries. Next, we delve deeper into the multi-messenger implications by examining prospects for detecting electromagnetic counterparts, specifically kilonovae, accompanying GW detections. Our findings illustrate that next-generation GW observatories will facilitate timely follow-up of kilonovae from these mergers, and that these kilonovae will be detectable by advanced telescopes such as the Vera C. Rubin Observatory and the Nancy Grace Roman Space Telescope.

Precise estimation of binary properties also allows us to constrain the formation and evolution of NSBH mergers. We discuss methods to distinguish between different formation scenarios using GW observables and population synthesis modeling. Demonstrating their applicability, we apply these methods to GW230529 and effectively rule out certain formation channels discussed in the literature. Moreover, we highlight how precise spin measurements of neutron stars in NSBH binaries can provide further insights into their formation histories.

Finally, we quantify the cosmological potential of NSBH mergers, particularly as “gray sirens”—sources combining elements of dark and bright sirens. We project the ability of NSBH binaries detected by future detector networks in resolving the Hubble tension, showing that these systems can help constrain Hubble-Lemaître constant with better than

2% precision within the next ten years. This underscores the substantial impact of NSBH mergers as powerful complementary tools for cosmological measurements, leveraging both precise distance measurements and enhanced localizability enabled by electromagnetic counterparts.

Overall, this dissertation establishes NSBH mergers as pivotal astrophysical and cosmological tools, highlighting their unique contributions to GW astronomy, multi-messenger astrophysics, and precision cosmology, and setting a foundation for future theoretical and observational exploration.

Table of Contents

List of Figures

List of Tables

Acknowledgements

Perhaps the real treasure was the friends we made along the way.
— Unknown

Pursuing a PhD in Physics has been one of the most rewarding and transformative experiences of my life, and I owe much of that to my advisor, Bangalore Sathyaprakash. Sathya has not only guided me through the technical depths of gravitational-wave physics, but more importantly, has taught me how to think like a scientist—with intellectual honesty, self-skepticism, and a relentless pursuit of excellence. One of his greatest strengths as a mentor lies in his ability to recognize that different students thrive under different styles of guidance. In my case, I work best when given the freedom to pursue my own ideas, and Sathya offered exactly that—always providing space for independent exploration while remaining a steady and supportive presence. During one of the more difficult phases of my PhD, when I was navigating postdoctoral applications and grappling with intense self-doubt, Sathya took the time to go on a walk with me and talk through my anxieties. That simple act of kindness grounded me, reminded me of my worth, and helped me move forward with clarity and confidence. He has been the best mentor I could have asked for, and I carry his example with me as I mentor others.

I am deeply grateful to my dissertation committee members—Eugenio Bianchi, David Radice, and Derek Fox—for their thoughtful feedback and support throughout my PhD. Their insights have helped shape this dissertation in meaningful ways. I have also had the privilege of collaborating with Eugenio and David, and both experiences have been immensely enriching. From Eugenio, I have learned how to approach problems with depth and clarity; every conversation with him has left me with a more profound understanding of the subject at hand. From David, I have come to appreciate the value of rigor and efficiency—his meticulous approach to research and his ability to tackle complex problems with clarity are qualities I aspire to emulate.

I have spent the entirety of my PhD at the Institute for Gravitation and the Cosmos (IGC), and I am deeply thankful for the collaborative, welcoming, and intellectually vibrant environment it has provided. The spirit of camaraderie and open exchange at the IGC has played a vital role in shaping my development and productivity as a researcher. I am especially grateful to Abhay Ashtekar, whose kindness, curiosity, and scientific insight have left a lasting impression on me. His passion for physics is infectious, and I will always cherish our discussions. I would also like to thank Sarah Shandera, Donghui Jeong, Stephanie Wissel, Kohta Murase, Chad Hanna, and Martin Bojowald—not only for their engaging scientific and non-scientific conversations, but for helping to foster the

collaborative and supportive community that makes the IGC such a special place.

During my time at Penn State, I have been fortunate to form friendships that have sustained me, especially during moments when I was too overwhelmed to take care of myself. A simple "thank you" cannot fully capture the depth of my gratitude, but it is a place to begin. I am especially thankful to Ssohrab, Arnab, Jyotirmay, Monica, and Avi for being unwavering sources of support, laughter, and perspective throughout my PhD. This journey would not have been the same without you. I am equally grateful to Jacob, Erick, Bryce, Maarten, Joshua, Matt, Garrett, Shomik, Suri, Victoria, Wilson, Neev, Samira, Shio, Prathamesh, Divya, Becca, Rachel, Joey, Rishabh, Anirban, Mauricio, Yi, Estuti, Stephen, Daniel, Chaosong, Sarvesh, Anubhav, Abhinav, Amogh, and Samarth—thank you for the conversations, the shared struggles, the celebrations, and the quiet moments in between.

To my fellow group members—Sanika, Shiksha, Viviana, Wendy, Mercan, Samanvitha, and Leo—your brilliance and dedication have not only inspired me but also made our group a vibrant and motivating space to grow. I am deeply grateful for your presence.

I have had the privilege of overlapping with several exceptionally talented postdoctoral researchers at the IGC. Learning from them—and calling them friends—has been a highlight of my PhD experience. My heartfelt thanks to Anuradha, Rahul, Surabhi, Tommaso, Leo, Koustav, Rossella, Samuele, James, Mukul, Mainak, Maitreya, Edu, Peter, Tetyana, and Vaishak for your generosity, insight, and friendship.

I am also deeply appreciative of the staff at Penn State and the IGC, whose tireless efforts behind the scenes have made our lives as graduate students smoother and more manageable. I would like to especially thank Randi Neshteruk, Natasha Urbanik, Nicholas Mateer, Courtney Shaffer, Julianne Mortimore, Melissa Diamanti, Kendall Thomas, and Brian Moore for their consistent support and patience over the years.

Beyond Penn State, I have been fortunate to collaborate with brilliant scientists whose perspectives have meaningfully shaped both my research and my development as a physicist. I am especially grateful to Ashley Villar, who served on my dissertation committee during her time at Penn State, and to Aditya Vijaykumar, who has been not only a close collaborator but also a trusted friend. I also extend my sincere thanks to Debatri Chattopadhyay, Hsin-Yu Chen, Jose Ezquiaga, Lionel London, Shubhansu Tiwari, Purnima Narayan, Chinmay Kalaghatgi, Anna Puecher, Soumen Roy, Ajit Mehta, Abhirup Ghosh, Luca Reali, Floor Broekgaarden, Nikhil Sarin, and Sylvia Biscoveanu for the many stimulating discussions and valuable collaborations. I am particularly thankful to Alessandra Corsi, Emanuele Berti, and K. G. Arun, whose guidance and encouragement over the years have left a lasting impact.

Finally, I owe everything to my family and friends back home in India. To my parents—your love, sacrifices, and unwavering belief in me have been the bedrock of all that I have achieved. My partner, Akshadha, has been a constant source of affection, strength, and inspiration throughout this journey. Despite the physical distance, you have all made me feel supported and never alone. Every call, every word of encouragement, and every quiet act of resilience has carried me through the most difficult moments. I am also deeply grateful to my best friends—Jaddu, Prathmesh, and Ayush—and to my

extended family back home, for standing by me with pride and patience, for grounding me in where I come from, and for celebrating every milestone as if it were your own. This dissertation is not only the result of academic effort, but a testament to the enduring, invisible support of those who have anchored me from afar.

The research presented in this dissertation has utilised computational resources made available as part of the LIGO Scientific Collaboration, specifically those provided by LIGO Laboratory and the Institute for Computational and Data Sciences at Penn State University, and supported by the National Science Foundation (NSF) grants PHY-0757058, PHY-0823459, OAC-2346596, OAC-2201445, OAC- 2103662, OAC-2018299, and PHY-2110594. The research has been funded by the NSF under award numbers: PHY-2207638, AST-2307147, PHY-2308886, and PHY-2309064. Any opinions, findings, and conclusions or recommendations expressed in this publication are those of the author(s) and do not necessarily reflect the views of the NSF.

To my parents and my partner, Akshadha—
the fundamental constants in the ever-evolving equation of my life.

Chapter 1
A new sound in the cosmos

Somewhere, something incredible is waiting to be known.
— Sharon Begley[1]

Astronomy, at its core, is the science of observation. From Hans Lippershey submitting the first patent for a telescope and Galileo Galilei pointing his telescope skyward, humanity embarked on a profound journey to decode the Universe using electromagnetic (EM) signals—light, in all its forms. Over centuries, visible starlight guided us from our own celestial neighborhood, revealing planets, stars, and nebulae, to distant galaxies stretching the scale of the observable cosmos. Each advancement in observational technology enriched our understanding of known phenomena and consistently surprised us with unexpected revelations.

In the past century, astronomy underwent a profound transformation as observational capabilities expanded dramatically across the entire EM spectrum, far beyond visible light. Each new observational band—radio, infrared, ultraviolet, X-ray, and gamma-ray—opened fresh windows into the cosmos, uncovering phenomena invisible to traditional optical telescopes. Radio astronomy, pioneered in the 20$^{\text{th}}$ century, enabled the serendipitous discovery of cosmic microwave background radiation [10], confirming the Big Bang model of the Universe, while also discovering radio pulses from magnetized and rapidly rotating neutron stars (called pulsars) [11]. Infrared astronomy allowed the study of celestial objects obscured by interstellar dust, uncovering exoplanets [12] as well as young stars in star clusters [13]. Ultraviolet and X-ray astronomy offered insights into energetic phenomena, such as hot young stars, active galactic nuclei [14, 15] and binaries of black holes and neutron stars [16], whereas gamma-ray observations helped examine extreme astrophysical events, like supernovae [17] and mergers of neutron stars [18].

The 21$^{\text{st}}$ century has marked the emergence of a groundbreaking astronomical probe—gravitational waves (GWs). First predicted by Einstein in 1916 [19, 20], GWs are

[1]This quote is often misattributed to Carl Sagan [9].

perturbations in spacetime that propagate at the speed of light. To understand how they are produced, let us consider an analogy with EM radiation. EM radiation originates from time-varying multipole moments of a charge distribution. As the monopole moment of the distribution equals the total charge, which is strictly conserved, monopole EM radiation is forbidden. Thus, at leading order, EM radiation is dipolar. Similarly, in GW generation, the gravitational monopole moment corresponds to the total mass and is conserved. However, unlike electromagnetism, the gravitational dipole moment is also conserved, as a direct consequence of linear momentum conservation. Therefore, GW emission requires the mass-energy distribution to possess at least a time-varying quadrupole moment.

The passage of GWs manifests physically as a stretching and squeezing of spacetime itself. Consider two freely-falling test masses initially separated by a certain distance: the effect of a passing GW would periodically alter this separation, providing a measurable signature of GW perturbations. It was precisely through the detection of such minute spatial distortions that the Laser Interferometer Gravitational-Wave Observatory (LIGO) achieved the first direct detection of GWs on September 14, 2015 [21]. With GWs, we had discovered a new sense; we could now "listen" to the universe in addition to looking at it!

1.1 Listening to the universe with GWs

To quantify these spatial distortions, we utilize Einstein's quadrupole formula [20], which expresses the GW metric perturbation h_{ij} (in the transverse-traceless gauge) as directly proportional to the second time derivative of the mass quadrupole moment Q_{ij}:

$$h_{ij} = \frac{2G}{c^4}\frac{1}{D}\frac{d^2Q_{ij}}{dt^2}, \tag{1.1}$$

where G is the gravitational constant, c is the speed of light, and D is the distance between the GW source and the observer.

To estimate the amplitude of GWs emitted from a binary system, consider a binary with total mass M, orbital separation r, orbital velocity v, and orbital frequency ω. By employing dimensional analysis, we approximate the mass quadrupole moment as $Q_{ij} \sim Mr^2$, and its second time derivative as $\frac{d^2}{dt^2} \sim \omega^2$. Using Kepler's third law, the orbital separation is related to the frequency by $r = (GM/\omega^2)^{1/3}$. Hence, the GW

amplitude can be approximated as:

$$|h_{ij}| \propto \frac{G}{c^4}\frac{1}{D}Mr^2\omega^2 \approx 10^{-22}\left(\frac{100\ \mathrm{Mpc}}{D}\right)\left(\frac{M}{1\,\mathrm{M}_\odot}\right)^{5/3}\left(\frac{\omega}{100\ \mathrm{Hz}}\right)^{2/3}. \tag{1.2}$$

This shows that GW amplitudes, representing fractional changes in the separation of test masses, are extremely small. The amplitude is larger for binaries that are more massive than the Sun, orbiting at frequencies around 100 Hz. Such high-frequency and high-mass systems imply orbital separations thousands of times smaller than the Sun's radius, achievable only in binaries consisting of compact objects like neutron stars (NSs) and black holes (BHs).

LIGO detectors employ 4 km long Michelson-Morley-type laser interferometers to measure these minuscule fractional changes in length induced by passing GWs [22–24]. The first direct detection, event GW150914 [21], originated from the merger of a binary black hole (BBH) system with a total mass of approximately $65\,\mathrm{M}_\odot$ located around 450 Mpc away. Remarkably, this event corresponded to measuring a GW amplitude of $\mathcal{O}(10^{-20})$, translating into an actual displacement of the interferometer arms of $\mathcal{O}(10^{-16})$ meters. Subsequently, the first binary neutron star (BNS) merger, GW170817 [25], observed jointly with the Virgo detector in Italy [26, 27], was confidently linked to short gamma-ray bursts (SGRBs) and kilonovae (KNe) [18, 28, 29], firmly establishing these mergers as sources of heavy element nucleosynthesis through the r-process [30, 31], thus heralding the era of multimessenger astronomy (MMA). Since these landmark detections, nearly one hundred compact binary mergers have been observed by the global network of GW detectors, leading to stringent tests of general relativity [32], precise measurements of compact binary population characteristics [33], constraints on cosmological parameters [34], and insights into the NS equation of state (EOS) [35].

To achieve precise GW measurements, signals must overcome various noise sources inherent to ground-based detectors. These noise contributions include anthropogenic disturbances, seismic vibrations, thermal fluctuations, shot noise, gravity gradient noise, and quantum effects (see Ref. [36] for a review). Collectively, these noise sources limit detector sensitivity, thus restricting the distance and fidelity at which compact binary mergers can be observed.

Despite these limitations, GW observations enable us to address fundamental questions spanning multiple scientific disciplines. These include testing general relativity, studying relativistic astrophysics, advancing nuclear physics, exploring dark matter candidates, and investigating cosmology and physics beyond the standard model. Such broad scientific

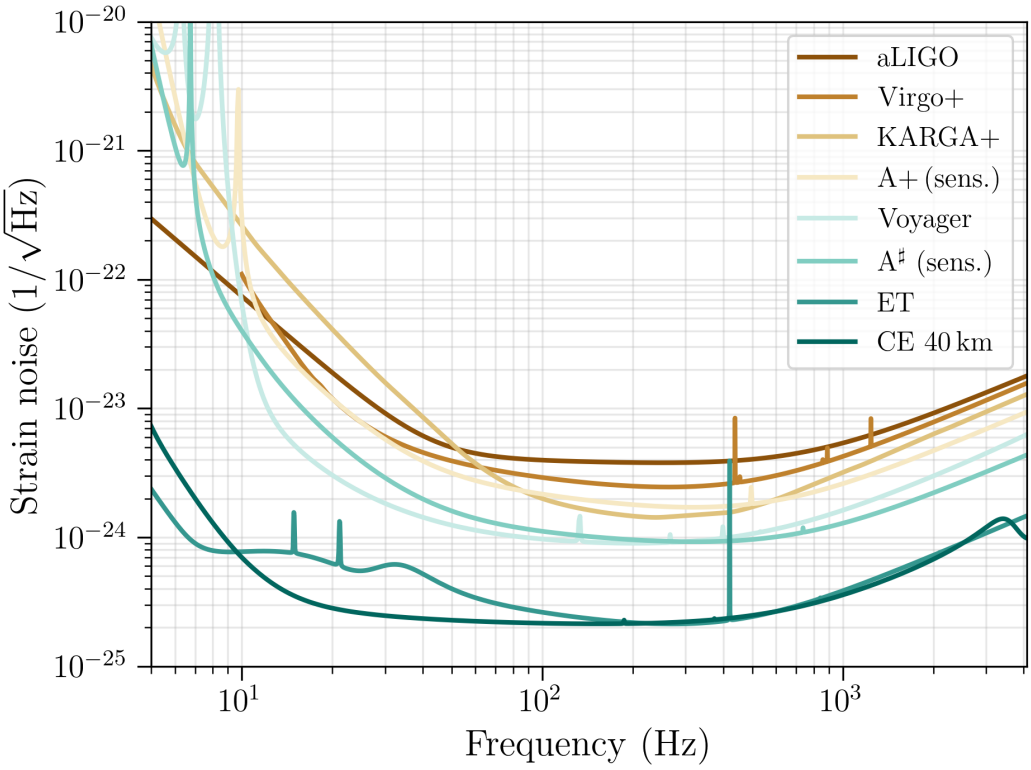

Figure 1.1: The ASDs for the proposed advancements to the current detectors as well as for the planned XG detectors. We also include the ASD for the aLIGO sensitivity for comparison.

reach is possible only if GWs offer observational access to diverse astrophysical and cosmological regimes. Examples include BBH mergers from epochs when the universe was forming its earliest stars, BNS mergers from beyond redshifts corresponding to the peak star-formation era, and stochastic GW backgrounds generated in the primordial universe [37, 38].

To fully exploit the transformative potential of GW astronomy, enhancing the sensitivity and scale of GW detectors is crucial. Toward this goal, several technological advancements and next-generation (XG) ground-based GW observatories have been proposed:

- **A+ sensitivity [39, 40]-** The LIGO detectors at Hanford, Livingston, and the planned detector in Aundha, India [41] (referred to in this chapter as LIGO-India or LIGO-I), the Virgo detector in Italy, and the KAGRA [42–44] detector in Japan are expected to upgrade to A+ or similar sensitivities, with lower quantum noise and thermal coating noise, improving the aLIGO sensitivity by about 50%. The

A+ sensitivity increases the range for BNS detection to 1.9 times and BBH sources to 1.6 times that achieved by the aLIGO detectors.

- **Voyager/A$^\sharp$ sensitivity** [45, 46]**-** The original Voyager upgrade intends to improve the aLIGO sensitivities by about 2 to 4 times. This is accomplished by reducing the quantum shot noise and using cryogenically cooled test masses with an amorphous silicon coating that reduces the thermal noise associated with the mirrors. The A$^\sharp$ technology, on the other hand, achieves similar improvement in sensitivity while keeping the test masses at room temperature, but using heavier test masses and improved coating and quantum squeezing.

- **Cosmic Explorer** [47–49]**-** The Cosmic Explorer (CE) project refers to the proposed next-generation XG L-shaped detector design with 40 km arms, i.e., 10 times the size of the current LIGO detectors. Due to the scaled-up length of the arms, CE detectors result in $\mathcal{O}(10) - \mathcal{O}(100)$ improvement in sensitivity, depending on the frequency, as compared to A+. Currently, there are several proposals for the configuration of the CE detectors, including the option of having just one of the two detectors, or having two detectors such that the second detector is smaller with 20 km arms instead, which can be tuned to BNS post-merger signals.

- **Einstein Telescope** [50, 51]**-** Einstein Telescope (ET) is the proposed XG underground detector in Europe with three detectors placed along the vertices of an equilateral triangle of side 10 km. The detectors are planned to have a *xylophone* design with each side containing two interferometers. With the longer arms, triangular-xylophone design, and measures to suppress fundamental noise sources, ET is expected to have sensitivities similar to CE.

The amplitude spectral densities (ASDs) characterizing the noise budget corresponding to these enhancements have been plotted in Fig. 1.1.

1.2 Turning GW data into science

The GW strain measured by interferometers encodes rich information about the properties of the emitting binary. Since the detectors are sensitive to both the amplitude and the phase of the incoming signal, it is possible to infer the physical parameters of the binary by analyzing the detected waveform. In this section, we examine how the amplitude and

phase of the GW depend on the binary parameters, and outline the techniques used to extract these parameters from the observed data.

1.2.1 Why can we extract binary parameters from GWs?

In general relativity, a propagating GW possesses two independent degrees of freedom. In the transverse-traceless gauge, the strain projected on the plane orthogonal to the propagation direction can be written as

$$h_{ab} = \begin{pmatrix} h_+ & h_\times \\ h_\times & -h_+ \end{pmatrix}, \tag{1.3}$$

where h_+ and $h_\times$ represent the two GW polarizations. In a chosen coordinate basis $\hat{e}_x$ and $\hat{e}_y$ on the transverse plane, one can define the polarization tensors as

$$\boldsymbol{e}_+ = \hat{e}_x \otimes \hat{e}_x - \hat{e}_y \otimes \hat{e}_y, \tag{1.4}$$

$$\boldsymbol{e}_\times = \hat{e}_x \otimes \hat{e}_y + \hat{e}_y \otimes \hat{e}_x, \tag{1.5}$$

such that the strain tensor can be decomposed as $\boldsymbol{h} = h_+\boldsymbol{e}_+ + h_\times\boldsymbol{e}_\times$. Under a rotation of the coordinate system by an angle θ, the polarizations transform as

$$h'_+ = \cos 2\theta\, h_+ + \sin 2\theta\, h_\times, \tag{1.6}$$

$$h'_\times = -\sin 2\theta\, h_+ + \cos 2\theta\, h_\times. \tag{1.7}$$

A rotation by $\pi/4$ thus interchanges the two polarization states, demonstrating the quadrupolar character of gravitational radiation.

Using the quadrupole approximation, the polarization amplitudes from a binary system of total mass M, symmetric mass ratio $\eta = (m_1 m_2)/(m_1 + m_2)^2$, separation R, orbital frequency ω, corresponding phase Φ, and distance D from the observer, can be expressed as [52]

$$h_+ = \frac{1}{D}\frac{4GM\eta\omega^2R^2}{c^4}\left(\frac{1+\cos^2\iota}{2}\right)\cos 2\Phi(t), \tag{1.8}$$

$$h_\times = \frac{1}{D}\frac{4GM\eta\omega^2R^2}{c^4}\cos\iota\,\sin 2\Phi(t). \tag{1.9}$$

Here, ι denotes the inclination angle between the binary's orbital angular momentum

and the line of sight. Substituting R using Kepler's law leads to simplified expressions in terms of the GW frequency $f_{\rm GW}$,

$$h_+ = \frac{4}{D}\left(\frac{G\mathcal{M}_c}{c^2}\right)^{5/3}\left(\frac{\pi f_{\rm GW}}{c}\right)^{2/3}\left(\frac{1+\cos^2\iota}{2}\right)\cos\Phi_{\rm GW}(t), \tag{1.10}$$

$$h_\times = \frac{4}{D}\left(\frac{G\mathcal{M}_c}{c^2}\right)^{5/3}\left(\frac{\pi f_{\rm GW}}{c}\right)^{2/3}\cos\iota\,\sin\Phi_{\rm GW}(t), \tag{1.11}$$

where $\mathcal{M}_c = M\eta^{3/5}$ is the chirp mass and $f_{\rm GW} = \omega_{\rm GW}/2\pi = \omega/\pi$. Consequently, $\Phi_{\rm GW}(t) = 2\Phi(t)$. The corresponding radiated power in the quadrupole approximation is given by [52]

$$P = \frac{32}{5}\frac{c^5}{G}\left(\frac{G\mathcal{M}_c\,\omega_{\rm GW}}{2c^3}\right)^{10/3}. \tag{1.12}$$

To understand the leading-order phase evolution of the binary, consider its energy given by the sum of kinetic and potential components,

$$E = -\frac{Gm_1m_2}{2R}. \tag{1.13}$$

As the binary emits GWs, it loses energy, causing the separation R to shrink (by Eq. 1.13) and the orbital frequency ω to rise (via Kepler's law). This leads to increased GW emission and a self-reinforcing inspiral culminating in merger. This is reflected in Eqs. 1.10 and 1.11, where the strain amplitude increases with frequency. Substituting for R in Eq. 1.13, the binary's energy becomes

$$E = -\left(\frac{G^2\mathcal{M}_c^5\,\omega_{\rm GW}^2}{32}\right)^{1/3}. \tag{1.14}$$

The radiated power is $-dE/dt$, and equating with Eq. 1.12 yields the frequency evolution,

$$\dot{f}_{\rm GW} = \frac{96\pi^{8/3}}{5}\left(\frac{G\mathcal{M}_c}{c^3}\right)^{5/3} f_{\rm GW}^{11/3}. \tag{1.15}$$

The leading-order GW phase as a function of time is then given by

$$\Phi_{\rm GW}(t) = 2\pi\int_{t_c}^{t} dt'\, f_{\rm GW}(t') = -2\left(\frac{5G\mathcal{M}_c}{c^3}\right)^{-5/8}(t_c - t)^{5/8} + \Phi_{\rm GW}(t_c), \tag{1.16}$$

where t_c is the time of coalescence. We see that both the amplitude and the phase of the waveform depend directly on $\mathcal{M}_c$ at leading order, making it the best-constrained

parameter in GW observations. However, as $\mathcal{M}_c$ is a combination of the component masses, measuring η is also necessary to break degeneracies and extract individual masses. The dependence of the waveform on η and on the spins of the binary components arises at higher orders in the waveform expansion.

A systematic approach to include such corrections involves solving Einstein's equations perturbatively using the post-Newtonian (PN) approximation (see Ref. [53] for a detailed review). This formalism expands the two-body dynamics and the GW signal as a power series in the small parameter $x \sim (GM/c^2R)^{1/2} \sim v/c$, where v is the characteristic orbital velocity. The GW phase evolution in the frequency domain can then be written as a PN expansion of the form

$$\Phi_{\rm GW}(f) \sim v^{-5} \sum_{k=0}^{N} \Phi_k(\vec{\theta}), v^k, \tag{1.17}$$

where the term proportional to v^k corresponds to the $(k/2)^{\rm th}$ PN order, and N corresponds to the power up to which the PN expressions have been calculated (the latest addition being the 4.5PN calculation for the GW phase for a non-spinning binary [54]). In this expansion, the 1PN term introduces dependence on η, while the leading-order spin effects appear at 1.5PN through spin-orbit coupling terms. During the early inspiral, the signal is dominated by lower-order PN terms, with higher-order corrections becoming increasingly important as the binary approaches merger. The parameter dependence encoded in the PN coefficients thus enables extraction of intrinsic binary properties from the GW signal.

There is an additional layer of complexity introduced by cosmology. As GWs traverse cosmological distances before reaching our detectors, they are influenced by the expansion of the Universe. To account for this, we begin with the Friedmann–Lemaître–Robertson–Walker metric in comoving coordinates,

$$d\tau^2 = dt^2 - a(t)^2 \left(\frac{dr^2}{1 - Kr^2} + r^2 d\Omega \right), \tag{1.18}$$

where $a(t)$ is the scale factor, and $K = 0$ (spatially flat), $+1$ (closed), or -1 (open) denotes the spatial curvature. For a comoving source located at coordinate distance r, the physical separation from an observer at the origin is

$$r_p = a(t) \int_0^r \frac{dr}{\sqrt{1 - Kr^2}}. \tag{1.19}$$

In a spatially flat Universe ($K = 0$), this simplifies to $r_p = a(t)\, r$.

To quantify redshift effects, consider a light ray (or gravitational wavefront) propagating radially inward. Since $d\tau = 0$ along a null geodesic, we obtain

$$\frac{dt}{a(t)} = \frac{dr}{\sqrt{1 - Kr^2}}. \tag{1.20}$$

Integrating this for two successive wave crests—one emitted at t_e and observed at t_o, and the next emitted at $t_\mathrm{e} + \Delta t_\mathrm{e}$ and observed at $t_\mathrm{o} + \Delta t_\mathrm{o}$—and noting that the right-hand side is time-independent, yields

$$\int_{t_\mathrm{o}}^{t_\mathrm{e}} \frac{dt}{a(t)} = \int_0^r \frac{dr}{\sqrt{1 - Kr^2}} = \int_{t_\mathrm{o}+\Delta t_\mathrm{o}}^{t_\mathrm{e}+\Delta t_\mathrm{e}} \frac{dt}{a(t)}. \tag{1.21}$$

Assuming small Δt, this implies

$$\frac{\Delta t_\mathrm{o}}{a(t_\mathrm{o})} = \frac{\Delta t_\mathrm{e}}{a(t_\mathrm{e})} \quad \Rightarrow \quad \Delta t_\mathrm{o} = \Delta t_\mathrm{e}(1 + z), \tag{1.22}$$

where the redshift is defined as $1 + z = a(t_\mathrm{o})/a(t_\mathrm{e})$. Consequently, the observed frequency is redshifted: $f_\mathrm{o} = f_\mathrm{e}/(1 + z)$.

To illustrate the observational consequences, consider an EM source with intrinsic luminosity L_e and observed luminosity L_o, and define the observed flux as

$$F = \frac{L_\mathrm{o}}{4\pi D^2} = \frac{dE_\mathrm{o}/dt_\mathrm{o}}{4\pi[a(t_\mathrm{o})d_c]^2}, \tag{1.23}$$

where d_c is the comoving distance. Accounting for redshifted energy ($E_\mathrm{o} = E_\mathrm{e}/(1 + z)$) and time intervals ($dt_\mathrm{o} = dt_\mathrm{e}(1 + z)$), we obtain

$$F = \frac{dE_\mathrm{e}/dt_\mathrm{e}}{4\pi[a(t_\mathrm{o})d_c(1 + z)]^2} = \frac{L_\mathrm{e}}{4\pi D_L^2}, \tag{1.24}$$

defining the luminosity distance as $D_L = a(t_\mathrm{o})\, d_c(1 + z)$. The relation between D_L and z can be expressed as a series expansion [55]:

$$D_L = \frac{cz}{H_0}\left[1 + \frac{1 - q_0}{2}z + \ldots\right], \tag{1.25}$$

where $H_0 = \dot{a}(t_\mathrm{o})/a(t_\mathrm{o})$ is the Hubble–Lemaître constant and $q_0 = -\ddot{a}(t_\mathrm{o})/(a(t_\mathrm{o})H_0^2)$ is the deceleration parameter. Thus, combining precise luminosity distance measurements with redshift measurements (say, from spectroscopy) enables inference of cosmological parameters [56].

To connect this framework with GWs, we revisit the waveform amplitude from Eq. 1.10. Applying the redshift transformations $d \to a(t_o)d_c$ and $f_{\mathrm{GW},E} \to f_{\mathrm{GW},O}(1+z)$, we find

$$\mathcal{A}_{\mathrm{GW}} \propto \frac{\mathcal{M}_c^{5/3} f_{\mathrm{GW},E}^{2/3}}{D} \to \frac{(1+z)^{2/3}\mathcal{M}_c^{5/3} f_{\mathrm{GW},O}^{2/3}}{a(t_o)d_c} = \frac{[\mathcal{M}_c(1+z)]^{5/3} f_{\mathrm{GW},O}^{2/3}}{D_L}. \tag{1.26}$$

The redshifted amplitude thus retains the same functional form as in a non-expanding Universe, but with D replaced by D_L and the source-frame chirp mass replaced by the redshifted (detector-frame) chirp mass, $\mathcal{M}_c(1+z)$. This has two important implications:

- The component masses inferred from GW observations are redshifted, $m_1(1+z)$ and $m_2(1+z)$. For example, a $60\,\mathrm{M}_\odot$ binary merging at $z = 1$ will appear observationally as a $120\,\mathrm{M}_\odot$ system. Likewise, its merger frequency of ~ 80 Hz in the source frame will be redshifted to ~ 40 Hz in the detector frame, mimicking the signal from a more massive binary.

- While the GW amplitude depends on the luminosity distance D_L, extracting D_L from the amplitude alone is challenging due to its degeneracy with $\mathcal{M}_c(1+z)$. However, since the frequency evolution (or "chirping") of the GW signal also depends on $\mathcal{M}_c(1+z)$, measuring both the amplitude and phase evolution allows D_L to be inferred from the GW signal alone. Once D_L is determined, an independent redshift measurement, e.g., via EM counterparts, enables constraints on cosmological parameters. This intrinsic ability of GWs to yield absolute distance measurements without external calibrators earns them the designation of *standard sirens* [57]. Their application to cosmology is discussed in detail in Chapter 5.

In addition to enabling direct distance measurements, GW observations also offer the potential for precise source localization, which is crucial for identifying coincident EM counterparts [29] and host galaxies of compact binary mergers [25]. Accurate localization has significant astrophysical implications, such as understanding merger environments [58], as well as cosmological applications, including standard siren cosmology and host-galaxy identification [59–62]. Although individual GW detectors are not inherently directional, source localization is achieved through triangulation, by exploiting the differences in signal arrival times across a network of spatially separated detectors. Since GWs propagate at the speed of light, the time delay between detectors depends on the direction of the source relative to the baseline connecting them. For two detectors separated by a vector

$\vec{L}$ and a GW arriving from direction $\hat{n}$, the time delay is given by

$$\Delta t = \frac{\vec{L} \cdot \hat{n}}{c}. \tag{1.27}$$

This constraint defines a ring of constant time delay on the sky. With a network of three or more detectors, multiple independent time delays can be measured, which uniquely determine the direction $\hat{n}$ to the source on the celestial sphere.

The precision of this localization depends on the timing uncertainty σ_t in each detector, which is influenced by the signal-to-noise ratio (SNR) and bandwidth of the detected signal [63]. Specifically, higher SNR and longer bandwidth signals result in smaller timing uncertainty. For a baseline of length $L = |\vec{L}|$, the angular resolution can be approximated by

$$\Delta\theta \approx \frac{c\,\sigma_t}{L}. \tag{1.28}$$

For instance, the two LIGO detectors, separated by approximately 3000 km and with typical timing uncertainties of order $\sigma_t \sim 1$ ms, yield a localization precision of $\Delta\theta \sim 0.1$ rad. Increasing the baseline or reducing timing uncertainty significantly improves localization. In this context, the addition of the LIGO-India detector will be pivotal– by extending the network baseline by nearly a factor of four, it is expected to substantially enhance source localization capabilities [64].

1.2.2 How can we extract binary parameters from GWs?

Having described how GWs are parameterized by astrophysical properties, we now turn to how these signals are measured by detectors. The strain observed in a GW interferometer is a linear combination of the two GW polarizations, modulated by the detector's antenna pattern functions. The detector response at time t is given by

$$h(t;\boldsymbol{\theta}) = F_+(\alpha,\delta,\psi)\,h_+(t;\boldsymbol{\theta}) + F_\times(\alpha,\delta,\psi)\,h_\times(t;\boldsymbol{\theta}), \tag{1.29}$$

where $\boldsymbol{\theta} = \{\mathcal{M}_c(1+z), \eta, \boldsymbol{\chi}_1, \boldsymbol{\chi}_2, \iota, D_L, t_c, \phi_c\}$ denotes the source parameters: redshifted chirp mass, symmetric mass ratio, dimensionless spin vectors $\boldsymbol{\chi}_i$, inclination angle ι, luminosity distance D_L, time of coalescence t_c, and coalescence phase ϕ_c. The antenna pattern functions F_+ and $F_\times$ depend on the source's right ascension α, declination δ, and polarization angle ψ, and describe the directional sensitivity of the detector [65].

The calibrated detector output $d(t)$ is modeled as a sum of the true astrophysical

signal $h(t;\boldsymbol{\gamma})$ and instrumental noise $n(t)$:

$$d(t) = h(t;\boldsymbol{\gamma}) + n(t), \tag{1.30}$$

where $\boldsymbol{\gamma} = \boldsymbol{\theta} \cup \{\alpha, \delta, \psi\}$ is the full parameter set. The noise $n(t)$ is assumed to be a zero-mean, stationary Gaussian process. Under the wide-sense stationarity (mean and autocovariance do not depend on time) assumption, the noise correlation matrix depends only on the time difference: $C_n(t_i, t_j) = \langle n(t_i)n(t_j)\rangle = C_n(|t_i - t_j|)$. Taking the Fourier transform yields the one-sided power spectral density (PSD) $S_n(f)$, which characterizes the frequency-dependent sensitivity of the detector.

Under these assumptions, the likelihood of observing the data $d(t)$ given a model $h(t;\boldsymbol{\gamma})$ is

$$\mathcal{L}(d|\boldsymbol{\gamma}) \propto \exp\left[-\frac{1}{2}(d - h(\boldsymbol{\gamma}), d - h(\boldsymbol{\gamma}))\right], \tag{1.31}$$

where (a, b) denotes the noise-weighted inner product,

$$(a, b) = 4\,\mathrm{Re}\int_0^\infty \frac{\tilde{a}^*(f)\tilde{b}(f)}{S_n(f)}\,df. \tag{1.32}$$

The matched-filter SNR is defined as $\rho = \sqrt{(d|h)}$.

Bayesian inference provides a principled framework to estimate the posterior probability distribution over the parameter space $\boldsymbol{\gamma}$ given the data d. According to Bayes' theorem,

$$p(\boldsymbol{\gamma}|d) = \frac{\mathcal{L}(d|\boldsymbol{\gamma})\,\pi(\boldsymbol{\gamma})}{\mathcal{Z}}, \tag{1.33}$$

where $\pi(\boldsymbol{\gamma})$ is the prior distribution on the parameters, and $\mathcal{Z}$ is the evidence:

$$\mathcal{Z} = \int \mathcal{L}(d|\boldsymbol{\gamma})\,\pi(\boldsymbol{\gamma})\,d\boldsymbol{\gamma}. \tag{1.34}$$

The posterior distribution $p(\boldsymbol{\gamma}|d)$ encodes all the information about the parameters after accounting for the data and prior knowledge. To obtain the posterior for a specific parameter γ_i, one marginalizes over the remaining nuisance parameters:

$$p(\gamma_i|d) = \int p(\boldsymbol{\gamma}|d)\,\left(\prod_{j\neq i} d\gamma_j\right). \tag{1.35}$$

While the evidence $\mathcal{Z}$ is not directly required for parameter estimation, it plays a central role in model selection. Given two competing models M_0 and M_1, the ratio of

evidences,

$$\mathcal{B}_{10} = \frac{\mathcal{Z}_1}{\mathcal{Z}_0}, \tag{1.36}$$

is the Bayes factor, which quantifies the degree to which the data favor one model over the other. Because evidence integrates the likelihood over the prior space, more complex models (with larger prior volume) are penalized unless the data provides sufficiently strong support. This built-in preference for simplicity is known as Occam's penalty. We will utilize Bayesian model selection in Chapter 4.

Although Bayesian inference is powerful, it is computationally intensive, especially when dealing with high-dimensional parameter spaces or computationally expensive waveform models. In such scenarios, the Fisher information matrix offers a computationally inexpensive alternative to approximate parameter uncertainties in the high-SNR regime. The Fisher matrix quantifies the curvature of the log-likelihood around its maximum and thus provides an estimate of the expected measurement precision. What follows is a heuristic derivation of the Fisher information matrix approach. A detailed and rigorous exposition can be found in Ref. [66].

Starting from the Gaussian likelihood,

$$\ln \mathcal{L}(\boldsymbol{\gamma}) = -\frac{1}{2}(d - h(\boldsymbol{\gamma}), d - h(\boldsymbol{\gamma})) + \text{const}, \tag{1.37}$$

and assuming the data is well-described by a signal at the true parameters $\boldsymbol{\gamma}_0$, i.e., $d(t) \approx h(t; \boldsymbol{\gamma}_0)$, we Taylor-expand the log-likelihood around $\boldsymbol{\gamma}_0$:

$$\ln \mathcal{L}(\boldsymbol{\gamma}) \approx \ln \mathcal{L}(\boldsymbol{\gamma}_0) - \frac{1}{2}\sum_{i,j} \Gamma_{ij}(\gamma_i - \gamma_{0,i})(\gamma_j - \gamma_{0,j}), \tag{1.38}$$

where the Fisher matrix is defined as

$$\Gamma_{ij} = -\mathbb{E}\left[\frac{\partial^2 \ln \mathcal{L}}{\partial \gamma_i \partial \gamma_j}\right], \tag{1.39}$$

where $\mathbb{E}[p(x)]$ refers to the expectation value of $p(x)$. To evaluate this, we compute the first derivative of the log-likelihood:

$$\frac{\partial}{\partial \gamma_i} \ln \mathcal{L} = (d - h(\boldsymbol{\gamma}), \partial_{\gamma_i} h(\boldsymbol{\gamma})). \tag{1.40}$$

At $\boldsymbol{\gamma} = \boldsymbol{\gamma}_0$, this becomes:

$$\left.\frac{\partial \ln \mathcal{L}}{\partial \gamma_i}\right|_{\gamma_0} = (n, \partial_{\gamma_i} h), \tag{1.41}$$

whose expectation is zero since n is a zero-mean Gaussian process. Taking the second derivative yields:

$$\frac{\partial^2 \ln \mathcal{L}}{\partial \gamma_i \partial \gamma_j} = -(\partial_{\gamma_i} h, \partial_{\gamma_j} h) + (d - h, \partial^2_{\gamma_i \gamma_j} h). \tag{1.42}$$

Taking the expectation over noise, the second term vanishes since $\mathbb{E}[d - h] = \mathbb{E}[n] = 0$, resulting in

$$\Gamma_{ij} = (\partial_{\gamma_i} h, \partial_{\gamma_j} h). \tag{1.43}$$

The inverse of the Fisher matrix approximates the covariance matrix:

$$\Sigma_{ij} \approx (\Gamma^{-1})_{ij}, \tag{1.44}$$

with $\sqrt{\Sigma_{ii}}$ representing the 1σ uncertainty in γ_i. Since this approach only involves evaluating inner products of waveform derivatives, it provides a fast and practical method for forecasting parameter constraints. We utilize this approach in Chapters 2, 3, and 5.

1.3 The gift of mass asymmetry

While the binary parameters can be extracted from GW data, inherent degeneracies among parameters can limit the precision of their estimation. One well-known example is the D_L–ι degeneracy. As seen from the quadrupolar waveform expressions in Eqs. 1.10 and 1.11, while $\mathcal{M}_c$ is robustly inferred from the phase evolution, there exists a degeneracy between the inclination angle ι and the luminosity distance D_L, both of which only affect the amplitude. Specifically, a nearby edge-on system ($\iota = \pi/2$) can appear similar to a more distant face-on system ($\iota = 0$). Similar degeneracies arise between the symmetric mass ratio η and the effective aligned spin $\chi_{\rm eff}$, particularly when relying only on the quadrupole-dominated phase evolution (see Chapter 4).

Thankfully, beyond the dominant quadrupolar mode, the GW signal also includes contributions from higher-order modes (HOMs). The full waveform can be written as a sum over spin-weighted spherical harmonic modes as,

$$h(t, \boldsymbol{\theta}) = \sum_{\ell=2}^{\infty} \sum_{m=-\ell}^{\ell} Y^{\ell m}_{-2}(\iota, \phi_0)\, h_{\ell m}(t, \boldsymbol{\theta}), \tag{1.45}$$

where $h_{\ell m}$ denotes the (ℓ, m) mode waveform, $Y^{\ell m}_{-2}$ is the spin-weighted spherical harmonic of weight -2, and $\boldsymbol{\theta}$ represents the set of intrinsic and extrinsic binary parameters. The symmetry relation $h_{\ell m}(t) = (-1)^{\ell} h^{*}_{\ell -m}(t)$ connects positive and negative m modes. Given this redundancy, we will restrict to the positive m modes for brevity in the rest of this chapter. While the $(\ell = 2, m = \pm 2)$ modes dominate for most systems, the inclusion of HOMs becomes increasingly important for systems with asymmetric component masses or high inclination angles.

Different (ℓ, m) modes encode different combinations of the binary parameters, thereby breaking degeneracies present in the quadrupole-only signal. The amplitude of each mode is modulated by $Y^{\ell m}_{-2}(\iota, \phi_0)$, making the total strain highly sensitive to the inclination angle. Figure 1.2 shows $|Y^{\ell m}_{-2}(\iota, \phi_0 = 0)|$ as a function of ι. For face-on binaries ($\iota = 0$), only the $(2, 2)$ and $(3, 2)$ modes have significant power, while other HOMs become prominent for edge-on orientations.

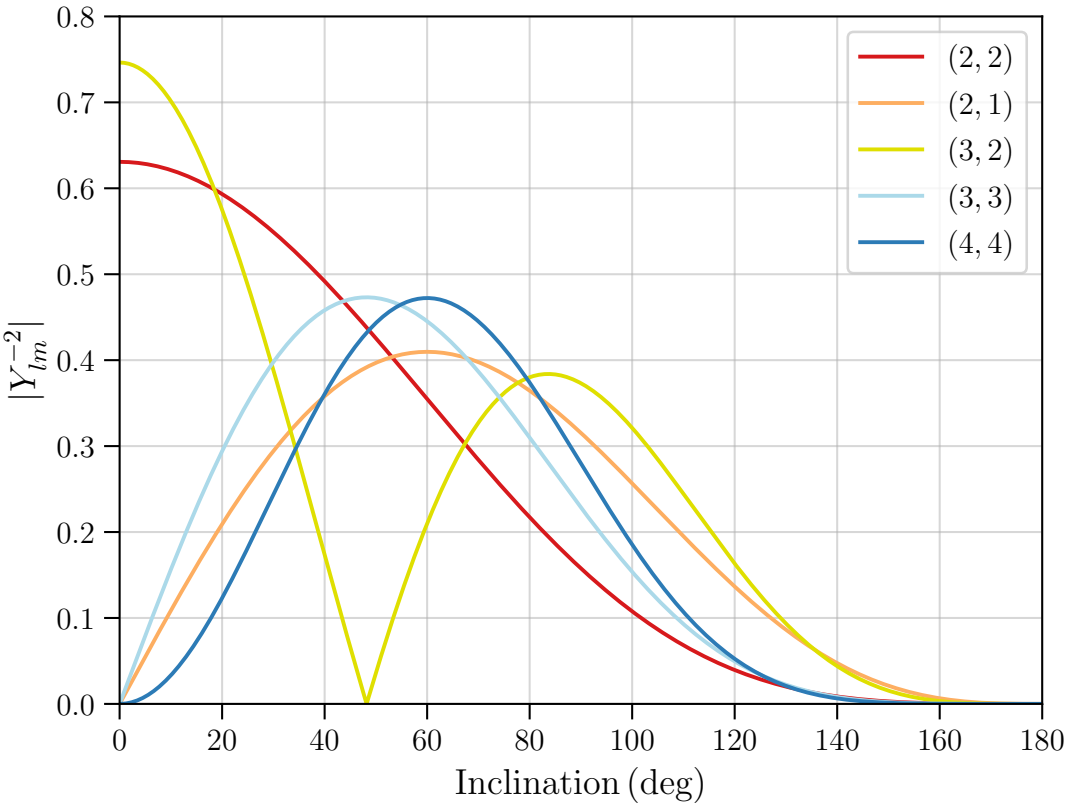

Figure 1.2: The variation of the absolute value of Y^{-2}_{lm} with the inclination angle for different HOMs. $|Y^{-2}_{l-m}|$ are same as $|Y^{-2}_{lm}|$ but mirrored about 90°.

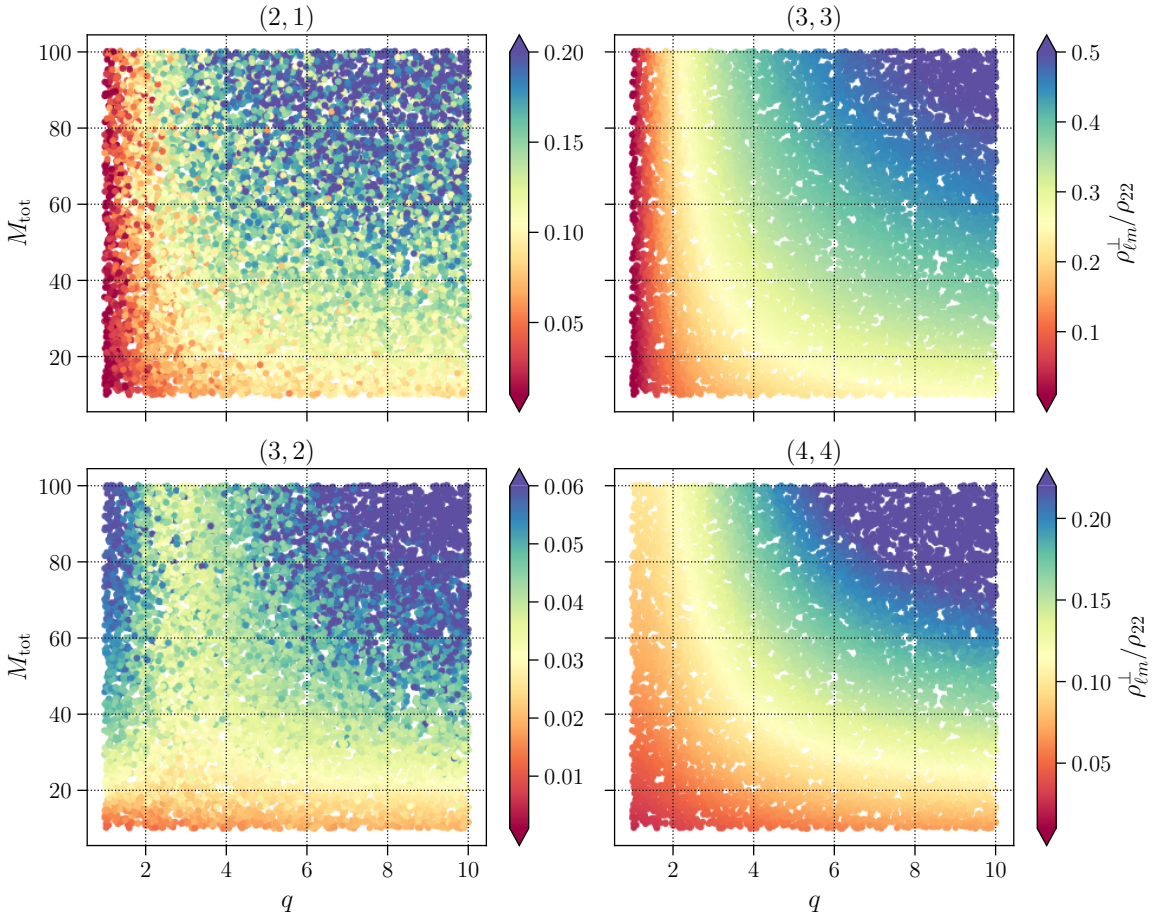

Figure 1.3: The ratio of the orthogonal SNR in the (ℓ, m) modes compared to the $(2, 2)$ mode, as a function of the total mass and the mass ratio of the binary.

The detectability of HOMs also depends on intrinsic binary parameters. During the inspiral, the phase of the (ℓ, m) mode is approximately related to the quadrupolar phase by $\Phi_{\ell m} \approx \frac{m}{2}\Phi_{22}$. Hence, the merger of the compact objects corresponds to higher frequencies for HOMs (e.g., merger corresponds to $1.5 f_{\rm merge}$ for the $(3, 3)$ mode). Since the sensitivity of current LIGO-Virgo-KAGRA (LVK) detectors peaks in the $\mathcal{O}(100)$ Hz range, increasing the total binary mass $M_{\rm tot}$ lowers $f_{\rm merge}$ and shifts the HOMs into the sensitive band, thereby enhancing their contribution to the signal.

In terms of amplitude hierarchy, the $(2, 2)$ mode enters at leading order (0PN) in the PN expansion, while modes such as $(2, 1)$ and $(3, 3)$ appear at 0.5PN, and $(3, 2)$ and $(4, 4)$ at 1PN [8, 53, 67]. This ordering can be motivated by considering the structure of higher multipole contributions to the radiation.

The next-to-leading order corrections to the quadrupole formula (c.f. Eq. 1.1) take

the form

$$h \propto \frac{d^\ell}{dt^\ell} Q_\ell, \tag{1.46}$$

where $\ell = 3$ and $\ell = 4$ correspond to the octupolar and hexadecapolar moments, respectively. Dimensionally, $Q_l \sim Mr^l$, and since $r \propto v^{-2}$, it follows that $Q_\ell \sim Mv^{-2\ell}$. Additionally,

$$\frac{d^\ell}{dt^\ell} \sim f^\ell \sim v^{3\ell}, \tag{1.47}$$

so that the waveform amplitude scales as $h \propto v^\ell$. Hence, the octupolar ($\ell = 3$) and hexadecapolar ($\ell = 4$) modes are suppressed by factors of v and v^2, respectively, relative to the leading quadrupolar ($\ell = 2$) radiation. This explains why the $(3, 3)$ and $(4, 4)$ modes first appear at 0.5PN and 1PN order, respectively. Furthermore, $\ell + m =$ odd modes arise from current multipoles and are further suppressed by a factor of v compared to mass-type multipoles ($\ell + m =$ even) [53]. As a result, the $(2, 1)$ and $(3, 2)$ modes appear at 0.5PN and 1.5PN, respectively.

HOMs thus naturally become more significant closer to merger and in binaries with larger total mass $M_{\rm tot}$, where the merger frequency enters the sensitive band of the detector earlier. Moreover, in equal-mass, non-spinning binaries, the waveform is symmetric under a rotation of the phase $\phi \to \phi + \pi$, which suppresses all odd-m modes like $(2, 1)$ and $(3, 3)$. These modes grow with increasing mass ratio $q = m_1/m_2 \geq 1$, making mass-asymmetric binaries especially favorable for detecting HOMs.

To quantify the impact of mass asymmetry and total mass on HOMs, we compute the orthogonal SNR contribution of each mode, defined as [68]:

$$\rho^\perp_{\ell m} = \sqrt{(\tilde{h}_{\ell m}, \tilde{h}_{\ell m}) - \frac{(\tilde{h}_{\ell m}, \tilde{h}_{22})^2}{(\tilde{h}_{22}, \tilde{h}_{22})}}, \tag{1.48}$$

where $\tilde{h}$ is the frequency-domain waveform. Figure 1.3 presents the relative strength of different HOMs with respect to the $(2, 2)$ mode as a function of $M_{\rm tot}$ and q. As expected, the contribution of HOMs increases with both $M_{\rm tot}$ and mass asymmetry. While the $(2, 2)$ mode remains dominant across the parameter space considered, the $(3, 3)$ mode consistently emerges as the second-strongest for asymmetric binaries, followed by $(2, 1)$ and $(4, 4)$. The $(3, 2)$ mode contributes the least, primarily due to its significant overlap with the $(2, 2)$ mode, quantified by $(\tilde{h}_{\ell m}, \tilde{h}_{22})$, which suppresses the orthogonal SNR component, $\rho^\perp_{32}$. Nevertheless, for nearly equal-mass systems, both the $(3, 2)$ and $(4, 4)$ modes can become relevant, particularly when the total SNR is sufficiently high.

While the analysis in this dissertation is restricted to systems with spins aligned to the orbital angular momentum, it is important to note that spin-orbit misalignment, leading to precession of the orbital angular momentum and the component spins, can further enhance HOM contributions [69]. In particular, the modes in the inertial frame, $h^J_{\ell m}$, which track the total angular momentum $\boldsymbol{J}$, are expressed as linear combinations of modes in the co-precessing frame, $h^L_{\ell m'}$, which track the orbital angular momentum $\boldsymbol{L}$. This mixing occurs over $m' \in [-\ell, \ell]$, leading to an effective redistribution of power among modes [70]. As a result, precession-induced mixing can amplify certain HOMs in the inertial frame, such as the $(2,1)$ mode due to contributions from the co-precessing $(2,2)$ mode, and the $(3,2)$ mode arising from the co-precessing $(3,3)$ mode.

1.4 A new class of binary mergers– neutron star-black hole systems

Neutron star–black hole (NSBH) mergers are unique astrophysical sources of GWs. The mass of NSs is expected to be less than $3\,\mathrm{M}_\odot$ [71], while BHs detected by the LVK observatories span the range $[5, 150]\,\mathrm{M}_\odot$. As a result, NSBH systems are inherently mass-asymmetric. Indeed, as we will see in Chapter 3 (c.f. Fig. 3.4), approximately 30%–50% of NSBH events are expected to exhibit a mass ratio greater than 4. As discussed earlier, such asymmetry enhances the excitation of HOMs in the GW signal. This, in turn, improves binary parameter estimation, particularly the measurement of distance, leading to better three-dimensional localization.

By virtue of containing a NS, NSBH mergers can also produce EM counterparts. During the inspiral phase, the NS may be tidally disrupted by the BH. This disruption can occur either outside or inside the innermost stable circular orbit (ISCO) of the BH. If the disruption occurs within R_{ISCO}, the NS may be swallowed whole and no EM counterpart is generated. However, if the disruption takes place outside R_{ISCO}, a fraction of the NS matter can be dynamically ejected and/or form an accretion disk around the remnant BH. This remnant material can then power detectable EM emission.

Whether a NSBH merger produces observable EM counterparts is therefore determined by the interplay between the tidal disruption radius and the ISCO radius of the BH. A necessary condition for disruption is the onset of mass shedding, which occurs when the

tidal force at the NS surface exceeds its self-gravity. This condition is given by [72]

$$\frac{2GM_{\rm BH}R_{\rm NS}}{r^3} \gtrsim \frac{GM_{\rm NS}}{R_{\rm NS}^2}, \tag{1.49}$$

where $M_{\rm BH}$ is the mass of the BH, $M_{\rm NS}$ is the mass of the NS, $R_{\rm NS}$ is the radius of the NS, and r is the separation between the BH and the NS. Note that we ignore the tidal elongation (and possibly rotational flattening) of the NS (this appears as a factor c_R multiplied to $R_{\rm NS}$ in Ref. [72]). This yields the mass-shedding separation,

$$r_{\rm ms} := 2^{1/3}\left(\frac{M_{\rm BH}}{M_{\rm NS}}\right)^{1/3} R_{\rm NS}. \tag{1.50}$$

This condition is necessary but not sufficient—tidal disruption and ejection typically occur at smaller separations, after substantial mass loss from the NS. The actual observability of the disruption depends critically on whether it occurs outside the ISCO. For a Kerr BH, the ISCO radius depends sensitively on the dimensionless spin parameter χ, and is given by

$$R_{\rm ISCO} = \hat{R}_{\rm ISCO}(\chi)\frac{GM_{\rm BH}}{c^2}, \tag{1.51}$$

where $\hat{R}_{\rm ISCO}(\chi)$ is a monotonically decreasing function of χ. This behavior arises due to the frame dragging effect, wherein a Kerr BH twists the surrounding spacetime as a result of its spin. When the BH spin is aligned with the orbital angular momentum, frame dragging enhances the orbital motion, allowing the companion to stably orbit at a smaller radius without plunging into the BH. Consequently, the value of $R_{\rm ISCO}$ decreases. In contrast, if the BH spin is anti-aligned with the orbital angular momentum, frame dragging acts against the orbital motion, increasing the effective radius required for a stable orbit and resulting in a larger $R_{\rm ISCO}$.

EM counterparts can only form when $r_{\rm ms} > R_{\rm ISCO}$. The ratio of these radii is expressed as

$$\frac{r_{\rm ms}}{R_{\rm ISCO}} = \frac{2^{1/3}}{\hat{R}_{\rm ISCO}(\chi)}\left(\frac{M_{\rm BH}}{M_{\rm NS}}\right)^{-2/3}\left(\frac{GM_{\rm NS}}{c^2R_{\rm NS}}\right)^{-1}. \tag{1.52}$$

This expression reveals that tidal disruption is favored when the binary mass ratio is small, i.e., the BH mass is comparable to that of the NS. It also depends on the NS compactness, $\mathcal{C} = GM_{\rm NS}/(c^2R_{\rm NS})$; more compact NSs are harder to disrupt, making EM counterparts less likely. Finally, large BH spin (aligned with the orbital angular momentum) decreases $R_{\rm ISCO}$, thereby increasing the likelihood of disruption and EM emission.

Thus, within the NSBH population, systems with small mass ratios and high aligned spins are promising EM sources and strong candidates for MMA. In contrast, systems with significant mass asymmetry will exhibit pronounced HOM content, enabling precise parameter estimation. These two subpopulations highlight the dual scientific utility of NSBH mergers: as multi-messenger beacons and as high-fidelity GW-only scientific probes.

This dissertation explores both of these utilities in detail. In Chapter 2, we investigate the detectability of NSBH mergers with XG observatories, and use the Fisher matrix to assess parameter estimation precision. Chapter 3 evaluates the MMA prospects, including forecasts for yearly EM counterpart detections. Chapter 4 discusses how NSBH measurements can inform their formation history, constraining compact binary formation channels. Finally, in Chapter 5, we leverage the ability of NSBH mergers to provide either EM counterparts or precise luminosity distances to forecast constraints on H_0. A summary and future outlook are presented in Chapter 6.

Declaration

Portions of the text and figures presented in this chapter are adapted from the author's previously published or forthcoming works. These include Ref. [73], which appeared in Physical Review D (published by the American Physical Society), and Ref. [74], which is currently in preparation.

Chapter 2
Uncovering the cosmic population of NSBH mergers

There is no better high than discovery.
— Edward O. Wilson

2.1 Introduction

By the end of 2019, the Advanced Laser Interferometer Gravitational-Wave Observatory (aLIGO) [22–24] and the Advanced Virgo (AdV) [26, 27] detector had made a multitude of GW detections coming from BBH and BNS mergers [75]. In January 2020, the network made its first detection of a binary comprising a neutron star and a black hole, marking the first discovery ever of NSBH binaries in astronomy [76]. This discovery not only proved the existence of NSBH systems that merge within Hubble time, but it has also provided the first direct constraint on the local merger rate of these systems [33, 76].

Detecting NSBH mergers is crucial for a diverse range of astrophysical pursuits. Multiple formation channels are proposed to explain the formation and merger of NSBH systems, such as the isolated binary formation channel [77], dynamical formation in globular [78–80] or young stellar clusters [81, 82], population III stars [83] and others. These channels have varying, and often distinct, predictions for the mass and spin distributions of BHs and NSs. The detection of NSBH mergers will enhance our understanding of the population characteristics and also help identify the preferred scenarios for the formation of the NSBH binaries in the universe [84]. An extensive catalog of NSBH events will provide the redshift distribution of such systems, giving information about the star-formation rate (SFR) and preferred time-delay models that best explain their evolution. Just like BNS systems, NSBH systems are also expected to be sources of SGRBs and KN emissions [85–88], making them interesting candidates for MMA. NSBH detections

followed by SGRBs can be used as GW standard sirens [89]. One can also measure the fraction of SGRBs produced by BNS and NSBH systems [90], giving information about the preferred production mechanism of SGRBs. NSBH detections have also been shown to be potential candidates for the measurement of Hubble constant [61, 91, 92] and are capable of estimating it to larger distances than the BNS systems. GWs from NSBH mergers, with or without an EM counterpart, can also be used to constrain the NS EOS [93–98].

Fortunately, with the proposed advancements to current GW detectors and plans in place to construct more sensitive detectors (c.f. Section 1.1), we expect both the quantity and the quality of the NSBH detections to improve. In this study, we will analyze the performance of the six ground-based GW detector networks listed in Table 2.1. These networks are expected to be operational over timescales ranging from five to twenty years.

Table 2.1: The six XG ground-based GW detector networks that are included in the analysis, with the abbreviation used to refer to the network.

Network	Detectors
HLVKI+	LIGO (HL+), Virgo+, KAGRA+, LIGO-I+
VK+HLIv	Virgo+, KAGRA+, LIGO (HLI-Voy)
HLKI+E	LIGO (HL+), KAGRA+, LIGO-I+, ET
VKI+C	Virgo+, KAGRA+, LIGO-I+, CE-North
KI+EC	KAGRA+, LIGO-I+, ET, CE-North
ECS	ET, CE-North, CE-South

Several studies have looked at the possible improvements in the detection of GWs from compact binaries with the onset of XG detector networks [47, 99–101]. In this study, we assess the detection capability of the six GW detector networks for NSBH mergers and the science that can be extracted from these detections. This is carried out using `GWBENCH` [102], a software package that computes the SNR and the Fisher information matrix for a given GW network and waveform model from which one can obtain the errors in intrinsic and extrinsic parameters as well as the localization area of the signal on the sky.

This chapter is organized as follows. The parameters that characterize the populations of NSBH binaries are described in Sec. 2.2. The section also explains the methodology used to assess the measurement abilities of the networks. Next, we compare the detection capabilities of the six GW detector networks. In Sec. 2.3, we calculate the efficiency of

the detector networks and list the *reach* for each network. Using the efficiency and the estimated 'event-based' local merger rate density for NSBH systems, we calculate the yearly detection rate for each detector network. In Sec. 2.4, we present the quality of measurement of the NSBH detections and the accuracy with which several intrinsic and extrinsic parameters can be measured. In particular, we estimate how well events can be localized in the sky, to assess the possibility of an EM follow-up of GW signals from NSBH mergers (see Chapter 3 for a detailed discussion on MMA prospects with NSBH detections). In Sec. 2.5, we summarize our results and present our conclusions regarding the science that can be extracted from the NSBH detections using GW detector networks.

2.2 Population and Methodology

In order to evaluate the detection capabilities of the GW detector networks, we construct populations of NSBH systems and use a Fisher information matrix (FIM) approach to assess the performance of these networks in detecting GWs from the systems. Sec. 2.2.1 describes the properties of the populations and the rationale behind the assumptions that went into generating them. Sec. 2.2.2 describes the FIM approach and lists the parameters that were used to compute the FIMs.

2.2.1 Injection parameters

With the limited number of NSBH mergers detected, their population characteristics remain uncertain. While there are studies [2, 103, 104] that infer the mass and spin distributions from the set of detected NSBH events, the conclusions are susceptible to change with future detections. Due to the uncertainty in the properties of the actual population, we look at two populations to assess the science case of future GW detector networks.

For the first population, hereinafter referred to as *Pop-1*, we account for the fact that our knowledge of the NSBH population parameters is limited and choose broad distributions to describe the population. The black hole mass distribution is chosen to follow the `POWER+PEAK` [33] distribution between $[3\,\mathrm{M}_\odot, 100\,\mathrm{M}_\odot]$ and the neutron star mass is sampled from a uniform distribution between $[1\,\mathrm{M}_\odot, 2.9\,\mathrm{M}_\odot]$, where the upper bound on the NS mass has been set using Ref. [71]. The spins of both NSs and BHs are assumed to be aligned with the orbital angular momentum of the binary. With $(\boldsymbol{\chi_1}, \boldsymbol{\chi_2})$ denoting the dimensionless spin vectors of the BH and the NS, this implies that

$\chi_{1x} = \chi_{1y} = \chi_{2x} = \chi_{2y} = 0$. Neutron stars are assumed to be slowly rotating, with their spins chosen from a uniform distribution between $[-0.05, 0.05]$, while BH spins are taken from a uniform distribution between $[-0.75, 0.75]$.

One must note that for Pop-1 the masses and spins of BHs and NSs are sampled independently, ignoring any correlations that may exist between their properties due to physical processes involved in binary formation and evolution. To account for possible correlations, the masses and spins in the second population, hereinafter referred to as *Pop-2*, are derived from the *fiducial* model in Ref. [1]. The fiducial model is a binary population synthesis model for NSBH systems that form through the isolated binary formation channel. The model was constructed using `COMPAS` [105] and involved various physical assumptions summarized in Table 1 of Ref. [1]. For BH spins, we use metallicity-dependent fits provided in Eqs. (2) and (3) in Ref. [2]. It is expected that the angular momentum transport at the time of compact object formation is quite effective in removing most of the rotational energy from the core, making the formed NS/BH nearly non-rotating, if born first. If close enough to its compact object companion, the progenitor of the second-born NS/BH can tidally spin it up [4, 106–108]. Thus, the fit only applies to systems where the NS progenitor is formed first, allowing the progenitor of the second-born BH to have high spins as it can get tidally spun up by its companion. BHs are assumed to be non-spinning for the rest of the systems where the BH progenitor is formed first. Further, the NS spins are set to be zero. The BH and NS mass and spin profiles for Pop-2 are shown in Fig. 2.1.

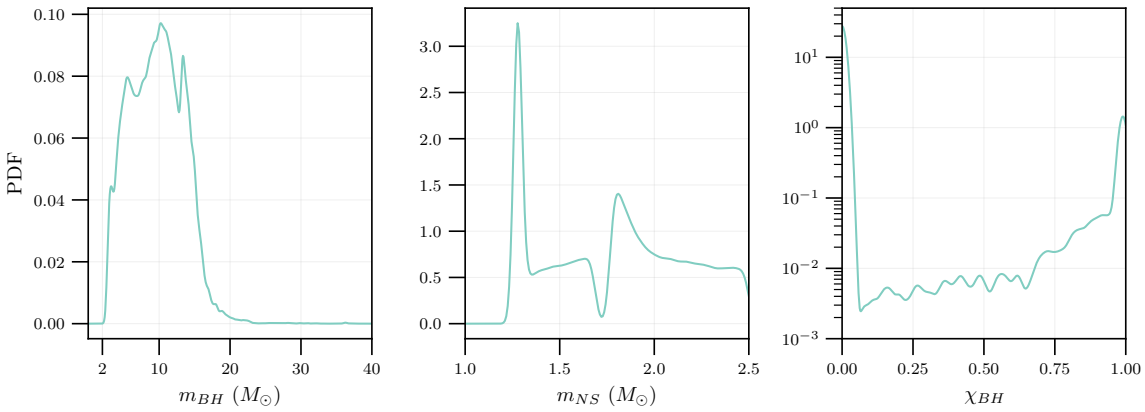

Figure 2.1: The probability density function (PDF) plots for the masses of the BH and the NS in Pop-2 derived from the fiducial model in Ref. [1] and the spins of BH derived from the fits in Ref. [2].

For each population, we generate 250,000 injections per redshift bin in each of the

six redshift bins: $z \in [0.02, 0.05]$, $[0.05, 1]$, $[1, 2]$, $[2, 4]$, $[4, 10]$ and $[10, 50]$. The luminosity distance D_L for each injection is obtained from the redshift z using `ASTROPY.PLANCK18` [109, 110]. $\cos(\iota)$ and $\cos(\delta)$, where ι and δ are the inclination angle and the declination respectively, are sampled uniformly between $[-1, 1]$. The right ascension α and the polarization angle ψ are sampled from a uniform distribution with bounds $[0, 2\pi]$. t_c and ϕ_c are the time and phase of coalescence respectively and can be chosen arbitrarily, we fix them to be 0. The above-mentioned parameters are summarized in Table 2.2.

Table 2.2: Parameters that characterize the two populations used in this study to evaluate the detection capabilities of the future detectors.

Parameter	Pop-1		Pop-2	
	Neutron Star	Black Hole	Neutron Star	Black Hole
Mass m	[1,2.9] $M_\odot$	[3,100] $M_\odot$	[1.26,2.50] $M_\odot$	[2.6,39.2] $M_\odot$
Mass Model	Uniform	`POWER+PEAK` [33]	Derived from the fiducial model [1]	
Spin χ	[-0.05,0.05]	[-0.75,0.75]	0	[0,1]
Spin Model	Aligned Uniform		Aligned	Eqs. (2) and (3) in Ref. [2]
z	Uniform in six bins: [0.02,0.05], [0.05,1], [1,2], [2,4], [4,10] and [10,50]			
D_L	z converted using `ASTROPY.Planck18`			
$\cos(\iota)$	Uniform in [-1,1]			
α	Uniform in [0,2π]			
$\cos(\delta)$	Uniform in [-1,1]			
ψ	Uniform in [0,2π]			
t_c, ϕ_c	0			

Once the 250,000 injections per redshift bin are generated, we logarithmically divide the total redshift range, i.e., $[0.02, 20]$, into 50 bins and randomly pick events from each of the finer bins according to the merger rate corresponding to that bin. This allows us to have a random collection of events in each bin and mitigate selection biases. The calculation of the merger rate as a function of redshift is given in Sec. 2.3.2. The end

product is the population of NSBH mergers assuming an observation time of 10 years for all the networks.

2.2.2 Methodology

The detector response to a GW signal is given by,

$$h^{(A)}(t, \boldsymbol{\mu}) = \; F_{+}^{(A)}(\alpha, \delta, \psi, \boldsymbol{\beta})\, h_{+}^{(A)}(t, \boldsymbol{\lambda}) + \; F_{\times}^{(A)}(\alpha, \delta, \psi, \boldsymbol{\beta})\, h_{\times}^{(A)}(t, \boldsymbol{\lambda}), \tag{2.1}$$

where h_+ and $h_\times$ are the two GW polarizations and F_+ and $F_\times$ are the *antenna pattern functions*. The index A denotes the detector. The antenna pattern functions depend on variables that describe the location of the source of GWs in the sky, i.e., α and δ, the polarization angle ψ, and the variables that describe the location of the detector itself, $\boldsymbol{\beta}$ (Tab. III in Ref. [102] lists the angles that describe the location for several detectors). The strain for each polarization depends on time t, the time and phase of coalescence, t_c and ϕ_c, and on the parameters that describe the source of GWs, $\boldsymbol{\lambda} = \{\mathcal{M}, \eta, \boldsymbol{\chi_1}, \boldsymbol{\chi_2}, \iota, D_L\}$, where $\mathcal{M}$ is the chirp mass, η is the symmetric mass ratio, ι is the inclination angle and D_L is the luminosity distance of the binary. Since we have assumed both the components of the binary to have aligned spins, $(\boldsymbol{\chi_1}, \boldsymbol{\chi_2}) = (\chi_{1z}, \chi_{2z})$. For a given detector, $\boldsymbol{\beta}$ is fixed. Thus, the strain h is a time-dependent function of $\boldsymbol{\mu} = \{\alpha, \delta, \psi, \mathcal{M}, \eta, \chi_{1z}, \chi_{2z}, \iota, D_L, t_c, \phi_c\}$.

We use the FIM to estimate the error in the measurement of these parameters using future ground-based GW detectors. The FIM calculation assumes the detector noise to be Gaussian and provides an analytical way to obtain the errors in the form of a covariance matrix Σ

$$\Sigma_{ij} = \Gamma_{ij}^{-1} = \left(\frac{\partial h}{\partial \theta_i}, \frac{\partial h}{\partial \theta_j} \right)^{-1}, \tag{2.2}$$

where h is the GW waveform, θ_i is the i^{th} parameter in $\boldsymbol{\mu}$, and Γ is the FIM. To obtain the FIM and the measurement errors, we use `GWBENCH` [102], which is a publicly available Python package that calculates the covariance matrix by numerically inverting the FIM. The package can apply numerical differentiation recipes to the GW waveforms that are part of the LIGO Algorithm Library (LAL) [111]. For our study, we use the `IMRPhenomXHM` [112] waveform model, which is a frequency-domain waveform for non-precessing BBH systems and includes contributions from higher-order modes. The waveform is suitable for BBH systems and cannot account for the tidal effects that can manifest in NSBH mergers. As tidal effects appear at the fifth PN order and only

contribute to the strain near the merger, we do not expect their exclusion in the calculation of FIM to significantly alter the results presented in this chapter. Additionally, we prefer using `IMRPhenomXHM` instead of a traditional NSBH-suited waveform like `PhenomNSBH` [113] due to the inclusion of higher-modes in the former model which is known to improve the estimation of parameters [114] and allows us to obtain a more realistic estimate of the measurement capabilities of detector networks. To calculate the FIM, the derivatives are taken with respect to parameters $\boldsymbol{\mu}$. `GWBENCH` also provides the SNR and the 90%-credible sky localization error Ω_{90}, which are used to compare the performance of detector networks.

2.3 Network Efficiency and Detection Rate

With increased detector sensitivities, we not only expect to probe the universe up to higher redshifts but also expect to detect events with unprecedented SNRs. Our expectations can be quantified in terms of the *network efficiency* and *detection rate*.

2.3.1 Network efficiency

We first introduce the notion of *matched-filtering* SNR and then use it to define the efficiency of a network. The matched-filter SNR ρ_A corresponding to a signal incident on a detector A is defined as,

$$\rho_A^2 = 4 \int_{f_L}^{f_U} \frac{|\tilde{h}_A(f)|^2}{S_n^A(f)} df, \tag{2.3}$$

where $\tilde{h}_A(f)$ is the frequency-domain waveform obtained by taking the Fourier transform of $h_A(t)$, $S_n^A(f)$ is the PSD of detector A and f_L and f_U are the lower and upper-frequency cutoffs. Then, for a network with N detectors, the matched-filtering SNR ρ is given by,

$$\rho^2 = \sum_{i=1}^{N} \rho_i^2. \tag{2.4}$$

At a given redshift, the network efficiency is defined as the fraction of events (at that redshift) that are detected by the network with a matched-filtering SNR greater than the threshold SNR ρ_*. We calculate the efficiency of networks listed in Table 2.1 as a function of redshift for two threshold SNRs: $\rho_* = 10$ and $\rho_* = 100$. The threshold $\rho_* = 10$ corresponds to the SNR above which we claim detection and $\rho_* = 100$ gives a measure of high-SNR events that can be detected. To calculate the efficiency, we logarithmically

divide the total redshift range, from $z = 0.005$ to $z = 20$, into 50 bins. For each bin $[z, z + dz]$, the efficiency ϵ is calculated by,

$$\epsilon\left(\rho_*, z\right) = \frac{1}{N_z} \sum_{k=1}^{N_z} \Pi\left(\rho_k - \rho_*\right), \tag{2.5}$$

where N_z is the number of events in that redshift bin and $\Pi(x)$ is the Heavyside function. The efficiency for the detector networks as a function of redshift for the two threshold SNRs is given in the left panel of Fig. 2.2. Note that Fig. 2.2 only shows the efficiency and the detection rate for Pop-1, since they are almost identical for Pop-2.

In order to compare the detector networks based on their detection efficiencies, we a measure called the *reach* of the detector. The reach (z_r) is defined as the redshift at which the efficiency of the network drops to 0.5, i.e., it is the redshift at which only half of all the coalescence events will be detected with SNR greater than ρ_*. As the efficiency is monotonic, this implies that the reach is equal to the redshift at which at least 50% of the events *within* that redshift will be observed with SNR greater than ρ_*. It must be noted that the definition of reach varies across literature and care must be taken when comparing results from different studies.

The values for the reach of the networks for both populations are given in Table 2.3. For the detection of NSBH systems in Pop-1, i.e., $\rho_* = 10$, the `HLVKI+` network has a reach of $z = 0.21 \sim 1$ Gpc and is expected to miss events beyond ~ 6 Gpc. As most of the high-SNR events are the ones that are situated close-by, the reach for $\rho_* = 100$ drops to $z = 0.022$. The Voyager upgrades improve the reach by a factor of ~ 2 for both the population models. All networks in our study that have at least one of the ET or CE detectors have a reach $z_r > 1$, with the ECS network having the longest detection range of all, with a reach of $z = 6$, probing the star formation rate and metallicity distribution up to high redshifts.

2.3.2 Detection Rate

The detection rate is defined as the number of NSBH mergers up to a given redshift that are detected by a network in a year with a matched-filtering SNR greater than the threshold SNR. It depends on the total merger rate as well as the efficiency of the network. In the detector frame, the total merger rate R_d up to redshift z is given by

$$R_d(z) = \int_0^z \frac{1}{(1+z')} \frac{dR}{dz'} = \int_0^z \frac{\dot{n}(z')}{(1+z')} \frac{dV}{dz'}, \tag{2.6}$$

Table 2.3: The reach for the six detector networks for the cases when the threshold SNR $\rho_* = 10$ and $\rho_* = 100$.

Network	*Pop-1*		*Pop-2*	
	$\rho_* = 10$	$\rho_* = 100$	$\rho_* = 10$	$\rho_* = 100$
HLVKI+	0.21	0.022	0.23	0.023
VK+HLIv	0.47	0.045	0.5	0.049
HLKI+E	1.6	0.12	1.6	0.13
VKI+C	2.7	0.19	2.9	0.2
KI+EC	3.9	0.24	4.2	0.25
ECS	6	0.32	6.6	0.34

where $\dot{n}(z')$ is the merger rate density in the comoving frame, dV/dz' is the comoving volume element (which itself is a function of redshift) and the $(1 + z')$ term in the denominator converts the detection rate from the source frame to the detector frame by accounting for the time dilation. Among these mergers, only a fraction are detected by a network, which is determined by the efficiency of the network. Hence, the detection rate $D_R(z)$ is given by

$$D_R(z) = \int_0^z \epsilon(z', \rho_*) \frac{\dot{n}(z')}{(1+z')} \frac{dV}{dz'}. \tag{2.7}$$

Note that the calculation of the detection rate depends on the model used to calculate the merger rate density $\dot{n}(z)$. Further, $\dot{n}(z)$ is calibrated by setting the local ($z = 0$) value equal to the observed local merger rate density for NSBH systems. We follow the SFR model described in Ref. [115] which utilizes the GRB data to calculate the SFR up to high redshifts. In addition to the SFR, there is a time delay between the formation and the merger of compact binaries, which is described by various time-delay models [116–118]. Following Ref. [119], we choose the log-normal time delay model proposed in Ref. [116] for our study. The redshift distribution based on these assumptions can be expressed in an analytical form and is presented in Refs. [119, 120]. The inferred local merger rate density is reported to lie between 7.8–140 $\text{Gpc}^{-3}\ \text{yr}^{-1}$ [33]. We calibrate $\dot{n}(z)$ by fixing the local merger rate density, $\dot{n}(0) = 45\ \text{Gpc}^{-3}\ \text{yr}^{-1}$, which is the median event-based NSBH merger rate density reported in Ref. [76], calculated assuming that the observed NSBH systems are a representative of the NSBH population. The obtained curves for detection rate as a function of redshift for the six detector networks are shown in the right panel of Fig. 2.2. The grey region shows the uncertainty in the NSBH merger rate which is due to the uncertainty in the value of the local merger rate density. Based on

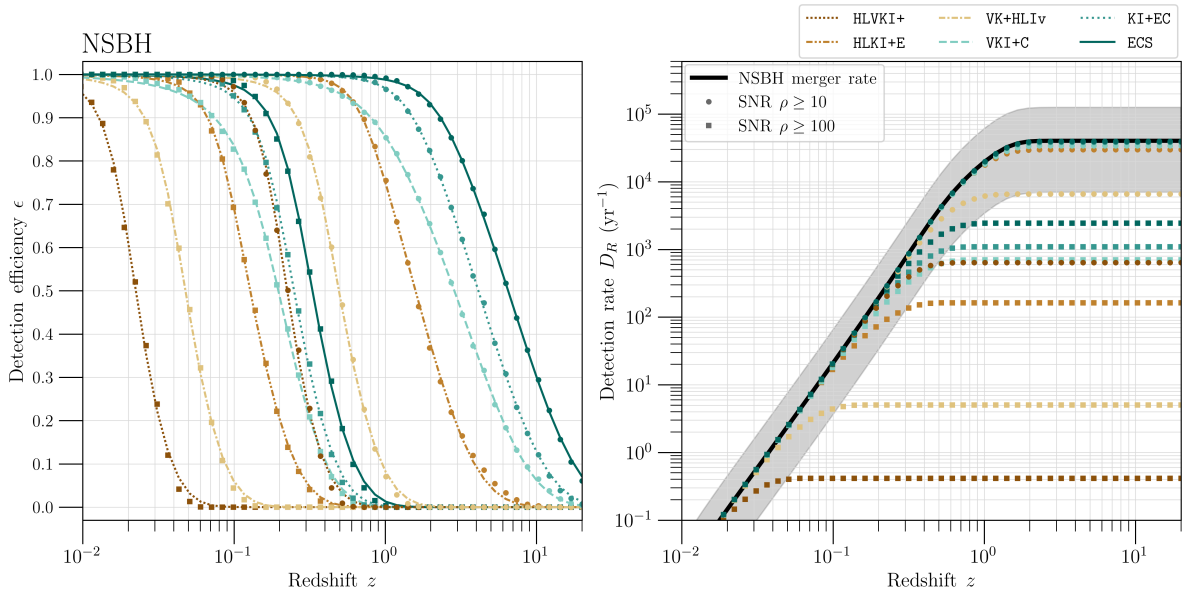

Figure 2.2: *Left panel:* The network efficiency curves for the six XG detector networks. The markers represent the efficiency at corresponding redshift values, and the lines are the *best-fit* sigmoid functions which are good approximations of the efficiency curves. *Right panel:* The detection rate as a function of redshift for the detector networks. The black solid line refers to the total NSBH merger rate. The gray shaded area shows the variation in the total merger rate due to the uncertainty in the value of the local merger rate density.

the model used, we obtain the cosmic merger rate for NSBH systems, i.e., the number of NSBH mergers up to $z = 20$ to be $4.0^{+8.5}_{-3.3} \times 10^4$ yr^{-1}, where the upper and lower bounds are calculated using the upper and lower bounds of the local merger rate density.

With $\dot{n}(0) = 45$ Gpc^{-3} yr^{-1}, from the right panel of Fig. 2.2, we expect $\mathcal{O}(100)$ detections in `HLVKI+`, $\mathcal{O}(10^3)$ for `VK+HLIv` and $\mathcal{O}(10^4)$ for `HLKI+E`, `VKI+C`, `KI+EC` and `ECS`, with SNR $\rho > 10$ every year. Thus, every network that has at least one XG detector is expected to observe $\mathcal{O}(10^4)$ events every year. Moreover, the `ECS` network is expected to detect 97% of the cosmic population of NSBH mergers with SNR $\rho > 10$.

2.4 Measurement quality and sky localization

In Sec. 2.3, we noted that the XG networks will not only detect a large number of events, but a significant number of these events will also be detected at high SNRs. Using the methods described in Secs. 2.2.1 and 2.3.2, we construct the cosmic population of NSBH systems. The expected number of events detected with SNR greater than 10, 30, and

100, are presented in Table 2.4. When comparing the numbers for the Pop-1 and Pop-2 populations, we find them to be of the same order. However, there are more events with higher SNRs in Pop-1 as compared to Pop-2. This is attributed to the different BH mass models in the two populations: about 0.5% of the events in Pop-2 have BH mass greater than $20\,M_\odot$, whereas, in Pop-1, $\sim 17\%$ of the events have BH mass greater than $20\,M_\odot$. This, along with the fact that higher total mass binaries are expected to be detected at higher SNRs, explains the small differences in the number of systems belonging to the two populations detected with SNRs greater than certain threshold SNRs. The `HLVKI+` detector is expected to detect $\mathcal{O}(100)$ events with SNR > 10 and $\mathcal{O}(10)$ with SNR > 30 every year, but it is unlikely to detect any NSBH mergers with SNR greater than 100. However, improving the sensitivities of the three LIGO detectors with Voyager upgrades results in the detection of $\mathcal{O}(10^3)$, $\mathcal{O}(100)$ and $\mathcal{O}(1)$ events every year with SNR > 10, 30 and 100 respectively. The inclusion of the Einstein Telescope in the `HLKI` network with A+ sensitivities further improves this number to $\mathcal{O}(10^4)$ detections with SNR > 10 every year, and $\mathcal{O}(100)$ detections with SNR > 100 every year. The remaining three networks all of which contain the `CE-North` detector, i.e., `VKI+C`, `KI+EC` and `ECS` are expected to detect $\mathcal{O}(10^5)$ and $\mathcal{O}(10^4)$ events every year with SNR > 10 and 30 respectively. The `ECS` network is expected to detect the most number of NSBH mergers with SNR > 100, detecting $\mathcal{O}(10^3)$ events every year, an order of magnitude greater than the expected values for the `VKI+C` network.

High fidelity events, i.e., events that are detected with a large SNR, allow for accurate estimation of parameters, like masses and spins, which not only aid in differentiating NSBH from BBH and BNS mergers (based on component masses) but also in testing the predictions of general relativity. Further, high-precision measurements of the masses and spins of the compact objects will unravel the population characteristics of the NSBH systems and help test the predictions of various channels that explain the formation of such systems. Given that a fraction of NSBH mergers is also expected to result in the generation of kilonovae, accurate luminosity distance and sky area measurements will allow an independent measurement of the Hubble-Lemaître constant up to greater distances than BNS systems [61]. In Figs. 2.3 and 2.4, we present the cumulative density function (CDF) plots portraying the parameter measurement abilities of the six detector networks for Pop-1 and Pop-2 respectively. In particular, we present the CDFs for SNR ρ, 90%-credible sky area Ω_{90}, fractional error in the luminosity distance $\Delta D_L/D_L$, absolute error in the inclination angle $\Delta\iota$ (in radians), fractional error in the chirp mass $\Delta\mathcal{M}/\mathcal{M}$, absolute error in the symmetric mass ratio $\Delta\eta$ and the absolute errors in the

Table 2.4: The cosmic merger rate per year and the number of events that are detected every year with SNRs greater than 10, 30, and 100 for the six detector networks. The lower and upper bounds in the reported numbers are calculated using the uncertainty in the local merger rate density for NSBH mergers.

Cosmic Rate	$4.0^{+8.5}_{-3.3} \times 10^4$ yr^{-1}		
SNR ρ	> 10	> 30	> 100
	Pop-1		
HLVKI+	$5.1^{+10.8}_{-4.3} \times 10^2$	$1.5^{+3.1}_{-1.2} \times 10$	$0.0^{+0.5}_{-0.0}$
VK+HLIv	$5.7^{+12.1}_{-4.7} \times 10^3$	$2.1^{+4.6}_{-1.8} \times 10^2$	$4.1^{+8.8}_{-3.7}$
HLKI+E	$2.9^{+6.0}_{-2.4} \times 10^4$	$5.5^{+11.6}_{-4.5} \times 10^3$	$1.7^{+3.4}_{-1.4} \times 10^2$
VKI+C	$3.3^{+7.1}_{-2.8} \times 10^4$	$1.3^{+2.7}_{-1.0} \times 10^4$	$6.6^{+14.3}_{-5.5} \times 10^2$
KI+EC	$3.8^{+8.0}_{-3.1} \times 10^4$	$1.8^{+3.8}_{-1.5} \times 10^4$	$1.0^{+2.2}_{-0.8} \times 10^3$
ECS	$3.9^{+8.3}_{-3.3} \times 10^4$	$2.5^{+5.2}_{-2.0} \times 10^4$	$2.3^{+4.8}_{-1.9} \times 10^3$
	Pop-2		
HLVKI+	$4.8^{+10.2}_{-4.0} \times 10^2$	$1.1^{+2.9}_{-1.0} \times 10$	$0.0^{+0.4}_{-0.0}$
VK+HLIv	$5.5^{+11.6}_{-4.5} \times 10^3$	$1.9^{+4.0}_{-1.6} \times 10^2$	$3.7^{+8.5}_{-3.3}$
HLKI+E	$2.8^{+6.0}_{-2.3} \times 10^4$	$5.0^{+10.6}_{-4.1} \times 10^3$	$1.2^{+2.6}_{-1.0} \times 10^2$
VKI+C	$3.3^{+7.0}_{-2.7} \times 10^4$	$1.2^{+2.6}_{-1.0} \times 10^4$	$5.4^{+11.3}_{-4.5} \times 10^2$
KI+EC	$3.8^{+8.0}_{-3.1} \times 10^4$	$1.7^{+3.6}_{-1.4} \times 10^4$	$8.5^{+18.0}_{-7.0} \times 10^2$
ECS	$3.9^{+8.3}_{-3.2} \times 10^4$	$2.4^{+5.1}_{-2.0} \times 10^4$	$1.9^{+4.1}_{-1.6} \times 10^3$

dimensionless aligned spins of the black hole and the neutron star, i.e., $\Delta\chi_1$ and $\Delta\chi_2$ respectively.

From Figs. 2.3 and 2.4, we see that the overall trend in measurement quality when comparing different detector networks is the same for both populations. From the plots for SNR, we see that both `ECS` and `KI+EC` detect almost all the NSBH mergers with $\rho > 10$, whereas `HLKI+E` and `VKI+C` detect only $\sim 80\%$ of the events with $\rho > 10$. The fraction falls to $\sim 1\%$ for the `HLVKI+` network. Voyager upgrades improve the detectability by an order of magnitude, detecting $\sim 15\%$ of the events. For the fractional error in $\mathcal{M}$ and the absolute error in η, we see that all the networks detect almost all the events with $\Delta\mathcal{M}/\mathcal{M}$ better than 10^{-4} and $\Delta\eta$ better than 10^{-3}, going up to precision of $\mathcal{O}(10^{-8})$ and $\mathcal{O}(10^{-7})$ respectively for $\mathcal{O}(10)$ events. This points to the estimation of the binary masses with unprecedented precision using future GW detector networks. Further, for all detected events, the spins of both the compact objects can be measured better than

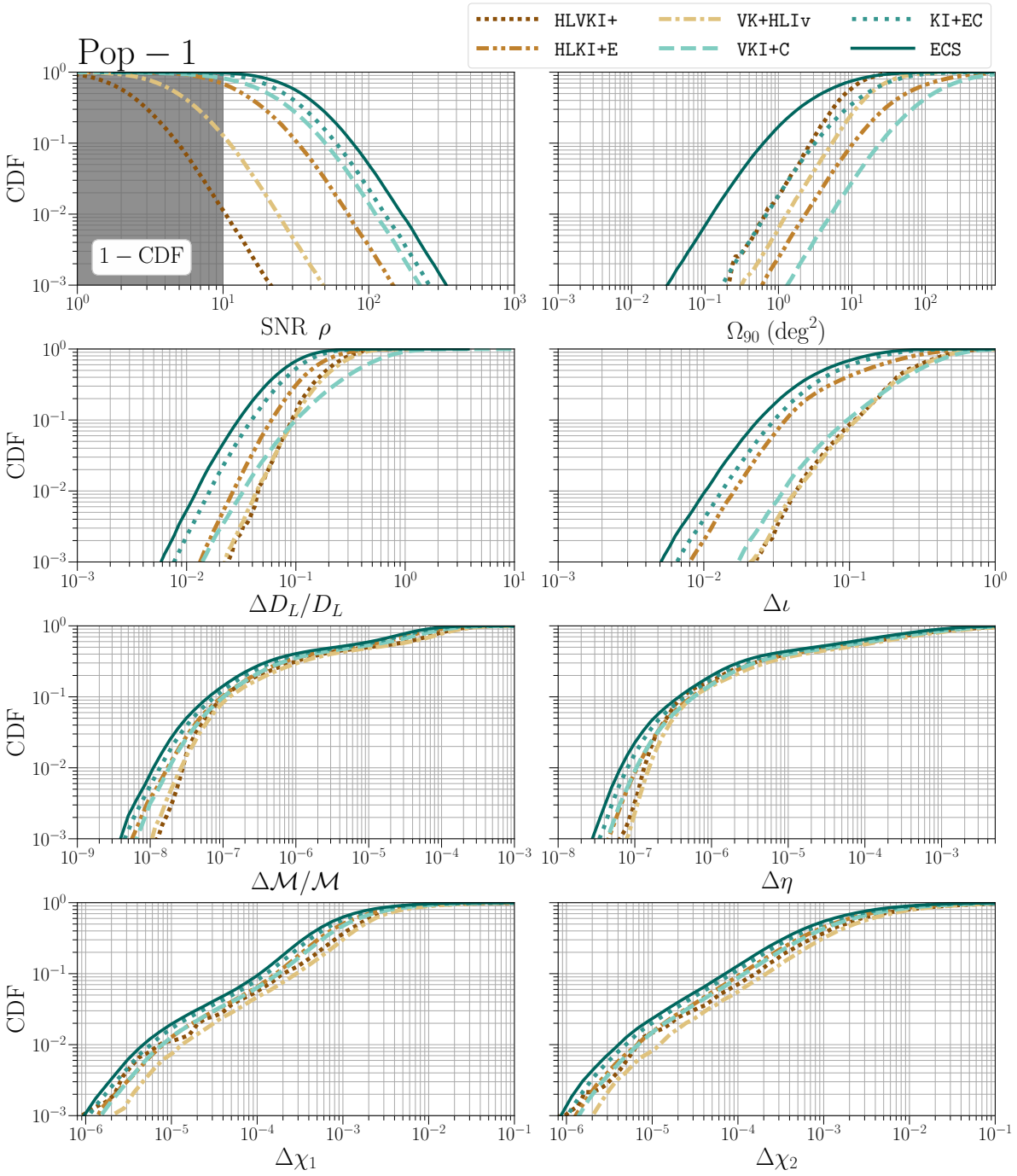

Figure 2.3: The CDF plots showing the trends in SNR ρ and sky-localization Ω_{90} of the detected events in Pop-1. It also shows the CDFs for fractional errors in chirp mass and luminosity distance, i.e., $\Delta\mathcal{M}/\mathcal{M}$ and $\Delta D_L/D_L$, and absolute errors in inclination angle, symmetric mass ratio and the spins of the BH and the NS, i.e., $\Delta\iota$, $\Delta\eta$, $\Delta\chi_1$ and $\Delta\chi_2$, respectively.

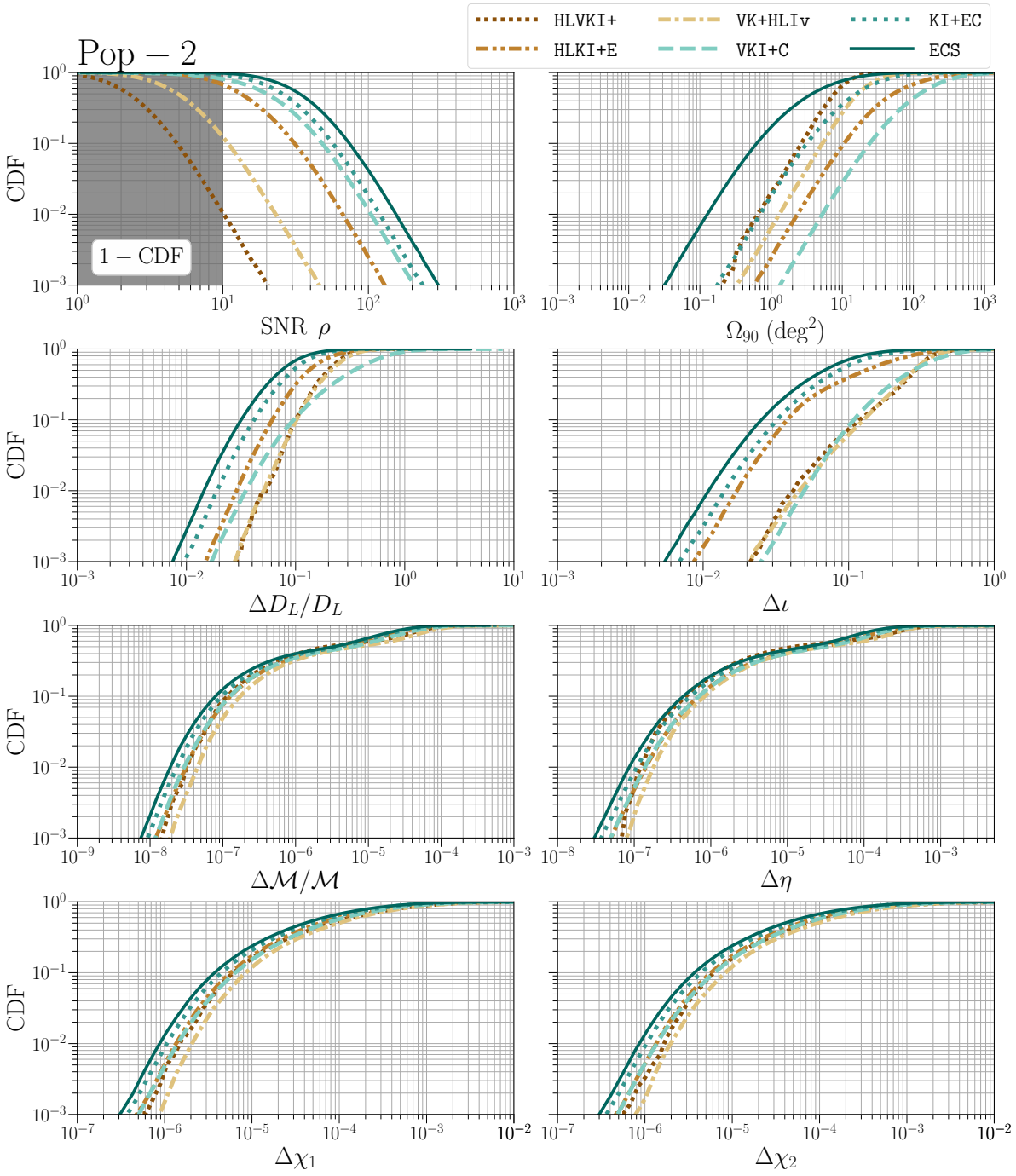

Figure 2.4: The CDF plots for the SNR, sky-localization, fractional errors in chirp mass and luminosity distance, and absolute errors in the inclination angle, symmetric mass ratio and the spins of the BH and the NS for the detected events in Pop-2.

an absolute error of 10^{-2}. This precision in spin measurements will uncover the spin distributions of BHs and NSs involved in NSBH mergers and shed light on the physics involved in the formation of these binaries.

The visibility of the EM transients that may follow the GW chirp depend on the luminosity distance between the binary and the observer and the orientation of the binary with respect to the line-of-sight of the observer. In addition, precise localization of the event can aid the follow-up efforts of EM telescopes and prove decisive in detecting EM transients. Figures 2.3 and 2.4 show that the `ECS` and the `KI+EC` networks detect almost all their events with fractional errors in the luminosity distance better than 20% and absolute error in inclination angle better than 0.2 rad. While `VK+HLIv` indeed detects more events than `HLVKI+`, the overlapping CDF plots for $\Delta\mathcal{M}/\mathcal{M}$, $\Delta\eta$, $\Delta\chi_1$ and $\Delta\chi_2$, $\Delta D_L/D_L$ and $\Delta\iota$ show that the fraction of events detected with certain measurement quality remains the same between the two networks. In fact, the events that `HLVKI+` does detect, it does a remarkable job at localizing them in the sky, resolving 90% of its events to better than $20\,\mathrm{deg}^2$, alongside the `ECS` network. The `ECS` network performs the best in terms of sky localization as well, detecting $\mathcal{O}(10)$ events every year with a resolution $\sim \mathcal{O}(10^{-2})\,\mathrm{deg}^2$. For comparison, the localization of GW170817 using the `HLV` network was $16\,\mathrm{deg}^2$ [121]. The number of detections per year for each detector network with $\Omega_{90} \leq 10$, 1 and 0.1, and $\Delta D_L/D_L \leq 0.1$ and 0.01 for both the populations are listed in Table 2.5. The corresponding plot is shown in Figs. 2.5 and 2.6 for the two populations, respectively, which convey the relationship between the SNR, the 90%-credible sky area, and the redshift associated with the binary for events in both the populations. With `HLVKI+`, we can expect to detect $\mathcal{O}(1)$ event every 10 years for which the sky position is localized to better than $1\,\mathrm{deg}^2$. `VKI+C` is expected to detect about twice the number of events detected by `HLVKI+` with the same sky localization, whereas `VK+HLIv` and `HLVKI+E` are expected to detect about 4 and 7 times as many events, respectively. `KI+EC` will not only detect ~ 60 events every year with the sky localization better than $1\,\mathrm{deg}^2$, it is also expected to see $\mathcal{O}(1)$ event *every year* with the localization better than $0.1\,\mathrm{deg}^2$. `ECS` is expected to outperform `KI+EC` by an order of magnitude, detecting $\mathcal{O}(10)$ events every year with localization better than $0.1\,\mathrm{deg}^2$ and ~ 5 events in a span of 10 years localized to an area smaller than $0.01\,\mathrm{deg}^2$. As the position of these small number of events is localized to such a small area in the sky, it could even be possible to identify their host galaxies with only the GW signal (subject to the completeness of galaxy catalogues) [59, 122].

Table 2.5: The number of detections per year for the six detector networks with 90%-credible sky area less than 10, 1, 0.1 and 0.01 deg^2 and fractional error in luminosity distance less than 0.1 and 0.01.

Metric	Ω_{90} (deg)^2				$\Delta D_L/D_L$	
Quality	≤ 10	≤ 1	≤ 0.1	≤ 0.01	≤ 0.1	≤ 0.01
			Pop-1			
HLVKI+	$2.9^{+6.1}_{-2.4} \times 10^2$	$8.7^{+19.5}_{-7.3}$	$2.0^{+2.0}_{-2.0} \times 10^{-1}$	0	$6.1^{+12.8}_{-4.8} \times 10$	$0.0^{+0.1}_{-0.0}$
VK+HLIv	$1.4^{+2.9}_{-1.1} \times 10^3$	$3.1^{+7.1}_{-2.6} \times 10$	$6.0^{+13.0}_{-6.0} \times 10^{-1}$	0	$5.9^{+12.7}_{-4.9} \times 10^2$	$3.0^{+9.0}_{-3.0} \times 10^{-1}$
HLKI+E	$2.4^{+5.1}_{-2.0} \times 10^3$	$6.0^{+13.4}_{-4.9} \times 10$	$1.9^{+2.3}_{-1.9}$	0	$8.2^{+17.5}_{-6.8} \times 10^3$	$9.9^{+22.1}_{-8.4}$
VKI+C	$8.1^{+17.3}_{-6.6} \times 10^2$	$1.9^{+4.1}_{-1.6} \times 10$	$2.0^{+6.0}_{-2.0} \times 10^{-1}$	0	$3.1^{+6.5}_{-2.5} \times 10^3$	$1.1^{+2.2}_{-0.9} \times 10$
KI+EC	$1.2^{+2.6}_{-1.0} \times 10^4$	$6.1^{+13.0}_{-5.0} \times 10^2$	$1.4^{+3.1}_{-1.2} \times 10$	$2.0^{+4.0}_{-2.0} \times 10^{-1}$	$1.9^{+4.0}_{-1.6} \times 10^4$	$7.6^{+15.0}_{-6.0} \times 10$
ECS	$2.9^{+6.1}_{-2.4} \times 10^4$	$6.1^{+13.0}_{-5.0} \times 10^3$	$2.4^{+5.1}_{-1.9} \times 10^2$	$5.1^{+9.8}_{-4.2}$	$2.5^{+5.4}_{-2.1} \times 10^4$	$1.8^{+3.7}_{-1.5} \times 10^2$
			Pop-2			
HLVKI+	$3.0^{+6.4}_{-2.5} \times 10^2$	$9.1^{+20.3}_{-7.7}$	$0.0^{+0.3}_{-0.0}$	0	$4.4^{+8.3}_{-3.7} \times 10$	$0.0^{+0.1}_{-0.0}$
VK+HLIv	$1.4^{+2.9}_{-1.1} \times 10^3$	$3.2^{+6.8}_{-2.6} \times 10$	$4.0^{+15.0}_{-4.0} \times 10^{-1}$	0	$4.7^{+9.7}_{-3.9} \times 10^2$	$0.0^{+0.3}_{-0.0}$
HLKI+E	$2.3^{+4.9}_{-1.9} \times 10^3$	$5.9^{+12.2}_{-4.8} \times 10$	$9.0^{+35.0}_{-8.0} \times 10^{-1}$	0	$8.2^{+17.3}_{-6.7} \times 10^3$	$7.1^{+16.3}_{-6.2}$
VKI+C	$8.2^{+17.2}_{-6.7} \times 10^2$	$1.8^{+3.8}_{-1.5} \times 10$	$3.0^{+5.0}_{-3.0} \times 10^{-1}$	0	$3.3^{+6.9}_{-2.7} \times 10^3$	$4.8^{+8.3}_{-4.0}$
KI+EC	$1.2^{+2.6}_{-1.0} \times 10^4$	$6.0^{+12.6}_{-4.9} \times 10^2$	$1.2^{+3.1}_{-1.0} \times 10$	$0.0^{+0.3}_{-0.0}$	$1.9^{+4.0}_{-1.6} \times 10^4$	$3.7^{+7.5}_{-3.1} \times 10$
ECS	$2.9^{+6.2}_{-2.4} \times 10^4$	$6.1^{+12.8}_{-5.0} \times 10^3$	$2.3^{+4.9}_{-1.9} \times 10^2$	$4.5^{+11.7}_{-3.8}$	$2.6^{+5.5}_{-2.1} \times 10^4$	$9.1^{+19.0}_{-7.6} \times 10$

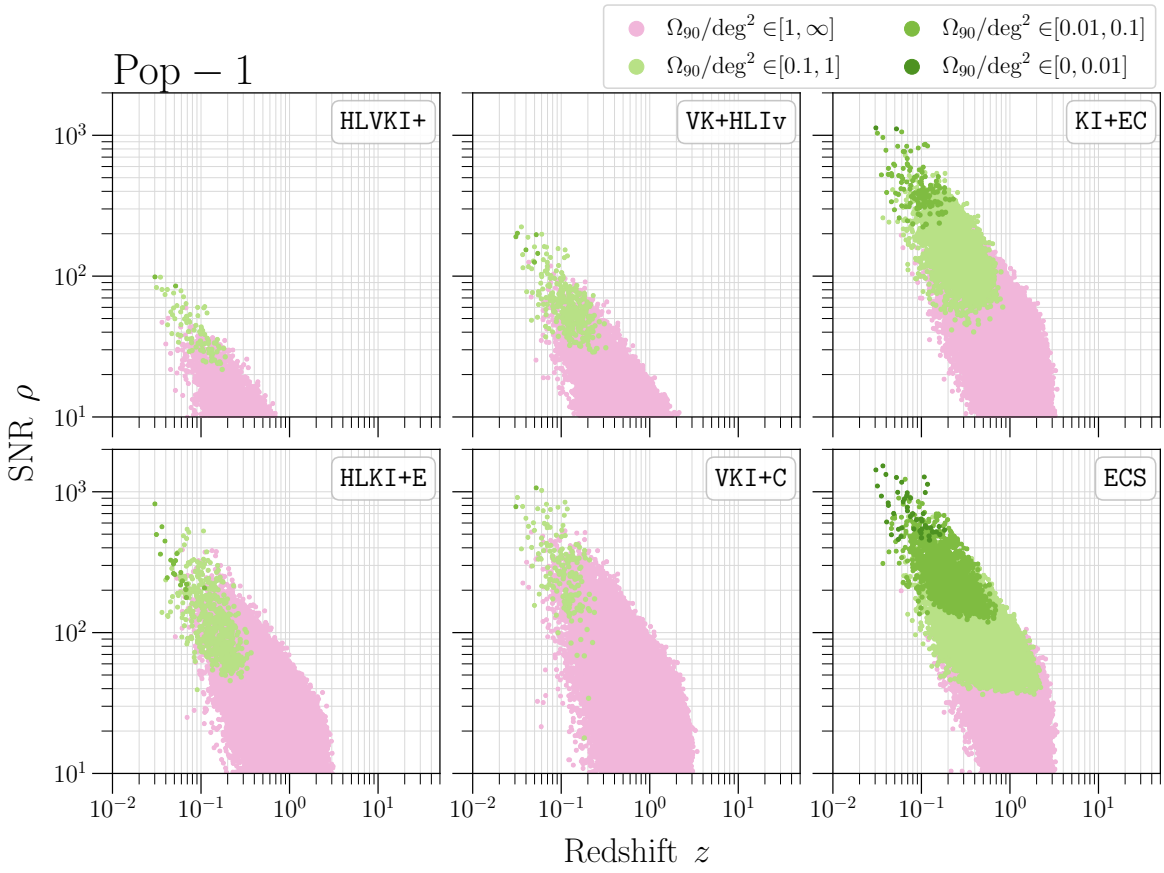

Figure 2.5: Plot showing the relationship between SNR ρ, sky localization Ω_{90} and the redshift z for events belonging to the Pop-1 population, corresponding to the six GW detector networks. Each marker is an event detected by the corresponding detector network in an observation time of 10 years. The color of the marker conveys how well that event can be localized in the sky using GW observation.

2.5 Conclusions

NSBH binaries were first discovered in 2020 during the third observing run of the LIGO and Virgo detectors. With two confirmed detections we can be confident that these intriguing systems will be abundantly observed by upgraded detectors and new observatories. With large mass asymmetries and black hole spins either large or misaligned with the orbital angular momentum, we can expect NSBH signals to reveal relativistic gravity in action with unprecedented detail. NSBH binaries will be particularly interesting as they could emit a significant fraction of their energy in higher multipole modes allowing precision tests of general relativity but also enabling accurate measurement of the Hubble parameter.

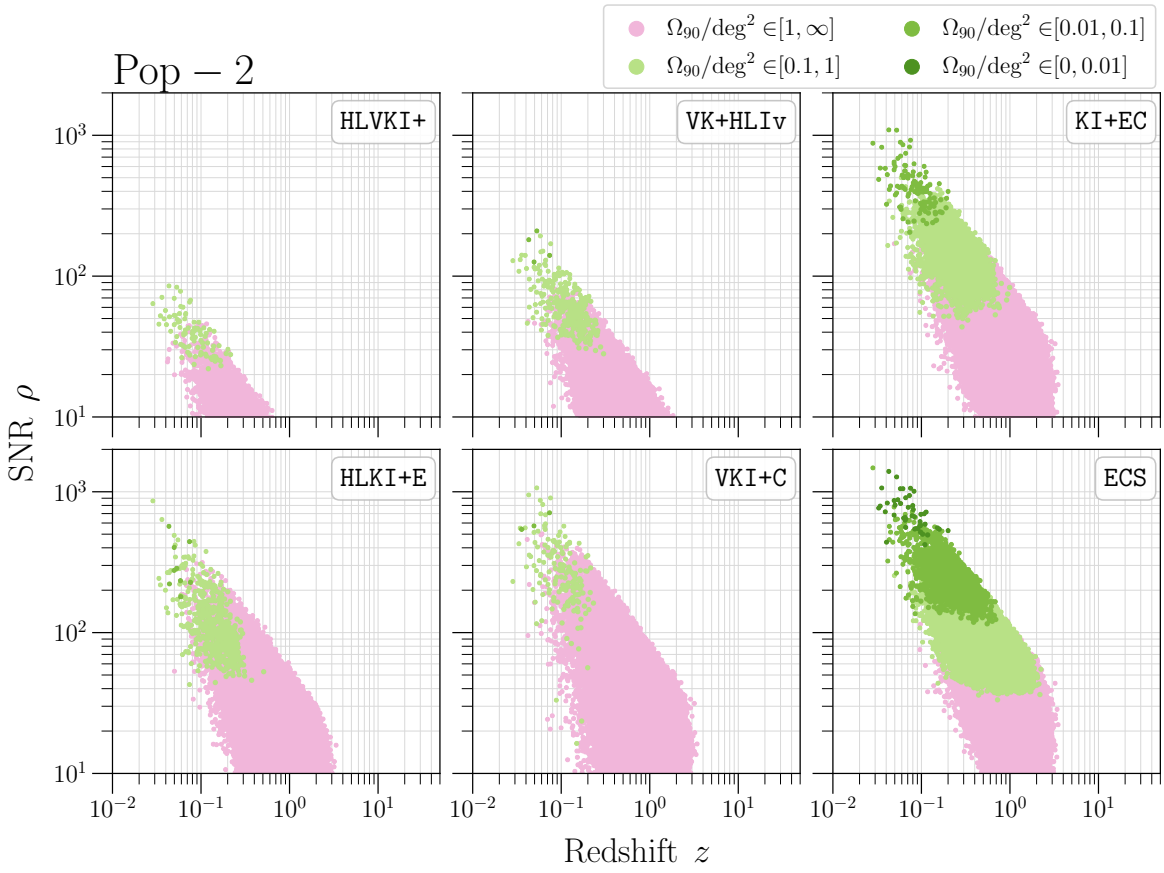

Figure 2.6: Plot showing the relationship between ρ, Ω_{90} and z for events belonging to the Pop-2 population, in an observation time of 10 years.

In this chapter, we have evaluated the science potential of NSBH binaries in two networks comprising of upgraded LIGO and Virgo (A+ and Voyager upgrades) and four networks comprising of one or more of Cosmic Explorer and Einstein Telescope operating in tandem with upgraded LIGO and Virgo (cf. Fig. 1.1 and Table 2.1). We consider two different population models for NSBH systems (cf. Table 2.2) but our main conclusions equally apply to both of the populations. The performance of the networks was evaluated using several metrics as follows:

Detection rate: The cosmological merger rate of NSBH populations, assuming they evolve with redshift in the same way star formation rate does (apart from time delays), is about 40,000 events per year (c.f. Fig. 2.2, right panel and Table 2.4). At the detection SNR threshold of $\rho_* = 10$, the A+ and Voyager upgrades will see 1% and 10% of the mergers, respectively, while future observatories will observe more than 90% of this population. There is great utility to large catalogs as they can help discriminate

between different astrophysical formation channels of NSBH or facilitate cosmological measurements. For other applications, such as tests of general relativity, the signal quality is of prime importance. While imminent upgrades will not witness high fidelity signals of SNR > 100, several tens to hundreds of such events will be observed each year by CE and ET.

Detection efficiency: The merging population of NSBH increases steeply with redshift as the star formation rate grows, but tapers off at around a redshift of $z = 2$ (c.f. Fig. 2.2, right panel). While the A+ and Voyager upgrades will have a *redshift reach* of $z \sim 0.2$ and $z \sim 0.5$, respectively (c.f. Fig. 2.2, left panel), future networks will have a reach of $z \sim 1.5$ to 6 depending on the number of detectors in the network. In particular, the ECS network comprising of one Einstein Telescope and two Cosmic Explorers will observe more than 90% of all the sources at $z = 2$. This degree of completeness will help mitigate systematics arising from an incomplete catalog.

Sky localization: A metric of importance is the degree to which a source can be localized in the sky. Precise localization helps in the EM follow-up of GW transients, measurement of cosmological parameters, identification of lensed events, and so on. Imminent upgrades will localize hundreds to thousands of events to within 10 deg^2 but it takes a pair of XG observatories to localize 30% of the events, or tens of thousands, to within the same error region. The number of events that can be localized to within 1 deg^2 is typically a factor 30 smaller for all networks except the network with three XG observatories, for which it reduces only by a factor of 5. However, not all of these events can be followed up even by the best optical and infrared telescopes, but only mergers within a redshift of 0.5. Within this redshift, the number of available sources for EM follow-up won't change for A+ and Voyager networks, but they are ten times smaller, i.e., thousands of mergers, for XG observatories.

In summary, NSBH mergers will not only be seen in plenty with the next generation observatories, but they will also provide insights into some of the key science questions in astrophysics and cosmology.

Declaration

The author of this dissertation was responsible for generating all the results that are presented in this chapter. The contents of this chapter have been published in the journal Physical Review D of the American Physical Society with reference [73].

Chapter 3
Facilitating multi-messenger astronomy with NSBH mergers

The universe is a communion of subjects, not a collection of objects.
— Thomas Berry

3.1 Introduction

As discussed extensively in Chapter 2, XG GW observatories such as Cosmic Explorer (CE) and Einstein Telescope (ET) are poised to significantly advance our understanding of NSBH mergers. The substantial enhancements in detector sensitivity will yield unprecedented numbers of NSBH detections, extending the observational horizon deeper into the cosmos and greatly refining our capability to measure both intrinsic and extrinsic binary parameters precisely.

However, the scientific potential of NSBH mergers extends far beyond GW observations alone. These systems are promising multi-messenger sources, anticipated under favorable conditions to produce EM counterparts such as KNe and SGRBs. While Chapter 2 primarily addressed the detectability and parameter measurability of NSBH mergers from a purely GW perspective, this chapter broadens our focus to explore MMA prospects arising from these detections. In particular, we assess the feasibility of detecting EM counterparts to GW signals from NSBH mergers and discuss the wider astrophysical implications of these observations.

We begin by examining the specific conditions under which NSBH mergers are likely to generate bright and detectable EM counterparts. Leveraging the detection capabilities and sky-localization precision of XG networks detailed previously, we quantify the prospects for successful EM follow-up and multi-wavelength observations in Sec. 3.2. In Sec. 3.3, we conduct a detailed case study of GW230529 [3], an NSBH merger observed

during the fourth observing run of the LVK detectors. Although no EM counterpart was identified for this event, our analysis quantifies the expected ejecta from the tidal disruption of the NS and explores the detectability of associated kilonova emission using the capabilities of the Vera C. Rubin Observatory.

In summary, this chapter synthesizes the gravitational-wave detection perspectives outlined in Chapter 2 with broader astrophysical insights achievable through multi-messenger observations, emphasizing the pivotal role of EM counterparts in enriching our scientific

3.2 Detecting EM counterparts of NSBH mergers

As discussed in Section 1.4, during the inspiral phase of an NSBH merger event, the NS can be tidally disrupted by the BH, which can either happen when the NS is outside the ISCO, or when the NS is within it. If the tidal disruption occurs when the NS is closer to the BH than R_{ISCO}, any tidally-disrupted material is swallowed by the BH and no EM counterpart is generated. When the NS gets disrupted outside R_{ISCO}, a fraction of the NS mass can both, be dynamically ejected, and form an accretion disk around the remnant BH. This material present outside the remnant powers the EM counterparts which may be detectable by an EM telescope. The possible EM counterparts include SGRBs and KNe, among others. KNe are produced by the radioactive decay of decompressed NS material, while the mechanism that produces gamma-ray bursts is still not fully understood, but it is believed to require strong magnetic fields [72, 86]. The possibility of detecting GWs along with the EM counterpart makes NSBH mergers exciting prospects for MMA.

In the following subsections, we will explore the potential of NSBH mergers detected with XG observatories as candidates for MMA. In Sec. 3.2.1, we discuss the sub-population considered for the MMA study. We also present plots detailing the accuracy in the luminosity distance, inclination angle, and 90%-credible sky-area measurement for the events in this sub-population. In Sec. 3.2.2, we discuss the possibility of sending *early-warning* alerts to EM telescopes in order to maximize the science output from EM detections. Finally, in Sec. 3.2.3, we examine KN as a potential EM counterpart to gravitational waves. We present the expected number of KN detections corresponding to NSBH merger events detected with the six GW detector networks and describe the method used to compute the same.

3.2.1 Sub-population for MMA

For the purpose of MMA, we restrict our population to events that lie within a redshift of $z = 0.5$. While SGRBs can be detected up to larger redshifts than $z = 0.5$, our study will be focusing on the detection of KNe, which are not expected to be visible to the EM telescopes beyond this redshift (as will be seen in Sec. 3.2.3). For this sub-population, we look at the measurement accuracy in the luminosity distance, inclination angle, and sky-localization for the six networks. Table 3.1 shows the number of detections per year for each network with 90%-credible sky area $\Omega_{90} < 10$, 1 and 0.1, and fractional error in luminosity distance $\Delta D_L/D_L < 0.1$ and 0.01. The corresponding CDF plots for SNR ρ, Ω_{90}, $\Delta D_L/D_L$ and $\Delta\iota$ for both the populations are presented in Fig. 3.1.

From Fig. 2.2 in Chapter 2, we saw that all the networks with at least one of the XG observatories detect almost all the events up to a redshift of $z = 0.5$, with `ECS` detecting about half of those events with SNRs greater than 100. The Voyager network detects $\sim 90\%$ of the events whereas `HLVKI+` detects only 20% of the events. Figure 3.1 shows no significant differences between the CDF plots for the two populations. All the networks measure the luminosity distances for almost all the events better than a fractional error of 30%, with `ECS` and `KI+EC` constraining the luminosity distance to better than 10% for all the events.

To maximize the chances of a telescope detecting the EM counterpart, the estimated sky area from the GW detection should be within the field-of-view (FOV) of the EM telescope. FOVs of some of the EM telescopes are listed in Table 3.2 and have been denoted in the plots for Ω_{90} in Figs. 3.1 and 3.2. The FOV of the Rubin observatory is an order of magnitude bigger than any other telescope listed in Table 3.2, allowing it to see many more EM transients compared to any other telescope. As a result, less than 0.5% of the events detected by `HLVKI+` will be visible to telescopes other than Rubin, whereas only $\sim 10\%$ of the events detected by `ECS` can be localized in the sky to an area smaller than the FOV of telescopes other than Rubin. In general, EM telescopes can slew and cover multiple patches in the sky, which will increase the number of EM counterparts they will be able to detect. For instance, if the *Roman Space Telescope* with a FOV of $0.28\,\mathrm{deg}^2$ can slew and observe five patches in the sky, covering an area of $\sim 1\,\mathrm{deg}^2$, then it can detect potential EM counterparts of $\sim 3\%$ of the events detected by `HLVKI+` within $z = 0.5$ and $\sim 60\%$ of the events detected by the `ECS` network in the same sub-population. However, the main focus of time-domain survey projects like the Rubin observatory and the *Roman* telescope is to detect supernovae, which are much brighter and evolve much slower than the typical KN. Thus, it is not only difficult for

Table 3.1: For the sub-population with events for which $z < 0.5$, the table lists the number of detections per year for the six detector networks with 90%-credible sky area $\Omega_{90} < 10$, 1, 0.1 and 0.01 deg^2 and fractional error in luminosity distance $\Delta D_L/D_L < 0.1$ and 0.01.

Metric	Ω_{90} (deg)^2				$\Delta D_L/D_L$	
Quality	≤ 10	≤ 1	≤ 0.1	≤ 0.01	≤ 0.1	≤ 0.01
			Pop-1			
HLVKI+	$2.9^{+6.1}_{-2.4} \times 10^2$	$8.7^{+19.5}_{-7.3}$	$2.0^{+2.0}_{-2.0} \times 10^{-1}$	0	$6.0^{+12.3}_{-4.7} \times 10$	$0.0^{+0.1}_{-0.0}$
VK+HLIv	$1.0^{+2.2}_{-0.9} \times 10^3$	$3.1^{+7.1}_{-2.6} \times 10$	$6.0^{+13.0}_{-6.0} \times 10^{-1}$	0	$3.9^{+8.2}_{-3.2} \times 10^2$	$3.0^{+9.0}_{-3.0} \times 10^{-1}$
HLKI+E	$1.4^{+3.0}_{-1.2} \times 10^3$	$6.0^{+13.4}_{-4.9} \times 10$	$1.9^{+2.3}_{-1.9}$	0	$2.5^{+5.3}_{-2.0} \times 10^3$	$9.9^{+22.1}_{-8.4}$
VKI+C	$6.8^{+14.6}_{-5.6} \times 10^2$	$1.9^{+4.1}_{-1.6} \times 10$	$2.0^{+6.0}_{-2.0} \times 10^{-1}$	0	$8.7^{+18.4}_{-7.2} \times 10^2$	$9.4^{+19.6}_{-7.4}$
KI+EC	$3.2^{+6.7}_{-2.6} \times 10^3$	$5.6^{+12.1}_{-4.7} \times 10^2$	$1.4^{+3.1}_{-1.2} \times 10$	$2.0^{+4.0}_{-2.0} \times 10^{-1}$	$3.5^{+7.4}_{-2.9} \times 10^3$	$7.0^{+13.7}_{-5.4} \times 10$
ECS	$3.7^{+7.8}_{-3.1} \times 10^3$	$2.2^{+4.8}_{-1.9} \times 10^3$	$2.3^{+5.0}_{-1.9} \times 10^2$	$5.1^{+9.8}_{-4.2}$	$3.6^{+7.7}_{-3.0} \times 10^3$	$1.4^{+2.9}_{-1.1} \times 10^2$
			Pop-2			
HLVKI+	$3.0^{+6.4}_{-2.5} \times 10^2$	$9.1^{+20.3}_{-7.7}$	$0.0^{+0.3}_{-0.0}$	0	$4.4^{+8.3}_{-3.7} \times 10$	$0.0^{+0.1}_{-0.0}$
VK+HLIv	$1.1^{+2.3}_{-0.9} \times 10^3$	$3.2^{+6.8}_{-2.6} \times 10$	$4.0^{+15.0}_{-4.0} \times 10^{-1}$	0	$3.5^{+7.4}_{-2.9} \times 10^2$	$0.0^{+0.3}_{-0.0}$
HLKI+E	$1.5^{+3.1}_{-1.2} \times 10^3$	$5.9^{+12.2}_{-4.8} \times 10$	$9.0^{+35.0}_{-8.0} \times 10^{-1}$	0	$2.5^{+5.3}_{-2.1} \times 10^3$	$7.1^{+16.3}_{-6.2}$
VKI+C	$7.1^{+15.1}_{-5.9} \times 10^2$	$1.8^{+3.8}_{-1.5} \times 10$	$3.0^{+5.0}_{-3.0} \times 10^{-1}$	0	$9.2^{+19.4}_{-7.6} \times 10^2$	$4.8^{+8.3}_{-4.0}$
KI+EC	$3.2^{+6.8}_{-2.6} \times 10^3$	$5.7^{+12.0}_{-4.7} \times 10^2$	$1.2^{+3.1}_{-1.0} \times 10$	$0.0^{+0.3}_{-0.0}$	$3.5^{+7.4}_{-2.9} \times 10^3$	$3.7^{+7.4}_{-3.1} \times 10$
ECS	$3.7^{+7.9}_{-3.1} \times 10^3$	$2.3^{+4.9}_{-1.9} \times 10^3$	$2.3^{+4.8}_{-1.9} \times 10^2$	$4.5^{+11.7}_{-3.8}$	$3.6^{+7.7}_{-3.0} \times 10^3$	$8.6^{+18.1}_{-7.2} \times 10$

Table 3.2: The field of view (FOV) of some of the EM telescopes. Among them, we have used the Rubin Observatory and the *Roman Telescope* to comment on the detectability of kilonovae in Sec. 3.2.3. The space telescopes in the list have been *italicized*.

Telescope	FOV (deg^2)	Telescope	FOV (deg^2)
Rubin [6, 7]	9.6	*Swift–XRT* [123]	0.12
EUCLID [124]	0.54	Keck [125]	0.11
Athena [126]	0.35	VLT [127]	0.054
Roman [5, 128]	0.28	ELT [129]	0.028
Chandra X-ray [130]	0.15	GMT [131]	0.008
Lynx [132]	0.13	*HST–WFC3* [133]	0.002

these surveys to detect KN in the first place, but the surveys might also miss the optimal time window to observe a KN without a targeted search. This emphasizes the need for target-of-opportunity (TOO) follow-up to GW events in order to utilize the full potential of MMA [104, 134, 135].

3.2.2 Early-warning alerts

The GW detectors start detecting gravitational radiation from the inspiral phase itself, i.e., much before the actual merger happens. Specifically, if a detector starts detecting the signal at a lower frequency cutoff of f_L, then time to coalescence τ is given by [136]

$$\tau \approx \left(\frac{0.25}{\eta}\right)\left(\frac{2.8\,\mathrm{M}_\odot}{M}\right)^{\frac{5}{3}}\left(\frac{5\mathrm{Hz}}{f_L}\right)^{\frac{8}{3}} \times 6.4 \times 10^3\ \mathrm{s}, \tag{3.1}$$

where M is the total redshifted mass of the binary. For the same total mass, the more asymmetric the binary (i.e., the smaller η is), the larger the time to merger. However, as the binary gets heavier, the time to merger decreases. Additionally, a smaller f_L means that the detector is able to capture the inspiral phase from an earlier time. For a reference NSBH system with source-frame masses of $m_{NS} = 1.5\,\mathrm{M}_\odot$ and $m_{BH} = 8\,\mathrm{M}_\odot$ respectively, and $f_L = 20$ Hz with the system at a redshift of $z = 0.1$, the time to coalescence $\tau \approx 30$ seconds, and it increases to about 2.5 minutes when f_L is lowered to 11 Hz. Thus, *early-warning* (EW) alerts [137] with the estimated sky position, based on the data collected by then, can be sent to the EM telescope before the merger, allowing for possible latency in the process, and give time to the telescope to slew in position

and still record the EM radiation that is generated during and after the merger. Early observations can allow the EM telescopes to capture prompt emission as well as make early optical and ultraviolet observations that give us information about the r-process nucleosynthesis [138].

Following Ref. [99], we present data for two values of time to coalescence, $\tau_{\rm EW} = 120$s and 300s. While Ref. [99] also gives data for $\tau_{\rm EW} = 600$s, we do not find any NSBH events in either Pop-1 or Pop-2 that qualify that criteria. Equation (3.1) can be inverted to calculate f_L (referred to as $f_{\rm EW}$ in this context) for the given values of $\tau_{\rm EW}$ for every event. f_{EW} is the frequency of the GW signal from which the system has time $\tau_{\rm EW}$ left until coalescence. We only consider those events that have accumulated SNR > 10 in the particular detector network at the time the alert is sent, and for which $f_{EW} > 11$ Hz. However, even if an EW alert is sent to the EM telescope *adequately* early, it is not of much use if the associated sky position reported by the GW detector is too large for the telescope to search for the EM counterpart. As the EM telescopes can look for these counterparts by observing multiple patches of the sky, they can often cover an area that is larger than their FOV. In Table 3.3, we present the number of observations every year where an EW alert can be sent 120s and 300s before the merger. We further categorize the events based on how well they are localized, showing numbers for detections that are localized to $\Omega_{90} \leq 100$, 10 and 1 deg^2 at the time when the alert is sent. We do not list the numbers for `HLVKI+`, `VK+HLIv` and `VKI+C` as no events satisfying the criteria were found, which is also evident from the corresponding CDF plots in Fig. 3.3.

From Table 3.3, we see that EW alerts can be sent to only $\mathcal{O}(10)$ events for `HLKI+E` such that the sky position of the events is also constrained better than 100 deg^2, whereas it can be sent for $\mathcal{O}(100)$ events for the `KI+EC` and the `ECS` networks. The corresponding numbers drop by two orders of magnitude if the EW is sent 5 minutes before coalescence. We also observe that the number of events for which the EW alert can be sent 5 minutes before the merger is higher in Pop-2 compared to Pop-1. We attribute this difference to the fact that, in general, we expect systems in Pop-1 to have higher total masses compared to systems in Pop-2 (due to the broader distributions of NS and BH masses in Pop-1) which leads to longer signals in Pop-2 [as can be seen from Eq. (3.1)]. In addition, the number of events with $\Omega_{90} \leq 10$ deg^2 is $\mathcal{O}(10)$ times lower than the number of events for which $\Omega_{90} \leq 100$. For the events for which $10\,\text{deg}^2 \leq \Omega_{90} \leq 100\,\text{deg}^2$, Rubin would need to cover at most 10 sky patches to follow up a possible EM counterpart, whereas any other telescope listed in Table 3.2 would need to slew and cover $\mathcal{O}(100)$ sky patches to detect any possible EM transient.

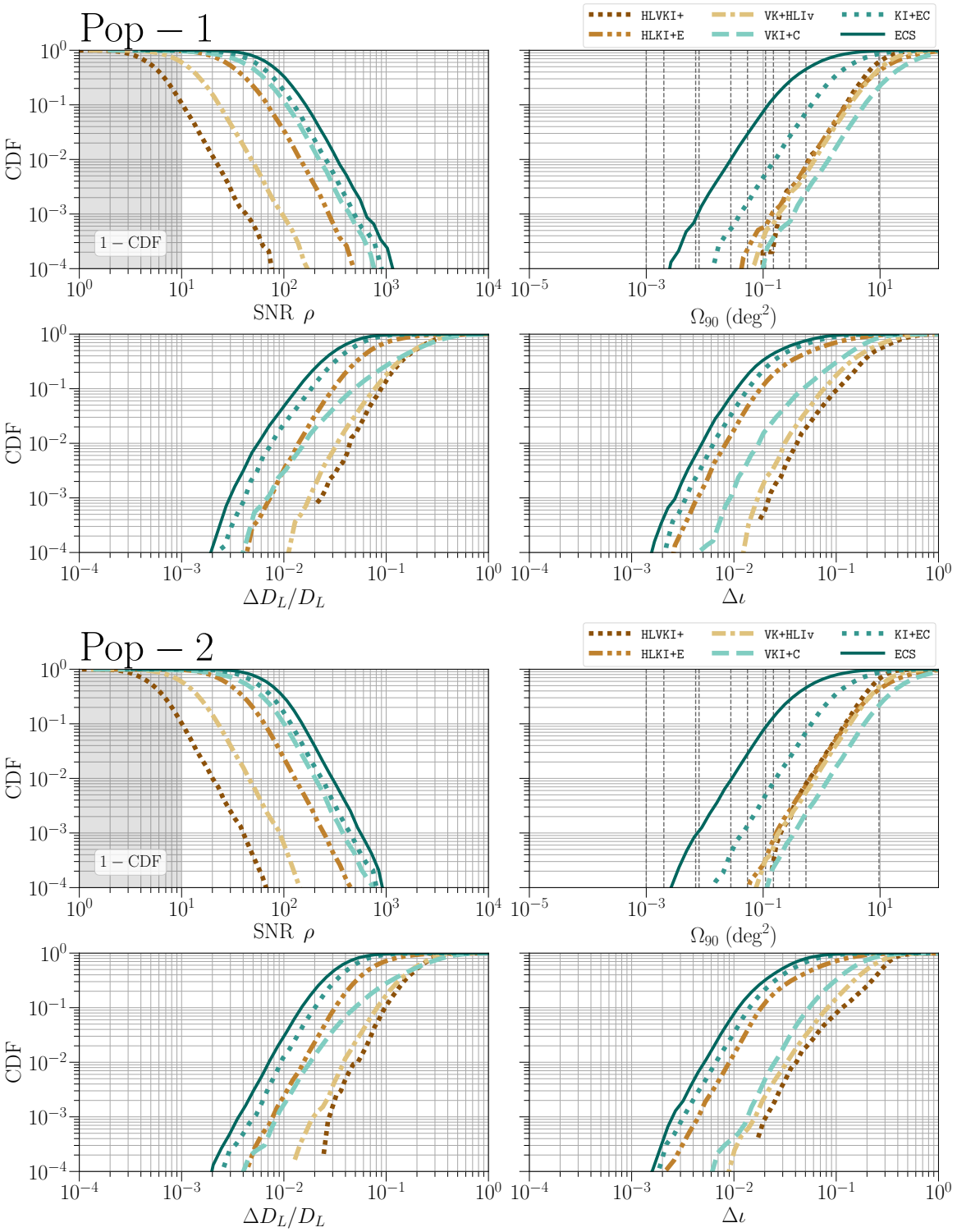

Figure 3.1: The CDF plots for SNR ρ, 90%-credible sky area Ω_{90}, fractional error in luminosity distance $\Delta D_L/D_L$ and absolute error in the inclination angle $\Delta\iota$ for the sub-population restricted to $z < 0.5$. The vertical black dotted lines in the plot for Ω_{90} correspond to the FOV of the various EM telescopes listed in Table 3.2.

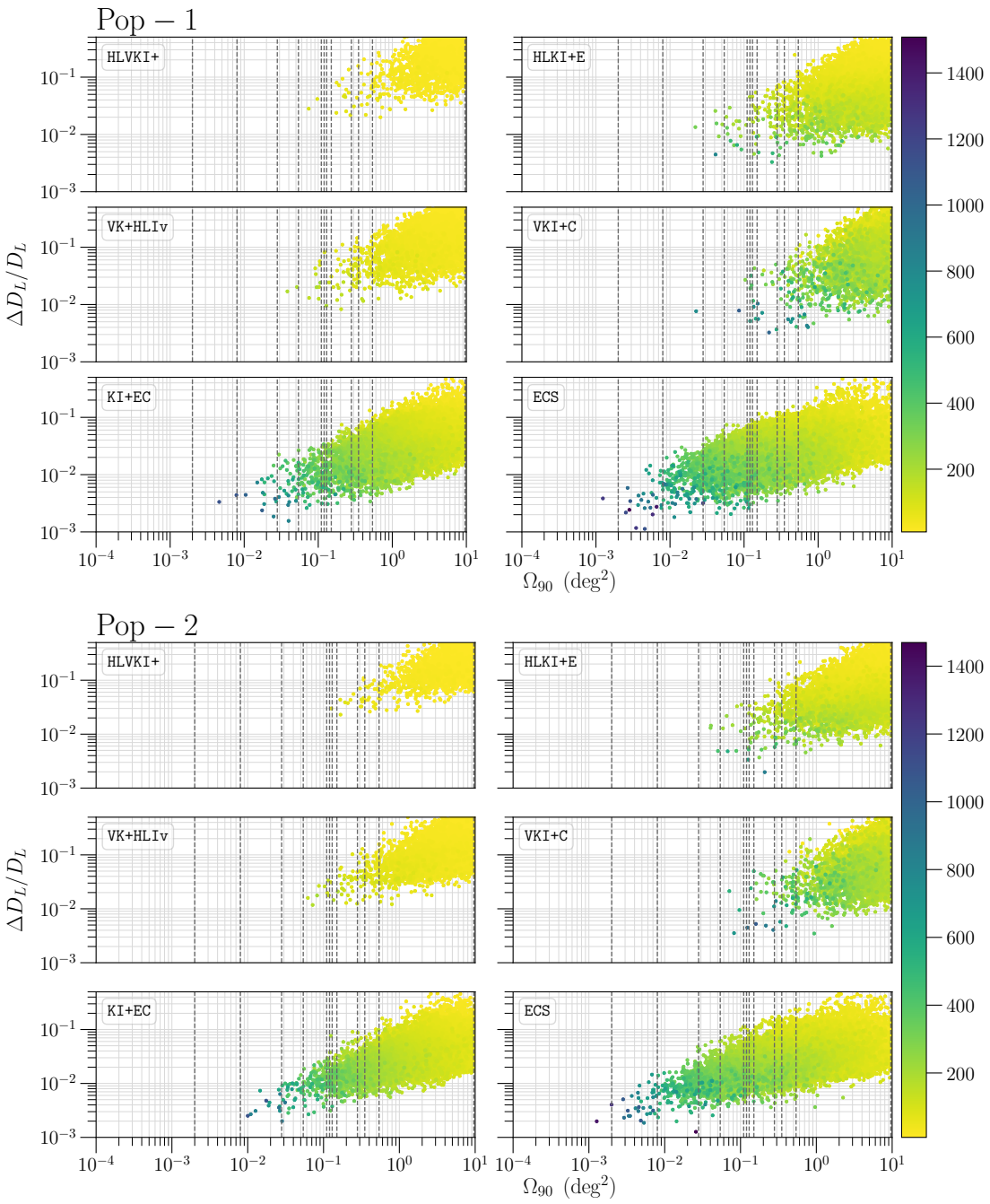

Figure 3.2: The figure shows the relationship between the fractional error in luminosity distance $\Delta D_L/D_L$, 90%-credible sky area Ω_{90} and the SNR (denoted by the color bar) of the events in Pop-1 and Pop-2 for which $z < 0.5$. Each of these events, detected in an observation span of 10 years, appears as a spot placed according to the associated measurement errors in luminosity distance and sky position. The color of the dots represents the SNR with which that particular event was detected in a GW detector network.

Figure 3.3 shows that, while there are events detected by `VKI+C` with SNR $\rho > 10$ five minutes before their mergers, their sky position cannot be localized to better than $100\,\mathrm{deg}^2$. This is consistent with the performance of `VKI+C` in constraining Ω_{90} compared to the other networks, as can be seen from Fig. 3.3. Moreover, none of the events that are *eventually* detected by `HLVKI+` and `VK+HLIv` networks accumulate SNR in excess of 10 in their respective detector networks 2 minutes or 5 minutes before their mergers.

Table 3.3: The number of detections per year for `HLKI+E`, `KI+EC` and `ECS` for which an EW alert can be sent 120s and 300s before the merger, with 90%-credible sky area measured to be better than 100, 10, 1 deg^2 at the time when the alert is sent.

EW Time	$\tau_{\mathrm{EW}} = 120$ s			$\tau_{\mathrm{EW}} = 300$ s		
$\Omega_{90}\,(\mathrm{deg}^2)$	≤ 100	≤ 10	≤ 1	≤ 100	≤ 10	≤ 1
			Pop-1			
HLKI+E	$2.9^{+5.9}_{-2.5} \times 10$	$1.9^{+3.3}_{-1.7}$	$0.0^{+0.2}_{-0.0}$	$0.0^{+0.3}_{-0.0}$	0	0
KI+EC	$3.5^{+7.5}_{-2.9} \times 10^2$	$2.4^{+6.0}_{-2.1} \times 10$	$5.0^{+24.0}_{-5.0} \times 10^{-1}$	$9.0^{+30.0}_{-9.0} \times 10^{-1}$	$0.0^{+0.5}_{-0.0}$	0
ECS	$5.6^{+11.8}_{-4.6} \times 10^2$	$6.1^{+12.9}_{-5.1} \times 10$	$1.7^{+5.7}_{-1.5}$	$1.4^{+3.5}_{-1.3}$	$5.0^{+12.0}_{-5.0} \times 10^{-1}$	0
			Pop-2			
HLKI+E	$2.4^{+5.0}_{-2.1} \times 10$	$1.2^{+2.4}_{-0.9}$	0	$4.0^{+9.0}_{-4.0} \times 10^{-1}$	$0.0^{+0.1}_{-0.0}$	0
KI+EC	$3.3^{+7.2}_{-2.7} \times 10^2$	$2.2^{+4.7}_{-1.8} \times 10$	$1.0^{+25.0}_{-0.0} \times 10^{-1}$	$5.8^{+11.6}_{-4.7}$	$8.0^{+9.0}_{-8.0} \times 10^{-1}$	0
ECS	$5.3^{+11.4}_{-4.4} \times 10^2$	$5.7^{+11.9}_{-4.6} \times 10$	$1.5^{+4.4}_{-0.9}$	$7.4^{+16.0}_{-5.8}$	$1.8^{+1.9}_{-1.6}$	$0.0^{+0.1}_{-0.0}$

3.2.3 Kilonova Detection

During a NSBH merger, the companion BH can cause tidal disruption of the NS resulting in the generation of neutron-rich ejecta. The presence of neutron-rich substances in the expanding ejecta leads to fission and further neutron capture, leading to the production of a wide variety of radioactive elements heavier than iron. These unstable nuclei eventually decay radioactively heating up the ejecta, which leads to approximately isotropic quasithermal emission in the ultraviolet (UV), optical, and infrared (IR) bands.

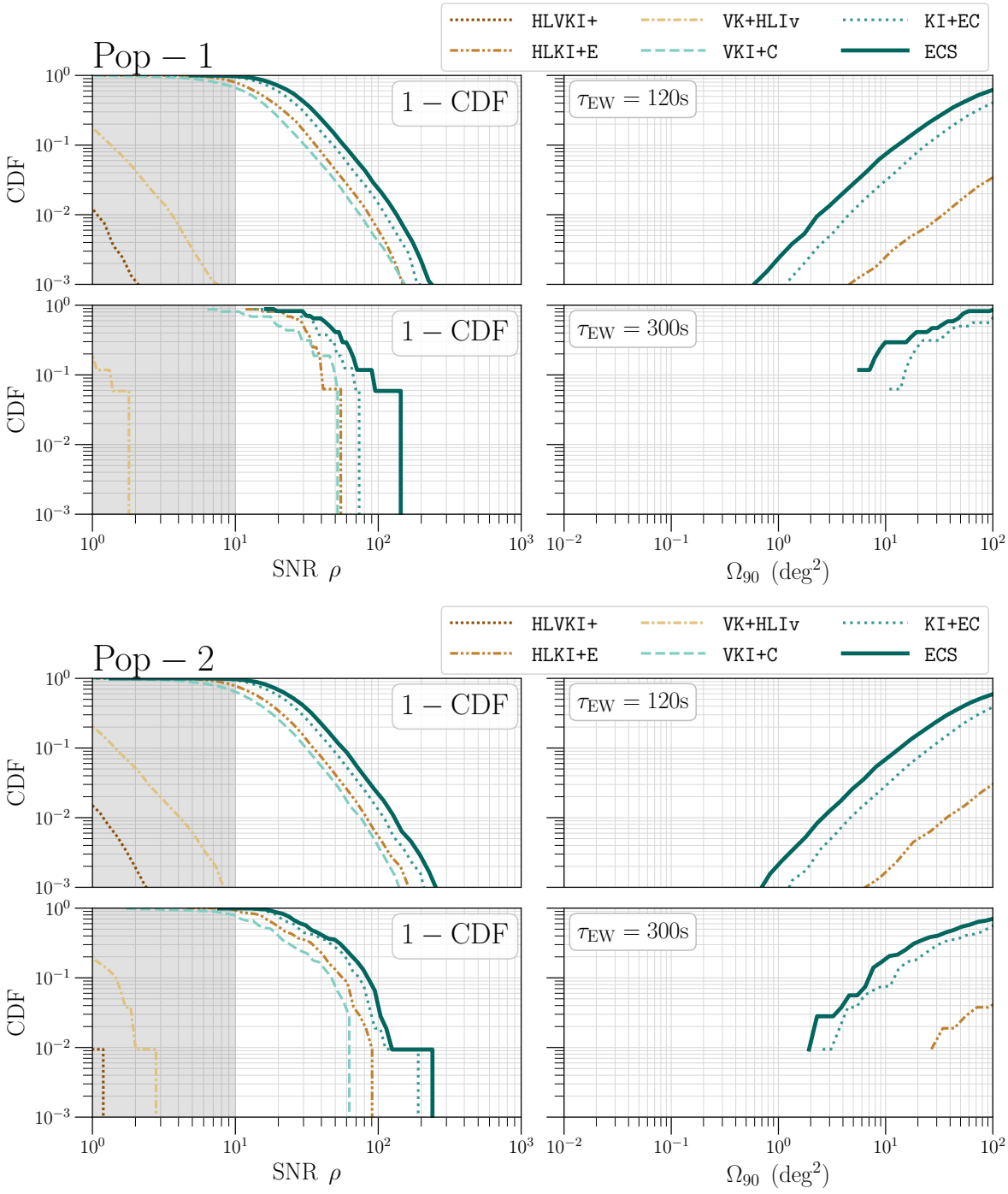

Figure 3.3: The CDF plots for events for which early-warning alerts can be sent 2 minutes and 5 minutes before their respective mergers.

This transient is known as kilonova and serves as one of the most promising EM counterparts to GW radiation from BNS/NSBH systems [72, 86].

For a given EOS, the tidal disruption of the NS, and consequently the generation of a KN, depends on the mass-ratio ($q = m_{BH}/m_{NS}$) associated with the binary and the dimensionless spin of the BH χ_{BH}. Only BHs with low mass (hence, low q) and high prograde ($\chi_{BH} > 0$) spin are expected to tidally disrupt the NS before it passes the R_{ISCO} [72]. However, given the population parameters used and the bias towards detecting systems with higher masses, we see that higher q systems are preferred over lower q ones (see Fig. 3.4). Thus, the GW chirp of only a fraction of NSBH systems is expected to have KN as the EM counterpart [139–142]. The detected NSBH events are seen to have $q > 4$ and $\chi_{BH} \approx 0$ [104], which is consistent with the fact that no corresponding KN were detected. Moreover, population-based analysis where the population is based on current observations posits that a tiny fraction, if at all, of NSBH systems are expected to be *EM bright*, i.e., capable of generating an EM counterpart [103].

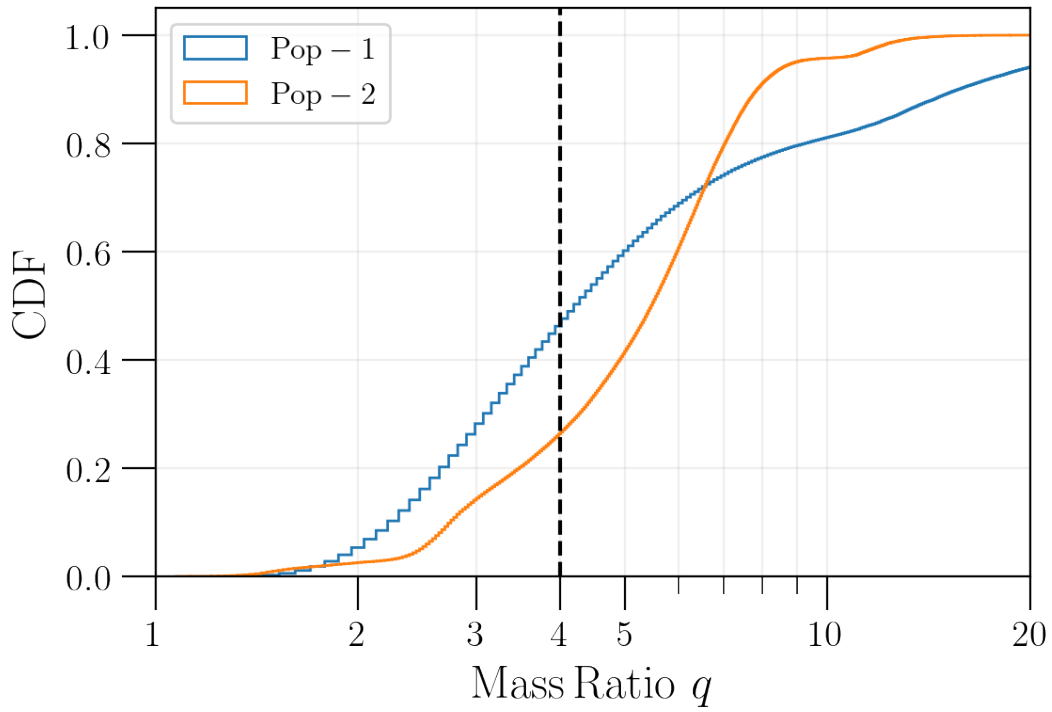

Figure 3.4: The CDF plots for the mass ratio of the events belonging to the two populations that were detected by the ECS network. The black dashed vertical line separates the $q \leq 4$ region from the $q > 4$ region. Only events with $q \leq 4$ have been considered for the KN study.

In this study, we report the number of KN detections per year, for each population

model corresponding to the detections made by the six GW detector networks. We select the events from the population with $q \leq 4$ and $0 \leq \chi_{BH} \leq 0.75$, that are detected by each of these detectors with SNR $\rho > 10$, and obtain the bolometric KN light curve (in case of non-zero ejecta mass) for these events. To obtain the light curve, we follow the recipes from Refs. [143, 144] for "BHNS" systems. This involves the calculation of the remnant mass, i.e., the estimated baryon mass outside the BH approximately 10 ms after the merger, and the mass of the dynamical ejecta. The formula in Ref. [145] gives the *normalized* remnant mass which, when multiplied by the baryonic mass of the initial NS, gives the remnant mass outside the BH. While Ref. [144] approximates the baryonic mass of the NS using the formula from Ref. [146], we calculate it from the TOV data corresponding to each EOS. The mass of the dynamical ejecta is obtained using the fits from Ref. [143]. The mass of the disk surrounding the BH is calculated by subtracting the mass of the dynamical ejecta from the remnant mass. A fraction of the disk mass can become gravitationally unbound, which is referred to as disk wind. This fraction is computed by using the formula [144]:

$$\xi = \frac{M_{ej}}{M_{disk}} = \xi_1 + \frac{\xi_2 - \xi_1}{1 + e^{1.5(q-3)}}, \tag{3.2}$$

where $\xi_1 \in (0.04, 0.32)$ and $\xi_2 \in (0.14, 0.44)$. We set ξ_1 and ξ_2 to the average values of the upper and lower bounds used in Ref. [144], i.e., $\xi_1 = 0.18$ and $\xi_2 = 0.29$ respectively. The velocity of the dynamical ejecta is approximated using Ref. [144] and the velocity of the disk wind is set to $0.1c$ [147, 148]. The opacities for the dynamical ejecta lie in the range (1–10) cm^2 g^{-1} due to the Lanthanide rich r-process nucleosynthesis while the disk, after getting irradiated by neutrinos, becomes relatively optically thin with opacity in the range (0.1–1) cm^2 g^{-1}. Because of uncertainties in the nucleosynthetic calculations, we fix dynamical and disk matter opacity to 8 and 0.5, respectively. The luminosity curves for both the dynamical ejecta and the unbound disk mass are individually determined by integrating the heating function (which accounts for the heating due to $\beta-$decay), approximated by a power law and implemented by using the numerical fit from Ref. [149]. The luminosity for the dynamical ejecta and the unbound disk mass at each time are added to calculate the total bolometric luminosity curve for the system.

To report the KN detections, we consider the observing EM telescopes to be the Vera Rubin Observatory and the *Nancy Grace Roman Space Telescope*. Table 3.4 lists the photometric bands for the telescopes, the corresponding 5σ single-exposure limiting magnitudes for point sources ($m_{\rm lim}$), and the effective wavelength ($\lambda_{\rm eff}$) for each band. In

Table 3.4: The six filters in the Rubin Observatory and the *Roman Telescope*, with the corresponding single-exposure (30s) limiting magnitudes [5,7] and the effective wavelength (λ_{eff}) used for each band in order to calculate the photometric band estimates.

Vera C. Rubin Observatory			Roman Telescope		
Band	m_{lim} (AB mag)	λ_{eff} (Å)	Band	m_{lim} (AB mag)	λ_{eff} (Å)
u	23.9	3546	R	26.2	6160
g	25.0	4670	Z	25.7	8720
r	24.7	6156	Y	25.6	10600
i	24.0	7472	J	25.5	12900
z	23.3	8917	H	25.4	15800
y	22.1	10305	F	24.9	18400

order to obtain the estimates for the photometric bands from the bolometric luminosity curve, we calculate the blackbody temperature and the radius of the ejecta as a function of time and use them to calculate the associated spectral flux density f_ν:

$$f_\nu = \frac{2h\nu^3}{c^2} \frac{1}{e^{\frac{h\nu}{kT}} - 1} \left(\frac{R}{D_L}\right)^2, \tag{3.3}$$

where h is the Planck constant, ν is the frequency corresponding to λ_{eff} of a particular band, c is the speed of light, k is the Boltzmann constant, T is the blackbody temperature, R is the radius of the ejecta and D_L is the luminosity distance of the system. The spectral flux can then be converted to AB magnitude (AB mag) using

$$m_{\text{AB}} = -2.5 \log_{10} f_\nu \, - \, 48.6. \tag{3.4}$$

For a given band, if the minimum value of the m_{AB} time-series is less than the limiting magnitude m_{lim} for that band (i.e., the peak luminosity of the KN is brighter than the threshold for the band), then we claim that the KN will be *observed* by the corresponding EM telescope. In contrast, the criteria for *detection* of a KN requires more consideration. Specifically, two consecutive exposures with a time lag of > 30 minutes can be used to rule out fast-moving objects, like asteroids. Note that the model used to generate a KN assumes the emission to be isotropic. Angle dependence in the luminosity function can result in lower peak luminosities than what we obtain, potentially lowering the number of detections. However, as the code used to generate KN light curves is only valid for systems where $\chi_{BH} < 0.75$, the number of KNe we report is inherently lower than what can be expected for the two populations, as systems with high prograde BH spins are

expected to result in KN emission for larger mass ratios. Furthermore, the analysis uses limiting magnitudes for the two telescopes corresponding to single exposure times of 30s for Rubin and 67s for *Roman* [5]. Longer exposure times, possibly due to TOO searches, can improve the limiting magnitudes resulting in more KN detections than the ones reported in this study. For a more comprehensive treatment towards detection of KNe from NSBH mergers, see Ref. [119].

The amount of ejecta in an NSBH merger depends on the unknown NS EOS. To account for this ignorance, for each system we compute the luminosity curves for three EOSs with varying stiffness: `APR4` [150], `DD2` [151] and `ALF2` [152]. The mass-radius curves for the three EOSs and the corresponding curves for the tidal deformability parameter Λ are given in Fig. 3.5. We find that the largest number of KN detections are obtained with the g and r-filter in the Rubin observatory and the R-filter in the *Roman* telescope. We will present a detailed analysis for detections corresponding to the r-filter in Rubin and the R-filter in *Roman*. The number of detections for all the filters for the two telescopes can be found in Tables 3.8 and 3.9.

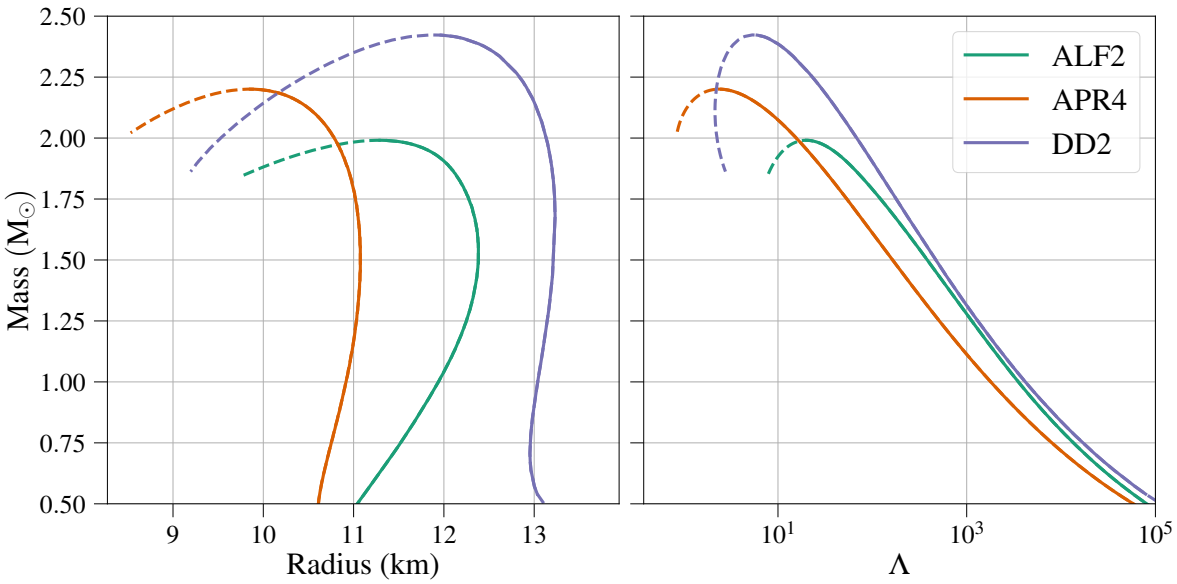

Figure 3.5: The mass-radius relationship for the three equations of state considered in this study, along with the corresponding values of tidal deformability parameter Λ. The dashed part depicts the unstable branch with $dr/dm > 0$.

Figure 3.6 shows the peak luminosities of KNe for events in Pop-1 and Pop-2 as a function of redshift in an observation time of 10 years. The largest number of KNe are obtained for `DD2` and the least for `APR4`. This is consistent with the fact that `DD2` is the stiffest among the three EOSs considered, whereas `APR4` is the softest (see Fig. 3.5).

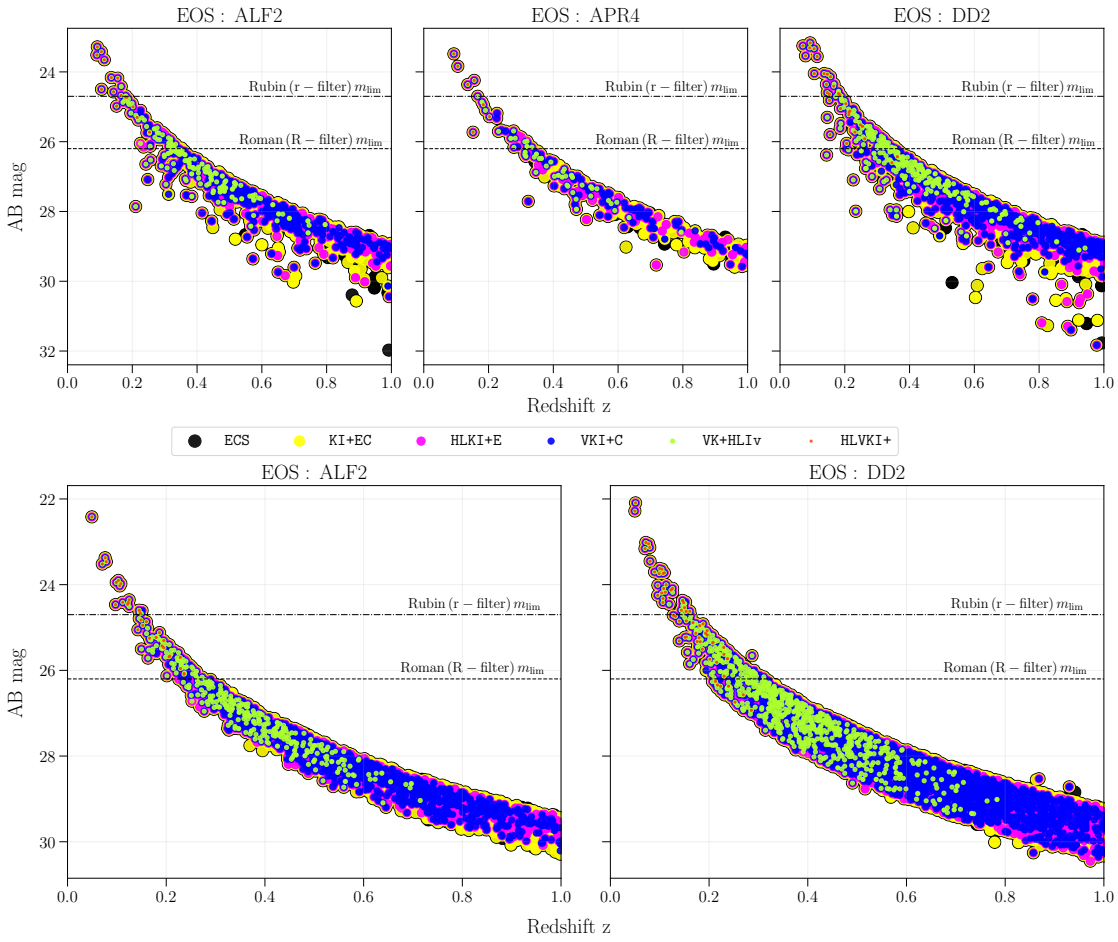

Figure 3.6: *Top panel:* The peak luminosity of KNe associated with detected NSBH mergers in Pop-1 in a span of 10 years, as a function of redshift for the three EOSs. The color of the dots denotes the GW detector that detected the corresponding NSBH merger event. The size of the dots denotes the number of merger events detected by the particular GW network, in an observation span of 10 years, that result in a KN. The dashed and dashed-dotted horizontal lines denote the limiting magnitudes for the R-filter in *Roman* and $r-$filter in Rubin respectively. *Bottom panel:* The peak luminosity of KNe associated with NSBH mergers in Pop-2 detected in an observation time of 10 years, as a function of redshift. No KNe are obtained for the `APR4` EOS for Pop-2 events (see Table 3.6).

The *Roman* telescope has a better limiting magnitude ($m^R_{\rm lim} = 26.2$) than the Rubin observatory ($m^r_{\rm lim} = 24.7$) and, consequently, it is expected to observe more KNe, which is also seen in Fig. 3.6. In fact, almost all the events observed by Rubin lie within $z \sim 0.2$, whereas *Roman* is able to see KNe up to $z \sim 0.4$. However, the number of KNe that *Roman* can observe is limited by its small FOV, ~ 34 times smaller than the FOV of

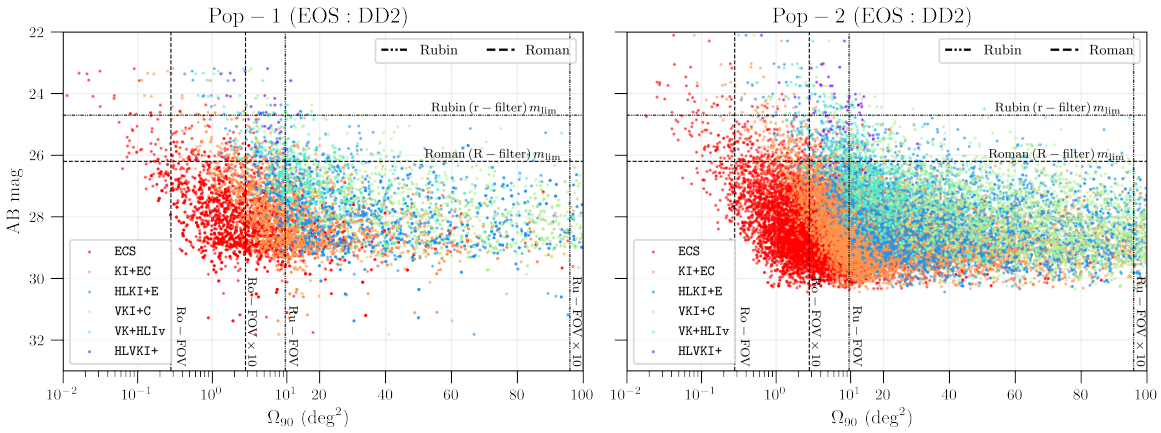

Figure 3.7: The peak luminosities of KNe, when `DD2` is used as the EOS for the NS, associated with detected NSBH mergers in Pop-1 and Pop-2 in a span of 10 years, as a function of Ω_{90} obtained from GW observations. The horizontal dashed and dashed-dotted lines show the limiting magnitudes for *Roman* (Ro) and Rubin (Ru) respectively. The vertical dashed (dashed-dotted) lines show the sky-area corresponding to the FOV and 10 times the FOV for *Roman* (Rubin).

Rubin. In Tables 3.5 and 3.6, we present the number of KNe observed by each telescope, in an observation time of 10 years, for the six GW detector networks. The events are categorized based on if they can be localized in the sky using GW observations to better than the FOV of the particular telescope, 10 times the FOV of the telescope or 100 deg^2. The upper and lower limits with each number in the table show the uncertainty in the number of KN detections from NSBH systems due to the uncertainty in the local merger rate of the NSBH mergers. We see that almost all the events that Rubin will observe will be localized to an area in the sky that is smaller than the FOV of the telescope. This is not the case for *Roman* as only GW events detected by `KI+EC` and `ECS` are seen to have $\Omega_{90} <$ FOV(*Roman*). If we assume that *Roman* can slew and cover 10 sky-patches, it is capable of observing 5–8 times (depending on the EOS) more KNe than the Rubin observatory. This is illustrated in Fig. 3.7, where we have plotted the peak luminosities of KNe corresponding to NSBH mergers from the two populations with the corresponding Ω_{90} obtained from GW observations. Increasing the sky area covered by Rubin to 10 times its FOV does not significantly increase the number of KNe seen by the observatory. For *Roman*, slewing the telescope to cover 10 times its FOV increases the number of KN detections by $\sim$ 2–10 times, depending on the GW detector and the EOS, still leaving out $\sim$ 10–50% of the events with $\Omega_{90} \leq 100$ deg^2 that it can potentially detect.

We also note that, in general, the number of expected KN observations corresponding

Table 3.5: The number of KN detections with the $r-$filter of Rubin Observatory and $R-$filter of the *Roman Telescope* for Pop-1 for an observation time of 10 years. The events are categorized based on if they can be localized in the sky, using GW observations, better than the FOV of the EM telescope, 10 times the FOV of the EM telescope, or 100 deg^2. They have been further divided into 3 columns based on the EOS that was used to generate the KNe light curves.

Pop-1									
Rubin $r-$filter									
Quality	$\Omega_{90} <$ FOV			$\Omega_{90} < 10 \times$ FOV			$\Omega_{90} < 100\,\mathrm{deg}^2$		
EOS	ALF2	APR4	DD2	ALF2	APR4	DD2	ALF2	APR4	DD2
HLVKI+	9^{+13}_{-7}	4^{+4}_{-3}	16^{+23}_{-13}	9^{+16}_{-8}	4^{+5}_{-3}	16^{+28}_{-15}	9^{+16}_{-8}	4^{+5}_{-3}	16^{+28}_{-15}
VK+HLIv	14^{+21}_{-12}	4^{+7}_{-3}	23^{+33}_{-19}	14^{+25}_{-13}	4^{+9}_{-3}	23^{+42}_{-22}	14^{+25}_{-13}	4^{+9}_{-3}	23^{+42}_{-22}
HLKI+E	14^{+21}_{-11}	4^{+7}_{-3}	23^{+33}_{-18}	14^{+25}_{-13}	4^{+9}_{-3}	23^{+42}_{-22}	14^{+25}_{-13}	4^{+9}_{-3}	23^{+42}_{-22}
VKI+C	14^{+17}_{-7}	4^{+5}_{-3}	23^{+29}_{-14}	14^{+25}_{-13}	4^{+9}_{-3}	23^{+42}_{-22}	14^{+25}_{-13}	4^{+9}_{-3}	23^{+42}_{-22}
KI+EC	14^{+24}_{-13}	4^{+9}_{-3}	23^{+40}_{-22}	14^{+25}_{-13}	4^{+9}_{-3}	23^{+42}_{-22}	14^{+25}_{-13}	4^{+9}_{-3}	23^{+42}_{-22}
ECS	14^{+25}_{-13}	4^{+9}_{-3}	23^{+42}_{-22}	14^{+25}_{-13}	4^{+9}_{-3}	23^{+42}_{-22}	14^{+25}_{-13}	4^{+9}_{-3}	23^{+42}_{-22}
Roman $R-$filter									
Quality	$\Omega_{90} <$ FOV			$\Omega_{90} < 10 \times$ FOV			$\Omega_{90} < 100\,\mathrm{deg}^2$		
EOS	ALF2	APR4	DD2	ALF2	APR4	DD2	ALF2	APR4	DD2
HLVKI+	0	0	0	3^{+4}_{-3}	1^{+0}_{-1}	6^{+7}_{-6}	16^{+30}_{-15}	7^{+6}_{-6}	29^{+52}_{-27}
VK+HLIv	0	0	0	8^{+16}_{-8}	3^{+5}_{-3}	19^{+42}_{-19}	66^{+131}_{-51}	23^{+50}_{-17}	118^{+242}_{-97}
HLKI+E	0^{+1}_{-0}	0	0^{+1}_{-0}	15^{+28}_{-14}	5^{+7}_{-4}	26^{+61}_{-25}	96^{+168}_{-74}	39^{+68}_{-30}	169^{+313}_{-138}
VKI+C	0	0	0	3^{+5}_{-3}	1^{+1}_{-1}	9^{+18}_{-9}	84^{+151}_{-64}	30^{+56}_{-22}	155^{+293}_{-126}
KI+EC	3^{+5}_{-3}	1^{+1}_{-1}	6^{+8}_{-6}	56^{+100}_{-45}	21^{+36}_{-15}	100^{+193}_{-84}	97^{+170}_{-75}	39^{+68}_{-30}	171^{+318}_{-140}
ECS	26^{+52}_{-20}	12^{+22}_{-9}	50^{+109}_{-41}	88^{+157}_{-68}	33^{+60}_{-25}	156^{+293}_{-128}	97^{+170}_{-75}	39^{+68}_{-30}	171^{+318}_{-140}

to events in Pop-2 is $\sim$ 1.5–3 times larger than for events in Pop-1. While a larger fraction of events in Pop-1 have $q < 4$ compared to Pop-2 (see Fig. 3.4), a significant fraction of systems in Pop-1 contain BHs with retrograde ($\chi_{BH} < 0$) spin, which is a disincentive to tidal disruption before R_{ISCO}. However, no KNe are detected for events in Pop-2 with `APR4` as the EOS. This can be explained by noticing that a large fraction of events in Pop-2 contain non-spinning and $5 - 15$ $M_\odot$ BHs (see Fig. 2.1 in Chapter 2) and are unable to tidally disrupt NSs that obey `APR4`, as `APR4` leads to the formation of the most compact NSs among the three EOSs (see Fig. 3.5).

As discussed before, the single-exposure observation criteria might not be suitable in practice, as one needs at least two exposures to differentiate KN emissions from fast-moving objects. For a more realistic picture regarding the number of KN detections, we use a TOO strategy for Rubin which is similar to the approaches discussed in Refs. [37,153].

Table 3.6: Same as Tabler 3.5, but for Pop-2 events.

Pop-2									
Rubin $r-$filter									
Quality	$\Omega_{90} <$ FOV			$\Omega_{90} < 10 \times$ FOV			$\Omega_{90} < 100\,\mathrm{deg}^2$		
EOS	ALF2	APR4	DD2	ALF2	APR4	DD2	ALF2	APR4	DD2
HLVKI+	16^{+16}_{-11}	0	31^{+33}_{-19}	16^{+18}_{-14}	0	31^{+41}_{-26}	16^{+18}_{-14}	0	31^{+41}_{-26}
VK+HLIv	19^{+22}_{-14}	0	37^{+58}_{-28}	19^{+30}_{-16}	0	37^{+82}_{-31}	19^{+30}_{-16}	0	37^{+82}_{-31}
HLKI+E	20^{+24}_{-15}	0	38^{+61}_{-30}	20^{+30}_{-17}	0	38^{+84}_{-32}	20^{+30}_{-17}	0	38^{+84}_{-32}
VKI+C	20^{+20}_{-15}	0	38^{+47}_{-23}	20^{+30}_{-17}	0	38^{+83}_{-32}	20^{+30}_{-17}	0	38^{+83}_{-32}
KI+EC	20^{+30}_{-17}	0	38^{+82}_{-32}	20^{+30}_{-17}	0	38^{+84}_{-32}	20^{+30}_{-17}	0	38^{+84}_{-32}
ECS	20^{+30}_{-17}	0	38^{+84}_{-32}	20^{+30}_{-17}	0	38^{+84}_{-32}	20^{+30}_{-17}	0	38^{+84}_{-32}
Roman $R-$filter									
Quality	$\Omega_{90} <$ FOV			$\Omega_{90} < 10 \times$ FOV			$\Omega_{90} < 100\,\mathrm{deg}^2$		
EOS	ALF2	APR4	DD2	ALF2	APR4	DD2	ALF2	APR4	DD2
HLVKI+	0	0	0	3^{+5}_{-2}	0	6^{+12}_{-4}	32^{+42}_{-27}	0	59^{+92}_{-51}
VK+HLIv	0	0	0	16^{+21}_{-12}	0	29^{+43}_{-24}	93^{+222}_{-76}	0	196^{+435}_{-163}
HLKI+E	0	0	0^{+2}_{-0}	22^{+42}_{-17}	0	44^{+84}_{-36}	122^{+275}_{-99}	0	260^{+542}_{-213}
VKI+C	0	0	0	7^{+10}_{-5}	0	14^{+21}_{-11}	115^{+262}_{-92}	0	243^{+511}_{-197}
KI+EC	7^{+9}_{-5}	0	12^{+18}_{-9}	79^{+173}_{-64}	0	160^{+330}_{-132}	124^{+281}_{-100}	0	267^{+555}_{-218}
ECS	50^{+94}_{-41}	0	100^{+182}_{-83}	115^{+262}_{-92}	0	247^{+512}_{-202}	124^{+281}_{-100}	0	267^{+555}_{-218}

To claim a KN detection with Rubin, it has to be observed in the $g+i$ filters on two consecutive nights. For each filter, we assume a 600s single-exposure observation, leading to a limiting magnitude of 26.62 for the $g-$filter and 25.62 for the $i-$filter (assuming the most optimistic configurations). To not take a large portion of Rubin's time by making it slew and cover 10 patches in the sky, we restrict ourselves to KNe for which the corresponding GW detections can constrain the sky-area associated with the binary to within $9.6\,\mathrm{deg}^2$, i.e., the FOV of Rubin. We also assume a duty cycle of 50% for the Rubin observatory. With these specifications, the number of KN detections with Rubin in an observation span of 10 years are listed in Table 3.7. We compare the values in Table 3.7 with the number of KNe observed in a span of 10 years for all events with $\Omega_{90} < 100$ deg^2 specified in Tables 3.8 and 3.9. It is seen that more KN detections are observed following the $g+i$ TOO strategy, compared to the KNe observed using a single filter and an exposure time of $30s$, despite the use of a more stringent sky-resolution criteria and 50% duty cycle in the TOO strategy. This is because we use an exposure time of $600s$ for the $g+i$ filters, which significantly improves the limiting magnitude of the g and i filters ($\sim 6\%$) compared to the single 30s-exposure case, leading to a greater

Table 3.7: The number of KN detections in an observation span of 10 years using the $g+i$ target-of-opportunity strategy with the Rubin observatory. The considered events have $\Omega_{90} \leq 9.6\,\mathrm{deg}^2$, which is equal to the FOV of the Rubin observatory. We also assume a duty cycle of 50%.

	Pop-1			**Pop-2**		
Network	ALF2	APR4	DD2	ALF2	APR4	DD2
HLVKI+	6^{+12}_{-6}	3^{+2}_{-3}	12^{+18}_{-11}	9^{+11}_{-7}	0	17^{+25}_{-14}
VK+HLIv	12^{+22}_{-10}	4^{+6}_{-4}	20^{+36}_{-16}	12^{+24}_{-10}	0	29^{+55}_{-25}
HLKI+E	12^{+30}_{-10}	5^{+11}_{-5}	22^{+45}_{-19}	14^{+26}_{-12}	0	34^{+67}_{-29}
VKI+C	8^{+16}_{-7}	3^{+3}_{-3}	16^{+28}_{-14}	12^{+18}_{-10}	0	23^{+41}_{-19}
KI+EC	20^{+40}_{-17}	6^{+14}_{-5}	30^{+63}_{-26}	16^{+39}_{-13}	0	44^{+101}_{-36}
ECS	20^{+41}_{-16}	6^{+14}_{-5}	32^{+66}_{-26}	16^{+40}_{-13}	0	45^{+106}_{-37}

number of KN detections. It is safe to assume that a similar strategy for *Roman* will improve the number of KN detections with *Roman* as well.

Depending on the EOS, one can expect to observe $\mathcal{O}(1)$ to $\mathcal{O}(10)$ KNe with Rubin and 0 to $\mathcal{O}(100)$ KNe with *Roman* in an observation span of 10 years. Even in the best case scenario, less than 10% of the events in the populations result in a KN, out of which less 10% are detected, giving the total number of detected KNe to be $< 1\%$ of the cosmic population of NSBH systems, which is consistent with the estimates reported in Refs. [103, 104]. There is a significant difference between the number of KNe expected to be observed based on the EOS used. This points to the possibility of deriving information about the EOS based solely on the number of KNe detected in the future. If we assume that the local merger rate is known to be around the median value of $45\,\mathrm{Gpc}^{-1}\mathrm{yr}^{-1}$, non-detectability of KNe from NSBH mergers in the coming years can point in favor of compact NSs governed by softer EOSs. Further, subject to the completeness of galaxy catalogs, detection of KNe from NSBH mergers will allow the localization of the host galaxy from which an accurate estimate of the redshift associated with the system can be obtained. Together with the constraints on luminosity distance, NSBH mergers can then be used as an independent tool to measure the Hubble constant [61, 91].

Table 3.8: Bandwise number of KN detections for both the EM telescopes, following the GW detections for the six GW detector networks for Pop-1. The numbers are reported for an observation time of 10 years.

Vera C. Rubin Telescope									
Filter	u			g			r		
EOS	ALF2	APR4	DD2	ALF2	APR4	DD2	ALF2	APR4	DD2
HLVKI+	0^{+2}_{-0}	0	1^{+4}_{-1}	10^{+17}_{-9}	4^{+5}_{-3}	16^{+30}_{-15}	9^{+16}_{-8}	4^{+5}_{-3}	16^{+28}_{-15}
VK+HLIv	0^{+2}_{-0}	0	1^{+4}_{-1}	13^{+25}_{-12}	5^{+9}_{-4}	22^{+46}_{-21}	14^{+25}_{-13}	4^{+9}_{-3}	23^{+42}_{-22}
HLKI+E	0^{+2}_{-0}	0	1^{+4}_{-1}	13^{+25}_{-12}	5^{+9}_{-4}	22^{+46}_{-21}	14^{+25}_{-13}	4^{+9}_{-3}	23^{+42}_{-22}
VKI+C	0^{+2}_{-0}	0	1^{+4}_{-1}	13^{+25}_{-12}	5^{+9}_{-4}	22^{+46}_{-21}	14^{+25}_{-13}	4^{+9}_{-3}	23^{+42}_{-22}
KI+EC	0^{+2}_{-0}	0	1^{+4}_{-1}	13^{+25}_{-12}	5^{+9}_{-4}	22^{+46}_{-21}	14^{+25}_{-13}	4^{+9}_{-3}	23^{+42}_{-22}
ECS	0^{+2}_{-0}	0	1^{+4}_{-1}	13^{+25}_{-12}	5^{+9}_{-4}	22^{+46}_{-21}	14^{+25}_{-13}	4^{+9}_{-3}	23^{+42}_{-22}
Filter	i			z			y		
EOS	ALF2	APR4	DD2	ALF2	APR4	DD2	ALF2	APR4	DD2
HLVKI+	5^{+9}_{-4}	2^{+1}_{-2}	10^{+19}_{-9}	2^{+3}_{-2}	0	4^{+7}_{-4}	0	0	0^{+2}_{-0}
VK+HLIv	5^{+12}_{-4}	2^{+2}_{-2}	10^{+24}_{-9}	2^{+3}_{-2}	0	4^{+7}_{-4}	0	0	0^{+2}_{-0}
HLKI+E	5^{+12}_{-4}	2^{+2}_{-2}	10^{+24}_{-9}	2^{+3}_{-2}	0	4^{+7}_{-4}	0	0	0^{+2}_{-0}
VKI+C	5^{+12}_{-4}	2^{+2}_{-2}	10^{+24}_{-9}	2^{+3}_{-2}	0	4^{+7}_{-4}	0	0	0^{+2}_{-0}
KI+EC	5^{+12}_{-4}	2^{+2}_{-2}	10^{+24}_{-9}	2^{+3}_{-2}	0	4^{+7}_{-4}	0	0	0^{+2}_{-0}
ECS	5^{+12}_{-4}	2^{+2}_{-2}	10^{+24}_{-9}	2^{+3}_{-2}	0	4^{+7}_{-4}	0	0	0^{+2}_{-0}
Nancy Grace Roman Observatory									
Filter	R			Z			Y		
EOS	ALF2	APR4	DD2	ALF2	APR4	DD2	ALF2	APR4	DD2
HLVKI+	16^{+30}_{-15}	7^{+6}_{-6}	29^{+52}_{-27}	16^{+29}_{-15}	6^{+5}_{-5}	25^{+47}_{-23}	14^{+29}_{-13}	6^{+5}_{-5}	25^{+45}_{-23}
VK+HLIv	66^{+131}_{-51}	23^{+50}_{-17}	118^{+242}_{-97}	43^{+103}_{-34}	11^{+33}_{-10}	69^{+162}_{-53}	38^{+87}_{-30}	11^{+31}_{-10}	62^{+155}_{-49}
HLKI+E	96^{+168}_{-74}	39^{+68}_{-30}	169^{+313}_{-138}	61^{+123}_{-49}	24^{+49}_{-21}	96^{+194}_{-76}	54^{+106}_{-44}	17^{+40}_{-15}	84^{+182}_{-68}
VKI+C	84^{+151}_{-64}	30^{+56}_{-22}	155^{+293}_{-126}	53^{+112}_{-42}	18^{+39}_{-16}	84^{+178}_{-66}	46^{+95}_{-37}	17^{+36}_{-15}	74^{+168}_{-60}
KI+EC	97^{+170}_{-75}	39^{+68}_{-30}	171^{+318}_{-140}	61^{+123}_{-49}	24^{+49}_{-21}	96^{+194}_{-76}	54^{+106}_{-44}	17^{+40}_{-15}	84^{+182}_{-68}
ECS	97^{+170}_{-75}	39^{+68}_{-30}	171^{+318}_{-140}	61^{+123}_{-49}	24^{+49}_{-21}	96^{+194}_{-76}	54^{+106}_{-44}	17^{+40}_{-15}	84^{+182}_{-68}
Filter	J			H			F		
EOS	ALF2	APR4	DD2	ALF2	APR4	DD2	ALF2	APR4	DD2
HLVKI+	14^{+29}_{-13}	6^{+5}_{-5}	25^{+42}_{-23}	13^{+24}_{-12}	5^{+5}_{-4}	22^{+42}_{-20}	10^{+17}_{-9}	4^{+5}_{-3}	16^{+28}_{-15}
VK+HLIv	35^{+78}_{-27}	11^{+27}_{-10}	53^{+129}_{-43}	28^{+61}_{-23}	9^{+19}_{-8}	45^{+105}_{-37}	15^{+27}_{-14}	4^{+10}_{-3}	27^{+51}_{-23}
HLKI+E	50^{+96}_{-40}	13^{+32}_{-11}	72^{+153}_{-60}	35^{+72}_{-29}	11^{+23}_{-9}	58^{+119}_{-48}	15^{+27}_{-14}	4^{+10}_{-3}	28^{+52}_{-23}
VKI+C	44^{+86}_{-35}	13^{+28}_{-11}	65^{+143}_{-54}	35^{+68}_{-29}	11^{+19}_{-9}	53^{+113}_{-44}	15^{+27}_{-14}	4^{+10}_{-3}	28^{+52}_{-23}
KI+EC	50^{+96}_{-40}	13^{+32}_{-11}	72^{+153}_{-60}	35^{+72}_{-29}	11^{+23}_{-9}	58^{+119}_{-48}	15^{+27}_{-14}	4^{+10}_{-3}	28^{+52}_{-23}
ECS	50^{+96}_{-40}	13^{+32}_{-11}	72^{+153}_{-60}	35^{+72}_{-29}	11^{+23}_{-9}	58^{+119}_{-48}	15^{+27}_{-14}	4^{+10}_{-3}	28^{+52}_{-23}

Table 3.9: Bandwise number of KN detections for both the EM telescopes, following the GW detections for the six GW detector networks for Pop-2. The numbers are reported for an observation time of 10 years.

Vera C. Rubin Telescope									
Filter	u			g			r		
EOS	ALF2	APR4	DD2	ALF2	APR4	DD2	ALF2	APR4	DD2
HLVKI+	4^{+5}_{-3}	0	6^{+9}_{-5}	17^{+22}_{-15}	0	33^{+44}_{-28}	16^{+18}_{-14}	0	31^{+41}_{-26}
VK+HLIv	4^{+5}_{-3}	0	6^{+9}_{-5}	21^{+46}_{-18}	0	42^{+93}_{-36}	19^{+30}_{-16}	0	37^{+82}_{-31}
HLKI+E	4^{+5}_{-3}	0	6^{+9}_{-5}	22^{+47}_{-19}	0	43^{+95}_{-37}	20^{+30}_{-17}	0	38^{+84}_{-32}
VKI+C	4^{+5}_{-3}	0	6^{+9}_{-5}	22^{+46}_{-19}	0	43^{+94}_{-37}	20^{+30}_{-17}	0	38^{+83}_{-32}
KI+EC	4^{+5}_{-3}	0	6^{+9}_{-5}	22^{+47}_{-19}	0	43^{+95}_{-37}	20^{+30}_{-17}	0	38^{+84}_{-32}
ECS	4^{+5}_{-3}	0	6^{+9}_{-5}	22^{+47}_{-19}	0	43^{+95}_{-37}	20^{+30}_{-17}	0	38^{+84}_{-32}
Filter	i			z			y		
EOS	ALF2	APR4	DD2	ALF2	APR4	DD2	ALF2	APR4	DD2
HLVKI+	8^{+13}_{-7}	0	16^{+23}_{-15}	1^{+4}_{-1}	0	6^{+12}_{-5}	0	0	1^{+0}_{-1}
VK+HLIv	8^{+14}_{-7}	0	16^{+29}_{-15}	1^{+4}_{-1}	0	6^{+12}_{-5}	0	0	1^{+0}_{-1}
HLKI+E	8^{+14}_{-7}	0	16^{+29}_{-15}	1^{+4}_{-1}	0	6^{+12}_{-5}	0	0	1^{+0}_{-1}
VKI+C	8^{+14}_{-7}	0	16^{+29}_{-15}	1^{+4}_{-1}	0	6^{+12}_{-5}	0	0	1^{+0}_{-1}
KI+EC	8^{+14}_{-7}	0	16^{+29}_{-15}	1^{+4}_{-1}	0	6^{+12}_{-5}	0	0	1^{+0}_{-1}
ECS	8^{+14}_{-7}	0	16^{+29}_{-15}	1^{+4}_{-1}	0	6^{+12}_{-5}	0	0	1^{+0}_{-1}
Nancy Grace Roman Observatory									
Filter	R			Z			Y		
EOS	ALF2	APR4	DD2	ALF2	APR4	DD2	ALF2	APR4	DD2
HLVKI+	32^{+42}_{-27}	0	59^{+92}_{-51}	29^{+37}_{-24}	0	56^{+80}_{-49}	26^{+35}_{-21}	0	53^{+74}_{-46}
VK+HLIv	93^{+222}_{-76}	0	196^{+435}_{-163}	61^{+144}_{-48}	0	136^{+291}_{-113}	49^{+119}_{-38}	0	119^{+257}_{-98}
HLKI+E	122^{+275}_{-99}	0	260^{+542}_{-213}	71^{+168}_{-56}	0	167^{+341}_{-137}	54^{+131}_{-41}	0	143^{+297}_{-116}
VKI+C	115^{+262}_{-92}	0	243^{+511}_{-197}	67^{+164}_{-52}	0	160^{+329}_{-130}	51^{+129}_{-38}	0	137^{+287}_{-110}
KI+EC	124^{+281}_{-100}	0	267^{+555}_{-218}	71^{+169}_{-56}	0	168^{+347}_{-137}	54^{+132}_{-41}	0	144^{+300}_{-116}
ECS	124^{+281}_{-100}	0	267^{+555}_{-218}	71^{+169}_{-56}	0	168^{+347}_{-137}	54^{+132}_{-41}	0	144^{+300}_{-116}
Filter	J			H			F		
EOS	ALF2	APR4	DD2	ALF2	APR4	DD2	ALF2	APR4	DD2
HLVKI+	24^{+31}_{-20}	0	51^{+72}_{-44}	20^{+24}_{-17}	0	44^{+66}_{-37}	10^{+16}_{-8}	0	32^{+41}_{-27}
VK+HLIv	40^{+91}_{-31}	0	100^{+223}_{-81}	25^{+64}_{-21}	0	75^{+170}_{-61}	10^{+21}_{-8}	0	38^{+82}_{-32}
HLKI+E	43^{+97}_{-34}	0	113^{+251}_{-92}	26^{+67}_{-22}	0	82^{+184}_{-66}	10^{+21}_{-8}	0	39^{+84}_{-33}
VKI+C	40^{+96}_{-31}	0	108^{+245}_{-87}	26^{+66}_{-22}	0	79^{+181}_{-63}	10^{+21}_{-8}	0	39^{+83}_{-33}
KI+EC	43^{+98}_{-34}	0	113^{+252}_{-92}	26^{+67}_{-22}	0	82^{+185}_{-66}	10^{+21}_{-8}	0	39^{+84}_{-33}
ECS	43^{+98}_{-34}	0	113^{+252}_{-92}	26^{+67}_{-22}	0	82^{+185}_{-66}	10^{+21}_{-8}	0	39^{+84}_{-33}

3.3 Case study: GW230529

The GW event GW230529_181500 [3], better known as GW230529, was observed exclusively by the LIGO Livingston detector [22]. The signal was detected with a SNR of $\gtrsim 11$ and a notably low false alarm rate of less than one event per thousand years, as determined by the PyCBC offline analysis. Assuming GW230529 originated from a NSBH merger on a quasi-circular orbit, parameter estimation analysis indicates component masses of $3.6^{+0.8}_{-1.2}, M\odot$ and $1.4^{+0.6}_{-0.2}, M\odot$ (90% credible intervals). This makes GW230529 the most symmetric mixed compact binary merger detected to date through gravitational waves.

In Chapter 4, we analyze GW230529 using astrophysically informed mass and spin priors to gain insights into the formation channels and evolutionary processes of this compact binary. To achieve this, we employ predictions from 15 binary population synthesis models of NSBH mergers presented by Ref. [1]. These models systematically explore variations in physical assumptions relative to the "fiducial" scenario, including the efficiency of mass transfer between binary components and natal kicks imparted to compact objects. A summary of these models is provided in Section 4.3 of Chapter 4. Using posterior samples derived from the parameter estimation incorporating these astrophysical priors, we can estimate the total ejecta mass, dynamical ejecta, and unbound disk ejecta corresponding to each formation scenario by applying empirical fitting formulae from Refs. [143, 144].

This calculation is performed using four different EOSs: `APR4` [150], `SLy` [154, 155], `DD2` [151, 156] and `H4` [157–159] (see Fig. 3.8 in for the corresponding mass-radius curves). Among these, `APR4` and `SLy` give relatively more compact NSs, whereas `DD2` and `H4` result in less compact ones. Thus, the latter two will produce more ejecta than the former. We find that `APR4` does not give any ejecta for samples corresponding to any population models. Fig. 3.9 shows the probability distribution of total ejecta for the remaining three EOS. Across population models, the total ejecta mass corresponding to `SLy` $\lesssim 0.01 M_\odot$, `DD2` $\lesssim 0.05 M_\odot$, and `H4` $\lesssim 0.07 M_\odot$. Most ejecta are produced for the samples corresponding to the "rapid SNe" population model, which is due to its preference for a more symmetric binary (c.f. Fig. 4.9). On the other hand, the "Unstable Case BB" population model results in no ejecta, due to its preference for more massive (hence, more compact) NS. Note that both "rapid SNe" and "Unstable Case BB" population models are disfavored compared to others, as discussed in Sec. 4.3.2.2 in Chapter 4.

Choosing the most optimistic scenarios, namely those corresponding to `H4` EOS, we

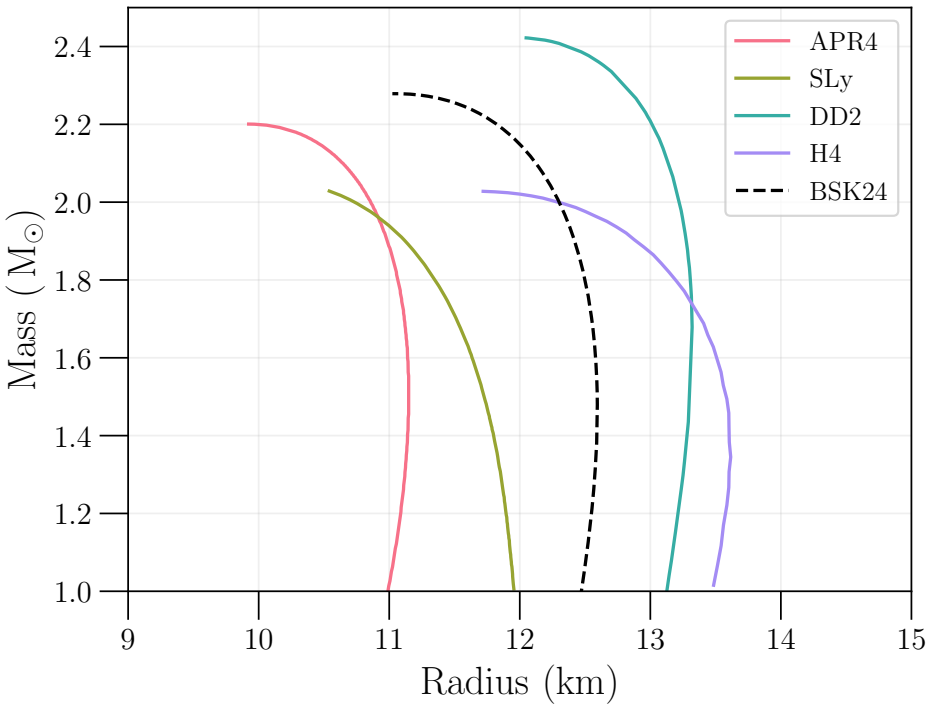

Figure 3.8: The mass-radius curves for the EoS chosen in this study. We also show the `BSK24` EoS which was used by Ref. [3].

calculate the bolometric KNe light curves. We convert them to bandwise light curves for the *ugrizy* filters for Roman. Figure 3.10 shows i-band curves together with the curve for maximum likelihood ($\mathcal{L}_{\rm max}$) binary parameters. We also compare the points from the detected light curve of GW170817 [160, 161] in the i-band.

From Fig. 3.10, we note that only the "Unstable case BB" mass transfer population model does not support a KN after the merger, a population model disfavored by our analysis. For all other population models, the KN is expected to be considerably dimmer than the one observed for GW170817. This is expected, given that the KN flux is inversely proportional to the distance squared and that GW230529 is located approximately five times further than GW170817 [3]. For all population models, the curves corresponding to the $\mathcal{L}_{\rm max}$ binary parameters prefer comparatively dimmer KNe, which is because the $\mathcal{L}_{\rm max}$ parameters correspond to more mass-asymmetric binary located further away.

Focusing on the KNe properties, we note that the luminosity in the i-band peaks a day after the merger for all population models except "unstable case BB". The peak luminosities corresponding to the $\mathcal{L}_{\rm max}$ binary parameters lie in the range $[23.97, 24.67]$ mag. For the "fiducial" population model and $\mathcal{L}_{\rm max}$ binary parameters, Table 3.10 shows the bandwise peak luminosities and its decay. The latter is the absolute difference

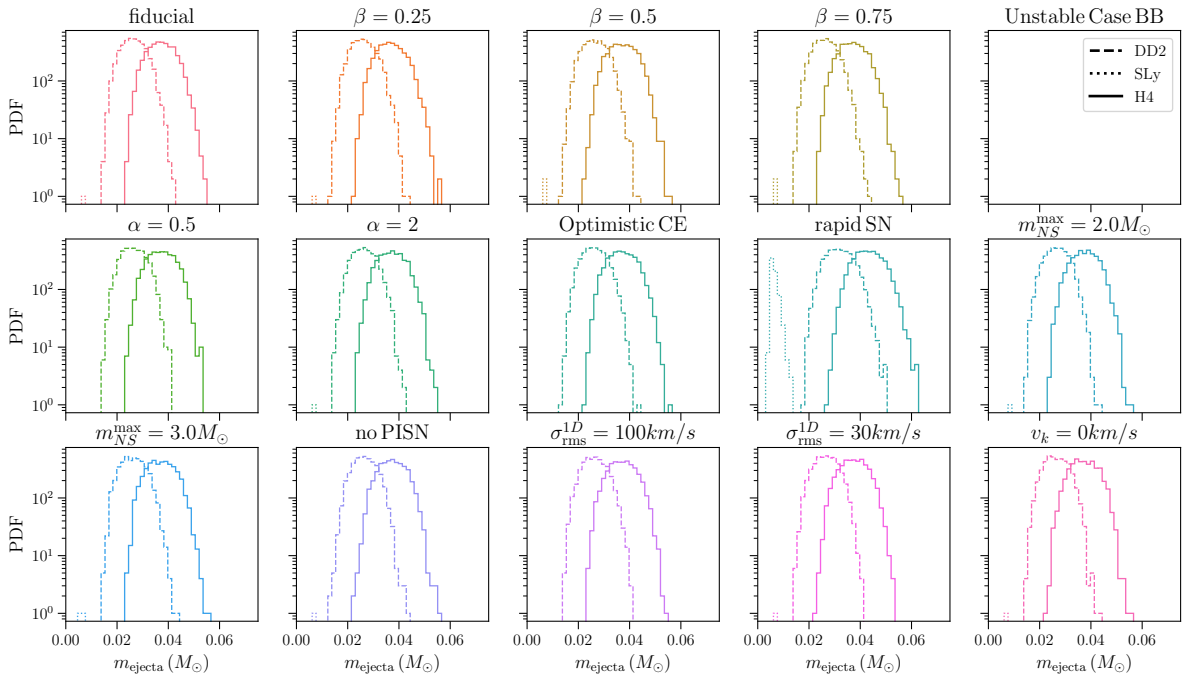

Figure 3.9: The probability distribution function (PDF) for the total ejecta mass for different EoS and corresponding to the various population models. No ejecta was obtained for the `APR4` EoS.

Table 3.10: The (optical) bandwise peak luminosities and decay in luminosity one day after peak for the KNe with $\mathcal{L}_{\rm max}$ binary parameters corresponding to the "fiducial" population model and the `H4` EOS. For comparison, the single-exposure (30s) bandwise limiting magnitudes corresponding to the Rubin Observatory ($m_{\rm RO}^{\rm lim}$) are also listed.

Band	$m_{\rm RO}^{\rm lim}$ ($m_{\rm AB}$)	Peak ($m_{\rm AB}$)	Decay ($m_{\rm AB}$)
u	23.9	26.63	1.85
g	25.0	25.80	1.04
r	24.7	25.05	0.59
i	24.0	24.61	0.35
z	23.3	24.27	0.16
y	22.1	24.04	0.10

between the peak luminosity and one day after it.

To gauge the KNe detectability, we compare the peak luminosity in each band with the corresponding limiting magnitude ($m_{\rm RO}^{\rm lim}$) of the Rubin Observatory for a single, 30s long exposure. While the KNe in the y-band is the brightest, Rubin wouldn't have observed it owing to its relatively poor sensitivity in this band. For the "fiducial" population model, peak luminosities in the gri bands come closest to the limiting magnitude threshold.

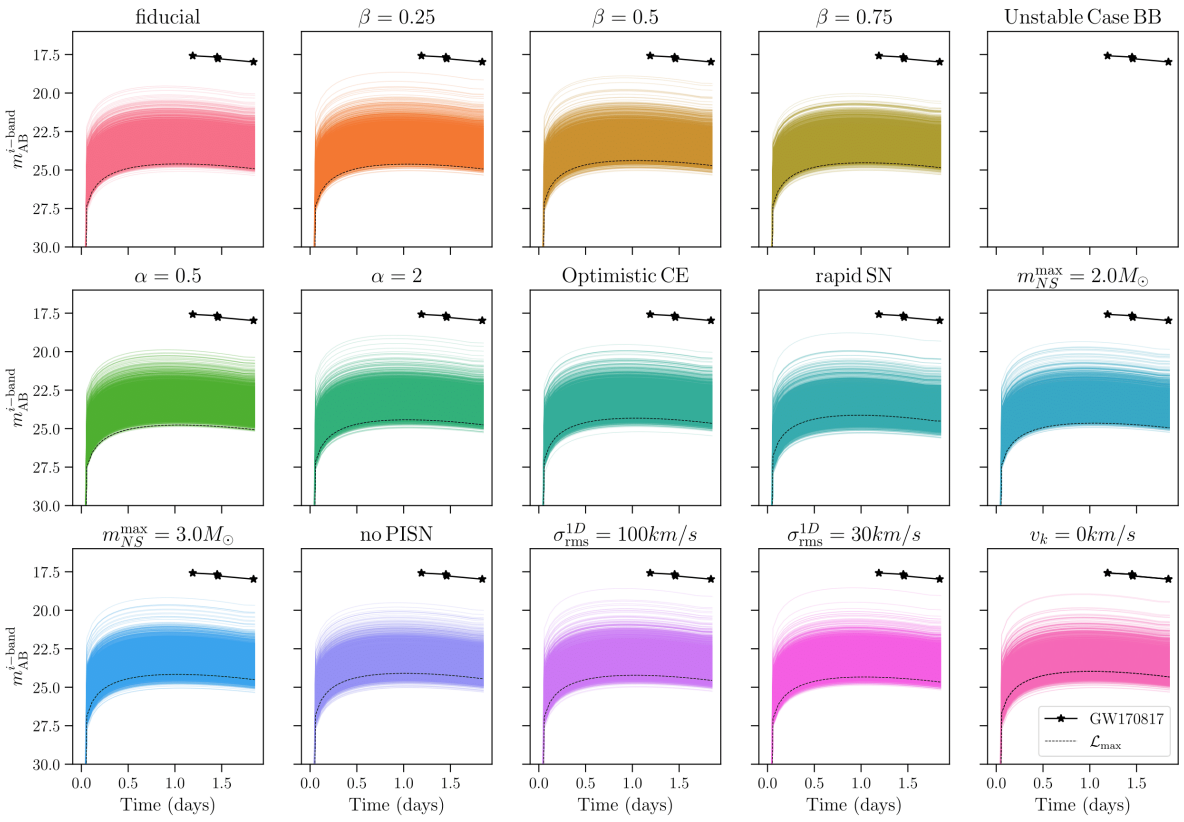

Figure 3.10: KNe light curves in the $i-$band corresponding to the different population models for the `H4` EoS. The dotted line shows the light curve associated with the maximum likelihood parameter estimates for each model.

However, a targeted observation with 600s exposure increases the limiting magnitude for the g and i bands to 26.62 and 25.62 [37, 61], respectively, making the KNe visible in these bands.

3.4 Conclusions

The detectability of KN emission from NSBH mergers depends on several key factors, including the binary mass ratio ($q = m_{\rm BH}/m_{\rm NS}$), the spin of the BH, and the NS EOS, which is currently uncertain. Brighter KNe and larger merger ejecta masses typically result from binaries with smaller mass ratios, higher BH spins, and stiffer EOS, such as `DD2`. Conversely, binaries with larger mass ratios and softer EOS, like `APR4`, generally yield dimmer KNe that may fail to form or remain too faint for detection. Despite the enhanced sensitivity provided by XG GW observatories and even under the most optimistic scenarios with stiffer EOS, the annual rate of mergers producing observable

KNe is anticipated to be limited to only a few events.

In our case study of GW230529—the most mass-symmetric NSBH merger observed during the fourth observing run of the LVK detectors—we calculated the associated KN light curves. Our analysis indicates that the resulting emission in the i-band is too faint for detection by typical wide-field searches conducted by the Rubin Observatory. However, targeted follow-up observations may still have detected the associated EM counterparts.

Early warnings of imminent mergers, issued minutes in advance, would significantly enhance telescope capabilities by allowing prompt observations of the onset of EM counterparts and potentially revealing the nature of the central engine powering associated gamma-ray bursts. Upcoming GW detector upgrades, such as A+ and Voyager, will not achieve precise localization alerts two or more minutes before merger. In contrast, XG observatories are projected to provide timely alerts for tens to hundreds of NSBH mergers per year, with sky localizations better than 100 deg^2. A few of these events could be localized approximately five minutes before merger, and a similar number might achieve localizations within 10 deg^2, significantly enhancing the prospects for multi-messenger observations.

Declaration

The author of this dissertation was responsible for generating all the results that are presented in this chapter. The scripts to obtain kilonovae light curves were adapted from Rahul Kashyap's repository. The posterior samples of GW230529 that were used to generate the ejecta and kilonovae constraints were produced by Koustav Chandra and Rossella Gamba. The contents of this chapter have been published in the journal Physical Review D by the American Physical Society with reference [73], and in the Astrophysical Journal of the American Astronomical Society with reference [162].

Chapter 4
Enabling astrophysical inference with NSBH mergers

All models are wrong, but some are useful.
— George Box

4.1 Introduction

The current ground-based GW detectors are sensitive to GW from binaries containing BHs and/or NSs. These compact objects form as the end-product of the evolution of massive stars. The formation mechanism of such compact binaries can be broadly classified into two types– first, where two closely-located massive stars evolve in isolation [163, 164], and second, where the binaries are formed due to dynamical interactions in dense stellar environments [165, 166]. The pathway followed for the binary formation and the processes it undergoes during its evolution leave their imprints on the system, particularly on the masses and spins of the components. Fortunately, by detecting the GWs from these systems, these parameters can be inferred, which provides important insights into the formation and evolution of the binary (e.g., see Ref. [167]). As different formation channels lead to different parameters of the components [168–170], and a single formation channel cannot explain the properties of the detected binaries [171], precise estimation of the mass and the spin distributions is pivotal for understanding the contributions of the various formation channels to the binary population.

The first direct detection of GW was from a $\sim 65\,\mathrm{M}_\odot$, nearly equal mass, BBH merger [21]. This detection proved that BBH can merge in Hubble time and allowed the determination of the merger rate for such binaries, rejecting pessimistic formation scenarios that predicted very low merger rate values [172, 173]. While the components' masses were more than the expectations from low-mass X-ray binary systems [174], they

were found to be consistent with both isolated and dynamical formation channels, provided that the corresponding metallicity is lower than solar metallicity [168, 175]. Since then, the Advanced Laser Interferometer Gravitational-Wave Observatory (aLIGO) [22–24, 40] and the Advanced Virgo (AdV) [26, 27] detector have detected ~ 100 mergers by the end of the third observing run [75]. Among these, the majority are BBH mergers, followed by two NSBH mergers and two BNS mergers. Using the detected BBH mergers, significant constraints have been placed on the mass spectrum of BH [33], revealing distinctive features that could contain information about the astrophysical processes at play [176–180]. While the predictions for the masses of the components from different formation channels can overlap, the spin values and orientations can encode decisive information for distinguishing between the formation scenarios [84, 181, 182]. The isolated binary formation channels are, predominantly, expected to create slowly spinning binaries with spins aligned with the orbital angular momentum [175, 183–186] (however, see Refs. [187–189]). On the other hand, binaries formed through dynamical exchanges are expected to have components with spins that are oriented isotropically [190] and possibly with large magnitudes [191]. Unfortunately, as the individual spins of the compact objects cannot yet be precisely measured using GW observations, the spin distribution of the BHs from the current observations remains uncertain [192], leading to a lack of clarity about the dominant formation channel for the detected population.

The properties of the cosmic population of BNS and NSBH mergers are even more uncertain, owing to the limited number of GW observations. Currently, our expectations are informed by the Galactic pulsar observations which point to a bimodal mass distribution with the dominant peak at $\sim 1.4\,\mathrm{M}_\odot$ and the minor peak at $\sim 1.8\,\mathrm{M}_\odot$ [193–195]. NS present in binaries are seen to coincide with the former peak [196, 197]. While GW170817 [25] seems to follow this trend as well, the component masses inferred for GW190425 [198] contradict it. Unlike the pulsar population, the NS in BNS and NSBH mergers detected using GWs so far are consistent with a uniform distribution in mass [33, 199].

In this chapter, we will show that the precise estimation of binary parameters with NSBH mergers renders them as powerful astrophysical probes. Specifically, in Sec. 4.2, we will demonstrate that the spin of the NS participating in the NSBH merger can be measured very precisely with XG observatories, and that this measurement can inform the formation and evolution of the NSBH binary. To emphasize the utility of NSBH mergers for astrophysical inference, in Sec. 4.3, we will again look at GW230529 with astrophysical informed priors and provide conclusive insights into the probable physical

processes underlying this binary formation.

4.2 Measuring small NS spin with NSBH mergers

Measuring the spin of the individual NS using GW is trickier. This is due to the following two reasons. Firstly, individual spins are difficult to measure. The GW signal for low-mass compact objects, like BNS and NSBH, is dominated by the inspiral—where the orbit of the binary shrinks due to the emission of GW. This part of the signal is well approximated with the PN formalism [53], where the dominant spin effect appears at 1.5 PN order and is best represented by the effective spin parameter [200],

$$\chi_{\rm eff} = \frac{m_1\chi_1 + m_2\chi_2}{m_1 + m_2} = \frac{\chi_1 + q\,\chi_2}{1+q}. \tag{4.1}$$

Here, (m_1, m_2) are the component masses, (χ_1, χ_2) are their dimensionless spin components aligned with the orbital angular momentum, and $q = m_2/m_1 \leq 1$ is the mass ratio. Further, the contribution to the GW phase for non-precessing systems to leading order in spin can be written as,

$$\Psi(f) = \frac{3}{128(\pi f\mathcal{M})^{5/3}}\left[1 + \nu^2\left(\frac{3715}{756} + \frac{55\eta}{9}\right) + \nu^3\left(\frac{113}{3}\chi_{\rm eff} - \frac{76\eta}{3}\chi_s - 16\pi\right)\right], \tag{4.2}$$

where $\mathcal{M} = M\eta^{3/5}$ is the chirp mass, $\eta = q/(1+q)^2$ is the symmetric mass ratio, $\nu = (\pi f M)^{1/3}$ is the PN expansion parameter, $M = m_1 + m_2$ is the total mass, f is the frequency of the quadrupolar part, and $(\chi_s = \chi_1 + \chi_2)/2$. The dominant effect of spins on the phase can be encapsulated in a reduced spin parameter, $\chi_{\rm PN}$, defined as

$$\chi_{\rm PN} = \chi_{\rm eff} - (76\eta/113)\chi_s. \tag{4.3}$$

As the lowest order contribution to the phase depends on the chirp mass $\mathcal{M}$, it is well measured. Now, looking specifically at the ν^2 (1 PN) and the ν^3 (1.5 PN) terms [201],

$$\Delta\Psi(f) = \frac{3\nu^2}{128(\pi f\mathcal{M})^{5/3}}\left[\frac{3715}{756} + \frac{55\eta}{9} + \nu\left(\frac{113}{3}\chi_{\rm PN} - 16\pi\right)\right], \tag{4.4}$$

we see that η, or equivalently the q, can be varied without varying $\mathcal{M}$ to mimic the effect of spin (though, it will also have to account for the changing ν with frequency) at this order. This, together with the dependence of $\chi_{\rm eff}$ on q, represents the degeneracy

between mass and spin parameters, which hampers the measurement of the individual spins [201, 202].

Secondly, the dimensionless spins of NS are expected to be small by the time of merger. Pulsar observations suggest that NS can be rapidly rotating. While most of the cataloged pulsars have periods $P \sim 0.5$ s, a significant and distinct fraction, called millisecond pulsars, can have periods $P \lesssim 30$ ms [203]. The fastest-rotating known pulsar, PSR J1748-2446ad, has a period of $P \sim 1.4$ ms, translating to a dimensionless spin $\chi \leq 0.4$ [25, 204]. The fastest-spinning NS that is part of a BNS that will merge within Hubble time is PSR J0737-3039, with a period of 22 ms [205]. While this is still rapid, pulsar rotation is expected to slow down with time. This is because pulsars accelerate charged particles which, in turn, emit radiation, and this radiation carries away the rotational kinetic energy. In fact, PSR J0737-3039 is expected to spin-down to $\chi \lesssim 0.04$ at merger [25]. As ground-based GW observatories are only expected to detect these binaries close to merger, the NS dimensionless spins are expected to be $\lesssim 0.04$.

Fortunately, the mass-spin degeneracy can be broken with the inclusion of HOMs and precession [69] in the waveform. In this work, we will restrict ourselves to non-precessing systems. While the quadrupolar $(2, 2)$ mode dominates the GW from equal-mass and face-on (inclination angle $\iota = 0°$) systems, the sub-dominant HOMs get activated for systems with unequal masses [8, 206] (and for precessing systems). We expect the contribution of these HOMs to increase with the asymmetry in the masses. As the NS mass function is restricted to a small range of values [207–214], we do not except significant contribution of HOMs in the inspiral of BNS mergers. On the other hand, NSBH mergers will have unequal masses. Population synthesis studies (like Ref. [1]) that have looked at NSBH mergers formed through isolated binary formation channels find that BH mass in NSBH mergers rarely exceeds $20\,\mathrm{M}_\odot$, with the peak of the mass function lying between $5\,\mathrm{M}_\odot - 15\,\mathrm{M}_\odot$. This is also supported by the inference of BH mass spectrum from detected NSBH mergers [103]. Given that the expected NS masses are less than $2\,\mathrm{M}_\odot$, NSBH systems will be largely asymmetric with $q \lesssim 0.4$. Thus, due to the contribution of HOMs to the GW signal, NSBH systems can be instrumental in measuring the NS spin ($\chi_{\rm NS}$).

In this section, we assess the precision with which $\chi_{\rm NS}$ can be measured from non-precessing NSBH mergers. The "non-precessing" choice is partly motivated by our focus on binaries formed through isolated binary formation channels (see Section 4.2.1.2) and partly due to computational feasibility (briefly discussed in Section 4.2.2). We find that the precision in the measurement of $\chi_{\rm NS}$ strongly depends on the BH spin ($\chi_{\rm BH}$), with

high BH spins ($\chi_{\rm BH} \geq 0.6$) being conducive to more precise $\chi_{\rm NS}$ measurement. We also show the importance of HOMs in improving the measurement precision, by comparing the bounds placed on $\chi_{\rm NS}$ using a waveform model that only contains the quadrupolar mode with one that also contains HOMs, at varying inclination angles. As the detected NSBH events fail to constrain $\chi_{\rm NS}$ [33, 75, 76], we focus on the abilities of XG GW observatories in measuring the same. We find that a five-detector A+ [39, 40] (three-detector A$^\sharp$) [46] network might distinguish $\chi_{\rm NS} = 0.04$ from zero at $1-\sigma$ confidence for an NSBH merger at ~ 30 (~ 50) Mpc, while a network with ET [37, 50, 51] and two CE [38, 47–49, 215] can accomplish the same for an NSBH merger at ~ 350 Mpc. Based on these results, we claim that *if* there exists a sub-population of NSBH binaries in nature that merge within Hubble time and contain rapidly spinning NS, then XG observatories will discern such NS from slowly or non-spinning ones, identifying extragalactic NS with millisecond rotational periods without EM observations.

In this section, we emphasize the significance of measuring the NS spin with high precision. However, it is also vital to highlight that breaking the mass-spin degeneracy also enhances BH spin measurements (see Section 4.2.3.1). This improvement holds astrophysical significance since accurately determining $\chi_{\rm BH}$ can provide valuable insights into the formation processes underlying binary creation. For a brief discussion on this aspect, refer to Section 4.2.1.2.

The rest of the section is structured as follows. In Section 4.2.1, we build on the motivation for this study. The description of the employed parameter estimation techniques, the NSBH systems that are considered, and the GW network configurations that are used are presented in Section 4.2.2. In Section 4.2.3, we show the constraints on $\chi_{\rm NS}$ that can be placed with NSBH mergers, accompanied by the analysis of how BH parameters, the presence of HOMs, and detector sensitivity can affect the precision with which $\chi_{\rm NS}$ can be estimated.

4.2.1 Motivation

In this section, we describe the motivation for considering NSBH mergers to precisely measure the NS spin. In Section 4.2.1.1, we use PN expressions to show the utility of HOMs in improving the measurement of $\chi_{\rm NS}$. In Section 4.2.1.2, we discuss the astrophysical processes that can lead to the formation of NSBH systems with rapidly spinning NS that merge within Hubble time.

4.2.1.1 Theoretical Arguments

In Section 4.1, we explained the degeneracy between the mass and spin parameters using the PN expansion of the GW phase to leading order in spin. We encapsulated the effect of spin to the phase at this order in the term $\chi_{\rm PN}$, which is a function of $\chi_{\rm eff}$ and χ_s. For BNS systems, the mass ratio is close to 1, leading to $\chi_{\rm eff} \sim \chi_s$. Thus, while these combinations of component spins can be measured to significant precision, it is difficult to disentangle the values of individual spins from them. These degeneracies could be affected due to higher-order spin effects, including the effect of spin-induced quadrupole moments on the phase [216–218]. However, given that the values of $\chi_{\rm NS}$ are expected to be small, we do not expect these effects to drastically improve the measurement of NS spins.

For NSBH systems, we expect $\chi_{\rm NS}$ to be small and the mass ratio to be much smaller than 1. With these assumptions,

$$\chi_{\rm eff} = \frac{\chi_{\rm BH} + q\,\chi_{\rm NS}}{1+q} \approx \chi_{\rm BH},$$

i.e., most of the information contained in $\chi_{\rm eff}$ is about $\chi_{\rm BH}$, as the contribution of $\chi_{\rm NS}$ is weighed down by q. While $\chi_{\rm BH}$ and $\chi_{\rm NS}$ are at equal footing in χ_s, the contribution of χ_s compared to $\chi_{\rm eff}$ is weighed down by η (as, by definition, $\eta \leq 1/4$).

The HOMs also contain contributions from the spins, which can help improve the measurements of individual spins of binary components. Revisiting the discussion from Chapter 1, the complex time-domain GW strain $h(t)$ can be decomposed in the basis of -2 spin-weighted spherical harmonics Y^{lm}_{-2},

$$h(t, \boldsymbol{\lambda}) = \sum_{l=2}^{\infty} \sum_{m=-l}^{l} Y^{lm}_{-2}(\iota)\, h_{lm}(t, \boldsymbol{\lambda}), \tag{4.5}$$

where ι is the inclination angle, and $\boldsymbol{\lambda}$ is the set of parameters, including masses and spins of the binary components, that affect the strain. For non-precessing systems, the $(l, \pm m)$ modes obey the symmetry $h_{lm} = (-1)^l\, \bar{h}_{l-m}$. The phase of (l, m) modes has an approximate relation to the phase of the $(2, 2)$ mode in the inspiral regime, given by $\Phi_{lm} \approx \frac{m}{2}\Phi_{22}$, which also means that the frequency corresponding to the $(l, \pm m)$ mode is $m/2$ times the frequency of the $(2, \pm 2)$ mode. On the other hand, the amplitudes of the HOMs contain important differences. Firstly, the relative contribution of the (l, m) mode to the signal depends on the inclination angle, which enters the equation through Y^{-2}_{lm}. Figure 1.2 in Chapter 1 shows the dependence of the absolute value of

Table 4.1: The table lists the leading-order spin terms that contribute to the amplitudes of some of the different (l, m) modes, retrieved from Ref. [8]. Here, the column titled PN lists the PN order of the leading order term that contributes to the amplitude of the mode, and the PN(χ) column lists the leading order at which the spin terms show up in the amplitudes of the respective modes. Similar to $\chi_{\rm eff}$, we introduce another combination of component spins and mass ratio, $\tilde{\chi} = \frac{\chi_{\rm BH} - q\,\chi_{\rm NS}}{1+q}$, which contains the leading order spin effects to the $(2, 1)$ and the $(3, 3)$ mode amplitudes. We have also used the asymmetric spin combination, $\chi_a = (\chi_{\rm BH} - \chi_{\rm NS})/2$.

Mode	PN	PN(χ)	Leading order spin terms
$(2,1)$	0.5	1	$\frac{4i}{R}\sqrt{\frac{\pi}{5}}\,\eta M\,\tilde{\chi}$
$(2,2)$	0	1.5	$\frac{32}{3R}\sqrt{\frac{\pi}{5}}\,\eta M\,\left(\chi_{\rm eff} - \eta\chi_s\right)$
$(3,2)$	1	1.5	$\frac{32}{3R}\sqrt{\frac{\pi}{7}}\,\eta^2 M\,\chi_s$
$(3,3)$	0.5	2	$\frac{3i}{2R}\sqrt{\frac{6\pi}{7}}\,\eta M\,\left((4-5\eta)\tilde{\chi} - 14\eta\chi_a\right)$
$(4,4)$	1	2.5	$\frac{256}{9R}\sqrt{\frac{\pi}{7}}\,\eta M\left[(-\frac{2}{3}+\frac{13}{5}\eta)\chi_{\rm eff} + \frac{2\eta}{5}\left(\frac{1}{3}-7\eta\right)\chi_s\right]$

Y^{-2}_{lm} with inclination for different modes. Secondly, various combinations of component spins contribute to the amplitude of the $(2, 2)$ mode and the HOMs. The leading-order spin contributions to h_{lm} are listed in Table 4.1, with lower-order terms only depending on mass parameters. Based on Table 4.1 and Fig. 1.2, we conclude the following:

- The leading order term in the $(2, 2)$ mode amplitude is at 0 PN. This makes $(2, 2)$ the dominant mode in the GW strain.
- Only the $(2, 2)$ and $(3, 2)$ modes contribute to the signal for face-on ($\iota = 0°$) systems. The $(2, 1)$, $(3, 3)$ and $(4, 4)$ modes peak at $\iota > 40°$.
- The $(2, 2)$, $(3, 2)$ and $(4, 4)$ modes contain positive combinations of spins, like $\chi_{\rm eff}$ and χ_s, whereas $(2, 1)$ and $(3, 3)$ modes contain negative combinations, like $\tilde{\chi}$ and χ_a.
- In their respective modes, the χ_s (χ_a) spin terms are suppressed by a factor of η compared to the $\chi_{\rm eff}$ ($\tilde{\chi}$) term.

The different ways in which the mass and spin terms interact in the various (l, m) modes help remove the degeneracy between these parameters. While $\chi_{\rm eff}$ and $\tilde{\chi}$ values for BNS

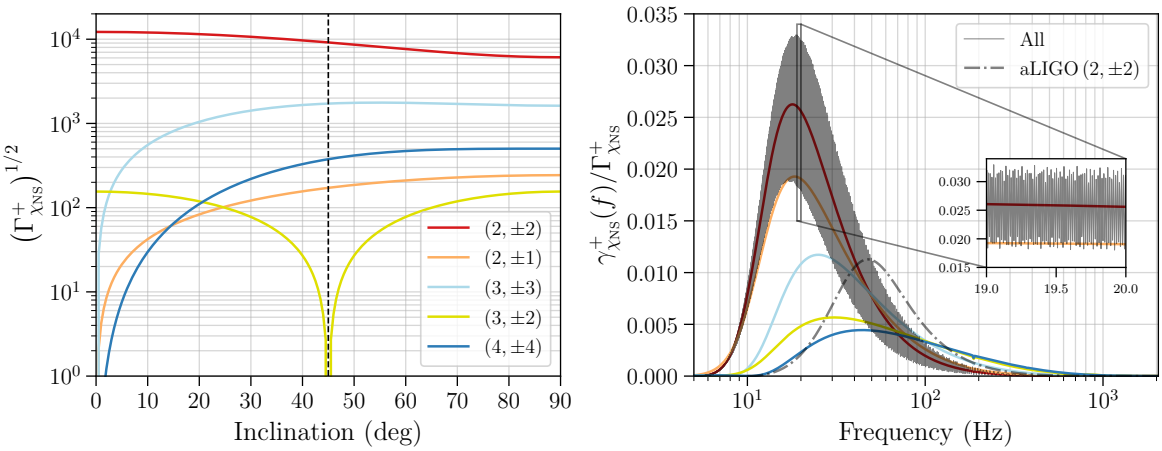

Figure 4.1: Left panel: The square-root of the Fisher term corresponding to $\chi_{\rm NS}$ for the various (l, m) modes as a function of inclination angle (see Equations (4.6)-(4.8) for definitions of the various terms). The dotted vertical line indicates $\iota = 45°$. Right panel: Assuming $\iota = 45°$, the figure shows the normalized Fisher term as a function of frequency for the different (l, m) modes separately, whereas the black curve shows the normalized Fisher term for the full waveform that contains all the modes. The highly oscillatory nature of the full waveform, due to constructive and destructive interference between modes, is highlighted in the inset. The 40 km CE PSD was used for obtaining the Fisher estimates. Using a different PSD, like that for aLIGO, which has worse sensitivity at lower frequencies, will shift the curves towards higher frequencies, which is shown for the $(2, \pm 2)$ mode with the dot-dashed line.

systems are expected to be small, they can be significant for NSBH systems if the BH is highly spinning. Larger values of $\chi_{\rm eff}$ and $\tilde{\chi}$ result in longer inspirals and greater imprints of spins on the amplitude and phase of the GW, which improves their measurability. Thus, we expect a correlation between greater $\chi_{\rm BH}$ values and better measurement of $\chi_{\rm NS}$. This expectation will be validated in Section 4.2.3.1.

To better illustrate the effect of HOMs, we calculate the Fisher matrix element ($\Gamma_{\chi_{\rm NS}}$) for a typical NSBH system using `gwbench` [102]. $\Gamma_{\chi_{\rm NS}}$ is a measure of the amount of information about $\chi_{\rm NS}$ that can be extracted from the GW strain. For demonstration, we choose the *plus* polarization of the strain and calculate

$$h^+_{lm,\chi_{\rm NS}}(f) = \frac{\partial h^+_{lm}(f)}{\partial \chi_{\rm NS}}, \tag{4.6}$$

$$\gamma^+_{\chi_{\rm NS}}(f) = \frac{h^+_{lm,\chi_{\rm NS}}(f)\, \bar{h}^+_{lm,\chi_{\rm NS}}(f)}{S_n(f)}, \tag{4.7}$$

$$\Gamma^+_{\chi_{\rm NS}} = 4\,{\rm Re} \int_{f_{\rm low}}^{f_{\rm high}} \gamma^+_{\chi_{\rm NS}}(f)\, df, \tag{4.8}$$

where $h^{+}_{lm}(f)$ is the *plus* polarization of the (l, m) mode in frequency-domain obtained using IMRPhenomXHM [112] for an NSBH system with $10\,\mathrm{M}_{\odot}$ BH, $1.4\,\mathrm{M}_{\odot}$ NS with the PSD (S_n) associated with the 40 km CE detector considered between $f_{\rm low} = 5$ Hz and $f_{\rm high} = 2048$ Hz. We choose $\chi_{\rm BH} = 0.4$ and $\chi_{\rm NS} = 0.04$. Note that the square-root of the inverse of the full Fisher matrix gives the measurement errors on the parameters. However, due to the process of inversion, the measurement precision on $\chi_{\rm NS}$ is not determined just from $(\Gamma^{+}_{\chi_{\rm NS}})^{-1/2}$ but has contributions from the correlations between $\chi_{\rm NS}$ and all the other GW parameters.

Hence, keeping in mind that $(\Gamma^{+}_{\chi_{\rm NS}})^{1/2}$ is only an indicator of the contribution of different modes, we show how these contributions vary with the inclination angle and the frequency in Fig. 4.1. The left panel shows the contributions of the different (l, m) modes to the measurement of $\chi_{\rm NS}$. The effect of the variation of $|Y^{-2}_{lm}|$ (c.f. Fig. 1.2) with inclination is apparent. As expected, the bulk of the information about $\chi_{\rm NS}$ comes from the $(2, \pm2)$ mode across the various inclination angles. The second strongest contribution comes from the $(3, \pm3)$ mode, which considerably informs the $\chi_{\rm NS}$ estimates for systems with $\iota > 20°$. At high inclination angles, the contribution from the $(3, \pm3)$ mode can reach about 1/3 the contribution of the $(2, \pm2)$ mode (see Ref. [68] for details on the importance of different modes). In the right panel, we show $\gamma^{+}_{\chi_{\rm NS}}(f)$ as a function of frequency, but normalized by its integral over the frequency band, $\Gamma^{+}_{\chi_{\rm NS}}$. The normalization removes information about the relative importance of each mode, which is already shown in the left panel, and allows the portrayal of frequency regions in which each of the modes dominates. The $(2, \pm2)$ and $(2, \pm1)$ modes contribute predominantly to the lower frequencies, whereas the other HOMs contribute to the higher frequencies as well. The information from the waveform that contains the $(2, \pm2)$ and the HOMs, shown in black, follows the $(2, \pm2)$ mode curve, with oscillations due to the constructive and destructive interference between the $(2, \pm2)$ mode and the HOMs [219].

It is important to note that the choice of $S_n(f)$ affects the frequency regions to which the different modes contribute the most. The PSD corresponding to CE 40 km is relatively flat at lower frequencies, where the systems spend the majority of their inspiral. However, aLIGO poor low-frequency sensitivity will result in the shift of the curves shown in the right panel of Fig. 4.1 towards higher frequency values. This shift has been specifically shown for the $(2, \pm2)$ mode with aLIGO sensitivity in Fig. 4.1.

From the theoretical considerations involving the PN theory and Fisher estimates, we conclude that the $(2, 2)$ mode will dominate the $\chi_{\rm NS}$ measurement, followed closely by the $(3, 3)$ mode, especially for near edge-on ($\iota = 90°$) systems. We highlighted that η

combines differently with different spin contributions in the amplitude of the HOMs. We also posit that a large $\chi_{\rm BH}$ value will be conducive to $\chi_{\rm NS}$ measurement.

4.2.1.2 Astrophysical Considerations

As discussed in Section 4.1, pulsar observations have shown that rapidly rotating NS can exist in binary configurations that merge within Hubble time. Further, in Section 4.2.1.1, we assert that for an NSBH system, larger values of BH spin will correspond to better measurements of the NS spin. In this section, we assess the formation scenarios for NSBH systems, via isolated binary formation channels, with a rapidly rotating NS and, preferably, a highly spinning BH.

One way NS can attain their spins is due to the collapse of an initially spinning Chandrashekhar core. However, as the mass transfer from the core to the outer layers before collapse is expected to be highly efficient [220], the cores right before collapse are likely to be slowly spinning, leading to slowly spinning compact stars post-collapse [185]. Recent studies [221, 222] suggest another method to spin-up the NS at birth— through stochastic accretion of in-falling matter after the core collapse supernova explosion. In fact, Ref. [222] finds that NS created in this way from lower mass ($< 10\,{\rm M}_\odot$) ZAMS stars have lower spins ($P \sim \mathcal{O}(10^3)$ ms) and natal kick velocities ($v_{\rm kick} \lesssim 200\,{\rm km\,s^{-1}}$), whereas those from higher mass ($> 10\,{\rm M}_\odot$) ZAMS stars generally have higher spins ($P \sim \mathcal{O}(10)$ ms) and natal kick velocities ($v_{\rm kick} \gtrsim 400\,{\rm km\,s^{-1}}$). While the latter is favorable for generating rapidly-spinning NS, the high kick velocities could disrupt the binary system, reducing the chance of such NS to exist in binary configurations. A similar trend is seen in BH, where BH formed after core-collapse are seen to have large spins and kicks, whereas those born from failed explosions have smaller values for spins and kicks [222, 223].

Stars present in binary configurations can undergo other physical processes that can lead to rapidly rotating compact objects. The primary, more massive, star is the first to evolve off the main sequence and undergo a supernova explosion to become a compact object. Assuming the binary survives this explosion, the second star evolves off the main sequence, expands and initiates the common envelope phase [224–227]. The common envelope extracts energy from the binary and, if ejected successfully, leaves behind a tighter binary with smaller period, containing a compact object and a Wolf-Rayet star (for other scenarios, see Ref. [1] and references therein). In certain cases, the Wolf-Rayet star can expand further and fill its Roche Lobe, leading to stable mass-transfer from this helium-star to the compact object [228, 229]. This mass transfer episode can spin-up the first-born compact object [229, 230]. If the BH is formed first, Ref. [231] shows

that super-Eddington accretion can result in highly spun-up ($\chi_{\rm BH} > 0.6$) BH. If the NS is formed first, its spin can be further increased (often referred to as recycling the NS/pulsar), leading to more massive NS with millisecond periods [196] and possible burial of their magnetic fields [4, 232]. As the spin-down rate of the NS increases with the magnetic field strength and decreases with mass, these recycled NS can have considerable spins at the time of merger. In their simulation study, Ref. [4] find that $\sim 20\%$ of the NSBH systems where NS is formed first contain a pulsar and more than 96% of such *radio-alive* systems are noted to be recycled. They also find that for a significant fraction of such binaries, $\chi_{\rm NS} > 0.05$ during merger. However, only $\sim 3\%$ of the NSBH systems in their simulations, that are expected to be detected by the LIGO-Virgo detectors, contain a first-born NS. For the rest of the systems, NS is born second and cannot get spun-up due to accretion. Other studies also estimate the rate of NSBH mergers with first-born NS to be subdominant to those with second-born NS, with the ratio of rates for the former to that of the latter ranging from $\mathcal{O}(0.001) - \mathcal{O}(0.1)$ [1, 2].

The helium core of the secondary, present in a close binary, can also get spun up due to tidal locking [106, 185, 233, 234]. Ref. [185] find that the spin of second-born BH can exceed the value of 0.5 for such systems. However, as the tidal torques depend on the orbital angular frequency, the binary has to be very close ($P_{\rm orb} \lesssim 1\,{\rm day}$ [235]) for tidal locking to take effect. Ref. [235] find that for the orbital period $P_{\rm orb} = 0.5\,{\rm day}$, second-born NS can be spun-up to millisecond periods. As shorter orbital separations are required for tidal synchronization, the companion has to be small enough to fit in the orbit. Compact objects like NS and BH make ideal companions that can tidally spin up the helium core, which is why it is the secondary that is expected to spin up appreciably due to tidal locking. Using Refs. [4, 106] find that a significant fraction of second-born BH in NSBH systems can have spins greater than 0.4. They also probe the effect of metallicity on the NS spins in NSBH mergers, finding that lower metallicity results in a lower mass loss through stellar winds. This results in more massive helium stars, which expand less and result in lower mass transfer. Thus, the NS are not efficiently recycled due to accretion for such systems.

While the problem of binary formation and evolution is dominated by modelling uncertainties, several plausible pathways lead to the formation of NSBH binaries with rapidly rotating components, even under the constraints of the isolated binary formation mechanisms. Although the actual merger rates and properties of such systems can only be ascertained with more observations, it is worth investigating if these properties can be precisely determined with future GW observatories. Given the specific and countable

scenarios that lead to the presence of a rapidly rotating NS during merger, decisively differentiating the spin of the NS from 0 can illuminate the astrophysical processes that contribute to cosmic binary formation and evolution, and the physics that affects the spin-down of NS. This is the objective of this section, and the particular question of the precision in the NS spin measurement will be answered in Section 4.2.3.

4.2.2 Methodology

To explore the precision with which $\chi_{\rm NS}$ can be measured using NSBH mergers, we apply Bayesian parameter estimation on simulated GW data. The GW data d is the detector response defined by,

$$d(t, \boldsymbol{\theta}) = n(t) + s(t, \boldsymbol{\theta}), \tag{4.9}$$

where $n(t)$ is the noise and $s(t, \boldsymbol{\theta})$ is the GW signal which depends on a set of intrinsic and extrinsic parameters (including masses and spins), $\boldsymbol{\theta}$. Then, the posterior distribution $p(\boldsymbol{\theta}|d)$ can be obtained using

$$p(\boldsymbol{\theta}|d) = \frac{p(d|\boldsymbol{\theta})\, p(\boldsymbol{\theta})}{\mathcal{Z}}. \tag{4.10}$$

Here, $p(d|\boldsymbol{\theta})$ is the likelihood function, $p(\boldsymbol{\theta})$ is the prior on the GW parameters, and $\mathcal{Z} = \int p(d|\boldsymbol{\theta})\, p(\boldsymbol{\theta})\, d\boldsymbol{\theta}$ is the evidence. The probability distribution for $\chi_{\rm NS}$ can be retrieved from the joint posterior distribution by marginalizing it over all other parameters [236],

$$p(\chi_{\rm NS}|d) = \int \left(\prod_{\theta_i \neq \chi_{\rm NS}} d\theta_i \right) p(\boldsymbol{\theta}|d). \tag{4.11}$$

The calculation of these posterior distributions is a computationally challenging task and is accomplished using stochastic samplers [237–239]. However, covering the prior space and sufficiently mapping the likelihood surface could involve $\mathcal{O}(10^8)$ likelihood evaluation, which can be time-consuming. This is especially true for the long and high SNR signals expected to be detected by XG observatories. Hence, several likelihood evaluation and sampling techniques have been introduced to speed up this process [240–255].

For accelerated parameter estimation, we use the relative binning technique [256–258] implemented in Bilby [259–261]. The relative binning technique relies on the assumption that the ratio of the waveform between neighboring points in the parameter space varies smoothly. The waveform corresponding to the maximum likelihood point in the parameter space is chosen as the fiducial waveform, and the waveforms around this point

are obtained using piecewise linear functions informed by this fiducial waveform. These approximations can amount to speed ups by $\mathcal{O}(10^3)$, without compromising significantly in the accuracy [257, 261]. However, waveforms that contain contributions of HOMs and involve precession can be highly oscillatory and may not be well-approximated by piecewise linear functions. While Ref. [261] show that the technique fairs well even for asymmetric systems, a mode-by-mode adaptation of relative binning has also been proposed [262], which approximates each (l, m) mode separately and then adds them together to obtain the full (approximated) waveform. As our study only considers NSBH systems whose spins are aligned with the orbital angular momentum, we use the original relative binning technique and its implementation in Bilby [261], but also validate our results against those obtained with our implementation of the mode-by-mode technique, and find them to be consistent.

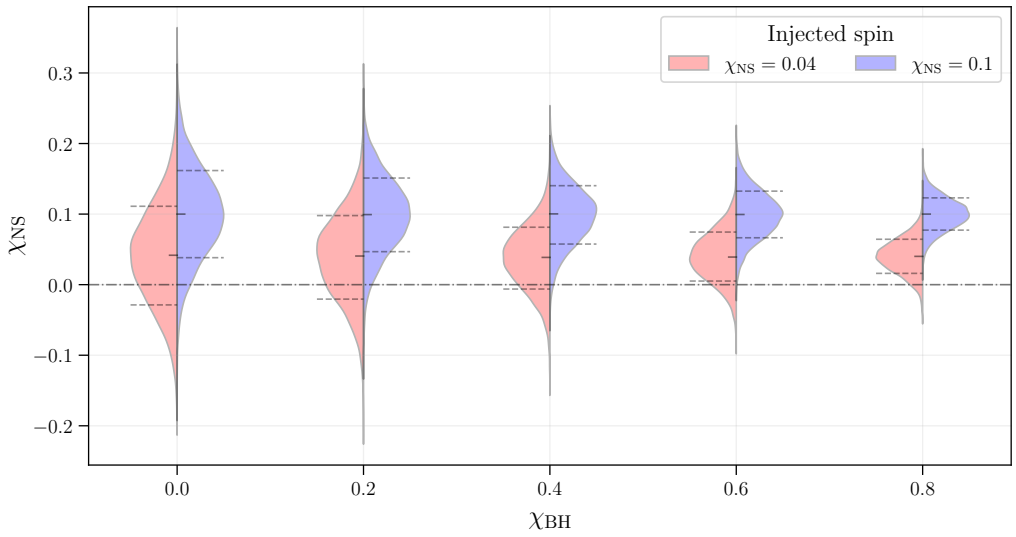

Figure 4.2: The posterior distributions for χ_{NS} as a function of χ_{BH}. The red and blue plots show the posteriors for systems where χ_{NS} is set to 0.04 and 0.1, respectively. Along with the posteriors, we also show the median (small solid horizontal line) and the boundaries of the $1-\sigma$ region (dashed horizontal lines). The posteriors correspond to a system with BH of mass $10\,M_\odot$ and NS of mass $1.4\,M_\odot$ at an inclination angle of 45°. The dash-dotted horizontal line indicates $\chi_{NS} = 0$.

The GW signals are generated using the IMRPhenomXHM waveform [112], which is an aligned-spin frequency-domain waveform that includes the $(2, 2)$, $(2, 1)$, $(3, 3)$, $(3, 2)$ and $(4, 4)$ modes. We set the right ascension $\alpha = 78.78°$, declination $\delta = -69.37°$, phase $\phi_c = 74.48°$, polarization angle $\psi = 152.34°$, and the geocentric time $t_c = 1126259642.413$

s. Other than Section 4.2.3.3 where we look at various detector sensitivities, we inject GW signals in a network of one ET and two CE (one with 40 km arms and the other with 20 km arms), henceforth referred to as the ECC network. Our simulated binaries comprise of NSBH systems with a $10\,M_\odot$ BH and a $1.4\,M_\odot$ NS (henceforth, referred to as 10+1.4 system), at $\iota = 45°$. We assess the effect of varying BH mass in Section 4.2.3.1 and ι in Section 4.2.3.2. The BH spins can range from [0,0.8], whereas the NS spins are only considered up to 0.1 (an informed upper-bound based on the results of Ref. [4]).

For all the simulations, we use uniform priors in χ_1 and χ_2 (i.e. $\chi_{\rm BH}$ and $\chi_{\rm NS}$, respectively) bounded between [-0.99,0.99], and uniform priors in component masses. For all other parameters, we choose the default Bilby priors. We predominantly use the `nessai` [252, 263, 264] and `pymultinest` [265] samplers for our runs, and perform spot-checks with the `dynesty` [266, 267] sampler to ensure consistency.

Note that the NS may get tidally disrupted by the BH before merger [72]. These tidal effects will affect the waveform and can potentially contribute to $\chi_{\rm NS}$ constraints due to spin-induced quadrupole moments. These effects are not considered in IMRPhenomXHM as it is predominantly used for BBH systems. While high BH spins favor the disruption of the NS, low mass ratio (i.e. a heavy BH) will disfavor it.

In this section, we have not considered several issues that will affect parameter estimation with XG observatories. Networks with ET and CE are expected to detect the majority of compact binary mergers that occur in the universe [37, 38]. Due to the abundance of mergers, several signals are expected to overlap at any instance, leading to confusion noise that may affect the detectability of individual events [268] and bias the parameter inference [269]. For a fraction of these signals which will be detected with high SNRs, the systematic errors due to the limited accuracy of the currently used waveforms will dominate the statistical errors in parameter measurement, resulting in a biased estimation of binary properties [270, 271]. These systematic biases increase with $\chi_{\rm BH}$ [272], which is especially relevant to this work. Another contributing hurdle is the systematic error due to detector calibration, which can lead to significant uncertainty in amplitude and phase between 20-2000 Hz [273, 274]. Such calibration errors can result in biased parameter, and cosmological, inference [275]. We do not account for these effects with the hope that these challenges will be mitigated before XG observatories are operational (e.g., see Refs. [276–278]).

4.2.3 Results

In this section, we show the results of the parameter estimation runs performed on simulated NSBH GW events. Focusing on the precision with which $\chi_{\rm NS}$ can be measured, we assess the impact of BH mass and spin as well as that of ι and HOMs on these measurements in Sections 4.2.3.1 and 4.2.3.2, respectively. Note that for a system situated at a particular luminosity distance D_L, changing the masses/spins of the compact objects or the inclination angle will affect the SNR associated with the detected signal, which has direct consequences for the bounds that can be placed on $\chi_{\rm NS}$. To isolate the effect of binary parameters from the effect of SNR, all the systems considered in Sections 4.2.3.1 and 4.2.3.2 have the same SNR (~ 700), which is achieved by varying D_L appropriately. The effect of detector sensitivity, luminosity distance (and, consequently, the SNR) are discussed in Section 4.2.3.3.

4.2.3.1 Effect of BH mass and BH spin

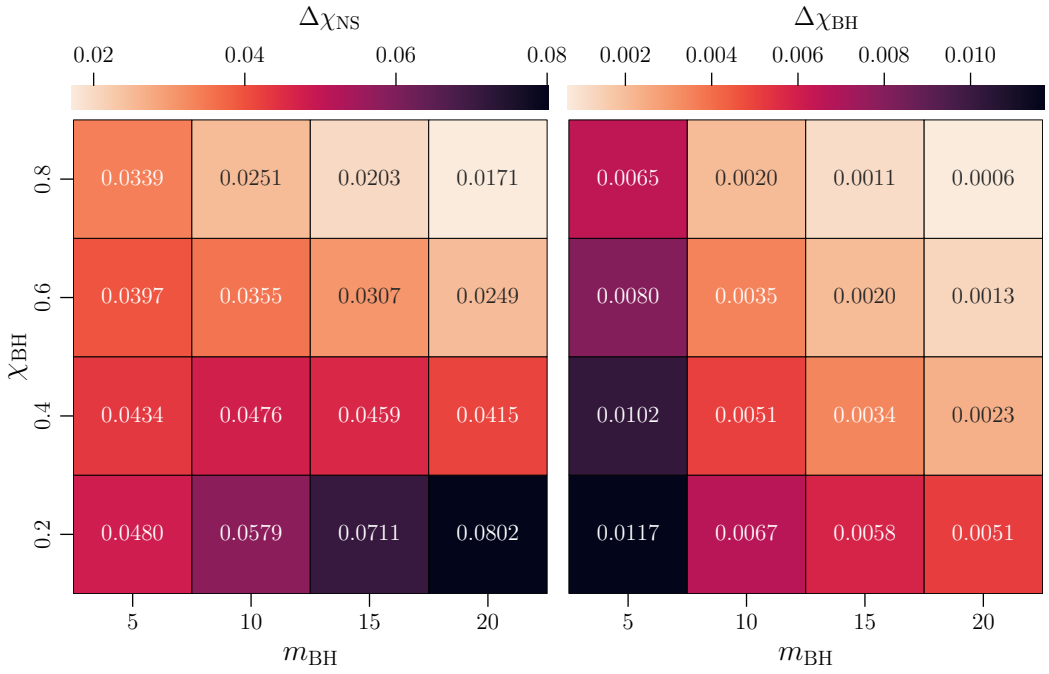

Figure 4.3: The half-widths of the 68% confidence intervals (i.e., one-sided $1-\sigma$ widths) corresponding to the bounds on $\chi_{\rm NS}$ (left panel) and $\chi_{\rm BH}$ (right panel) for the sixteen NSBH systems with BH mass in $\{5\,{\rm M}_\odot, 10\,{\rm M}_\odot, 15\,{\rm M}_\odot, 20\,{\rm M}_\odot\}$ and BH spin in $\chi_{\rm BH} \in \{0.2, 0.4, 0.6, 0.8\}$. The NS mass for all the systems was fixed to $1.4\,{\rm M}_\odot$, the NS spin to 0.04, and ι to 45°.

In Section 4.2.1.1, we claimed that a high value of $\chi_{\rm BH}$ should improve the $\chi_{\rm NS}$ measurement. To validate this, we consider 10+1.4 NSBH systems at $\iota = 45^\circ$ and varying $(\chi_{\rm BH}, \chi_{\rm NS})$ values, and report the 68% confidence interval (i.e., $1-\sigma$) on the inferred values of $\chi_{\rm NS}$ in Fig. 4.2. It is evident that the bounds on $\chi_{\rm NS}$ improve with higher $\chi_{\rm BH}$ values, which validates our expectations. For the chosen SNR (corresponding to systems located at $D_L \in (200, 205)$ Mpc), a highly-spinning NS with $\chi_{\rm NS} = 0.1$ can be easily differentiated from a non-spinning one, even for a non-spinning BH companion. A slightly slower NS with $\chi_{\rm NS} = 0.04$ can only be differentiated from 0 with $1-\sigma$ confidence at this SNR if $\chi_{\rm BH} > 0.4$. As the $\chi_{\rm NS}$ values are small, the bounds are not significantly affected by the true value of the NS spin.

The effect of the mass of the BH ($m_{\rm BH}$) needs greater care. Keeping the SNR constant, as $m_{\rm BH}$ increases, so does the contribution of the HOMs to the signal [68], which should be favorable for spin measurements. However, this also leads to a lower value for q (and η), which reduces the contribution of $\chi_{\rm NS}$ to $\chi_{\rm eff}$ and $\tilde{\chi}$, and of χ_s and χ_a to the amplitude of the modes (c.f. Table 4.1). To evaluate the effect of $m_{\rm BH}$, we fix the mass and spin of the NS to $1.4\,{\rm M}_\odot$ and 0.04, respectively, and perform parameter estimation for systems with $m_{\rm BH} \in \{5\,{\rm M}_\odot, 10\,{\rm M}_\odot, 15\,{\rm M}_\odot, 20\,{\rm M}_\odot\}$ and $\chi_{\rm BH} \in \{0.2, 0.4, 0.6, 0.8\}$. For this set of 16 events, we state the half-width of the 68% confidence interval of the bounds on $\chi_{\rm NS}$ and $\chi_{\rm BH}$ (referred to as $\Delta\chi_{\rm NS}$ and $\Delta\chi_{\rm BH}$, respectively) in Fig. 4.3.

The measurement precision of $\chi_{\rm BH}$ is about an order of magnitude better than $\chi_{\rm NS}$. As discussed in Section 4.2.1.1, most of the information to $\chi_{\rm eff}$ comes from $\chi_{\rm BH}$ for highly asymmetric NSBH systems, and $\chi_{\rm eff}$ being the best-measured spin parameter leads to a precise measurement of $\chi_{\rm BH}$ as well. Further, $\chi_{\rm BH}$ measurement improves both with increasing values of $\chi_{\rm BH}$ and $m_{\rm BH}$, which was anticipated earlier in this section. The behavior of bounds on $\chi_{\rm NS}$ is more interesting— when $\chi_{\rm BH}$ is small, bounds on $\chi_{\rm NS}$ worsen with increasing $m_{\rm BH}$, whereas when $\chi_{\rm BH} \geq 0.6$, the bounds on $\chi_{\rm NS}$ improve with higher $m_{\rm BH}$. This is due to two competing effects— as $m_{\rm BH}$ increases, $\chi_{\rm BH}$ measurement improves (and so, $\chi_{\rm NS}$ measurement should also improve), whereas the contribution of $\chi_{\rm NS}$ to $\chi_{\rm eff}$ and $\tilde{\chi}$ decreases (worsening the measurement of $\chi_{\rm NS}$). It turns out that at low $\chi_{\rm BH}$, the latter effect dominates and $\chi_{\rm NS}$ worsens as $m_{\rm BH}$ increases, whereas at high $\chi_{\rm BH}$, the former effect dominates and $\chi_{\rm NS}$ measurement improves with $m_{\rm BH}$. Stated differently, for high $\chi_{\rm BH}$ values, it is extremely well measured, and it is possible to distinguish between $\chi_{\rm BH}$ and the contribution from $q\,\chi_{\rm NS}$ in $\chi_{\rm eff}$ and $\tilde{\chi}$.

Hence, we see that the $\chi_{\rm NS}$ measurement strongly depends on the values of $\chi_{\rm BH}$. In agreement with our expectations from theoretical arguments, higher $\chi_{\rm BH}$ values

are conducive to better $\chi_{\rm NS}$ measurement. For NSBH systems with slowly spinning ($\chi_{\rm BH} < 0.4$) BH, the bounds on $\chi_{\rm NS}$ worsen with increasing $m_{\rm BH}$, whereas for NSBH systems with highly spinning BH, higher $m_{\rm BH}$ improves the measurement precision for $\chi_{\rm NS}$.

4.2.3.2 Effect of inclination and HOMs

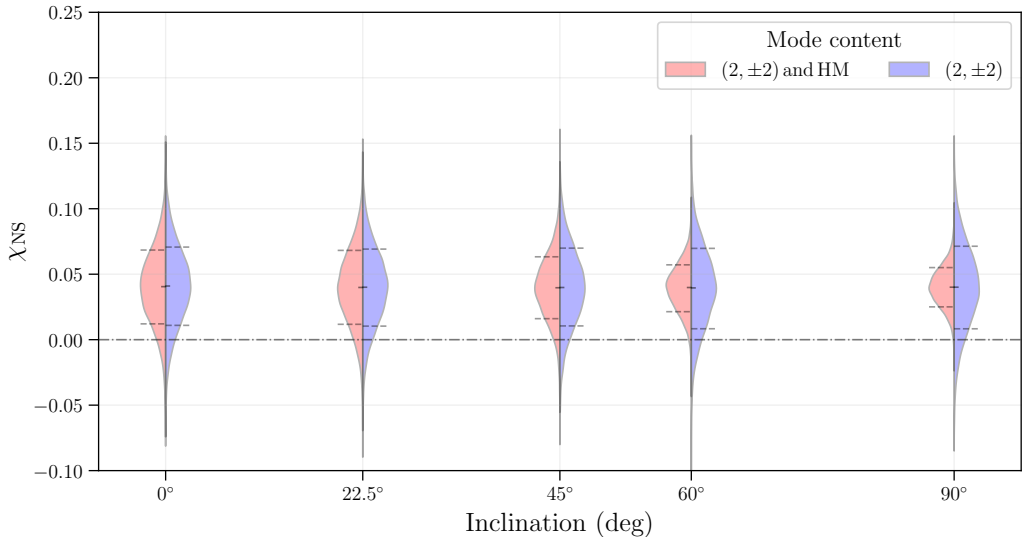

Figure 4.4: The posterior distributions for the spin of the NS as a function of the inclination angle. The red plots represent the systems for which the injection and the recovery were performed with a waveform that contains both the $(2, \pm 2)$ mode and the HOMs (IMRPhenomXHM), whereas the blue plots correspond to the systems where the waveform only has the $(2, \pm 2)$ mode (IMRPhenomXAS). The dash-dotted horizontal line indicates $\chi_{\rm NS} = 0$.

The relative contribution of HOMs to the GW waveform increases with inclination angle, which is expected to improve the constraints that can be imposed on $\chi_{\rm NS}$. To evaluate the usefulness of HOMs towards $\chi_{\rm NS}$ measurement, we compare the bounds on $\chi_{\rm NS}$ obtained when using a waveform model that contains the dominant $(2, \pm 2)$ mode as well as HOMs to a waveform model that only contains the $(2, \pm 2)$ mode. For the former, we continue the use of IMRPhenomXHM, and for the latter, we use IMRPhenomXAS [279], which is an aligned-spin waveform model which contains only the quadrupole mode.

We consider the 10+1.4 NSBH systems with $(\chi_{\rm BH}, \chi_{\rm NS}) = (0.8, 0.04)$. These are simulated at inclination angles $\iota \in \{0°, 22.5°, 45°, 60°, 90°\}$ and the D_L are set such

that all the systems are detected with the same SNR. The constraints on $\chi_{\rm NS}$ for these systems when injection and parameter estimation are performed with and without HOMs are shown in Fig. 4.4. The red plots show the bounds on $\chi_{\rm NS}$ for systems where the waveform contains HOMs, whereas the blue plots correspond to those that only contain the quadrupole mode. It is evident from the figure that $\chi_{\rm NS}$ measurement is significantly improved with the increase in the HOMs contribution to the waveform at greater ι. On the other hand, the constraints on $\chi_{\rm NS}$ for systems where only the quadrupole mode is used are not affected as ι is varied, as the signal SNR is kept constant. It is also important to note that the $\chi_{\rm NS}$ posteriors of the two sets of injections do not differ considerably till $\iota = 22.5°$. From this, we infer that for such 10+1.4 systems, HOMs are expected to noticeably affect $\chi_{\rm NS}$ measurements only at inclination angles $\iota \gtrsim 45°$. However, GW detections are biased against systems with high ι values; an edge-on system has similar SNR to a face-on system that is much farther away. Thus, while more GW systems are expected to be oriented face-off, they will be detected with lower SNR compared to face-on systems at the same D_L.

4.2.3.3 Effect of detector sensitivity

Till now, we have probed the effect of BH properties and HOMs on the measurability of $\chi_{\rm NS}$ by keeping the systems at the same SNR (~ 700). In this section, we look at the measurability as a function of D_L and detector sensitivities. For this purpose, we consider five XG networks- A+ (a network of five detectors at A+ sensitivity), A$^\sharp$ (a network of three detectors with A$^\sharp$ sensitivity), ET (the triangular ET observatory), CE40 (the 40 km CE observatory), and ECC (a network with the triangular ET, the 40 km CE and the 20 km CE observatories). We consider 10+1.4 NSBH systems at $\iota = 45°$. Parameter estimation is performed for two types of systems— first, with a slowly-spinning BH ($\chi_{\rm BH} = 0.2$), and second, with a rapidly-spinning BH ($\chi_{\rm BH} = 0.8$). In Fig. 4.5, we show the D_L (averaged over the sky) at which the NSBH mergers occur for different XG observatories to obtain (one-sided $1-\sigma$) $\Delta\chi_{\rm NS} = 0.04$ and 0.1. Along with the D_L, we also report the corresponding NSBH merger rate up to that distance, which is assumed to follow the Madau-Dickinson star-formation rate [280, 281] and the local merger rate density for NSBH systems is chosen to be $45\,{\rm Gpc^{-3}\,yr^{-1}}$ [33, 76] (see Ref. [38, 73] for more details).

For $\chi_{\rm BH} = 0.2$, Fig. 4.5 shows that the chances for A+ or A$^\sharp$ to constrain $\chi_{\rm NS}$ to even $\Delta\chi_{\rm NS} = 0.1$ are bleak, and it would only be possible to do so only for a *golden* event that may occur once every ten to hundred years. However, networks containing

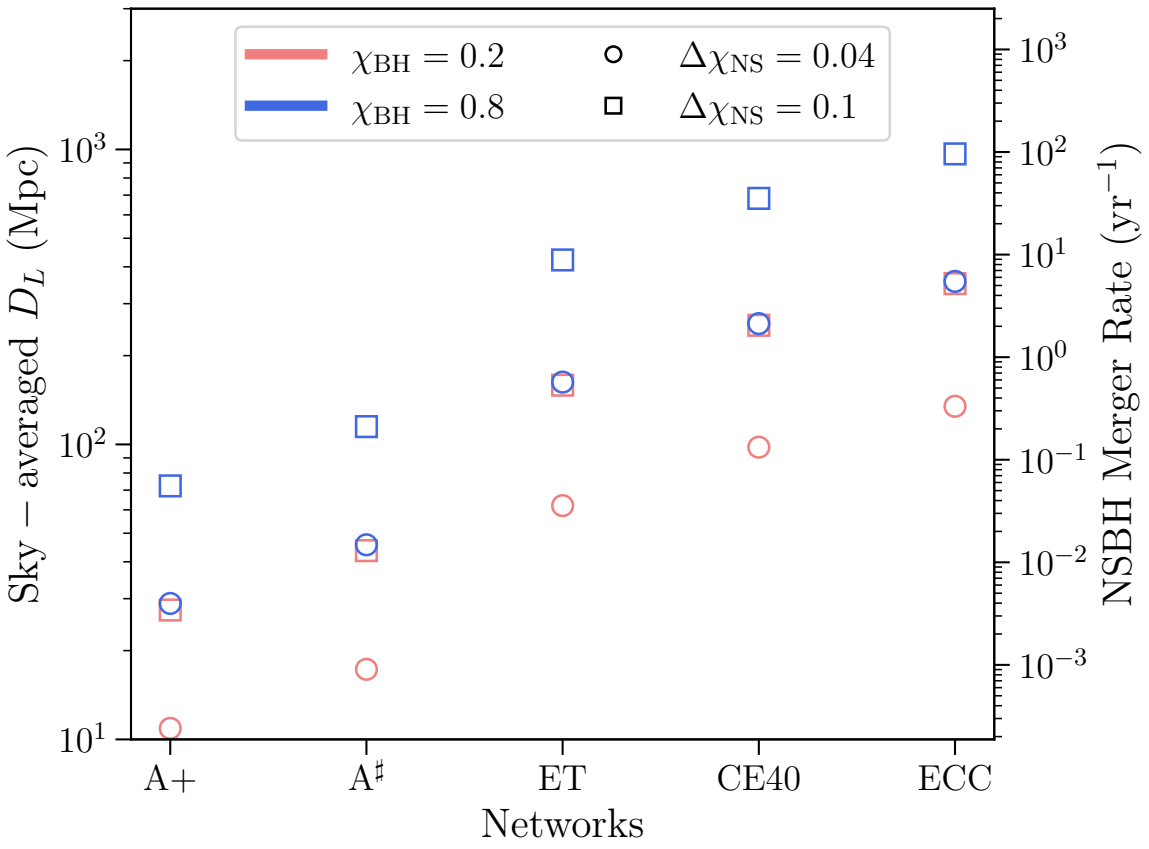

Figure 4.5: The sky-averaged D_L corresponding to each XG detector network for which a given $\Delta\chi_{\rm NS} \in \{0.04, 0.1\}$ bound can be achieved with a 10+1.4 NSBH system at $\iota = 45°$ and a given $\chi_{\rm BH} \in \{0.2, 0.8\}$. We also denote the corresponding NSBH merger rate per year that is expected at those distances.

ET and CE will be able to constrain $\chi_{\rm NS}$ to $\Delta\chi_{\rm NS} = 0.04$ for an event every few years, and $\Delta\chi_{\rm NS} = 0.1$ for a few events every year. For NSBH systems with rapidly spinning BH, A+ and A$^\sharp$ are expected to constrain $\chi_{\rm NS}$ to $\Delta\chi_{\rm NS} = 0.1$ for events occurring once in 10 years. Networks with just the ET and/or CE will be able to constrain $\chi_{\rm NS}$ to $\Delta\chi_{\rm NS} = 0.04$ for a few events every year, and to $\Delta\chi_{\rm NS} = 0.1$ for tens of events every year. In fact, the ECC detector can constrain $\chi_{\rm NS}$ to $\Delta\chi_{\rm NS} = 0.1$ for events merging at ~ 1000 Mpc. Up to this distance, we expect ~ 100 NSBH mergers every year, which increases the chances of detecting a highly spinning NS.

These estimates will depend on the choice of masses for the system as well as the inclination angle. Both these effects have been explored in the previous sections. Based on the current GW observations, $\chi_{\rm BH}$ in NSBH systems is expected to be low [103]. If this is indeed true for the cosmic NSBH population, then resolving NS spin well enough

to differentiate it from 0 may only be possible, realistically, for networks with CE and ET. However, if rapidly spinning BH were to merge with rapidly spinning NS, A+ and A$^\sharp$ networks may constrain $\chi_{\rm NS}$ well enough to distinguish such an NS from a slowly spinning one.

4.3 Inferring the formation scenario for GW230529

Electromagnetic observations have played a pivotal role in constraining the mass spectrum of NSs and BHs. Notably, X-ray and radio observations have consistently indicated that the maximum mass of NSs falls within the range of $2-2.6\ M_\odot$, while BH masses have been found to exceed $5\ M_\odot$ [174, 193, 194, 282–286]. Consequently, these detections have implied a notable absence of compact binaries within the mass range of $2.6-5\ M_\odot$, a notion reinforced by initial GW observations [287, 288]. However, SNe simulations have predicted the existence of BHs within this gap [289]. Furthermore, the recent observation of the binary merger GW230529 has provided conclusive evidence for the existence of compact objects within this mass range [3].

Measuring these mass parameters is part of the inverse problem. A Bayesian inference approach is typically employed, which necessitates model evaluations to reliably infer the posterior distribution for the parameters that characterize the observed signal [236, 290]. While the data containing GW230529 was matched against several state-of-art GW signal models, Ref. [3]'s initial analysis assumed priors that are effectively flat in component masses, spin magnitudes and isotropic spin orientations. These astrophysically-agnostic priors do not provide information about GW230529's possible formation mechanism.

Therefore, Ref. [3] reweighted the posterior samples using a few astrophysically-informed mass and spin distributions to constrain the source properties [103, 291–293]. For instance, the study revealed that the phenomenological population-informed prior, "Power-Law+Dip+Break", predicts significantly different component masses than uninformed priors. This demonstrates the substantial impact that prior choice can have on the inferred masses and spins of the GW230529 source. The observed differences are consistent with the model's preference for mass-symmetric systems, especially considering the event's low SNR.

Also, the employed astrophysically-informed priors are phenomenological and contain only an *observationally constrained* understanding of stellar and binary evolution. Further, Ref. [294] found that the GW230529's masses are close to those predicted in their BHNS population simulations.

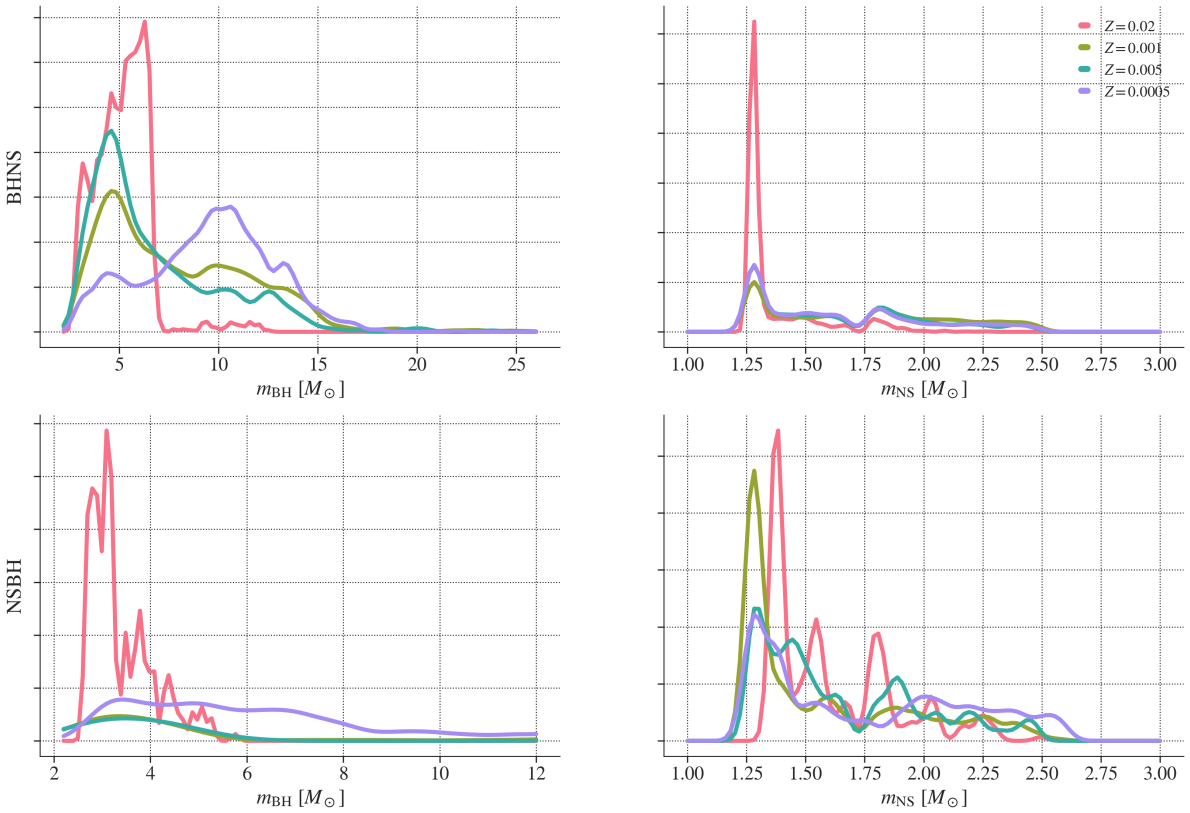

Figure 4.6: Predicted component mass distributions for BHNS (top panel) and NSBH systems (bottom panel) across varying sub-solar metallicities, as outlined in Ref. [4]. As can be observed, NSBH systems tend to produce binaries with lighter BHs across different metallicity.

In this section, we re-analyze the data containing GW230529 with population-informed priors to provide conclusive insights into the probable physical processes underlying this binary formation. Leading formation models of GW230529-like systems include the isolated evolution of massive binary stars in galactic fields via the common envelope process and the dynamical assembly aided by either a tertiary companion, multiple exchanges in dense clusters or gas-assisted migration (see Ref. [295] and references therein). While direct collapse leading to the formation of the primary component is unlikely due to its low mass, recent population synthesis models have argued the plausibility of such systems arising from isolated evolution scenarios [1, 4, 296, 297]. However, these models have major uncertainties such as mass loss, mass transfer and the impact of supernova explosions, resulting in a broad spectrum of merger rate predictions and varying mass and spin distributions.

We describe our methodology in Sec. 4.3.1, utilizing it subsequently in Sec. 4.3.2.1

to ascertain the nature of the merger—specifically, whether the NS or BH formed first. Consequently, in Sec. 4.3.2.2, we employ the evidence ratio of posterior samples and the distribution of log-likelihood ratios to distinguish between various formation models, shedding light on the most likely formation mechanism of GW230529.

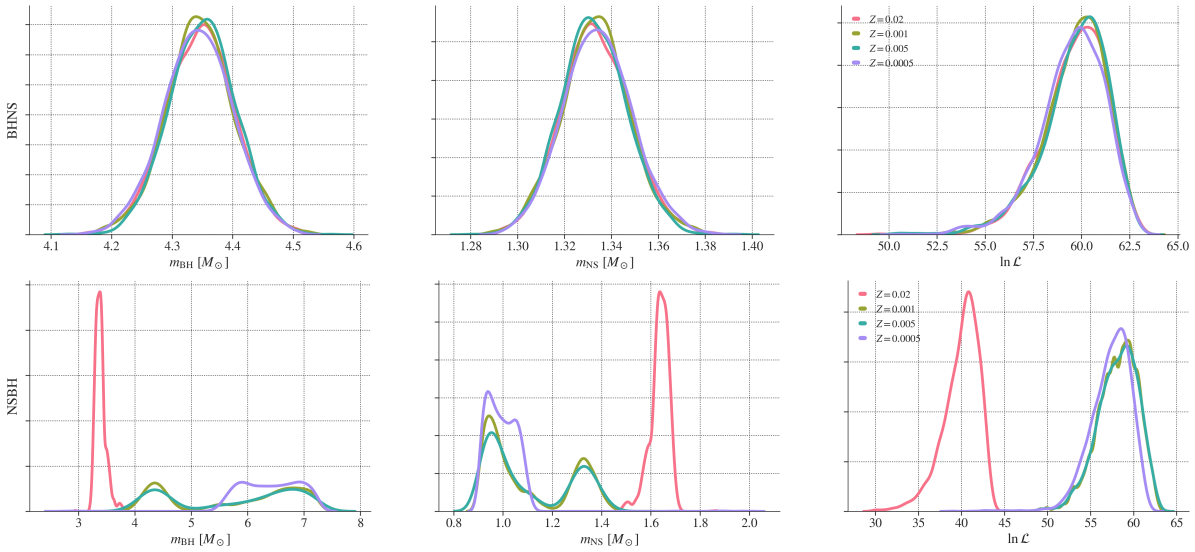

Figure 4.7: Posterior densities for the mass of GW230529 as inferred using population-inspired BHNS (top panel) and NSBH (bottom panel) priors described in Sec. 4.3.2.1. In the right-hand column, we include the log-likelihood ratio distribution.

4.3.1 Methods

We infer GW230529's properties by analysing 128s of LIGO Livingston data using the Bayesian PE library `bilby` [298] and the posterior sampling algorithm `dynesty` [299]. We assume a noise power spectrum given by the median estimate provided by `bayesline` [300] and use frequencies in the range of $20 - 1792$ Hz for evaluating the GW Transient log-likelihood ratio $\ln\mathcal{L}$. Furthermore, to speed up the likelihood evaluation, we include heterodyning (also known as relative binning; [256–258, 261]). For our analysis, we use the quasi-circular frequency-domain phenomenological waveform model, `IMRPhenomNSBH` [113, 218, 301–303]. This waveform approximant models signals using the dominant (quadrupole) harmonic and is specifically designed to model GWs emanating from BHNS mergers with mass ratios ranging from equal-mass up to $q = m_{\rm BH}/m_{\rm NS} = 15$. It also incorporates BH spins up to a dimensionless value of $\chi_{\rm BH} = 0.5$ and includes matter-effects through tidal parameters $\Lambda_{\rm NS}$ ranging from 0 to 5000.

However, unlike the original analyses, we exclude the marginalization over the systematic error in the measured astrophysical strain due to the detector calibration. This error is sub-dominant to the systematic errors from waveform modelling and prior choices, and we, therefore, neglect it [304]. Furthermore, as discussed in Sec. 4.3.2.2, we apply astrophysically motivated mass and spin priors while using uninformative priors for all other parameters. It is important to note that, for all our analysis, we utilise the BH and NS masses viz $m_{\rm BH}$ and $m_{\rm NS}$ priors derived from population synthesis models as two distinct, one-dimensional independent priors.

While various assumptions may be made to model the formation pathway of this system, one needs to determine the relative probability of two models (in this case, binary formation process) given the data. The Bayesian evidence, $\mathcal{Z}$, quantifies this support. Varying prior assumptions can yield differing parameter estimates; therefore, the Bayes Factor, $\mathrm{BF}^A_B = \mathcal{Z}_A/\mathcal{Z}_B$, indicates whether the prior assumption A is favoured or disfavoured compared to B based on the data. This comparison is particularly crucial as strong prior assumptions may bias the posteriors towards potentially arbitrary values at the expense of the evidence. Furthermore, we also compare the log-likelihood ratio distribution since certain models allow for broader priors and incur a higher Okkam penalty.

4.3.2 Astrophysical Implications

Ref. [3] found no conclusive evidence either supporting or refuting the presence of tidal effects in the GW230529 signal. This makes it difficult to determine the nature of the compact objects involved. However, they showed that the (lighter) secondary component appears to be a NS, while the (heavier) primary is likely a BH, when using observationally constrained priors. In this section, we investigate which of the binary components formed first and determine their formation mechanism.

4.3.2.1 BHNS or NSBH?

Black hole-neutron star binaries can generally be divided into two categories: (1) BHNS mergers, where the BH forms first, and (2) NSBH mergers, in which the NS forms first. While BHNSs are the dominant binaries according to population synthesis studies [4], NSBHs are more exciting as they can form radio pulsars, generate KN [305], and lead to precise measurement of NS spins [67].

To discriminate between the two, we analyze GW230529 using different predicted

distributions of the detectable BHNS and NSBH masses and spins for different metallicity choices ($Z = 0.02, 0.001, 0.005, 0.0005$) from the base model of Ref. [297]. These models are expected to be representative of the population of such binaries obtained from GW observations.

As can be seen in Fig 4.6, the BHNS (top panel) and NSBH (bottom panel) systems exhibit distinct mass spectra, with BHs in BHNS systems being more massive. This is because the heavier star evolves faster and remains massive enough to form a BH even after the mass transfer [306, 307]. In contrast, NSBH systems have more mass-symmetric progenitors, more so at higher metallicities. The heavier star transfers enough mass to its companion to form a NS, whereas its companion becomes a BH. However, at lower metallicities, reduced stellar winds lead to reduced mass loss, creating larger BHs that merge in a shorter time scale [306].

We use BH spins derived from fits in Ref. [4] for NSBH mergers but restricted to $\chi_{\rm BH} = 0.5$ as `IMRPhenomNSBH` is not calibrated for $\chi_{\rm BH} > 0.5$. Moreover, attaining spins greater than this would require an unphysical amount of matter accretion [308]. Although tidal synchronization can lead to higher BH spins, the fraction of such binaries is small [4]. For the BHNS case, we set $\chi_{\rm BH} = \chi_{\rm NS} = 0$ as the rotational velocities of NSs are anticipated to diminish over time due to EM radiation [309, 310]. As ground-based GW observatories are only expected to detect these binaries close to the merger, we assume that the BH and NS objects have negligible spin. Thus, for the second analysis, we effectively assume that the *source of GW230529 is a non-spinning BHNS binary*. This is because the efficiency of angular momentum transfer in BH progenitors is crucial for determining the spin characteristics of the resultant BH. In the dominant evolutionary scenarios involving helium (He) stars, efficient angular momentum transfer from core to envelope typically results in most of the He-star's core becoming non-spinning, and hence the final BH [311, 312]. In a NSBH system, however, the first-formed compact object (NS in this case), if sufficiently close and massive, can induce tidal interactions that potentially spin up the second-born BH at birth.

Figure 4.7 shows an obvious trend; the log-likelihood ratio distribution associated with the BHNS (top panel) has a higher median log-likelihood ratio value and contains a prominent peak compared to the NSBH case (bottom panel) for the same metallicity choices. Further, the BHNS hypothesis is preferred with a $\ln \mathrm{BF}^{\rm BHNS}_{\rm NSBH} > 17(9)$ for metallicity choice of $Z = 0.02(0.0005)$. Therefore, we will assume that GW230529 is a BHNS merger for the remainder of the article. Note that our results are robust against waveform systematics [162].

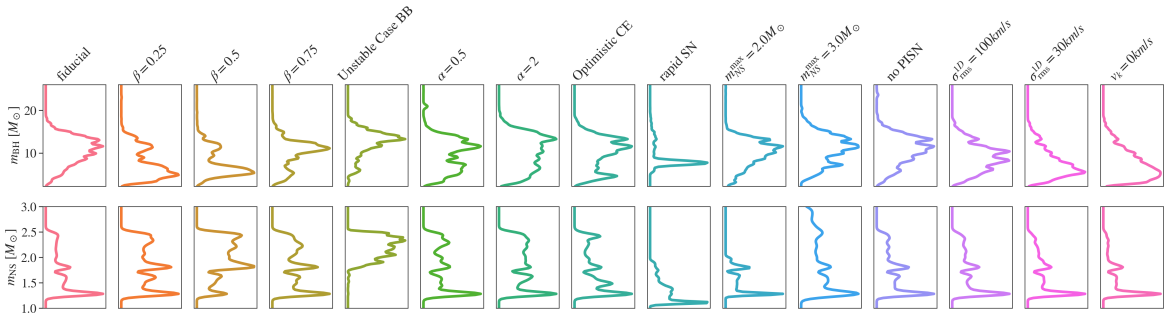

Figure 4.8: Predicted BHNS component mass distributions. Each row shows the 15 different population synthesis variations used by Ref. [1].

4.3.2.2 Constraints on binary evolution

The pathway leading to BHNS mergers is still debated. The prevailing hypothesis suggests that these mergers arise from two massive stars that were born in a binary and evolved in isolation, typically involving the common envelope episode that tightens the binary's orbit [295]. However, accurately estimating the rates of these mergers is challenging for several reasons.

Firstly, the physical processes that govern the evolution of massive binary star systems, including the dynamics of the common envelope phase [313], mass transfer efficiency between binary components, and the kicks imparted to stars during supernovae (SNe), are complex and poorly understood, leading to considerable uncertainty [314]. Secondly, uncertainties arise due to the star formation rate and the metallicity distribution within star-forming gas across cosmic time [315, 316]. Together, they significantly impact the detectable BHNS mass distributions.

Since we are interested in determining the physical process leading to GW23059's formation, we only focus on the uncertainties related to the physical processes. To that end, we, following Ref. [1], assumed 15 different binary population synthesis predictions for BHNS mass distribution. These models implement variations to the *fiducial* model in different aspects of physics relevant to the binary evolution, such as mass transfer efficiency between binary components and the kicks imparted to the stars. The resultant BH and NS mass distributions for the different models are shown in Fig 4.8, and we briefly summarise these models below.

The $\beta = 0.25, 0.5, 0.75$ models assume fixed mass transfer efficiencies. These models represent the fraction of mass lost by the donor star that its companion accretes. On the other hand, the "unstable case BB" model involves an unstable mass transfer phase from a stripped post-helium-burning star onto a BH.

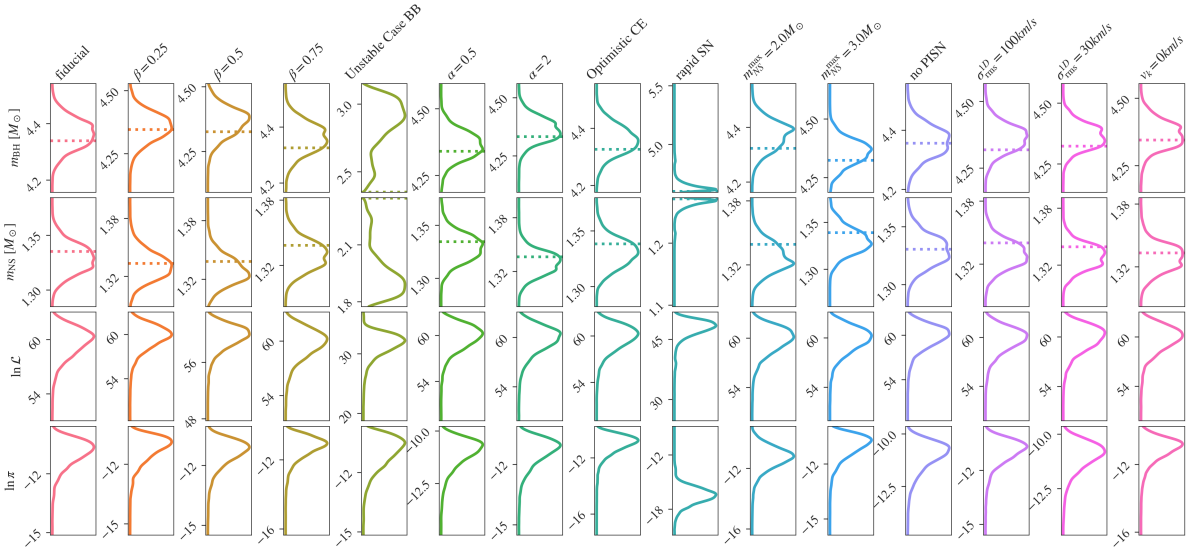

Figure 4.9: Posterior densities for the mass of GW230529 under different binary evolution assumptions. We also include the distributions of the log-likelihood and log-prior of the posterior samples. The dotted lines in the first two rows denote the maximum likelihood estimates of $m_{\rm BH}$ and $m_{\rm NS}$ respectively.

For the $\alpha = 0.5$ and $\alpha = 2$ models, a pessimistic common envelope scenario is assumed, where the donor stars struggle to successfully eject their envelopes, resulting in efficiency parameters of 0.5 and 2, respectively. Conversely, the "optimistic" common envelope scenario posits that these systems can survive such challenges.

To avoid creating a remnant mass gap between NSs and BHs, which contradict observations from X-ray binaries, Ref. [1] use a delayed remnant mass prescription in their simulations. However, the "rapid SNe" model adopts a faster remnant mass prescription and is consistent with current observations.

The models labeled as $m_{\rm NS}^{\rm max} = 2M_\odot$ and $m_{\rm NS}^{\rm max} = 3M_\odot$ set the maximum mass of NS to 2 and $3M_\odot$, respectively. It's worth noting that the latter case may be considered unrealistic since the maximum mass supported by current EoS for non-rotating NS is $\lesssim 2.9M_\odot$ [71].

The "no PISN" prescription excludes the pair-instability process, responsible for the scarcity of first-generation BHs with masses between 65–$120M_\odot$. Additionally, the $\sigma_{\rm cc} = 30$ km/s and $\sigma_{\rm cc} = 100$ km/s prescriptions explore variations of natal kicks compared to the one-dimensional root-mean-square velocity dispersion of $\sigma_{\rm cc} = 265$ km/s used in the fiducial model. These lower values can occur in ultra-stripped SNe and electron-capture SNe, leading to reduced binary disruption. Finally, the $v_{\rm k,BH} = 0$ km/s assumption posits that BHs receive no supernova natal kicks.

Fig 4.9 summarises our findings when assuming these populations. We observe that, except for the "unstable case BB" and "rapid SNe" models, the inferred posteriors are largely in agreement with each other. This alignment was anticipated, given that these two population models restrict the BH mass to a range outside the support for this signal. Moreover, we do not observe any trends in the log-prior distribution for the other models, which indicates that all the information about the evidence for and against binary evolution is contained in the distribution of the log-likelihood ratio. However, we also do not observe any differences in the shape and location of the log-likelihood ratio distribution, indicating that all models are equally likely. In fact, the $\ln \mathrm{BF}^{S}_{N}$ for all analyses, except for the "unstable case BB" and "rapid SNe" models, is approximately $63. \pm 0.15$. This suggests that the outputs of these analyses are statistically equivalent. The "unstable case BB" and "rapid SNe" models have $\ln \mathrm{BF}^{S}_{N}$ values of 37.0 and 51.87, respectively, indicating they are less favoured. This is because these priors prevent exploration of the higher likelihood region.

This is not surprising since the signal's SNR is low. Finally, it is noteworthy that, for the majority of our analysis, we determine the BH and NS masses to be $m_{\mathrm{BH}} = 4.3^{+0.08}_{-0.09} M_{\odot}$ and $m_{\mathrm{NS}} = 1.4^{+0.02}_{-0.02} M_{\odot}$, respectively, while finding that the $\ln \mathrm{BF}^{\mathrm{fiducial}}_{\mathrm{pop-agnostic}} \sim 1$.

4.4 Conclusions

GW observation can be used to infer source parameters that can illuminate the astrophysical processes involved in binary formation and evolution. Precise measurements of these parameters, particularly the mass and the spin of the binary components, can be used to distinguish between the different astrophysical formation channels. In this chapter, we have assessed the measurability of the spins of the NS using NSBH detections with XG GW detector networks. Furthermore, using GW230529 as a case study, we demonstrated how Bayesian model selection—combining GW parameter estimation with population synthesis simulations—can be employed to distinguish between, or rule out, specific formation scenarios for NSBH binaries.

In Section 4.2.1.1, we showed that HOMs can contribute significantly to the waveform and the measurement of the NS spin, especially at higher inclination angles, with $(3, \pm 3)$ being the second highest contributor to the χ_{NS} measurement. We also noted that η interacts with negative combinations of the component spins in the amplitude of the $(2, \pm 1)$ and the $(3, \pm 3)$ modes, and with the positive combinations of component spins in the $(2, \pm 2)$, $(3, \pm 2)$ and $(4, \pm 4)$ modes. These different interactions help mitigate

the mass-spin degeneracy. However, due to the narrow mass function of the NS, we do not expect an appreciable contribution of HOMs to the BNS signal. Hence, we instead look at the bounds that can be placed on $\chi_{\rm NS}$ with NSBH systems, which are naturally mass-asymmetric.

Using the relative binning technique of accelerated parameter estimation, we performed Bayesian analyses on a set of NSBH systems, the results of which are detailed in Section 4.2.3. We find that the constraints on $\chi_{\rm NS}$ are highly contingent on the spin of the companion BH, with high $\chi_{\rm BH}$ values improving the bounds on $\chi_{\rm NS}$ (c.f. Fig. 4.2). We also discussed the effect of $\chi_{\rm BH}$ on the measurement of $\chi_{\rm NS}$ when varying BH mass– for low $\chi_{\rm BH}$ (~ 0.2), the bounds on $\chi_{\rm NS}$ get worse as we increased the BH mass, whereas for a rapidly rotating BH ($\chi_{\rm BH} \gtrsim 0.6$), $\chi_{\rm NS}$ is measured better for a more massive BH (c.f. Fig. 4.3).

To show the improvements in $\chi_{\rm NS}$ measurement brought out by HOMs, we compare the posterior distribution of $\chi_{\rm NS}$ for 10+1.4 $M_\odot$ NSBH systems for two sets of injections at varying inclination angles— first, with a waveform that contains only the $(2, \pm 2)$ mode (IMRPhenomXAS), and second, with a waveform that contains the $(2, \pm 2)$ and HOMs (IMRPhenomXHM). We find that as the inclination angle increases (and so does the relative HOMs contribution (c.f. Fig. 4.1)), $\chi_{\rm NS}$ measurements improve considerably when HOMs are included in the waveform, whereas no significant change is seen in the $\chi_{\rm NS}$ measurement when HOMs is not included (c.f. Fig. 4.4), showing the utility of HOMs in $\chi_{\rm NS}$ measurement. Finally, we explored the effect of SNR and detector sensitivity on the measurability of $\chi_{\rm NS}$. We found that $\chi_{\rm NS} = 0.1$ can be distinguished from 0 with A+ and A$^\sharp$ for golden events that may occur once in every tens of years. However, if the BH is rapidly rotating ($\chi_{\rm BH} = 0.8$), networks with ET and CE will be able to make the same distinction for $\mathcal{O}(100)$ events, merging up to 1000 Mpc (c.f. Fig. 4.4).

Thus, if rapidly spinning NS were to merge with BH, XG observatories with ET and CE would be capable of differentiating such NS from non-spinning ones, making it the first discovery of such NS without EM observations. Such a discovery would be monumental for astrophysical studies on binary formation and evolution. As high values of aligned spins are conducive to the tidal deformation of NS before merger, such systems can also be important for multimessenger astronomy [73] and cosmology [61]. In this work, we have restricted ourselves to aligned-spin systems. However, with better parameter estimation techniques, this work can be extended to precessing (and even eccentric) NSBH mergers formed due to dynamical interactions. While precession will improve the relative contribution of HOMs, the additional spin and tilt parameters may increase

the uncertainty in $\chi_{\rm NS}$ measurement. Further, the asymmetry between $\pm m$ modes for precessing system can also play a role in measuring the spins of the components [317,318]. Thus, a similar study spanning various binary configurations (in terms of spin and tilt values) will be useful to ascertain if $\chi_{\rm NS}$ can be even better measured than what has been claimed in this work. Another possible extension would be to look at the prospects of detecting a sub-population of such rapidly spinning NS with NSBH systems. This may require less stringent bounds on $\chi_{\rm NS}$ for each event, which will increase the number of potential candidates that can contribute to the analysis.

Finally, we studied the origins of GW230529, assuming that it is a binary formed via the classical isolated binary evolution via the common envelope phase. As discussed in Sec 4.3.2.2, by leveraging the BHNS binary population synthesis model from Ref. [1], we present compelling evidence that the system's properties are consistent with the predictions derived from the isolated binary evolution pathway of BHNS systems. However, due to the event's relatively low SNR, we face difficulties in identifying the underlying physical mechanism driving its formation unequivocally. However, we could rule out with confidence certain formation mechanisms such as the one involving the "rapid SNe" or the "unstable case BB".

Declaration

The author of this dissertation was responsible for generating all the results presented in Sec. 4.2, and part of the results presented in Sec. 4.3, the rest of which were produced by Koustav Chandra and Rossella Gamba. The contents of this chapter have been published in the American Astronomical Society's Astrophysical Journal with reference [67] and reference [162].

Chapter 5
Constraining cosmological parameters with NSBH mergers

Measure what is measurable, and make measurable what is not so.
— Galileo Galilei

5.1 Introduction

The Hubble-Lemaître constant (H_0) informs us about the rate of expansion of the universe. Thus, precise measurement of H_0 is of fundamental importance to cosmology. Two of the most accurate measurements of H_0 come from the Planck Collaboration and the SH0ES Program. The Planck Collaboration obtains constraints on the Hubble-Lemaître parameter using the cosmic microwave background measurements. The latest study reports the value of Hubble-Lemaître to be $H_0 = 67.4 \pm 0.5\ \mathrm{km\,s^{-1}\,Mpc^{-1}}$ [319]. The SH0ES Program utilizes the Cepheid variable stars and the Type-Ia supernovae to obtain bounds on H_0. The reported value from this approach is $H_0 = 73.30 \pm 1.04$, which has a 5σ difference with Planck's measurement [56]. Several other analyses have reported measurements of H_0 [320] resulting in $4.0\sigma - 5.8\sigma$ discrepancy in the measurement of the Hubble-Lemaître constant from the early and the late universe. This discrepancy is known as the Hubble-Lemaître tension.

One way to resolve the tension is by using an independent method to measure the Hubble-Lemaître constant– using GWs. The method was first suggested in Ref. [57], predating the knowledge of tension in H_0 measurements. The *Schutz method* employs the fact that GW observations can be used to constrain the luminosity distance D_L associated with a compact binary. As GW observations can measure D_L directly and do not require a distance calibrator, they are also referred to as *standard sirens* [321]. The corresponding redshift can be obtained by host-galaxy identification if the merger

event is followed by an EM counterpart. Without the counterpart, one can look for galaxies in the sky patch acquired from the sky-area localization using GW detection. Each galaxy/galaxy cluster in that sky patch will have an associated redshift and give a value of H_0, with the true value of H_0 among them. Combining H_0 measurement associated with multiple such GW detections will help isolate the true value of H_0 from the noise. This is the statistical method suggested in Ref. [57] and is often referred to as the *statistical standard siren* approach. Another statistical approach makes use of the clustering information of the large-scale structures by cross-correlating a population of BBH sources with spectroscopic galaxies [322].

As BBH mergers are standard sirens that are not expected to be followed by EM counterparts, they are often called *dark sirens*. The sky position for a fraction of these dark sirens can be measured well enough such that, on average, only one galaxy will lie in that sky patch, allowing one to uniquely identify the host galaxy [59, 323, 324]. The host-galaxy identification is used to obtain the corresponding redshift measurement. Using this technique, Ref. [59] claim to resolve the tension in H_0 measurement with two years of observation using a planned 5 detector network `HLVKI` at `A+` sensitivities [39, 40], which is expected to be functional in the late 2020s. As the current detector sensitivities do not allow for such precise sky-area measurements, present analyses employ statistical methods by using Bayesian frameworks developed in Ref. [325, 326]. Using the statistical method with Gravitational-Wave Transient Catalog-2 (GWTC-2) [288], without GW170817, H_0 is constrained to $67.3^{+27.6}_{-17.9}$ km s^{-1} Mpc^{-1} [327].

In contrast to the BBH systems, BNS systems are expected to be followed by EM counterparts, which can then be used to identify the host galaxy and obtain the redshift. Thus, BNS systems can be used as *bright sirens*. This was first realized with the detection of GW170817 [25], which was the first GW event for which EM counterparts were detected [18, 29, 328]. Using the EM detection, the host galaxy was identified as NGC4993 and the Hubble-Lemaître constant was measured to be 70^{+12}_{-8} km s^{-1} Mpc^{-1} [329]. Note that this measurement alone is better than the combined measurement using GWTC-2 events without GW170817. In fact, Ref. [326] shows that BNS systems with detected counterparts constrain H_0 better than BBH systems without counterparts. Further, it has been shown that ~ 50 BNS mergers with counterparts will be enough to resolve the Hubble-Lemaître tension [326, 330]. There have also been studies that have combined the Hubble-Lemaître constant measurements from dark and bright siren approaches. Using GWTC-3 events [75], H_0 is estimated to be 68^{+12}_{-8} km s^{-1} Mpc^{-1} [34]. Similarly, Ref. [327] includes the Hubble-Lemaître constant measurement with GW170817 to the H_0 measured

using dark sirens to report an improved measurement of $H_0 = 72.2^{+13.9}_{-7.5}$ km s^{-1} Mpc^{-1}.

In January 2020, the LIGO-Virgo detectors recorded the first detection of an NSBH merger [76], adding another class of compact binary systems to the set of detected events. In general, depending on the characteristics of the system, NSBH mergers can be followed by EM counterparts [85–88] and can be used as bright sirens for H_0 measurement. In fact, NSBH systems can produce better bounds on H_0 than BNS systems if the local merger rate for NSBH systems is better than 1/10 the rate for BNS and if the NSBH systems are precessing [91]. Further, Ref. [92] shows that for an NSBH merger rate density of 610 Gpc^{-3} yr^{-1}, the `HLVKI` network with `A+` sensitivities might be able to resolve the Hubble-Lemaître tension in 5 years. However, the merger rate density chosen by this analysis has been ruled out by the event-based local merger rate density reported in GWTC-3 [33], with the new upper limit on the NSBH merger rate to be 140 Gpc^{-3} yr^{-1}. This will affect the constraints on H_0 reported by the work.

NSBH systems are interesting candidates for the measurement of the Hubble-Lemaître constant. The dominant contribution to the GW waveform comes from the quadrupolar $(2, 2)$ mode. However, when the binary consists of objects with unequal masses, subdominant higher-order modes can become important [206]. In general, the mass ratio $q = m_{\rm BH}/m_{\rm NS}$ for NSBH systems is greater than 2, which leads to the activation of the higher-order modes in the GW waveform. Inclusion of the higher-order modes breaks the inherent degeneracy between the luminosity distance D_L and the inclination angle ι in the GW waveform and leads to improved estimation of D_L and ι, among other parameters [331–334]. Also, the fractional error in luminosity distance $\Delta D_L/D_L$ is inversely proportional to the SNR. The SNR, in general, is higher for systems with heavier masses. That is why BBH are effective as dark sirens, and NSBH systems perform better than BNS systems as dark sirens for the measurement of H_0. Moreover, NSBH systems can measure H_0 up to a higher redshift than BNS systems by virtue of having a larger total mass. For the bright siren method, only NSBH systems with low q and high BH spin are favorable for the generation of a KN. On the other hand, most, if not all, BNS systems are expected to be followed by an EM counterpart. This makes BNS systems more efficient as bright sirens for Hubble-Lemaître constant measurement. However, the constraints on H_0 from NSBH events that qualify as dark sirens and the ones that qualify as bright sirens can be combined to calculate H_0 to better precision compared to only using the dark siren or the bright siren approach. Due to the ability to act both as dark and as bright sirens, we refer to NSBH systems as *gray sirens*.

In this chapter, we will assess the potential of NSBH systems to resolve the Hubble-

Table 5.1: The six XG ground-based GW detector networks that are included in the analysis, with the abbreviation used to refer to the network. In the text, `HLVKI+` and `VK+HLIv` are also referred to as the `A+` network and the Voyager network, respectively.

Network	Detectors
HLVKI+	LIGO (HL+), Virgo+, KAGRA+, LIGO-I+
VK+HLIv	Virgo+, KAGRA+, LIGO (HLI-Voyager)
VKI+C	Virgo+, KAGRA+, LIGO-I+, CE-North
HLKI+E	LIGO (HL+), KAGRA+, LIGO-I+, ET
KI+EC	KAGRA+, LIGO-I+, ET, CE-North
ECS	ET, CE-North, CE-South

Lemaître tension using GW observations and EM detections. This study uses results from Chapter 2 where we analyze the detectability, measurement ability, and the science that can be done with XG ground-based GW detector networks with NSBH mergers [73]. We consider NSBH events that can be detected by six future GW observatories. These networks include advancements like `A+` and Voyager sensitivities [45] for LIGO detectors, two 40 km long Cosmic Explorer (CE) detectors [47–49] and triangular-shaped Einstein Telescope with 10 km arms [50, 51]. The combinations of detectors making up the six networks are listed in Table 5.1.

Following Chapter 2, we construct two NSBH populations for an observation time of 10 years. The population parameters are described in Section 5.2. In Section 5.3, we describe the motivation behind using NSBH as dark sirens and as bright sirens. We also explain the use of the Fisher information matrix in calculating the measurement errors on H_0 using the errors in luminosity distance. In Sections 5.4 and 5.5, we discuss the performance of NSBH systems as dark sirens and bright sirens respectively. Using the results in these two sections, we justify the treatment of NSBH systems as gray sirens, showing results for the same in Section 5.6. Our conclusions are summarized in Section 5.7.

5.2 Population Characteristics

Due to the low number of NSBH detections, the population characteristics of NSBH systems are uncertain. While there have been attempts at deriving the mass and spin

Parameter	Pop-1		Pop-2	
	Neutron Star	Black Hole	Neutron Star	Black Hole
Mass m	[1,2.9] $M_\odot$	[3,100] $M_\odot$	[1.26,2.50] $M_\odot$	[2.6,39.2] $M_\odot$
Mass Model	Uniform	`POWER+PEAK` [33]	Derived from the fiducial model [1]	
Spin χ	[-0.05,0.05]	[-0.75,0.75]	0	[0,1]
Spin Model	Aligned Uniform		Aligned	Eqs. (2) and (3) in Ref. [2]
z	Uniform in six bins: [0.02,0.05], [0.05,1], [1,2], [2,4] and [4,10]			
D_L	z converted using `ASTROPY.Planck18`			
$\cos(\iota)$	Uniform in [-1,1]			
α	Uniform in $[0,2\pi]$			
$\cos(\delta)$	Uniform in [-1,1]			
ψ	Uniform in $[0,2\pi]$			
t_c, ϕ_c	0			

Table 5.2: The table summarizes the parameters that characterize the two population models considered in this study. The parameters are used to generate injections and carry out the analysis for the constraints that can be put on the Hubble-Lemaître constant using GW observations of NSBH systems.

distributions for the NS and the BH using the available events [103, 104], these models can change drastically with more detections in the coming years. From a theoretical standpoint, different formation channels can give distinct predictions regarding the masses and spins of the two components in NSBH systems [77–83]. To gauge these uncertainties, we consider two population models for NSBH systems- *Pop-1* and *Pop-2*. Pop-1 considers broad mass and spin distributions for NSBH systems. The BH mass follows the `POWER+PEAK` [33] distribution between $[3\,M_\odot, 100\,M_\odot]$ and the NS mass is sampled from a uniform distribution between $[1\,M_\odot, 2.9\,M_\odot]$. The spins for both the NS and the BH are assumed to be aligned with the orbital angular momentum of the binary system, i.e., $\chi_{1x} = \chi_{1y} = \chi_{2x} = \chi_{2y} = 0$. Here, the orbital angular momentum is assumed to be along the z direction and $(\boldsymbol{\chi_1}, \boldsymbol{\chi_2})$ denote the dimensionless spin vectors

of the BH and the NS, respectively. The NS spins are chosen from a uniform distribution between $[-0.05, 0.05]$ and the BH spins are taken from a uniform distribution between $[-0.75, 0.75]$. For Pop-2, the masses and spins for the NS and the BH are taken from the *fiducial* model in Ref. [1], which is a binary population synthesis model for NSBH systems which are formed through the isolated binary formation channel. The NS are assumed to be non-spinning, whereas BH have aligned spins and their magnitude is calculated using Eqs. (2) and (3) in Ref. [2]. The equations only apply to systems where the NS progenitor is formed first, allowing the second-born BH progenitor to have high spins as it can get tidally spun up by its companion [4, 106–108]. For each population, we generate 250,000 injections per redshift bin for five redshift bins: $z \in [0.02, 0.05]$, $[0.05, 1]$, $[1, 2]$, $[2, 4]$ and $[4, 10]$. The luminosity distance for each injection is obtained by converting the corresponding redshift, z, using `ASTROPY.PLANCK18` [109, 110]. $\cos(\iota)$ and $\cos(\delta)$, where ι and δ are the inclination angle and the declination respectively, are sampled uniformly between $[-1, 1]$. The right ascension α and the polarization angle ψ are sampled uniformly between $[0, 2\pi]$. t_c and ϕ_c are the time and phase of coalescence respectively and are fixed to 0 for all the injections. All the parameters for both populations have been summarized in Table 5.2.

We logarithmically divide the redshift range into 50 bins and randomly pick injections from each of these bins. The number of injections picked from a redshift bin corresponds to the expected number of NSBH mergers for that redshift range. This number is calculated by using a redshift distribution for the NSBH systems. We follow the analytical redshift distribution given in Ref. [120] that uses the star formation rate (SFR) model described in Ref. [115] with a log-normal time delay model proposed in Ref. [116]. The model is calibrated to match the local (i.e., at $z = 0$) merger rate density estimated by the LIGO-Virgo collaboration using the detected events. The inferred event-based local merger rate density is in the range $7.8 - 140$ Gpc^{-3} yr^{-1} [33]. We fix the local merger rate density for NSBH systems to 45 Gpc^{-3} yr^{-1} (which is the median value reported in Ref. [76]), resulting in a cosmic NSBH merger rate of $4.0^{+8.5}_{-3.3} \times 10^4$ yr^{-1}, where the upper and lower bounds are calculated using the upper and lower bounds on the local merger rate density. Using the redshift distribution and local merger rate density, we construct populations of NSBH events using Pop-1 and Pop-2 parameters corresponding to an observation time of 10 years. In the following sections, we will present results for both Pop-1 and Pop-2 events and for three local merger rate densities, *low:* 7.8 Gpc^{-3} yr^{-1}, *median:* 45 Gpc^{-3} yr^{-1} and *high:* 140 Gpc^{-3} yr^{-1}.

5.3 Motivation and Methodology

GWs can obtain an independent measurement of the Hubble-Lemaître constant as they can constrain the luminosity distance of the source, which can be used together with the associated redshift to obtain H_0. To calculate the errors in the measurement of the constant, we need to account for the uncertainty in the measurement of the luminosity distance and the involved cosmological parameters. Further, to achieve the corresponding redshift, we need to identify the galaxy that hosts the binary system. This can be accomplished in two ways-

1. *Dark siren approach:* If the sky-position of the binary can be localized using GW observations well enough that only one galaxy can lie in that sky patch, then the host galaxy can be uniquely identified.

2. *Bright siren approach:* If the compact binary merger is accompanied by an EM counterpart that is detected by one of the EM telescopes, then the sky-position of the counterpart will pinpoint the location of the host galaxy.

Once the redshift is acquired, the measurement errors in the luminosity distance and cosmological parameters can be appropriately combined for multiple events using FIMs to get constraints on the Hubble-Lemaître constant.

In this chapter, we work with compact binaries where the NS and the BH are assumed to be in a quasi-circular orbit and their spins are assumed to be aligned with the orbital angular momentum of the binary. In this case, the detector response to the GW is given by,

$$\begin{aligned} h^{(A)}(t, \boldsymbol{\mu}) = \; & F_{+}^{(A)}(\alpha, \delta, \psi, \boldsymbol{\nu})\, h_{+}^{(A)}(t, \mathcal{M}_c, \eta, \chi_1, \chi_2, \iota, D_L) \\ + \; & F_{\times}^{(A)}(\alpha, \delta, \psi, \boldsymbol{\nu})\, h_{\times}^{(A)}(t, \mathcal{M}_c, \eta, \chi_1, \chi_2, \iota, D_L). \end{aligned} \tag{5.1}$$

Here, $F_{+}^{(A)}$ and $F_{\times}^{(A)}$ are the antenna pattern functions corresponding to the detector A that depend on the location of the detector, denoted by $\boldsymbol{\nu}$, and the location of the source, expressed using the right ascension α, the declination δ and the polarization angle ψ. $h_{+}^{(A)}$ and $h_{\times}^{(A)}$ are the *plus* and *cross* polarizations of the GWs and are a function of variables that describe the properties of the source— chirp mass $\mathcal{M}_c$ and symmetric mass-ratio η are functions of the masses of the two compact objects, χ_1 and χ_2 are the dimensionless spins of the BH and the NS, ι is the angle between the line of sight of the observer and the total angular momentum of the binary and D_L is the luminosity

distance of the binary from the observer. Hence, for a given detector, the detector output is a time-dependent function of $\boldsymbol{\mu} = (\mathcal{M}_c, \eta, \chi_1, \chi_2, \iota, D_L, \alpha, \delta, \psi)$.

To obtain the errors in measurement of parameter $\boldsymbol{\mu}$, we utilize the FIM method implemented in `GWBENCH` [102]. The method gives the measurement errors in $\boldsymbol{\mu}$ as elements of the covariance matrix Σ, which is the inverse of the FIM Γ, defined as

$$\Sigma_{ij} = \Gamma^{-1}_{ij} = \left(\frac{\partial h}{\partial \theta_i}, \frac{\partial h}{\partial \theta_j}\right)^{-1}, \tag{5.2}$$

where h is the GW waveform in the frequency-domain, θ_i is the i^{th} parameter in $\boldsymbol{\mu}$ and $(\cdot\,,\cdot)$ is the noise-weighted inner product. The square root of the diagonal elements of the covariance matrix, i.e., $\Sigma^{1/2}_{ii}$, gives the uncertainty in the measurement of the i^{th} parameter.

Figure 5.1 shows the detection rate of NSBH systems for the six GW detector networks as a function of redshift. The pink-shaded area denotes the uncertainty in the local merger rate of NSBH systems. In this chapter, we will only look at systems located within the redshift of $z = 0.5$, as for the dark siren study, only systems within $z = 0.1$ are considered, and for bright sirens, we do not get any KN detections beyond $z \sim 0.4$ for the two telescopes we have used (c.f. Chapter 3). Up to the redshift of $z = 0.5$, our populations contain ~ 4000 NSBH systems, all of which are detected by networks with at least one detector as the CE or the ET detectors. The Voyager network, `VK+HLIv`, is seen to detect $\sim 75\%$ of these events, whereas the `A+` network, `HLVKI+`, detects only 15% of all the events. For the detected events, Fig. 5.2 shows the detection and measurement ability of the GW detector networks in the form of cumulative density function (CDF) plots for the SNR ρ, the fractional measurement errors in luminosity distance $\Delta D_L/D_L$ and 90%−credible sky area Ω_{90}. The corresponding numbers are presented in Table 3.1 in Chapter 3, where we list the number of detections every year that can be localized in the sky to $\Omega_{90} \leq 10$, 1 and 0.1 deg^2 and the fractional error in luminosity distance is better than 0.1 and 0.01. We see that, depending on the network, we can expect to detect $\mathcal{O}(10)$ to $\mathcal{O}(1000)$ events every year where $\Omega_{90} < 1$ deg^2, and also when the luminosity distance is constrained to better than 10%. Further, $\mathcal{O}(1)$ to $\mathcal{O}(1000)$ events in an observation time of 10 years can be constrained to better than 0.1 deg^2. The unprecedented measurement ability of XG ground-based GW detector networks, especially in the measurement of luminosity distances and sky localization, prompt the evaluation of the potential of NSBH systems as dark siren candidates.

In Chapter 3, we reported the number of KN detections corresponding to the NSBH

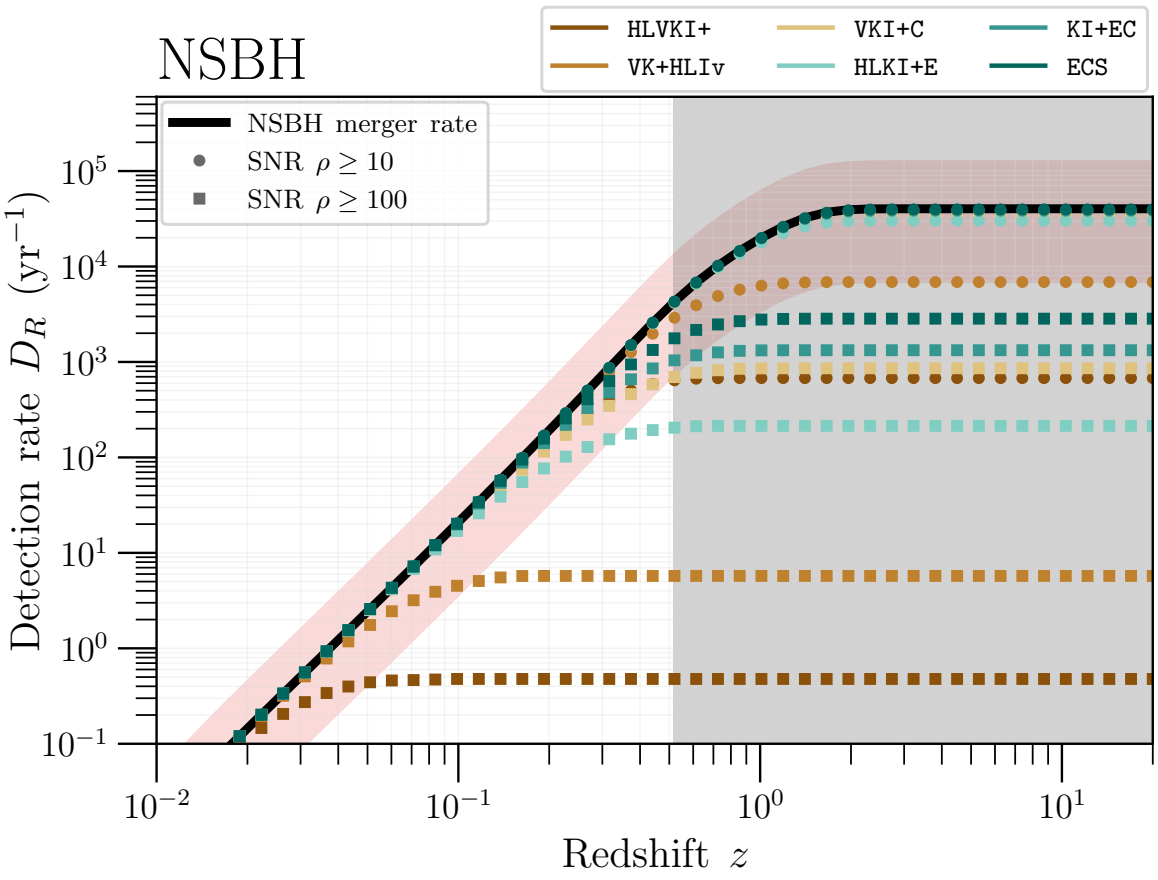

Figure 5.1: The detection rate of NSBH systems as a function of redshift for the six GW detector networks. The black solid line refers to the total NSBH merger rate. The pink-shaded area shows the variation in the total merger rate due to the uncertainty in the value of the local merger rate density. The gray shaded area covers the $z > 0.5$ region that is excluded from this analysis.

GW observations that can be expected using the Vera C. Rubin Observatory [6] and the Nancy Grace Roman Space Telescope [128]. We also showed that, depending on the EOS of the NS, we can expect to detect $\mathcal{O}(1)$ to $\mathcal{O}(10)$ KN detections using the $r-$filter in Rubin and $\mathcal{O}(1)$ to $\mathcal{O}(100)$ KN with $R-$filter in Roman, in an observation span of 10 years. As all of these events are within a redshift of $z \sim 0.4$, we expect the errors in luminosity distances to be in accordance with Fig. 5.2 and Table 3.1, i.e., for most of these events, the luminosity distances will be measured with accuracies better than 10% for the most advanced detector networks. The well-constrained luminosity distance with a detected EM counterpart points to the possibility of using NSBH systems as bright sirens for measuring the Hubble-Lemaître constant.

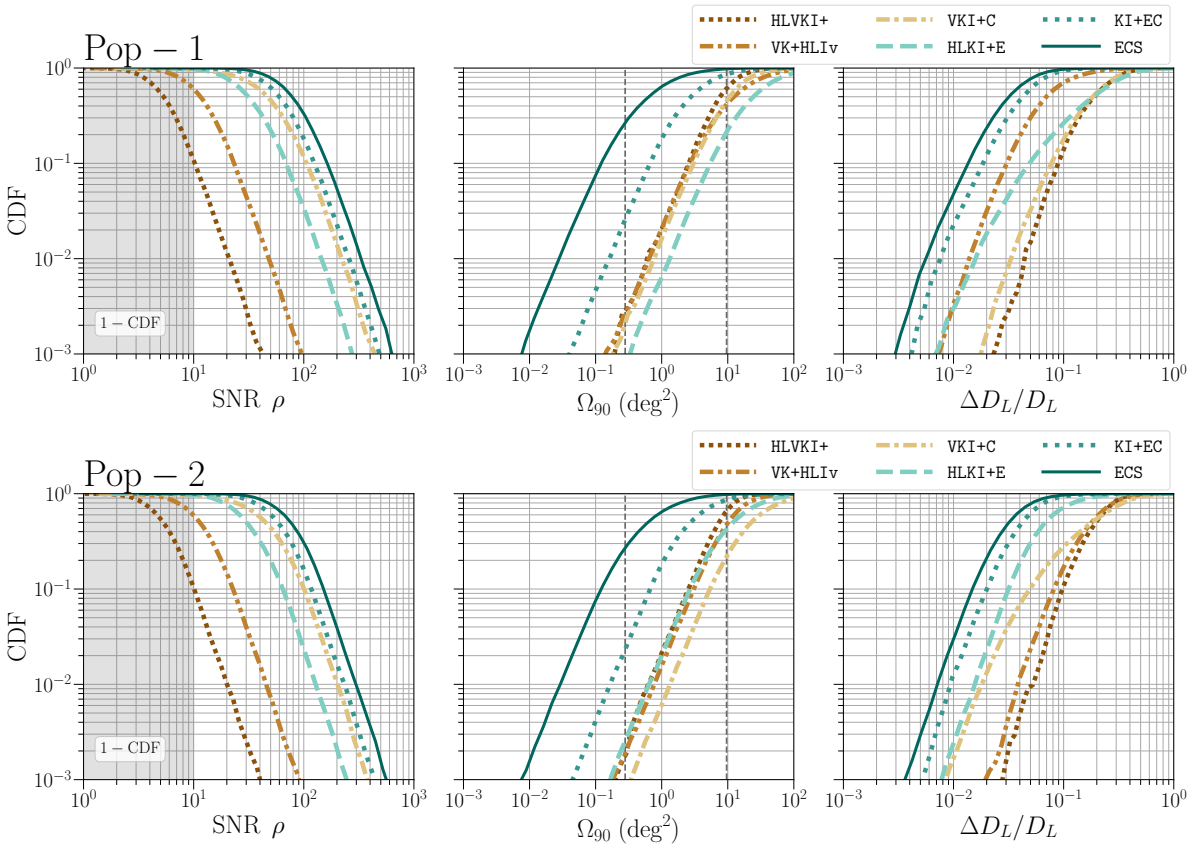

Figure 5.2: The cumulative density function plots for SNR ρ, 90%-credible sky area Ω_{90} and fractional error in luminosity distance $\Delta D_L/D_L$ for the population restricted to $z < 0.5$. The vertical black dotted lines in the plot for Ω_{90} correspond to the field of view (FOV) of the Roman Space Telescope (FOV = 0.28 deg^2 [5]) and the Rubin observatory (FOV = 9.6 deg^2 [5, 6])

To convert the errors in the measurement of luminosity distance into errors in measuring the Hubble-Lemaître constant, we assume the ΛCDM cosmology. The relationship between luminosity distance D_L and the redshift z can then be written as

$$\begin{aligned} D_L &= \frac{1+z}{H_0}\int_{1/(1+z)}^{1}\frac{dx}{x^2\sqrt{\Omega_\Lambda+\Omega_m\,x^{-3}}} \\ &= \frac{1+z}{H_0}\int_{1/(1+z)}^{1}\frac{dx}{x^2\sqrt{1-\Omega_m(1-x^{-3})}}, \end{aligned} \tag{5.3}$$

where Ω_m is the matter density, Ω_Λ is the dark energy density, and we have used $\Omega_\Lambda = 1 - \Omega_m$. As luminosity distance is a function of H_0 and the matter density, i.e., $D_L = D_L(\boldsymbol{\theta})$ with $\boldsymbol{\theta} = (H_0, \Omega_m)$ the corresponding FIM obtained by combining the

estimates from N events can be given as

$$\Gamma_{ij} = \sum_{k=1}^{N} \frac{1}{\sigma_{D_L}^2} \left(\frac{\partial D_L}{\partial \theta_i}\right) \left(\frac{\partial D_L}{\partial \theta_j}\right)\Bigg|_k , \tag{5.4}$$

i.e., we calculate the FIM for each event and then sum them over for all events. In Eq. (5.4), σ_{D_L} is the absolute error in luminosity distance for a particular GW observation. The expression for luminosity distance is obtained using the `Planck18` module of `astropy`. The FIM can then be numerically inverted to obtain the covariance matrix Σ, whose first and second diagonal elements give the squares of the absolute errors in H_0 and Ω_m, respectively.

This method is agnostic of any prior information we might have about Ω_m. Further, as we only consider events up to a redshift of $z = 0.5$, we do not expect Ω_m to be estimated well, which will also affect the estimates on H_0. A possible improvement comes from the realization that, while there is a disagreement between the Planck and the SH0ES measurements of the Hubble-Lemaître constant, their estimates on Ω_m are consistent. Planck reports $\Omega_m = 0.315 \pm 0.007$ and SH0ES measurement of q_0 is used to give $\Omega_m = 0.327 \pm 0.016$. We can include this information in our analysis by applying a Gaussian prior on Ω_m with variance given by

$$\sigma_{\Omega_m} = \sqrt{\sigma^2_{\text{Planck}} + \sigma^2_{\text{SH0ES}}} = 0.017. \tag{5.5}$$

A simple way to incorporate this prior in the FIM is to add the FIM term corresponding to Ω_m with $1/\sigma^2_{\Omega_m}$ [202], i.e.,

$$\Gamma_{22} = \sum_{k=1}^{N} \frac{1}{\sigma_{D_L}^2} \left(\frac{\partial D_L}{\partial \Omega_m}\right)^2 \Bigg|_k + \frac{1}{\sigma^2_{\Omega_m}} , \tag{5.6}$$

and the rest of the terms in the FIM are calculated the same way as before. The covariance matrix obtained using this FIM is expected to show better constraints for H_0 because the application of the prior on Ω_m restricts the parameter space of (H_0, Ω_m). In the following sections, we will report the fractional errors in H_0 for both the cases– without prior on Ω_m and with prior on Ω_m, and we will see that the inclusion of prior will significantly improve the measurement of the Hubble-Lemaître constant. Note that we also obtain bounds on H_0 with a broader prior on Ω_m where the width of the Gaussian prior is taken to be 5 times the previous value, i.e., $\sigma_{\Omega_m} = 0.085$. However, we do not observe significant changes in the bounds on H_0 with this broader prior, and all the

general conclusions drawn using the narrow prior still hold. Hence, we only report the results for the narrow prior on Ω_m, i.e., with $\sigma_{\Omega_m} = 0.017$.

5.4 NSBH systems as Dark Sirens

The detection of GWs from a compact binary merger allows us to constrain the sky-position of the binary using the right ascension and declination measurements [335]. The compact binary can be used as a dark siren to measure the Hubble-Lemaître constant if the 90%−credible sky area is small enough such that, on average, only one galaxy can be present in that patch of the sky. Using Eq. (7) in Ref. [122], we find that at a redshift of $z = 0.1$ (~ 476 Mpc), ~ 25 suitable galaxies can exist in a sky-area of $1\,\mathrm{deg}^2$. Thus, in a sky-patch of $0.04\,\mathrm{deg}^2$ contains, on average only ~ 1 galaxy. Consequently, we consider only those NSBH events for the dark siren study for which $\Omega_{90} < 0.04\,\mathrm{deg}^2$.

The combined FIM calculation and inversion to obtain the measurement errors on H_0 are done for two cases- first, without including any prior on Ω_m, and second, with prior on Ω_m, as specified in Section 5.3. We present the fractional errors in H_0 using dark sirens detected by the six GW detector networks in Fig. 5.3. The plots are shown for an observation time of 2 and 5 years and for three NSBH local merger rate densities, to account for the uncertainty in the local merger rate of NSBH systems. For a given local merger rate density, to pick dark sirens for an observation time of N years from our populations which contain events corresponding to an observation time of 10 years, we randomly pick $N/10$ fraction of dark siren events from the population and calculate the fractional error in H_0 using the combined FIM for the selected events. This process is repeated 1000 times, giving us 1000 instances of fractional errors in H_0 corresponding to a particular observation time, local merger rate, and detector network. The markers in Fig. 5.3 denote the median value of $\Delta H_0/H_0$ from these 1000 iterations and the corresponding error bars show the 68%−confidence region.

The error in H_0 decreases with the number of events N as $\sim \sqrt{N}$. Thus, the greater the number of events a detector network detects (with $\Omega_{90} < 0.04\,\mathrm{deg}^2$), the better the estimate of H_0 will be. Estimating the Hubble-Lemaître constant with measurement errors better than 2% is expected to resolve the tension between the Planck and the SH0ES measurements. Among the detected dark sirens, there can also be events where the luminosity distance is measured better than a fractional error of 2%, which can result in a sub-2% measurement of the Hubble-Lemaître constant just by using a single event. In addition, a collection of such events can be used to measure H_0 in different directions

and study the anisotropies in H_0 [336]. We call these mergers *golden events*. The number of dark sirens and the number of golden events that can be detected by the six GW detector networks in an observation time of 10 years are mentioned in Table 5.3.

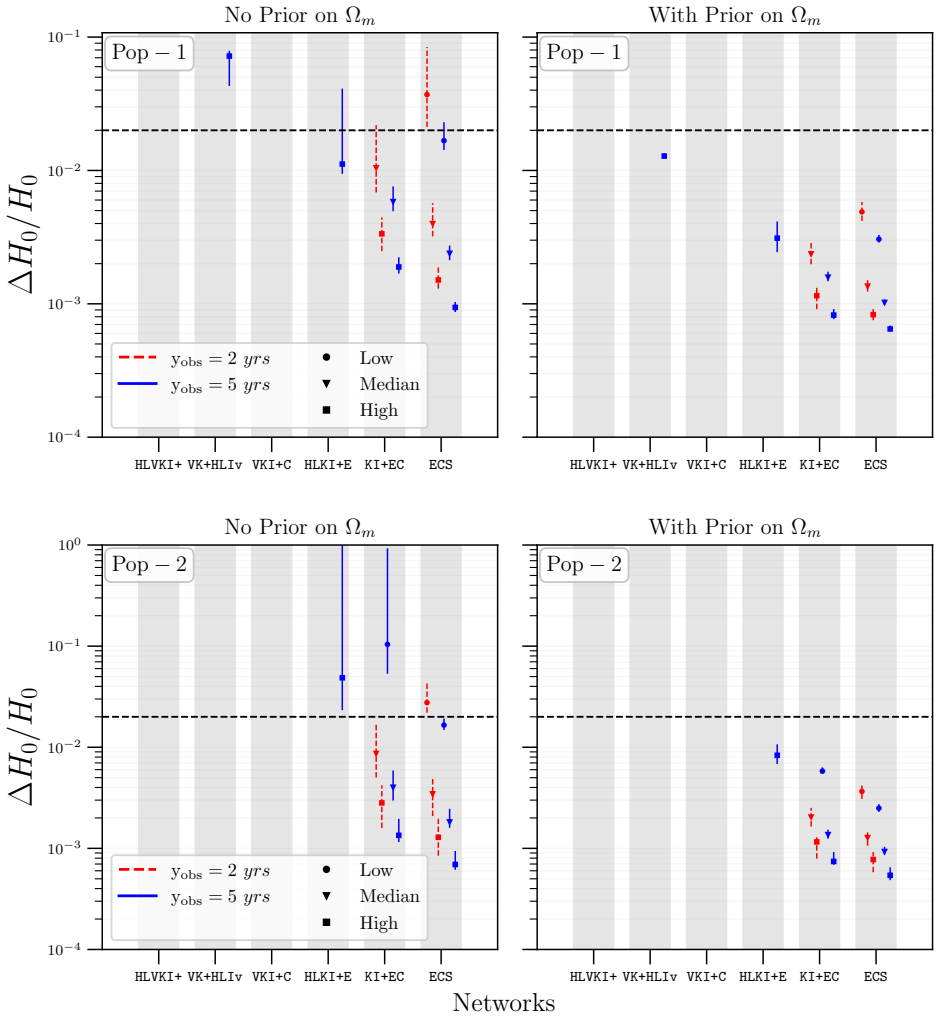

Figure 5.3: The fractional errors in H_0 measurement using NSBH systems as dark sirens for the observation time of 2 and 5 years and for three different values for the local merger rate of NSBH systems, low: $\dot{n}(0) = 7.8\,\mathrm{Gpc}^{-3}\,\mathrm{yr}^{-1}$, median: $\dot{n}(0) = 45\,\mathrm{Gpc}^{-3}\,\mathrm{yr}^{-1}$ and high: $\dot{n}(0) = 140\,\mathrm{Gpc}^{-3}\,\mathrm{yr}^{-1}$. The dotted black line corresponds to the 2% error in H_0 measurement which would be enough to resolve the Hubble-Lemaître tension.

.

From Table 5.3 and Fig. 5.3, we see that, regardless of the choice of population, local merger rates, or observation times considered in this study, the `A+` network will not detect any NSBH dark siren events. `VK+HLIv` is expected to detect $0-3$ NSBH dark siren events in 10 years, depending on the population model and the local merger rate

Table 5.3: The number of dark siren and golden event detections for both the population models with the six XG ground-based GW detectors in an observation time of 10 years.

Network	Pop-1		Pop-2	
	Dark	*Golden*	*Dark*	*Golden*
HLVKI+	0	0	0	0
VK+HLIv	1^{+2}_{-1}	1^{+2}_{-1}	0^{+1}_{-0}	0^{+1}_{-0}
VKI+C	1^{+1}_{-1}	1^{+1}_{-1}	0	0
HLKI+E	1^{+5}_{-1}	1^{+5}_{-1}	0^{+3}_{-0}	0^{+2}_{-0}
KI+EC	24^{+55}_{-22}	23^{+54}_{-21}	25^{+71}_{-21}	25^{+71}_{-21}
ECS	106^{+238}_{-91}	103^{+232}_{-88}	103^{+241}_{-85}	101^{+239}_{-84}

density. While the Hubble-Lemaître constant can be constrained using the detections from the Voyager network if the local merger rate is high, we cannot expect to bound H_0 better than 2% without including the prior on Ω_m. With the inclusion of the prior for Ω_m, `VK+HLIv` measures H_0 better than 2% for Pop-1 events. Note that when only one dark siren event is detected in a given observation time, the corresponding FIM is degenerate as it would amount to constraining two quantities, H_0 and Ω_m, using only one event. Thus, unless we fix Ω_m, which would mean that we know it exactly, the FIM cannot be inverted to obtain the measurement errors in H_0. As we consider Ω_m to be an unknown, Fig. 5.3 only shows the fractional errors in H_0 for those networks, observation times, and local merger rates for which more than one dark sirens are detected. Thus, no constraints on the Hubble-Lemaître constant are presented for the `VKI+C` network in Fig. 5.3 even though we can expect at most 2 mergers in an observation time of 10 years, which is equal to only 1 possible detection in 5 years. For the $0-6$ dark sirens events `HLKI+E` can detect, the constraints on H_0 for high merger rate and 5 years of observation vary with the choice of population. For Pop-1, even if the Ω_m prior is not included, H_0 can be measured well enough to resolve the tension. For events in Pop-2, we need to include the prior for Ω_m for measurements better than 2%.

Two of the most advanced GW detector networks considered in our study, `KI+EC` and `ECS`, can expect to detect $\mathcal{O}(10)$ to $\mathcal{O}(100)$ dark siren events in an observation time of 10 years. While both the networks can estimate the Hubble-Lemaître constant well enough to resolve the tension in an observation span of 2 years, `KI+EC` can only do so if the merger rate density is not low. With prior on Ω_m, `ECS` can resolve the tension in 2 years even for the case of low merger rate density. With a high merger rate and an observation

time of 5 years, ECS can measure the Hubble-Lemaître constant with measurement errors that are as small as $\mathcal{O}(10^{-4})$.

The number of NSBH events detected as dark sirens and as golden events is similar, if not the same, for each detector network and for both populations. That is because we only consider events within the redshift of $z = 0.1$ for the dark siren study. The XG detector networks perform well in terms of measurement ability at such distances, resulting in precise luminosity distance measurements. From Table 5.3, we note that there is a chance of observing a golden event as early as the Voyager era, which can help resolve the Hubble-Lemaître tension by itself. Obtaining $\mathcal{O}(1)$ to $\mathcal{O}(10)$ golden events *every year* with KI+EC and ECS will also allow one to probe the possible anisotropy in the value of the Hubble-Lemaître constant.

While we expect to detect $\mathcal{O}(10)$ dark siren/golden events every year with ECS, these constitute only 0.03% of all the NSBH events that ECS is expected to detect in a year. That makes both the occurrence and the observation of such events extremely rare. For comparison with BBH systems, a ECS-like network is expected to detect ~ 20 BBH dark siren events every year [59], which constitutes 0.02% of the BBH events that the network will detect that year [99]. If we only consider events with $z < 0.1$, $\sim 90\%$ of the BBH events and $\sim 50\%$ of the NSBH events detected by a ECS-like network are dark sirens. Further, Ref. [59] claims that the HLVKI+ network can resolve the Hubble-Lemaître tension within 2 years of observation with BBH systems, whereas we see that it is unable to detect any NSBH dark sirens in the span of 5 years. Thus, BBH systems perform better than NSBH systems as dark sirens in resolving the Hubble-Lemaître tension.

5.5 NSBH systems as Bright Sirens

The bright siren approach relies on observing an EM counterpart following the GW detection of the merger event. Observation of the EM counterpart pinpoints the location of the host galaxy. Identification of the host galaxy will lead to the measurement of redshift that, along with the distance measurement from GWs, can be used to measure the Hubble-Lemaître constant. This technique removes the stringent constraint on measuring the sky position using GWs to high accuracy as in the dark siren approach, potentially allowing more events to contribute to the Hubble-Lemaître constant measurement. However, a limiting factor is the low likelihood of observing an EM counterpart, which in our case is a KN, in the first place. The generation of a KN is sensitive to the population characteristics, especially the asymmetric mass ratio and the spin of the BH, and the

NS EOS. A population with predominantly non-spinning BHs (supported by the current observations [103, 104]) or one where BHs have retrograde ($\chi_{\rm BH} < 0$) spins, will disfavor KN generation. In contrast, a population that contains BHs with high prograde ($\chi_{\rm BH} > 0$) spins will encourage it [72]. Our two population models take both these effects into account- Pop-1 contains BHs with uniformly sampled spins from $[-0.75, 0.75]$, and Pop-2 contains predominantly non-spinning BHs with a small fraction ($\sim 5\%$) of BHs with high ($\chi_{\rm BH} > 0.75$) prograde spins.

As mentioned before, the EOS of the NS will significantly affect the generation of the KN. In particular, a *softer* EOS like `APR4` [150] will lead to a more compact NS and disfavor tidal disruption. On the other hand, a *stiffer* EOS like `DD2` [151] results in a less compact NS, allowing for tidal disruption of the NS before it passes the innermost stable circular orbit, $R_{\rm ISCO}$, and enabling the generation of the KN. We take this into consideration in our study by reporting the number of KN detections for three EOSs of varying stiffness: `ALF2` [152], `APR4` [150] and `DD2` [151]. We follow our previous work [73] to generate the light curves associated with the KN. We claim the detection of a KN if the peak luminosity of the KN is brighter than the limiting magnitude associated with a filter of a given telescope. In this study, we consider two EM telescopes, the Vera Rubin Observatory (henceforth, referred to as Rubin) and the Nancy Grace Roman Space Telescope (henceforth, referred to as Roman).

As noted in chapter 3, the $r-$filter in Rubin and the $R-$filter in Roman have similar effective wavelength ($\lambda_{\rm eff}$) correspond to some of the highest numbers of KN detections, so we consider these two filters in the current analysis. The specifications for the two telescopes, including the limiting magnitudes ($m_{\rm lim}$) are mentioned in Table 5.4. Tables 3.5 and 3.6 contain the number of KN detections for the two telescopes, categorized by the EOS and the 90%$-$credible sky area, for the median local merger rate density. The upper and lower limits of the listed values correspond to the high and low merger rate densities.

The number of bright sirens detected by each EM telescope for the three EOSs is presented in Table 5.5. Among these, we will also have golden events- events for which the measurement error in luminosity distance is $< 2\%$ and the merger is followed by a KN detected by the EM telescopes. Each of these golden bright siren events is capable of resolving the Hubble-Lemaître tension by itself. The number of golden events corresponding to each detector network and EOS is also listed in Table 5.5. All the numbers presented are for an observation time of 10 years and $\Omega_{90} < 10 \times$ FOV. The number of bright sirens detected can range from $\mathcal{O}(1)$ to $\mathcal{O}(100)$ in 10 years. For events

Table 5.4: Information about the two EM telescopes considered in this study. An exhaustive collection of such information for other EM telescopes can be found in Ref. [5].

Telescope	Rubin	Roman
FOV (deg^2)	9.6	0.28
Exposure time (s)	$30s$	$67s$
Filter	r	R
λ_{eff} (Å)	6156	6160
m_{lim} (AB mag)	24.7	26.2

in both populations, there is no chance of detecting golden bright sirens with `HLVKI+` and `VK+HLIv` networks. For `KI+EC` and `ECS`, unlike the dark siren case, only $10\% - 50\%$ of the bright siren events qualify as golden events, with `ECS` expected to detect $\mathcal{O}(1)$ golden events every year (unless `APR4` is the preferred NS EOS).

It is important to note that the detection criteria used above are only meant to give an estimate of the number of KN that can be detected. A realistic scenario involves a target-of-opportunity (TOO) follow-up strategy to detect KN events based on alerts from GW observations. We use one such TOO strategy in this work, where we consider a combination of $g + i$ filters in the Rubin observatory for the detection of the KN [153]. Specifically, the KN is said to be detected if the luminosity is brighter than the limiting magnitude of the g and the i filters on two consecutive nights with 600 seconds of exposure in each filter. The most optimistic values of limiting magnitudes obtained for an exposure of 600 s for the g and i filters are 26.62 and 25.62, respectively. In addition, we only consider events for which $\Omega_{90} \leq 9.6\,\mathrm{deg}^2$, i.e., their localization is smaller than the FOV of the Rubin telescope. The number of bright siren events and golden events observed using this strategy are given in Table 5.6. Comparing these values with the number of detections for Rubin in Table 5.5, we see that the TOO strategy leads to $2 - 3$ times higher number of detections. This is attributed to the longer exposure time ($600\,s$) which leads to the detections of intrinsically dimmer events and bright events that are farther away, compared to the detections made using single $30\,s$ exposures with Rubin. The trend in the detection of golden events is similar to that in Table 5.5, with no golden events detected with `HLVKI+` and `VK+HLIv`, and $\mathcal{O}(1)$ golden event detections with `ECS` every year.

To obtain the combined estimates on the measurement errors in H_0 corresponding to an observation span and merger rate density, we follow the same process used for dark sirens in Section 5.4 for each EOS and both the telescopes. The difference is that, instead

Table 5.5: Number of bright sirens and golden events detected by the two telescopes, using the $r-$filter in Rubin and the $R-$filter in Roman, in an observation span of 10 years, for ALF2 (A2), APR4 (A4), and the DD2 (D2) EOSs. The KN considered correspond to events that can be localized to a sky patch smaller than 10×FOV using GW observations, where FOV is the field of view of the particular telescope.

Type	Bright Sirens						Golden Events					
Filter	Rubin $r-$filter			Roman $R-$filter			Rubin $r-$filter			Roman $R-$filter		
EOS	A2	A4	D2	A2	A4	D2	A2	A4	D2	A2	A4	D2
Pop-1												
HLVKI+	9^{+16}_{-8}	4^{+5}_{-3}	16^{+28}_{-15}	3^{+4}_{-3}	1^{+0}_{-1}	6^{+7}_{-6}	0	0	0	0	0	0
VK+HLIv	14^{+25}_{-13}	4^{+9}_{-3}	23^{+42}_{-22}	8^{+16}_{-8}	3^{+5}_{-3}	19^{+42}_{-19}	0	0	0	0	0	0
VKI+C	14^{+25}_{-13}	4^{+9}_{-3}	23^{+42}_{-22}	3^{+5}_{-3}	1^{+1}_{-1}	9^{+18}_{-9}	1^{+1}_{-1}	0	1^{+1}_{-1}	1^{+1}_{-1}	0	1^{+1}_{-1}
HLKI+E	14^{+25}_{-13}	4^{+9}_{-3}	23^{+42}_{-22}	15^{+28}_{-14}	5^{+7}_{-4}	26^{+61}_{-25}	1^{+2}_{-1}	0	2^{+3}_{-2}	1^{+2}_{-1}	0	2^{+4}_{-2}
KI+EC	14^{+25}_{-13}	4^{+9}_{-3}	23^{+42}_{-22}	56^{+100}_{-45}	21^{+36}_{-15}	100^{+193}_{-84}	2^{+6}_{-2}	0^{+1}_{-0}	5^{+13}_{-5}	3^{+8}_{-2}	0^{+3}_{-0}	6^{+17}_{-5}
ECS	14^{+25}_{-13}	4^{+9}_{-3}	23^{+42}_{-22}	88^{+157}_{-68}	33^{+60}_{-25}	156^{+293}_{-128}	3^{+13}_{-3}	0^{+5}_{-0}	8^{+24}_{-8}	7^{+24}_{-6}	1^{+7}_{-1}	16^{+44}_{-15}
Pop-2												
HLVKI+	16^{+18}_{-14}	0	31^{+41}_{-26}	3^{+5}_{-2}	0	6^{+12}_{-4}	0	0	0	0	0	0
VK+HLIv	19^{+30}_{-16}	0	37^{+82}_{-31}	16^{+21}_{-12}	0	29^{+43}_{-24}	0	0	0	0	0	0
VKI+C	20^{+30}_{-17}	0	38^{+83}_{-32}	7^{+10}_{-5}	0	14^{+21}_{-11}	0	0	0^{+2}_{-0}	0	0	0^{+1}_{-0}
HLKI+E	20^{+30}_{-17}	0	38^{+84}_{-32}	22^{+42}_{-17}	0	44^{+84}_{-36}	1^{+6}_{-1}	0	4^{+11}_{-4}	1^{+3}_{-1}	0	2^{+4}_{-2}
KI+EC	20^{+30}_{-17}	0	38^{+84}_{-32}	79^{+173}_{-64}	0	160^{+330}_{-132}	5^{+15}_{-3}	0	13^{+31}_{-10}	6^{+19}_{-4}	0	19^{+39}_{-15}
ECS	20^{+30}_{-17}	0	38^{+84}_{-32}	115^{+262}_{-92}	0	247^{+512}_{-202}	7^{+17}_{-5}	0	18^{+42}_{-15}	16^{+40}_{-13}	0	38^{+81}_{-31}

of picking events where $\Omega_{90} < 0.04\,\mathrm{deg}^2$, we choose events for which the corresponding KN are detected by a given EM telescope. Figures 5.4 5.5 show the estimates on fractional errors in the measurement of H_0 using bright sirens without including a prior on Ω_m, whereas Figs. 5.6 and 5.7 show the errors when prior for Ω_m is included. We also calculate the bounds that can be put on H_0 using the $g+i$ TOO strategy, which are shown in Figs. 5.8 and 5.9.

Firstly, we do not get any bright sirens for `APR4`, which is the softest of the three EOSs, for events in Pop-2. Here, we note that the numerical fits used to generate the KN light curves are only valid for $\chi_{\rm BH} < 0.75$. Thus, even though Pop-2 has NSBH events

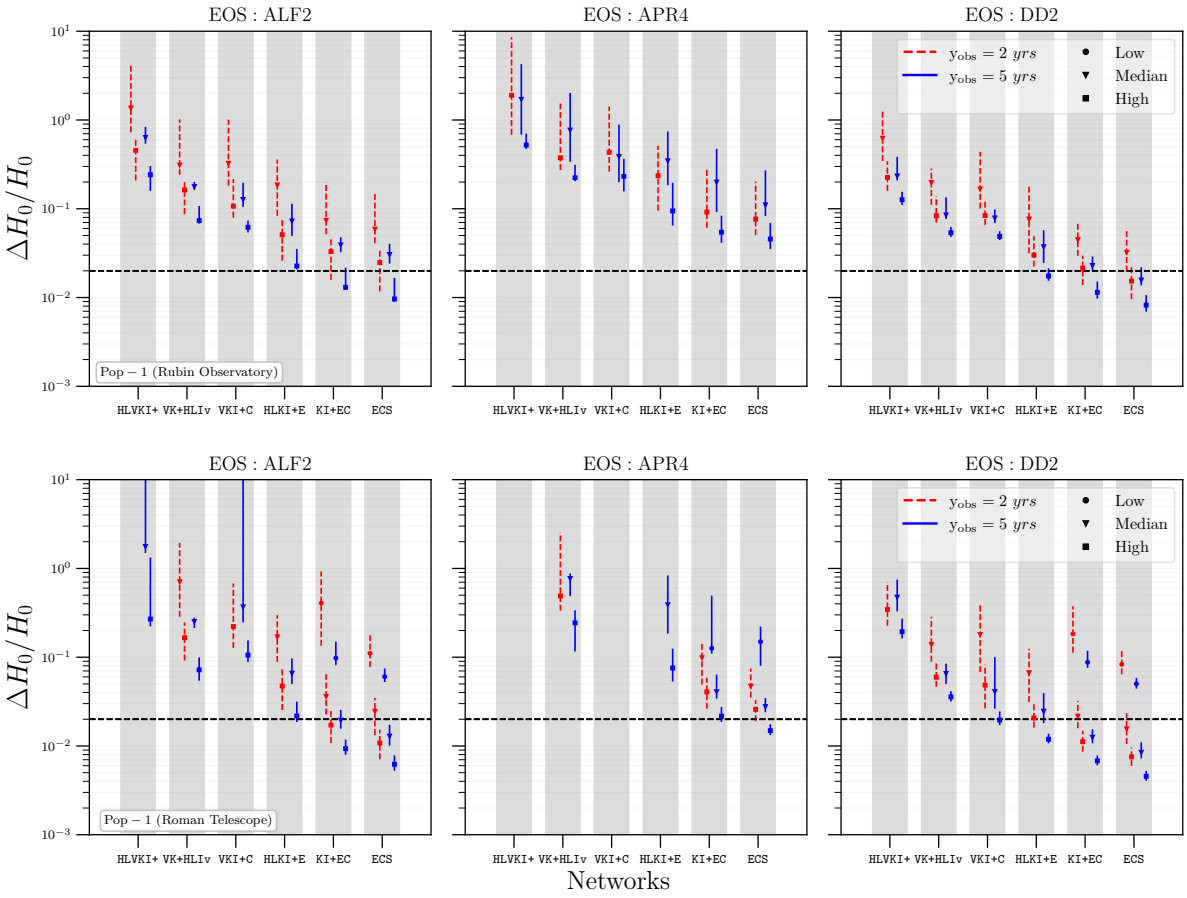

Figure 5.4: The fractional errors in H_0 measurement using NSBH systems from Pop-1 as bright sirens for the case when priors on Ω_m are *not* included.

with high BH spins and are favorable for KN generation, they have not been considered for the bright siren study. Hence, the numbers reported in this work might underestimate the actual number of detections.

Even for Pop-1, `APR4` gives the least number of KN detections and the worst bounds on H_0. For this EOS, with no prior for Ω_m, only `KI+EC` and `ECS` seem to have a chance at resolving the Hubble-Lemaître tension with Pop-1 events and KN detections with the Roman telescope. Even for the two remaining EOSs, `HLVKI+` cannot measure the Hubble-Lemaître constant better than an error of 2%, even in an observation span of 5 years. For `VK+HLIv` and `VKI+C`, the 2% mark lies outside the 68% confidence interval of the fractional error in H_0, making it improbable that these networks will resolve the Hubble-Lemaître tension in 5 years. `HLKI+E` will be capable of resolving the Hubble-Lemaître tension in 5 years of observation span, with `KI+EC` and `ECS` capable of doing the same in 2 years if the local NSBH merger rate is high. Moreover, for Pop-2 events, the

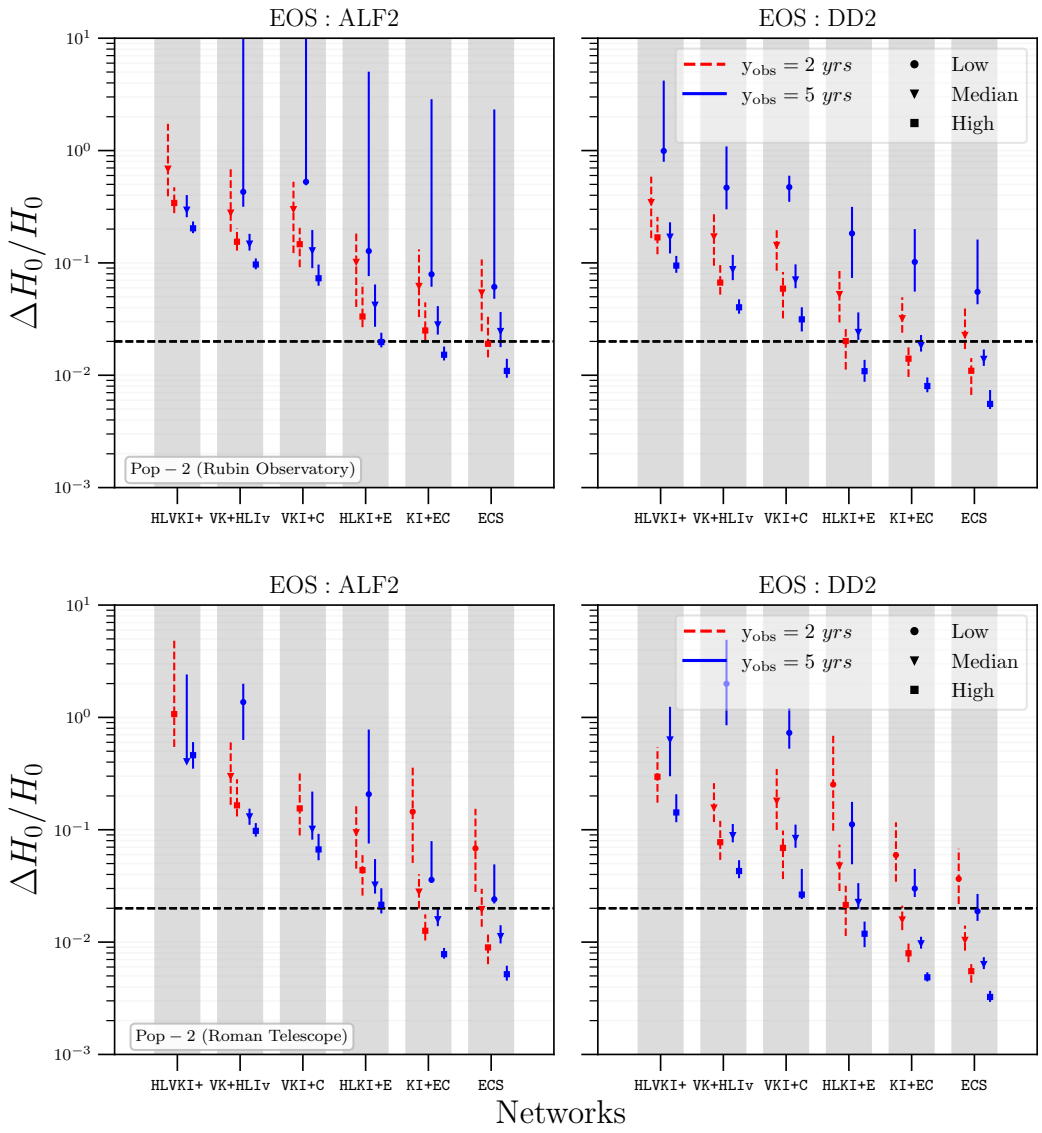

Figure 5.5: Same as Fig. 5.4 but for Pop-2.

Hubble-Lemaître tension can be resolved with the `ECS` network and the Roman telescope in 5 years of observation even if the local merger rate density of NSBH systems is on the lower end. Inclusion of the prior for Ω_m improves the errors on H_0 drastically, allowing the Voyager network to resolve the Hubble-Lemaître tension in 5 years. With Roman, both `KI+EC` and `ECS` can constrain the Hubble-Lemaître constant to better than 2% in only two years, even if the merger rate density of NSBH systems is low. When the $g + i$ TOO strategy is considered, we see that the H_0 measurement accuracy improves slightly compared to the case of Rubin, which is due to the greater number of KN detections.

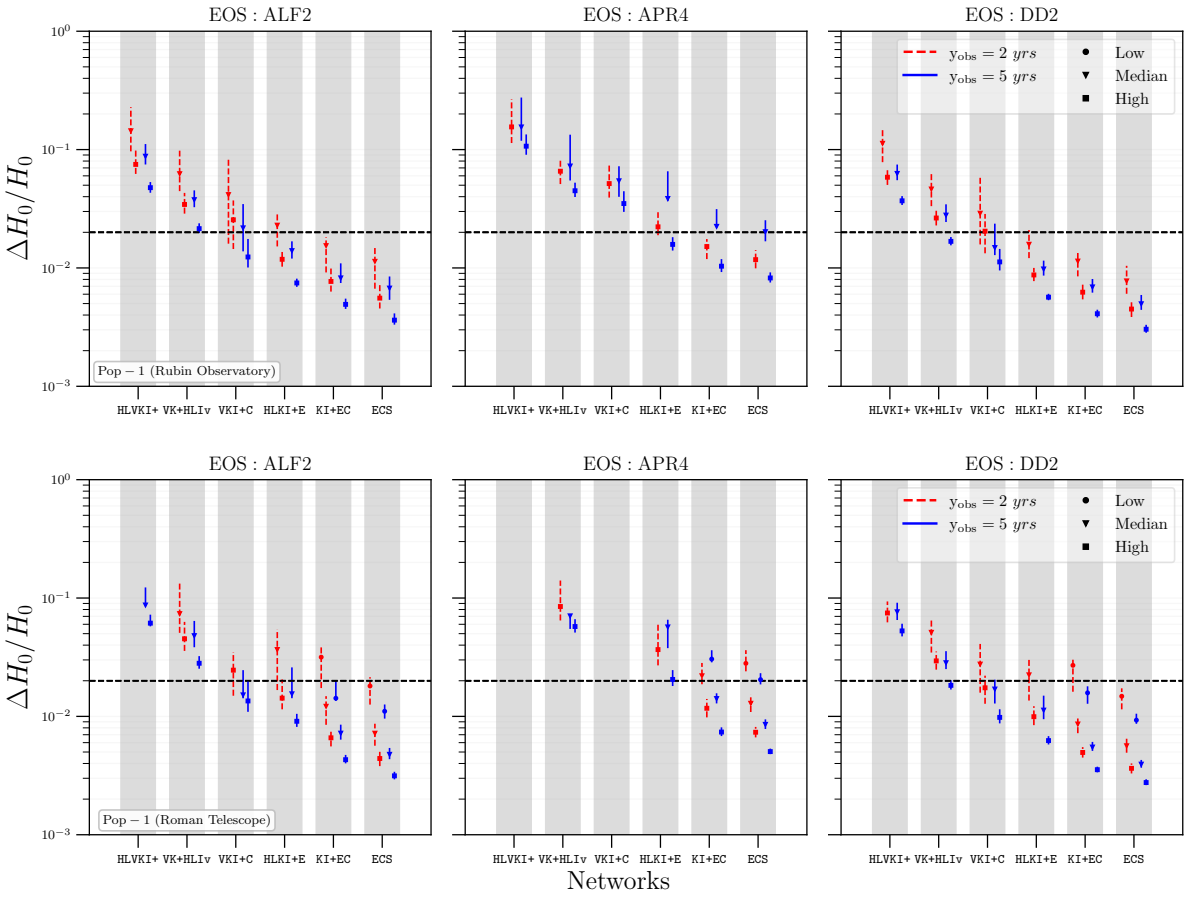

Figure 5.6: The fractional errors in H_0 measurement using NSBH systems from Pop-1 as bright sirens for the case when priors on Ω_m are included.

If using BNS systems as bright sirens, Ref. [337] finds that in 5 years of observation, the `HLV+` network (with 50% duty-cycle) with the Rubin observatory will constrain H_0 to $\sim 2\%$ with 12 bright siren observations every year. In comparison, for the best-case scenario, NSBH systems will result in a $\sim 3\%$ bound on H_0 with ~ 3 bright siren detections every year using `HLVKI+` (100% duty-cycle). With a median local merger rate ~ 8 times that of NSBH systems, BNS systems are expected to outperform NSBHs in bright siren measurements of the Hubble-Lemaître constant, unless the NSBH population contains highly spinning or precessing objects [91].

Compared to the dark siren case, we get ~ 2 times as many bright siren events detected with the Roman telescope. While these numbers are encouraging, it is crucial to note that the bright siren method relies heavily on the EOS used to describe the NS and the characteristics of the NSBH population. A soft EOS like `APR4` paired with Pop-2 results in zero KN detections, ruling out the bright siren approach for the resolution of

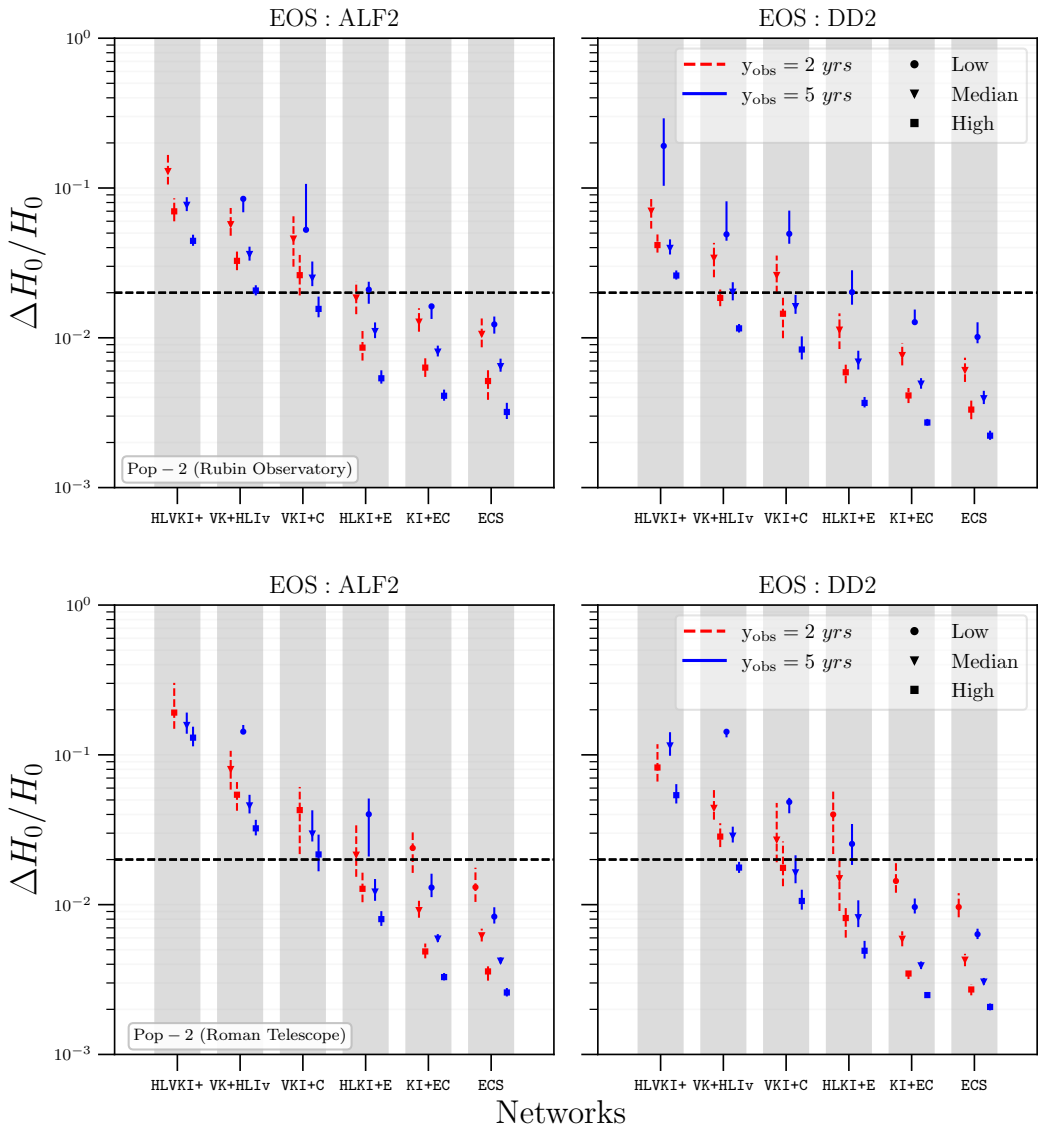

Figure 5.7: Same as Fig. 5.6 but for Pop-2.

Hubble-Lemaître constant using NSBH mergers. On the other hand, using a stiff EOS like `DD2` with either of the two populations and a high local merger rate can resolve the Hubble-Lemaître tension with `VK+HLIv` only in 2 years. Thus, the bright siren approach in resolving the Hubble-Lemaître tension is contingent on the NS EOS, the KN generation mechanism, the NSBH population characteristics, and the local merger rate density. Our treatment tries to account for some of these uncertainties by using multiple population models, EOSs, and local merger rate densities and estimating the range of measurement errors on H_0 using NSBH systems as bright sirens.

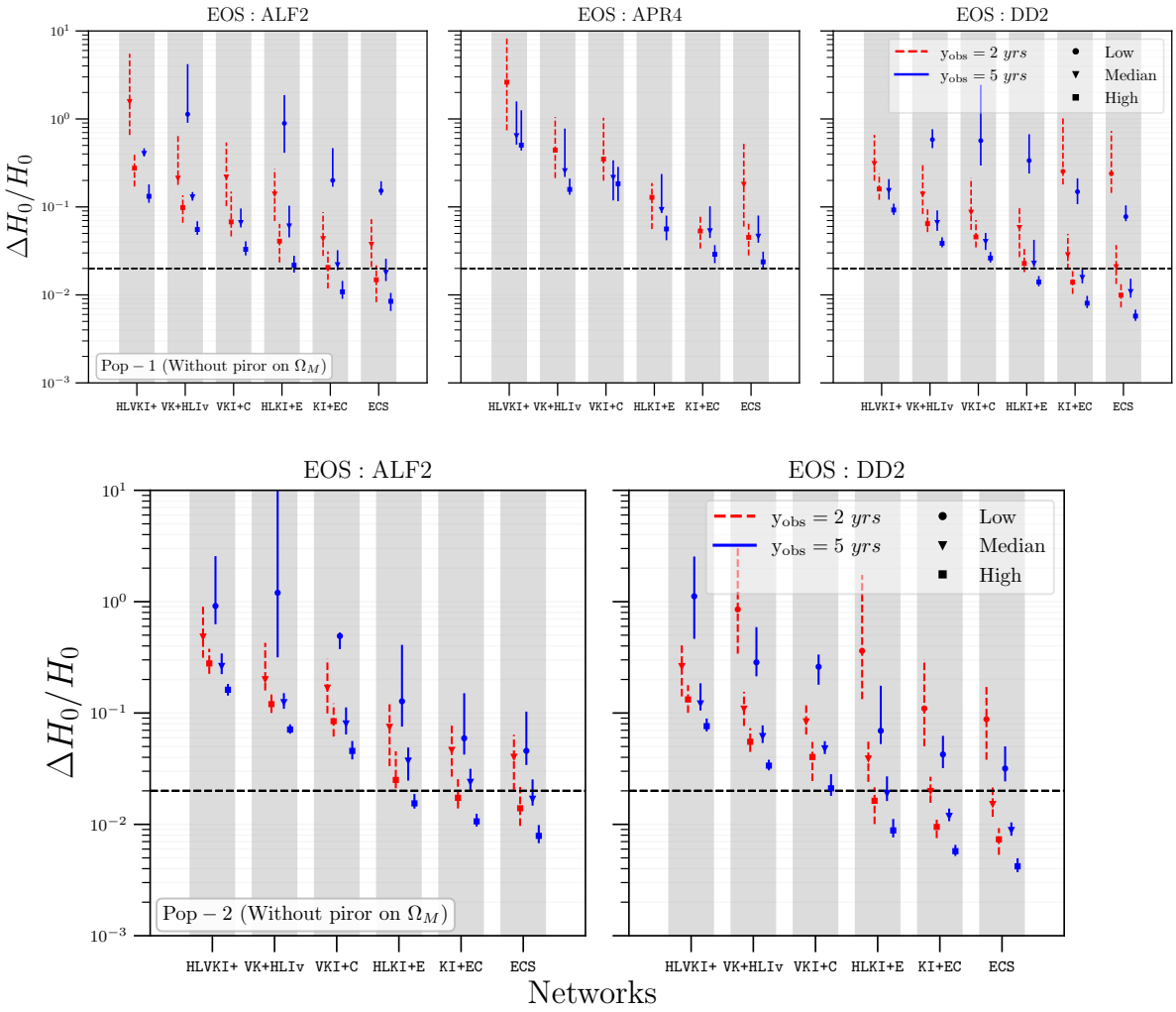

Figure 5.8: The fractional errors in H_0 measurement using NSBH systems from as bright sirens when the $g+i$ TOO strategy is followed with the Rubin observatory and priors on Ω_m are not included. The top panel shows constraints for NSBHs from Pop-1 and the bottom panel corresponds to systems from Pop-2.

5.6 Gray Sirens

In Sections 5.4 and 5.5, we evaluated the potential of NSBH systems as dark sirens and bright sirens, respectively. While networks like `HLVKI+` and `VKI+C` could not constrain the Hubble-Lemaître constant in an observation span of 5 years using the dark siren approach, the bright siren method enabled the measurement of H_0 with these detectors to better than 10% in the same observation span. Events detected by `KI+EC` and `ECS` performed well both as dark and as bright sirens. We also saw that the bright siren

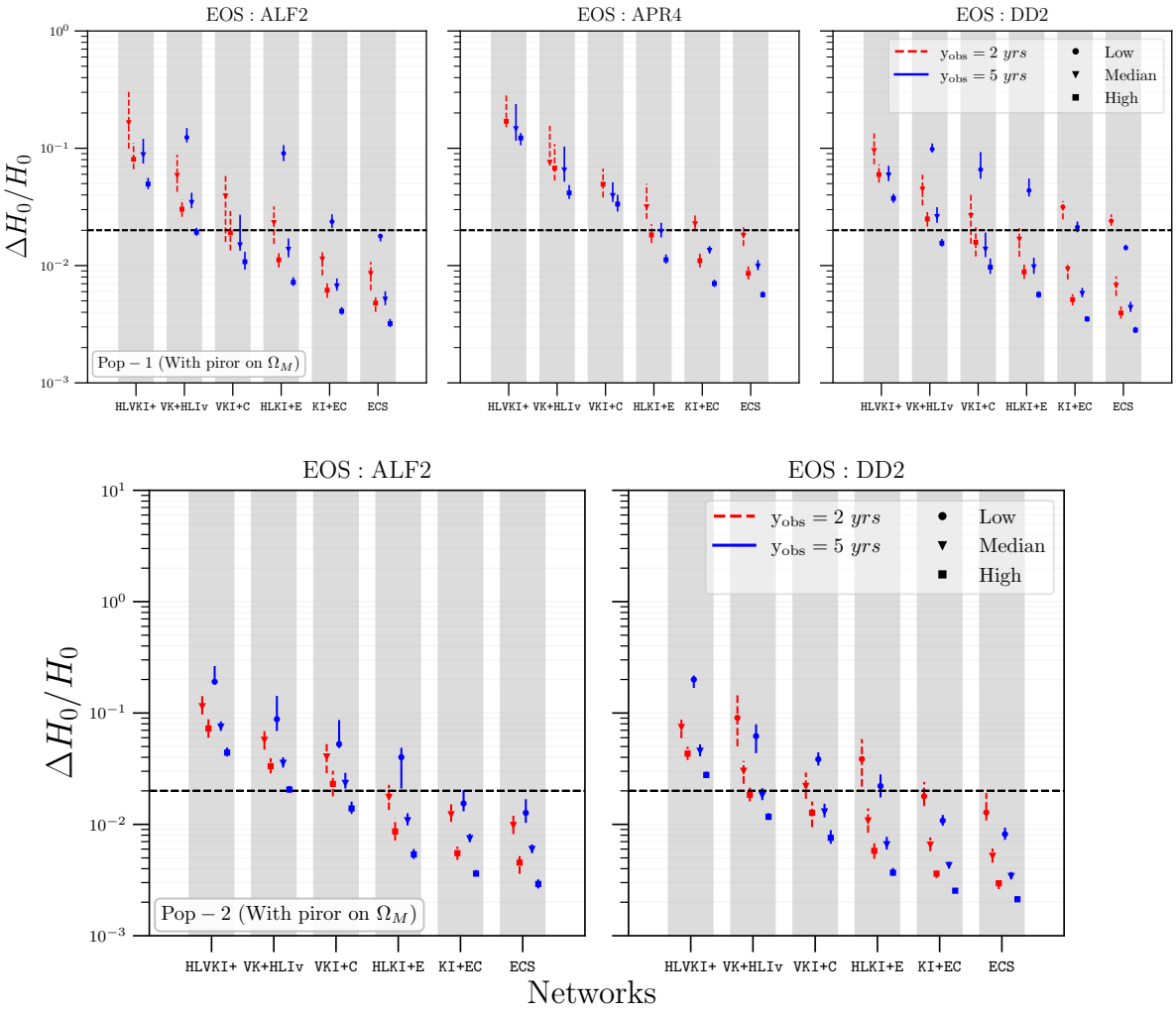

Figure 5.9: Same as Fig. 5.8 but with priors on Ω_M.

approach depends significantly on the EOS, with the worst bounds on H_0 obtained for `APR4`. The dark siren and the bright siren approaches have the same end product—measurement of the Hubble-Lemaître constant. Thus, the bounds on H_0 from both approaches can be combined to obtain a more precise measurement of H_0. This allows us to assess the utility of NSBH systems as *gray sirens*.

This is accomplished by picking events from our populations that either qualify as dark sirens or as bright sirens while making sure that we do not double-count events that can act both as dark and as bright sirens. Using the selected events, the combined FIM is calculated and used to get measurement errors on H_0 in the same way as was done in Sections 5.4 and 5.5. Figures 5.10 and 5.11 present the bounds on the Hubble-Lemaître constant measurement using the gray siren approach without and with prior on Ω_m,

Table 5.6: Number of bright sirens and golden events detected using the $g+i$ TOO strategy with Rubin in an observation span of 10 years, for ALF2 (A2), APR4 (A4), and the DD2 (D2) EOSs. The KN considered correspond to events that can be localized better than the FOV of Rubin using GW observations.

Type	Bright Sirens			Golden Events		
EOS	A2	A4	D2	A2	A4	D2
Pop-1						
HLVKI+	12^{+24}_{-11}	6^{+4}_{-5}	23^{+38}_{-21}	0	0	0
VK+HLIv	23^{+45}_{-19}	8^{+12}_{-7}	40^{+72}_{-33}	0	0	0
VKI+C	15^{+32}_{-13}	6^{+7}_{-5}	31^{+58}_{-26}	1^{+1}_{-1}	0	1^{+1}_{-1}
HLKI+E	25^{+58}_{-22}	10^{+22}_{-9}	43^{+91}_{-37}	1^{+2}_{-1}	0	2^{+3}_{-2}
KI+EC	39^{+81}_{-33}	12^{+29}_{-10}	60^{+126}_{-51}	4^{+12}_{-4}	0^{+3}_{-0}	6^{+19}_{-6}
ECS	40^{+82}_{-33}	12^{+29}_{-10}	65^{+131}_{-54}	8^{+23}_{-8}	2^{+9}_{-2}	13^{+35}_{-13}
Pop-2						
HLVKI+	18^{+23}_{-15}	0	34^{+51}_{-28}	0	0	0
VK+HLIv	25^{+47}_{-21}	0	58^{+111}_{-49}	0	0	0
VKI+C	24^{+35}_{-21}	0	46^{+82}_{-39}	0	0	0^{+2}_{-0}
HLKI+E	28^{+53}_{-24}	0	68^{+134}_{-58}	1^{+6}_{-1}	0	4^{+10}_{-4}
KI+EC	32^{+78}_{-26}	0	89^{+201}_{-72}	5^{+18}_{-3}	0	14^{+38}_{-11}
ECS	32^{+80}_{-26}	0	90^{+212}_{-73}	7^{+24}_{-5}	0	23^{+59}_{-19}

respectively. Figure 5.12 gives the constraints that can be put on the value of H_0 with gray sirens when the $g+i$ TOO strategy with Rubin is followed.

In Section 5.5, we noted that for Pop-2 events and `APR4` as the EOS we did not expect any KN events, rendering the bright siren approach moot. However, the NSBH dark siren events can still be used to constrain H_0. This is evident from the bottom two panels of Figs. 5.10 and 5.11, where H_0 is constrained better than 2% with `KI+EC` and `ECS` when the prior for Ω_m is not included, and also by `HLKI+E` when the prior is included. For the stiffer EOS, we see that all detector networks except `HLVKI+` have a chance to resolve the Hubble-Lemaître tension. The Voyager network might be able to resolve it in 5 years if the local merger rate is high. `KI+EC` and `ECS` will be able to resolve it in $2-5$ years regardless of the merger rate. As was the case for NSBH bright sirens, the

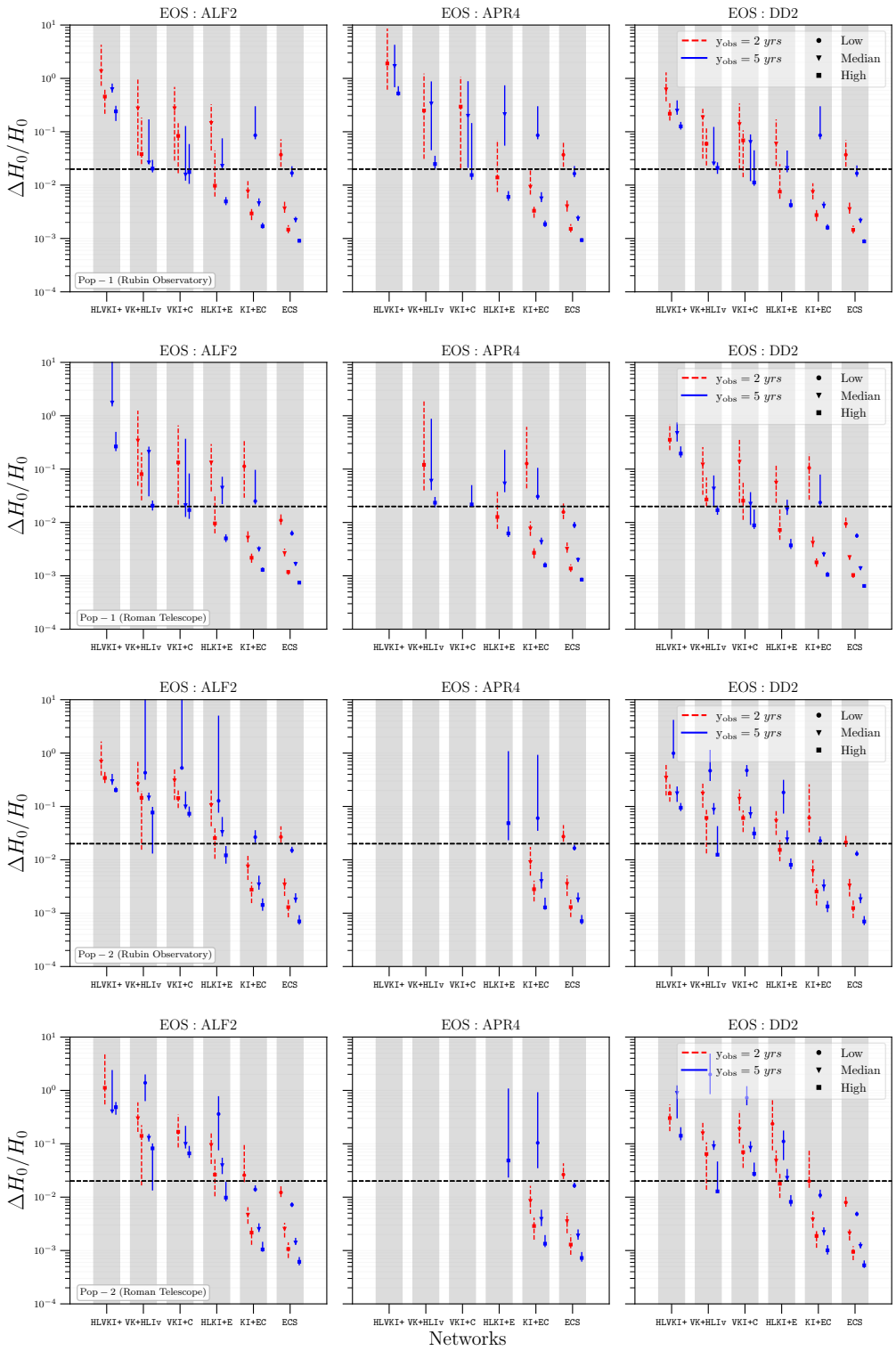

Figure 5.10: The fractional errors in H_0 measurement using NSBH systems as gray sirens for the case when priors on Ω_m are *not* included. The top two panels show the errors for events in Pop-1 and the bottom two panels show the errors for Pop-2.

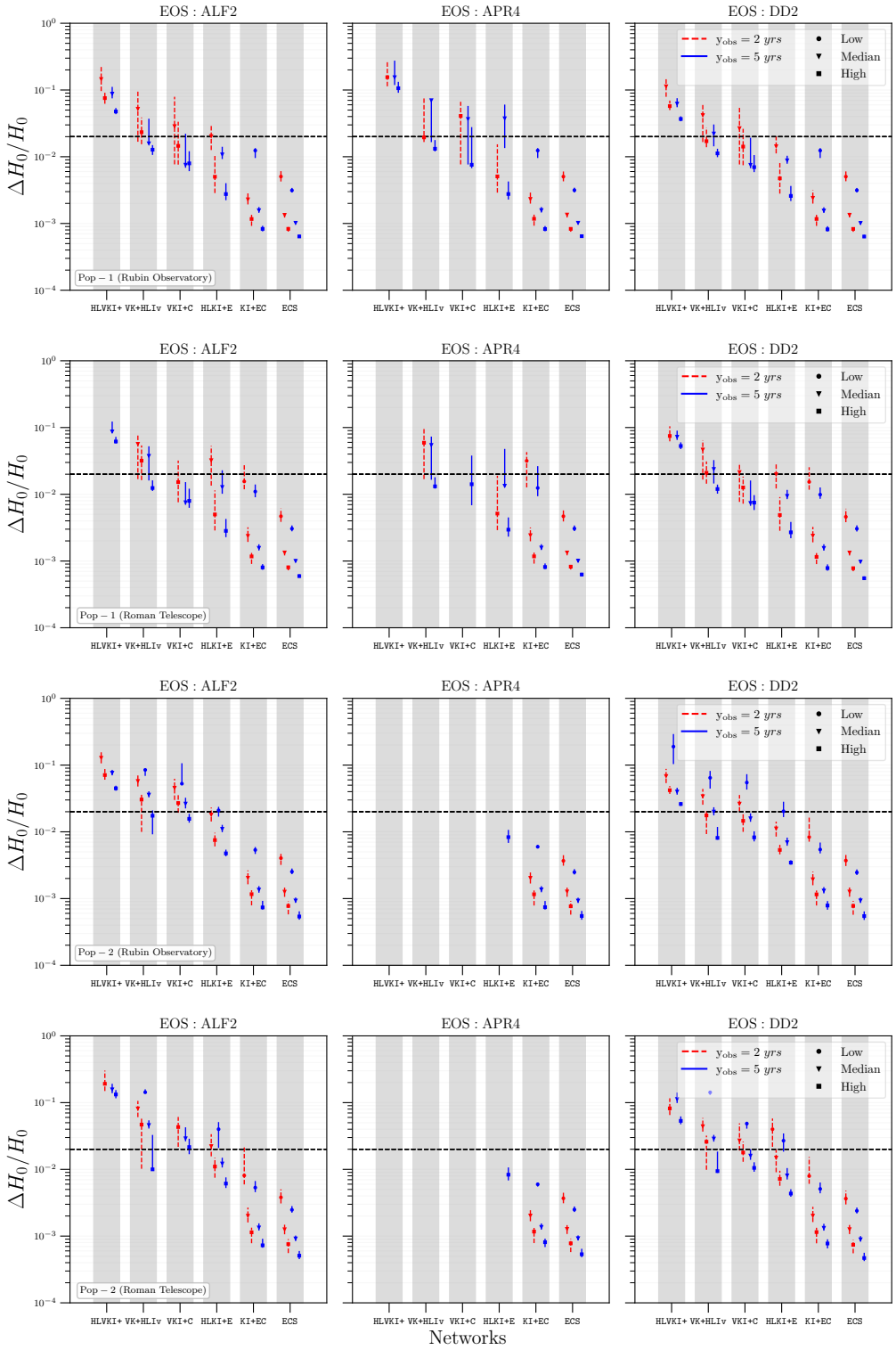

Figure 5.11: The fractional errors in H_0 measurement using NSBH systems as gray sirens for the case when priors on Ω_m are included. The top two panels show the errors for events in Pop-1 and the bottom two panels show the errors for Pop-2.

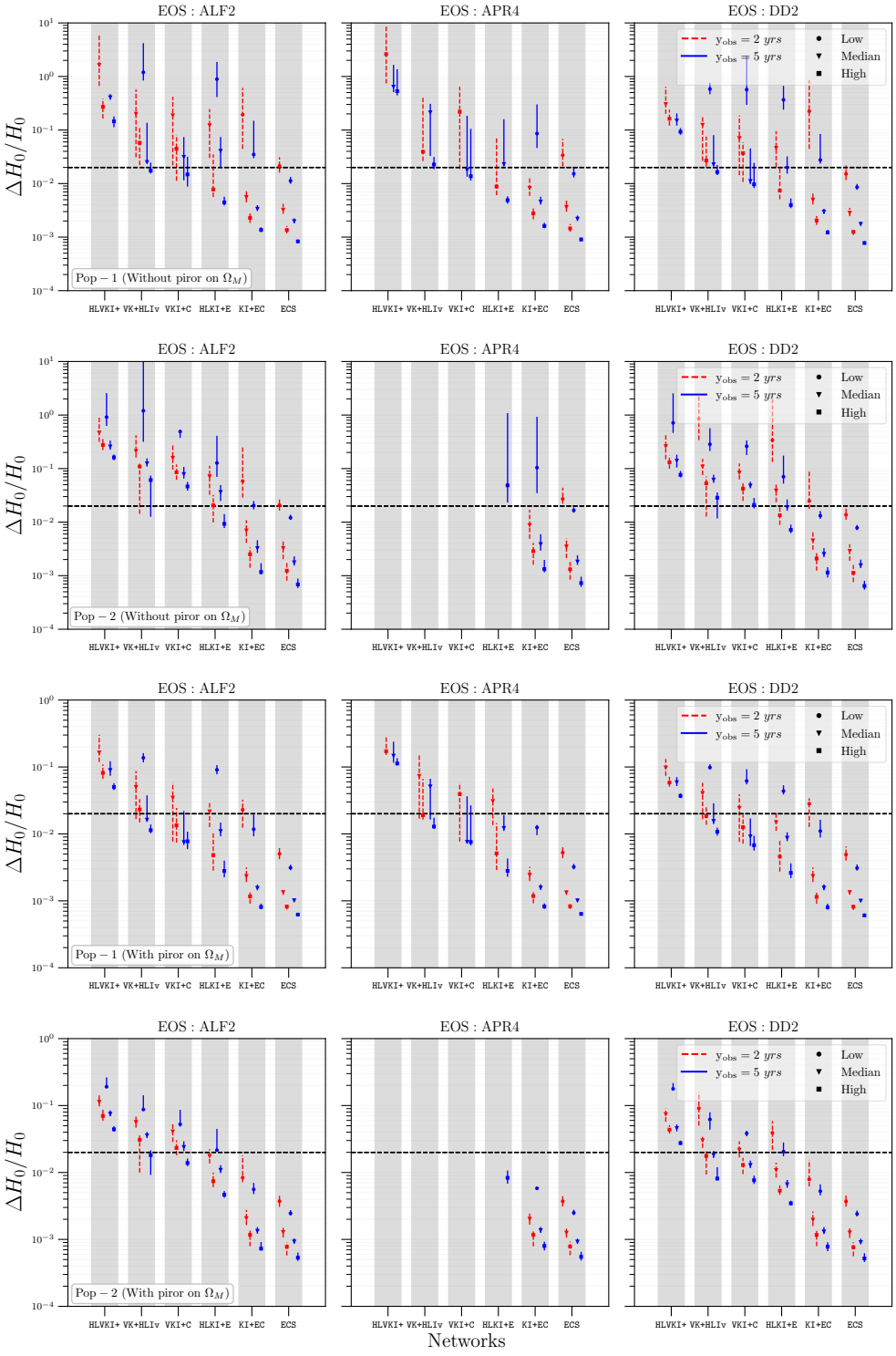

Figure 5.12: The measurement accuracy of H_0 using NSBH systems as gray sirens where the KN are detected using the $g + i$ TOO strategy. The top two panels show the errors for events in Pop-1 and Pop-2 when prior on Ω_m is not included, and the bottom two panels show the errors when prior on Ω_m is included.

Table 5.7: The number of detections using the gray siren approach, i.e., combining the dark and the bright sirens in an observation span of 10 years. For the bright sirens detected with the Rubin $r-$filter and Roman $R-$filter, we only consider events for which $\Omega_{90} \leq 10\times$FOV of the respective telescope. For bright sirens detected with Rubin telescope following the $g+i$ TOO strategy, we consider events for which $\Omega_{90} \leq$FOV of Rubin.

Filter	Rubin $r-$filter			Roman $R-$filter			Rubin $g+i$ TOO		
EOS	ALF2	APR4	DD2	ALF2	APR4	DD2	ALF2	APR4	DD2
Pop-1									
HLVKI+	9^{+16}_{-8}	4^{+5}_{-3}	16^{+28}_{-15}	3^{+4}_{-3}	1^{+0}_{-1}	6^{+7}_{-6}	12^{+24}_{-11}	6^{+4}_{-5}	23^{+38}_{-21}
VK+HLIv	15^{+27}_{-14}	5^{+11}_{-4}	24^{+44}_{-23}	9^{+18}_{-9}	4^{+7}_{-4}	20^{+44}_{-20}	24^{+47}_{-20}	9^{+14}_{-8}	41^{+74}_{-34}
VKI+C	15^{+26}_{-14}	5^{+10}_{-4}	24^{+43}_{-23}	4^{+6}_{-4}	2^{+2}_{-2}	10^{+19}_{-10}	16^{+33}_{-14}	7^{+8}_{-6}	32^{+59}_{-27}
HLKI+E	15^{+30}_{-14}	5^{+14}_{-4}	24^{+47}_{-23}	16^{+33}_{-15}	6^{+12}_{-5}	27^{+66}_{-26}	26^{+63}_{-23}	11^{+27}_{-10}	44^{+96}_{-38}
KI+EC	38^{+80}_{-35}	28^{+64}_{-25}	47^{+97}_{-44}	80^{+155}_{-67}	45^{+91}_{-37}	124^{+248}_{-106}	63^{+136}_{-55}	36^{+84}_{-32}	84^{+181}_{-73}
ECS	119^{+260}_{-103}	110^{+247}_{-94}	126^{+276}_{-110}	193^{+392}_{-158}	139^{+298}_{-116}	259^{+527}_{-216}	145^{+317}_{-123}	118^{+267}_{-101}	168^{+365}_{-142}
Pop-2									
HLVKI+	16^{+18}_{-14}	0	31^{+41}_{-26}	3^{+5}_{-2}	0	6^{+12}_{-4}	18^{+23}_{-15}	0	34^{+51}_{-28}
VK+HLIv	19^{+31}_{-16}	0^{+1}_{-0}	37^{+83}_{-31}	16^{+22}_{-12}	0^{+1}_{-0}	29^{+44}_{-24}	25^{+48}_{-21}	0^{+1}_{-0}	58^{+112}_{-49}
VKI+C	20^{+30}_{-17}	0	38^{+83}_{-32}	7^{+10}_{-5}	0	14^{+21}_{-11}	24^{+35}_{-21}	0	46^{+82}_{-39}
HLKI+E	20^{+33}_{-17}	0^{+3}_{-0}	38^{+87}_{-32}	22^{+45}_{-17}	0^{+3}_{-0}	44^{+87}_{-36}	28^{+56}_{-24}	0^{+3}_{-0}	68^{+137}_{-58}
KI+EC	45^{+101}_{-38}	25^{+71}_{-21}	63^{+155}_{-53}	104^{+244}_{-85}	25^{+71}_{-21}	185^{+401}_{-153}	57^{+149}_{-47}	25^{+71}_{-21}	114^{+272}_{-93}
ECS	123^{+270}_{-102}	103^{+241}_{-85}	140^{+319}_{-116}	218^{+502}_{-177}	103^{+241}_{-85}	349^{+747}_{-286}	135^{+320}_{-111}	103^{+241}_{-85}	192^{+447}_{-157}

adoption of the $g+i$ TOO strategy results in slightly better bounds compared to the case of Rubin discussed above, due to the increase in the number of KN detections. An important difference is that with the $g+i$ strategy, the Voyager network might be able to resolve the H_0 tension in 5 years even when the NSBH merger rate is not high, and instead, it is close to the median value.

Table 5.7 gives the number of NSBH detections that have been considered for the gray siren method, i.e., each event is either a dark siren, a bright siren, or both. As is evident when comparing the number of dark sirens in Table 5.3 and bright sirens in

Tables 5.5 and 5.6 to the gray siren events in Table 5.7, there are very few ($\sim \mathcal{O}(1)$) events that qualify as both dark and bright sirens. So, the square root of the sum of squares of the errors obtained from the dark and the bright siren approach is a good approximation of the expected measurement errors using the gray siren method.

An important use of the numbers reported in Table 5.7 and the Figs. 5.10 and 5.11 is to account for the change in the measurement errors of H_0 with the inclusion of factors that we have ignored. This is done by using the fact that the bounds on H_0 change approximately as $\sqrt{N}$, where N is the number of detections. For e.g., with the assumed 100% duty-cycle, the `A+` network with `DD2` as the EOS and Pop-2 events has a measurement error of 2.7% associated with the high local merger rate density, in an observation span of 5 years (see the plot in the third row and third column of Fig. 5.11). Now, if we assume a 50% duty-cycle, the measurement error increases to $2.7\% \times \sqrt{2} = 3.8\%$. As can be verified from the same plot, this is close to the error corresponding to a high merger rate and an observation span of 2 years with 100% duty-cycle. As another example, let us assume that the actual stiffness of the NS is somewhere in between that of `ALF2` and `DD2` and we observe 24 Pop-2 bright siren events with the `A+` network and Rubin in 10 years with median merger rate, which equates to 12 events in 5 years of observation. With `DD2`, we get 31 events in 10 years (from Table 5.5), or 16 events in 5 years, which corresponds to $\sim 4\%$ error in H_0 measurement (as there are no dark siren events for this network, we can use the plot in the third row and third column of Fig. 5.11 itself). Having 12 events instead of 16 in a span of 5 years would give the median error on H_0 for the assumed EOS and the `HLVKI+` network to be $\sim 5\%$. Following these steps, one can calculate the expected constraints on the Hubble-Lemaître constant using the gray siren approach with NSBH systems for different merger rates, observation times, duty cycles, the efficiency of the two telescopes in the detection of the EM counterpart, change in the exposure times for the telescopes, NS EOS, etc.

5.7 Conclusions

The tension between the early-universe and late-universe measurements of the Hubble-Lemaître constant has been an active area of research in cosmology and GW physics. The ability of GW observations to measure the luminosity distance without the need for an extra distance calibrator can be utilized to obtain an independent measure of the distance to the binary system. The measurement of luminosity distance from GW observation along with the value of the corresponding redshift from host-galaxy identification can

provide an independent estimate of the Hubble-Lemaître constant and help resolve the tension in H_0. The host can be identified by using an EM counterpart (if there is one), which is called the bright siren method, or without the EM counterpart, which is referred to as the dark siren method. BBH systems are heavier than BNS or NSBH systems and are detected with higher SNRs. For asymmetric BBHs, the activation of higher modes further improves parameter estimation, especially for the luminosity distance. This makes BBH systems ideal dark sirens. On the other hand, most, if not all, BNS systems are expected to be followed by EM counterparts. The detection of the EM counterpart can pinpoint the host galaxy and provide the redshift measurement needed to constrain H_0. Additionally, higher-mode activation in the post-merger of BNS systems can improve the luminosity distance measurement [336]. Thus, BNS systems are ideal bright siren candidates for H_0 measurement.

In this work, we assessed the potential of NSBH systems in resolving the H_0 tension. We obtained the measurement errors in luminosity distance using the FIM method with `GWBENCH`. We combined the FIM for multiple qualifying events to calculate the constraints that can be placed on the value of H_0 (assuming ΛCDM cosmology) using several GW detections. We performed this analysis for six ground-based GW networks (listed in Table 5.1), two population models: Pop-1 and Pop-2, three values of NSBH local merger rate densities: *low*- 7.8 $\mathrm{Gpc}^{-3}\ \mathrm{yr}^{-1}$, *median*- 45 $\mathrm{Gpc}^{-3}\ \mathrm{yr}^{-1}$ and *high*- 140 $\mathrm{Gpc}^{-3}\ \mathrm{yr}^{-1}$, two observation spans: 2 years and 5 years, and for two cases: without prior on Ω_m and with prior on Ω_m.

Due to asymmetric masses, NSBH systems can be used as dark sirens to resolve the Hubble-Lemaître tension. However, as was noted in Section 5.4, BBH systems are much more efficient as dark sirens and can constrain H_0 to less than 2% with 2 years of observations with the `HLVKI+` network [59]. While there is no hope of resolving the Hubble-Lemaître tension with NSBH dark sirens with the `HLVKI+` network, the Voyager network, `VK+HLIv`, can measure H_0 to less than 2% measurement uncertainty in an observation span of 5 years. More advanced networks like `KI+EC` and `ECS` can measure H_0 to a precision better than 1% with only 2 years of observation (see Fig. 5.3). Moreover, the `ECS` network will observe $\mathcal{O}(10)$ golden dark siren events, i.e., events that can individually measure H_0 with measurement uncertainty less than 2%, every year.

NSBH mergers can also be accompanied by EM counterparts, like short gamma-ray bursts and kilonovae (KN), rendering them as possible bright siren candidates for H_0 measurement. In Tables 3.5 and 3.6, we reported the number of expected KN detections using two telescopes: the Vera C. Rubin Observatory and the Nancy Grace Roman Space

Telescope, for three NS EOS of varying stiffness: `ALF2`, `APR4` and `DD2`, in an observation span of 10 years. We saw that the constraints on H_0 using the bright siren approach depend on population characteristics and the NS EOS (see Figs. 5.4, 5.5, 5.6, 5.7, 5.8 and 5.9). While H_0 could not be measured with any of the networks for Pop-2 events with the `APR4` EOS, networks with the Einstein Telescope or the Cosmic Explorer detectors could resolve the tension with Pop-1 events. For the other two EOS, it seemed unlikely that `HLVKI+` will be able to resolve the tension in 5 years, with the best measurement of H_0 having a fractional error of 2.6%. With Voyager sensitivity, `VK+HLIv` can resolve the tension in 5 years and `KI+EC` and `ECS` will be able to measure H_0 to better than 1% precision only in 2 years. We also expect `ECS` to detect $\mathcal{O}(1)$ golden bright siren events every year. However, based on our results, NSBHs cannot be expected to overtake BNS systems as bright sirens for H_0 measurement, as the BNS systems are expected to resolve the H_0 tension within 5 years with the `HLV+` network [337]. Note that our population models do not consider precessing NSBH systems. Precession can improve the distance measurement from NSBH systems and make them at par with BNS systems in the context of H_0 measurement [91].

In both dark and bright siren approaches, we expect to detect $\mathcal{O}(10)$ events every year with `ECS` that contribute towards the measurement of the Hubble-Lemaître constant. Due to the effectiveness of NSBH both as dark and as bright sirens, we refer to them as gray sirens. In Section 5.6, we combined the dark and bright siren events to calculate constraints on H_0. While it is still unlikely that `HLVKI+` will be able to resolve the Hubble-Lemaître tension in 5 years, `VK+HLIv` is expected to resolve it in the same duration (see Figs. 5.10, 5.11 and 5.12). Even for `APR4`, `HLKI+E`, `KI+EC` and `ECS` will be able to resolve the H_0 tension. With `ECS`, it would be possible to detect 10–30 NSBH gray (dark, bright, or both) siren events every year.

Several systematic uncertainties are associated with the measurement of H_0 using GWs. These include uncertainty due to instrumental calibration errors [273, 275], peculiar velocity fields [326, 338–340] and viewing angle [341]. The calibration errors can lead to a systematic error and uncertainty of $< 7\%$ in the amplitude of the GW [273] and are expected to reduce in future networks. The uncertainty in redshift measurement due to peculiar velocity associated with the host galaxy is dominant only for nearby galaxies. For example, for GW170817 which was $z \sim 0.01$ away, the uncertainty in peculiar velocity was 150 km/s, leading to a $\sim 5\%$ uncertainty in redshift measurement [329]. Most of the events considered in this study lie farther away compared to GW170817, for e.g., for dark sirens detected by `ECS`, $\sim 90\%$ of the events lie beyond $z = 0.05$, i.e., 5 times as far away

as GW170817. The nearest event considered in the study is twice as far as GW170817. Thus, we do not expect the effect of peculiar velocity uncertainties to considerably change the overall expectation regarding the resolution of H_0 with a particular GW network. Another source of systematic uncertainty is due to the viewing angle dependence of the detection of EM counterparts [341]. In particular, the models used to generate luminosity curves for KN for events in this study assume spherically symmetric emission. Viewing angle dependence can change the peak luminosity associated with a KN, which will affect the number of detections that have been reported in Tables 5.5, 5.6, 5.7, 5.7, 3.5 and 3.6. Even though we do not account for the possible aspherical nature of EM emission, the effect on the H_0 constraints can be calculated if the model describing the dependence of viewing angle on KN luminosity is known. For a suitable model, we can calculate the change in the number of KN detections. Using the $\sim \sqrt{N}$ dependence of H_0 bounds on the number of events N, we can use the numbers in Tables 5.5, 5.6, and 5.7, along with the measurement errors on H_0 from Figs. 5.4, 5.5, 5.6, 5.7, 5.8, 5.9, 5.10, 5.11, and 5.12 to approximately calculate the new bounds on H_0 (see Section 5.6 for examples of using this technique).

In this work, we saw that NSBH systems can be important sources for independent calculation of the Hubble-Lemaître constant and can resolve the Hubble-Lemaître tension as early as the Voyager era (∼mid 2030s). While our analysis relies on the FIM, it is the first comprehensive study that presents the expectation regarding the measurement of H_0 with NSBH systems and XG detectors using both dark and bright siren approaches. In the current work, we account for several uncertainties associated with NSBH systems by including two different population models, three local merger rates, two observation spans, and six ground-based GW detectors. We also give the associated number of events used and bounds on H_0 for all possible cases to allow the reader to extrapolate approximate bounds on H_0 for a general scenario. For the bright and gray siren methods, we generated KN light curves for three EOS using numerical relativity fits to portray a realistic picture of the scope of these methods. A possible direction for future work can be to use multiple KN models that include the viewing angle dependence to gauge its effect on the number of KN detections. Another important extension would be to repeat this analysis within a Bayesian framework. Historically, using Bayesian inference for a large number of events has been tedious, leading to the inclination toward FIM analysis for large-scale studies. With the introduction of new techniques for parameter estimation [257, 262, 342], the goal of implementing a fully-Bayesian study might be within reach.

Declaration

The author of this dissertation was responsible for generating all the results that are presented in this chapter. The contents of this chapter have been published in the journal Monthly Notices of the Royal Astronomical Society by Oxford University Press with reference [61].

Chapter 6
Conclusions and outlook

With increasing distance, our knowledge fades, and fades rapidly.
Eventually, we reach the dim boundary, the utmost limits of our telescopes.
There, we measure shadows, and we search among ghostly errors of measurement
for landmarks that are scarcely more substantial. The search will continue.
Not until the empirical resources are exhausted, need we pass
on to the dreamy realms of speculation.
— Edwin Hubble

This dissertation has explored the scientific promise of NSBH mergers as probes of GW astrophysics, multi-messenger astronomy, and cosmology in the era of advanced and next-generation detectors.

We began by assessing the detectability and measurability of NSBH mergers in future GW detector networks. Our results show that next-generation observatories such as Cosmic Explorer (CE) and Einstein Telescope (ET) will detect the vast majority of NSBH mergers out to redshifts $z \sim 2$, thereby ensuring high completeness that is vital for unbiased inference. Through detailed network comparisons, we established that while a single third-generation detector can provide good sensitivity, networks with multiple XG detectors significantly enhance localization capabilities. Particularly, networks with CE and ET can localize tens of thousands of events to within $10\,\mathrm{deg}^2$, and a smaller fraction to within $1\,\mathrm{deg}^2$, enabling electromagnetic follow-up for sources within $z \lesssim 0.5$. These results confirm that NSBH systems will not only be observed in large numbers, but will also be accompanied by precise parameter measurements that are necessary for probing their origin and implications.

In the context of multi-messenger astronomy, we analyzed the detectability of KN emission resulting from NSBH mergers. The KN brightness is highly sensitive to binary mass ratio, black hole spin, and the neutron star EOS. While stiff EOS and high black hole spin enhance the likelihood of forming bright KNe, our simulations indicate that

even in optimistic scenarios, the number of detectable KNe is limited to a few per year. A case study of GW230529, the most mass-symmetric NSBH candidate in the LVK O4 run, showed that its expected KN would be too dim for Rubin Observatory's wide-field detection. Nevertheless, targeted follow-up may still have been successful. We further demonstrated that only XG detector networks can deliver sky localizations of $\lesssim 100\,\mathrm{deg}^2$ minutes before merger, making them crucial for capturing early-time electromagnetic signals that can shed light on the nature of the remnant and the merger environment.

We then investigated how NSBH mergers can constrain astrophysical formation channels. Specifically, we focused on the measurability of the neutron star spin $\chi_{\rm NS}$, which can serve as a fossil record of the binary's evolutionary history. Using Bayesian inference and waveform models that include higher-order modes, we demonstrated that $\chi_{\rm NS}$ can be tightly constrained in systems where the black hole is rapidly spinning and the inclination angle is high. Inclusion of higher modes mitigates degeneracies with other parameters and significantly improves spin measurements. In particular, CE and ET can distinguish $\chi_{\rm NS} = 0.1$ from zero in $\mathcal{O}(100)$ events per year. Shifting to current detectors, we applied population synthesis-informed priors to GW230529, finding that it is consistent with formation via isolated binary evolution, while ruling out scenarios involving rapid supernovae or unstable Case BB mass transfer. These results highlight how precise estimation of NSBH binary parameters will allow the inference of their astrophysical histories.

In the final part of this dissertation, we assessed the use of NSBH mergers as standard sirens for cosmology. Combining dark and bright siren approaches, we explored the gray siren framework in which a fraction of events yield electromagnetic counterparts while others contribute through unique host-galaxy identification. Using Fisher Information Matrix analysis, we forecast constraints on the Hubble-Lemaître constant H_0 under a range of population models, merger rates, and observing durations. We found that Voyager-era (similar to $A^\sharp$; early 2030s) networks could reach percent-level H_0 constraints within 5 years, while CE-ET networks could achieve sub-percent precision within just 2 years. We also incorporated light curve models from numerical relativity fits for three EOS to predict KN detectability. Altogether, we showed that NSBH mergers can provide an independent and competitive avenue for resolving the current Hubble tension, particularly when used in conjunction with other GW sources.

While this dissertation has explored the potential of NSBH mergers as sources of electromagnetic radiation, several open questions remain. Although a KN was observed following the BNS GW170817, no KN has yet been definitively associated with an NSBH

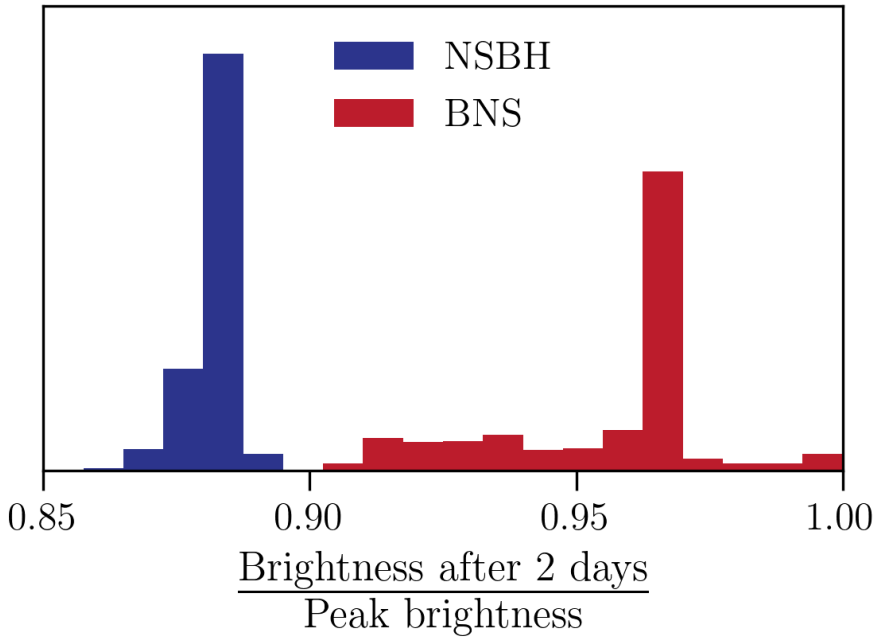

Figure 6.1: The histograms for the ratio of the peak luminosity of the KNe in the $u-$band ($\sim$ 3500 Å) with the luminosity in the band 2 days after the peak, for a simulated population of 10,000 BNS and NSBH mergers.

event, despite multiple detections. This leaves unresolved the contribution of NSBH mergers to heavy-element formation. Recent studies suggest that BNS mergers alone may be insufficient to account for r-process enrichment in the Milky Way [343], making it interesting to determine whether NSBH systems play a significant role in the same. Associating KNe with GW events remains observationally challenging due to limitations in detector duty cycles, sky localization, and the latency of EM alerts. As a result, developing a method to identify the origin of a KN from electromagnetic data alone would be invaluable. Motivated by the differing morphologies of BNS and NSBH mergers, one promising avenue involves distinguishing their KNe using light curve features. In ongoing work, we employ the semi-analytical formalism described in Chapter 3 and Ref. [161] to simulate KN light curves from NSBH and BNS mergers. Inspired by Ref. [344], we calculate the ratio of the u-band (mAB) brightness two days post-peak to the peak brightness for each event. The resulting distribution, shown in Fig. 6.1, reveals clear separation between KNe from NSBH and BNS systems, suggesting that they occupy distinct regions in this parameter space. This motivates a comprehensive study of KN morphologies—including viewing angle dependence and simulation-based modeling—to

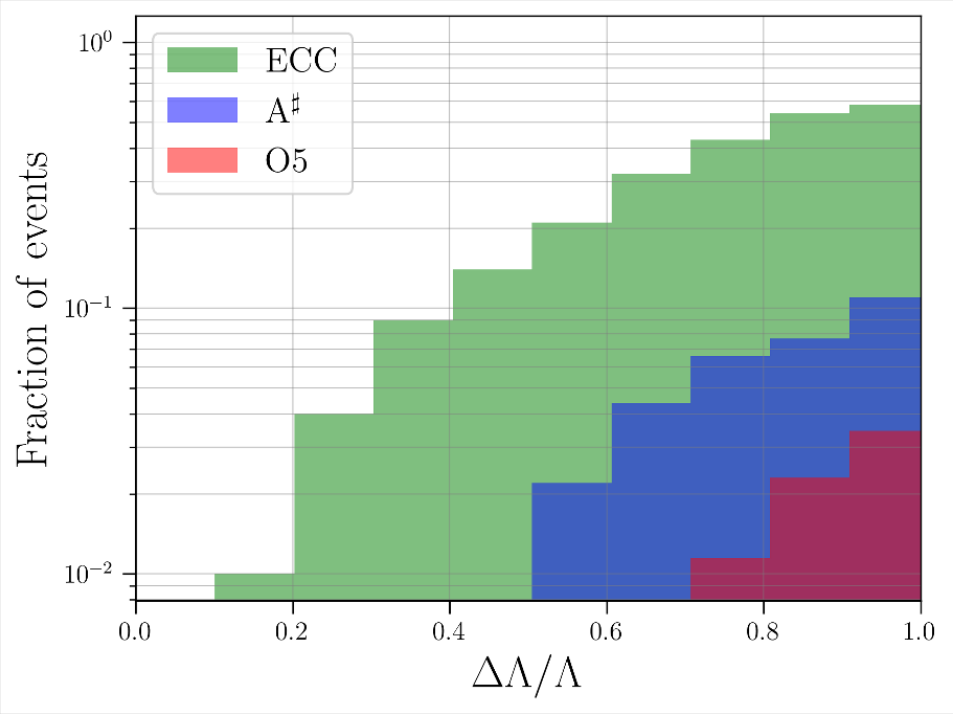

Figure 6.2: A cumulative density function plot of the fraction of NSBH detections (within $z < 0.2$) with different generations of GW observatories and the corresponding (1σ) measurement uncertainty on the tidal deformability parameter of the neutron star.

enable confident classification of KNe in the absence of a GW detection.

As discussed, the higher modes in GW signals from NSBH systems enhance estimates of the component masses, spins, and the distance to the source. Crucially, the detector-frame (redshifted) masses can be measured with high precision, providing insights into the mass spectrum of compact objects, which directly correlates with astrophysical binary formation scenarios. This redshifted mass spectrum, when compared across different distance bins, can be used to infer the redshift, offering a way to measure H_0, called the spectral siren method [345]. Alternatively, with an external redshift measurement—whether through host-galaxy identification or the detection of an EM counterpart—the precise GW-based distance constraint allows a direct estimate of H_0, called the standard/dark siren method. Both approaches provide valuable connections between GW observations and cosmological parameters. In cases where the black hole tidally disrupts the neutron star, its tidal deformability (Λ)—a parameter that encodes information about the star's EOS—can also be measured from the GW signal [346, 347]. NSBH mergers are particularly valuable in this regard because they provide a cleaner, more direct measurement of the tidal deformability compared to BNS systems, where

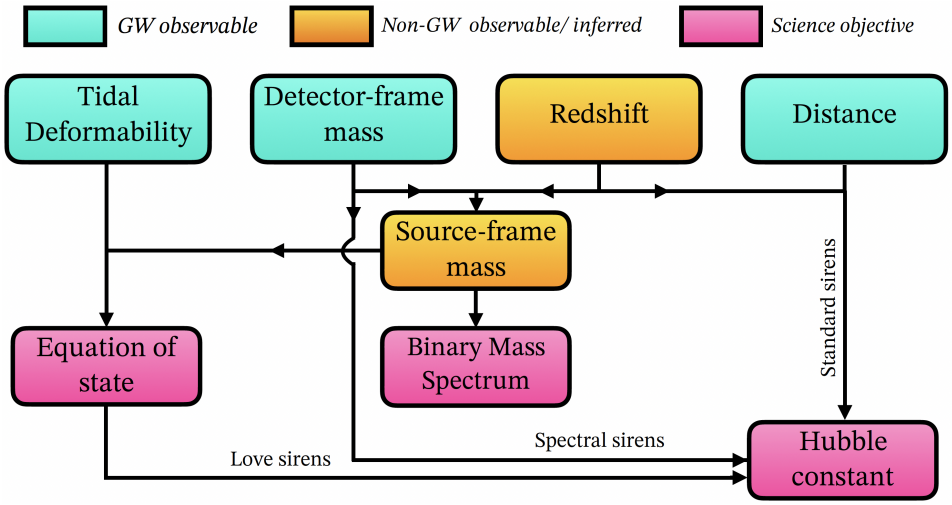

Figure 6.3: A flowchart showing the interdependencies between binary parameters and the inferred science.

the tidal signatures of both stars are entangled in the GW data. Figure 6.2 shows the expected fractional uncertainty in Λ for NSBH mergers at $z < 0.2$, for different generations of GW observatories. We find that networks including CE and ET can constrain Λ to better than 50% for approximately 10% of such events, while a network of detectors with A$^\sharp$-class sensitivity can achieve this for only about 1% of detections.

Importantly, the measurement of tidal deformability, combined with the detector-frame mass and redshift information, can be used to infer the EOS of the neutron star [348]. Conversely, if the EOS is known, tidal deformability and the redshifted detector-frame mass measurements yield the redshift and constrain H_0 (called the Love siren method) [349]. Despite the clear connections between the binary parameters and the science that can be inferred from their measurement (see fig 6.3), current studies often treat these approaches independently. Ignoring these correlations may lead to biased parameter estimation, particularly as we enter an era rich in GW detections, where joint inference frameworks will become increasingly critical. Such frameworks, which simultaneously incorporate information from multiple parameter spaces, have already demonstrated significant improvements in constraining astrophysical, nuclear, and cosmological parameters for BNS mergers [350]. Extending this methodology to NSBH systems will be prudent to fully realize their multi-faceted potential across GW cosmology and astrophysics.

In summary, this dissertation establishes the utility of NSBH mergers as a versatile class of GW sources. Their inherent mass asymmetry facilitates precise parameter esti-

mation, while their potential for electromagnetic counterparts enables multi-messenger exploration. Across four dimensions—detectability, multi-messenger follow-up, astrophysical inference, and cosmology—we demonstrate that NSBH binaries are poised to play a critical role in the next decade of GW science.

Bibliography

[1] F.S. Broekgaarden, E. Berger, C.J. Neijssel, A. Vigna-Gómez, D. Chattopadhyay, S. Stevenson et al., *Impact of massive binary star and cosmic evolution on gravitational wave observations I: black hole–neutron star mergers*, *Mon. Not. Roy. Astron. Soc.* **508** (2021) 5028 [2103.02608].

[2] D. Chattopadhyay, S. Stevenson, F. Broekgaarden, F. Antonini and K. Belczynski, *Modelling the formation of the first two neutron star–black hole mergers, GW200105 and GW200115: metallicity, chirp masses, and merger remnant spins*, *Mon. Not. Roy. Astron. Soc.* **513** (2022) 5780 [2203.05850].

[3] LIGO Scientific, Virgo,, KAGRA, VIRGO collaboration, *Observation of Gravitational Waves from the Coalescence of a 2.5–4.5 $M_\odot$ Compact Object and a Neutron Star*, *Astrophys. J. Lett.* **970** (2024) L34 [2404.04248].

[4] D. Chattopadhyay, S. Stevenson, J.R. Hurley, M. Bailes and F. Broekgaarden, *Modelling neutron star–black hole binaries: future pulsar surveys and gravitational wave detectors*, *Mon. Not. Roy. Astron. Soc.* **504** (2021) 3682 [2011.13503].

[5] E.A. Chase, B. O'Connor, C.L. Fryer, E. Troja, O. Korobkin, R.T. Wollaeger et al., *Kilonova Detectability with Wide-field Instruments*, *Astrophys. J.* **927** (2022) 163 [2105.12268].

[6] LSST collaboration, *LSST: from Science Drivers to Reference Design and Anticipated Data Products*, *Astrophys. J.* **873** (2019) 111 [0805.2366].

[7] *Rubin observatory system & lsst survey key numbers*, Last accessed 3 October 2022.

[8] Y. Pan, A. Buonanno, R. Fujita, E. Racine and H. Tagoshi, *Post-Newtonian factorized multipolar waveforms for spinning, non-precessing black-hole binaries*, *Phys. Rev. D* **83** (2011) 064003 [1006.0431].

[9] quoteresearch, "Quote Origin: Somewhere, Something Incredible Is Waiting To Be Known (2013); Quote Investigator; — quoteinvestigator.com." https://quoteinvestigator.com/2013/03/18/incredible/#1fe1741d-5392-4fc7-b3ca-3af9078f1408, 2013.

[10] A.A. Penzias and R.W. Wilson, *A Measurement of Excess Antenna Temperature at 4080 Mc/s.*, ApJ **142** (1965) 419.

[11] A. Hewish, S.J. Bell, J.D.H. Pilkington, P.F. Scott and R.A. Collins, *Observation of a Rapidly Pulsating Radio Source*, Nature **217** (1968) 709.

[12] D. Deming and H.A. Knutson, *Highlights of exoplanetary science from Spitzer*, *Nature Astronomy* **4** (2020) 453 [2005.11331].

[13] D. Majaess, *Discovering protostars and their host clusters via WISE*, Ap&SS **344** (2013) 175 [1211.4032].

[14] G.A. Shields, *Thermal continuum from accretion disks in quasars*, Nature **272** (1978) 706.

[15] B.D. Savage, *Ultraviolet-Optical Space Astronomy - Past, Present, and Future*, in *Ultraviolet-Optical Space Astronomy Beyond HST*, J.A. Morse, J.M. Shull and A.L. Kinney, eds., vol. 164 of *Astronomical Society of the Pacific Conference Series*, p. 3, Jan., 1999.

[16] E. Schreier, R. Levinson, H. Gursky, E. Kellogg, H. Tananbaum and R. Giacconi, *Evidence for the Binary Nature of Centaurus X-3 from UHURU X-Ray Observations.*, ApJ **172** (1972) L79.

[17] P.K. Blanchard et al., *JWST detection of a supernova associated with GRB 221009A without an r-process signature*, *Nature Astron.* **8** (2024) 774 [2308.14197].

[18] LIGO Scientific, Virgo, Fermi-GBM, INTEGRAL collaboration, *Gravitational Waves and Gamma-rays from a Binary Neutron Star Merger: GW170817 and GRB 170817A*, *Astrophys. J. Lett.* **848** (2017) L13 [1710.05834].

[19] A. Einstein, *Näherungsweise Integration der Feldgleichungen der Gravitation*, *Sitzungsberichte der Königlich Preussischen Akademie der Wissenschaften* (1916) 688.

[20] A. Einstein, *Über Gravitationswellen*, *Sitzungsberichte der Königlich Preussischen Akademie der Wissenschaften* (1918) 154.

[21] LIGO Scientific, Virgo collaboration, *Observation of Gravitational Waves from a Binary Black Hole Merger*, *Phys. Rev. Lett.* **116** (2016) 061102 [1602.03837].

[22] LIGO Scientific collaboration, *Advanced LIGO*, *Class. Quant. Grav.* **32** (2015) 074001 [1411.4547].

[23] aLIGO collaboration, *Sensitivity and performance of the Advanced LIGO detectors in the third observing run*, *Phys. Rev. D* **102** (2020) 062003 [2008.01301].

[24] M. Tse et al., *Quantum-Enhanced Advanced LIGO Detectors in the Era of Gravitational-Wave Astronomy*, *Phys. Rev. Lett.* **123** (2019) 231107.

[25] LIGO Scientific, Virgo collaboration, *GW170817: Observation of Gravitational Waves from a Binary Neutron Star Inspiral*, *Phys. Rev. Lett.* **119** (2017) 161101 [1710.05832].

[26] VIRGO collaboration, *Advanced Virgo: a second-generation interferometric gravitational wave detector*, *Class. Quant. Grav.* **32** (2015) 024001 [1408.3978].

[27] Virgo collaboration, *Increasing the Astrophysical Reach of the Advanced Virgo Detector via the Application of Squeezed Vacuum States of Light*, *Phys. Rev. Lett.* **123** (2019) 231108.

[28] M. Soares-Santos, et al., *The Electromagnetic Counterpart of the Binary Neutron Star Merger LIGO/Virgo GW170817. I. Discovery of the Optical Counterpart Using the Dark Energy Camera*, ApJ **848** (2017) L16 [1710.05459].

[29] LIGO Scientific, Virgo, Fermi GBM, INTEGRAL, IceCube, AstroSat Cadmium Zinc Telluride Imager Team, IPN, Insight-Hxmt, ANTARES, Swift, AGILE Team, 1M2H Team, Dark Energy Camera GW-EM, DES, DLT40, GRAWITA, Fermi-LAT, ATCA, ASKAP, Las Cumbres Observatory Group, OzGrav, DWF (Deeper Wider Faster Program), AST3, CAASTRO, VINROUGE, MASTER, J-GEM, GROWTH, JAGWAR, CaltechNRAO, TTU-NRAO, NuSTAR, Pan-STARRS, MAXI Team, TZAC Consortium, KU, Nordic Optical Telescope, ePESSTO, GROND, Texas Tech University, SALT Group, TOROS, BOOTES, MWA, CALET, IKI-GW Follow-up, H.E.S.S., LOFAR, LWA, HAWC, Pierre Auger, ALMA, Euro VLBI Team, Pi of Sky, Chandra Team at McGill University, DFN, ATLAS Telescopes, High Time Resolution Universe Survey, RIMAS, RATIR, SKA South Africa/MeerKAT collaboration, *Multi-messenger Observations of a Binary Neutron Star Merger*, *Astrophys. J. Lett.* **848** (2017) L12 [1710.05833].

[30] E. Pian et al., *Spectroscopic identification of r-process nucleosynthesis in a double neutron star merger*, *Nature* **551** (2017) 67 [1710.05858].

[31] D. Radice, S. Bernuzzi and A. Perego, *The Dynamics of Binary Neutron Star Mergers and GW170817*, *Ann. Rev. Nucl. Part. Sci.* **70** (2020) 95 [2002.03863].

[32] LIGO Scientific, VIRGO, KAGRA collaboration, "Tests of General Relativity with GWTC-3." 12, 2021.

[33] KAGRA, VIRGO, LIGO Scientific collaboration, *Population of Merging Compact Binaries Inferred Using Gravitational Waves through GWTC-3*, *Phys. Rev. X* **13** (2023) 011048 [2111.03634].

[34] LIGO Scientific, Virgo, KAGRA collaboration, *Constraints on the Cosmic Expansion History from GWTC–3*, *Astrophys. J.* **949** (2023) 76 [2111.03604].

[35] LIGO Scientific, Virgo collaboration, *GW170817: Measurements of neutron star radii and equation of state*, *Phys. Rev. Lett.* **121** (2018) 161101 [1805.11581].

[36] B.S. Sathyaprakash and B.F. Schutz, *Physics, Astrophysics and Cosmology with Gravitational Waves*, *Living Rev. Rel.* **12** (2009) 2 [0903.0338].

[37] M. Branchesi et al., *Science with the Einstein Telescope: a comparison of different designs*, *JCAP* **07** (2023) 068 [2303.15923].

[38] I. Gupta et al., *Characterizing gravitational wave detector networks: from $A^\sharp$ to cosmic explorer*, *Class. Quant. Grav.* **41** (2024) 245001 [2307.10421].

[39] J. Miller, L. Barsotti, S. Vitale, P. Fritschel, M. Evans and D. Sigg, *Prospects for doubling the range of Advanced LIGO*, *Phys. Rev. D* **91** (2015) 062005 [1410.5882].

[40] KAGRA, LIGO Scientific, Virgo collaboration, *Prospects for observing and localizing gravitational-wave transients with Advanced LIGO, Advanced Virgo and KAGRA*, *Living Rev. Rel.* **19** (2016) 1 [1304.0670].

[41] B. Iyer et al., *LIGO India Tech. Rep.*, 2011.

[42] KAGRA collaboration, *Detector configuration of KAGRA: The Japanese cryogenic gravitational-wave detector*, *Class. Quant. Grav.* **29** (2012) 124007 [1111.7185].

[43] KAGRA collaboration, *Overview of KAGRA: Calibration, detector characterization, physical environmental monitors, and the geophysics interferometer*, *PTEP* **2021** (2021) 05A102 [2009.09305].

[44] KAGRA collaboration, *Interferometer design of the KAGRA gravitational wave detector*, *Phys. Rev. D* **88** (2013) 043007 [1306.6747].

[45] LIGO collaboration, *A cryogenic silicon interferometer for gravitational-wave detection*, *Class. Quant. Grav.* **37** (2020) 165003 [2001.11173].

[46] P. Fritschel, K. Kuns, J. Driggers, A. Effler, B. Lantz, D. Ottaway et al., *Report from the lsc post-o5 study group*, Tech. Rep. T2200287, LIGO (2022).

[47] M. Evans et al., *A Horizon Study for Cosmic Explorer: Science, Observatories, and Community*, [2109.09882].

[48] LIGO Scientific collaboration, *Exploring the Sensitivity of Next Generation Gravitational Wave Detectors*, *Class. Quant. Grav.* **34** (2017) 044001 [1607.08697].

[49] D. Reitze et al., *Cosmic Explorer: The U.S. Contribution to Gravitational-Wave Astronomy beyond LIGO*, *Bull. Am. Astron. Soc.* **51** (2019) 035 [1907.04833].

[50] M. Punturo et al., *The Einstein Telescope: A third-generation gravitational wave observatory*, *Class. Quant. Grav.* **27** (2010) 194002.

[51] S. Hild et al., *Sensitivity Studies for Third-Generation Gravitational Wave Observatories*, *Class. Quant. Grav.* **28** (2011) 094013 [1012.0908].

[52] M. Maggiore, *Gravitational Waves. Vol. 1: Theory and Experiments*, Oxford University Press (2007), 10.1093/acprof:oso/9780198570745.001.0001.

[53] L. Blanchet, *Post-Newtonian Theory for Gravitational Waves*, *Living Rev. Rel.* **17** (2014) 2 [1310.1528].

[54] L. Blanchet, G. Faye, Q. Henry, F. Larrouturou and D. Trestini, *Gravitational-Wave Phasing of Quasicircular Compact Binary Systems to the Fourth-and-a-Half Post-Newtonian Order*, *Phys. Rev. Lett.* **131** (2023) 121402 [2304.11185].

[55] E.W. Kolb and M.S. Turner, *The early universe*, vol. 69, CRC Press (1990).

[56] A.G. Riess et al., *A Comprehensive Measurement of the Local Value of the Hubble Constant with 1 km s^{-1} Mpc^{-1} Uncertainty from the Hubble Space Telescope and the SH0ES Team*, *Astrophys. J. Lett.* **934** (2022) L7 [2112.04510].

[57] B.F. Schutz, *Determining the Hubble Constant from Gravitational Wave Observations*, *Nature* **323** (1986) 310.

[58] A. Vijaykumar, M. Fishbach, S. Adhikari and D.E. Holz, *Inferring Host-galaxy Properties of LIGO–Virgo–KAGRA's Black Holes*, *Astrophys. J.* **972** (2024) 157 [2312.03316].

[59] S. Borhanian, A. Dhani, A. Gupta, K.G. Arun and B.S. Sathyaprakash, *Dark Sirens to Resolve the Hubble–Lemaître Tension*, *Astrophys. J. Lett.* **905** (2020) L28 [2007.02883].

[60] A. Palmese, C.R. Bom, S. Mucesh and W.G. Hartley, *A Standard Siren Measurement of the Hubble Constant Using Gravitational-wave Events from the First Three LIGO/Virgo Observing Runs and the DESI Legacy Survey*, *Astrophys. J.* **943** (2023) 56 [2111.06445].

[61] I. Gupta, *Using grey sirens to resolve the Hubble–Lemaître tension*, *Mon. Not. Roy. Astron. Soc.* **524** (2023) 3537 [2212.00163].

[62] H.-Y. Chen, J.M. Ezquiaga and I. Gupta, *Cosmography with next-generation gravitational wave detectors*, *Class. Quant. Grav.* **41** (2024) 125004 [2402.03120].

[63] S. Fairhurst, *Triangulation of gravitational wave sources with a network of detectors*, *New J. Phys.* **11** (2009) 123006 [0908.2356].

[64] S. Pandey, I. Gupta, K. Chandra and B.S. Sathyaprakash, "The Critical Role of LIGO-India in the Era of Next-Generation Observatories." 11, 2024.

[65] S.V. Dhurandhar and M. Tinto, *Astronomical observations with a network of detectors of gravitational waves. I - Mathematical framework and solution of the five detector problem*, MNRAS **234** (1988) 663.

[66] M. Vallisneri, *Use and abuse of the Fisher information matrix in the assessment of gravitational-wave parameter-estimation prospects*, *Phys. Rev. D* **77** (2008) 042001 [gr-qc/0703086].

[67] I. Gupta, *Inferring Small Neutron Star Spins with Neutron Star–Black Hole Mergers*, *Astrophys. J.* **970** (2024) 12 [2402.07075].

[68] C. Mills and S. Fairhurst, *Measuring gravitational-wave higher-order multipoles*, *Phys. Rev. D* **103** (2021) 024042 [2007.04313].

[69] K. Chatziioannou, N. Cornish, A. Klein and N. Yunes, *Detection and Parameter Estimation of Gravitational Waves from Compact Binary Inspirals with Analytical Double-Precessing Templates*, *Phys. Rev. D* **89** (2014) 104023 [1404.3180].

[70] G. Pratten et al., *Computationally efficient models for the dominant and subdominant harmonic modes of precessing binary black holes*, *Phys. Rev. D* **103** (2021) 104056 [2004.06503].

[71] D.A. Godzieba, D. Radice and S. Bernuzzi, *On the maximum mass of neutron stars and GW190814*, *Astrophys. J.* **908** (2021) 122 [2007.10999].

[72] K. Kyutoku, M. Shibata and K. Taniguchi, *Coalescence of black hole–neutron star binaries*, *Living Rev. Rel.* **24** (2021) 5 [2110.06218].

[73] I. Gupta, S. Borhanian, A. Dhani, D. Chattopadhyay, R. Kashyap, V.A. Villar et al., *Neutron star-black hole mergers in next generation gravitational-wave observatories*, *Phys. Rev. D* **107** (2023) 124007 [2301.08763].

[74] I. Gupta et al., "Testing general relativity with amplitudes of the subdominant modes." 07, 2025.

[75] KAGRA, VIRGO, LIGO Scientific collaboration, *GWTC-3: Compact Binary Coalescences Observed by LIGO and Virgo during the Second Part of the Third Observing Run*, *Phys. Rev. X* **13** (2023) 041039 [2111.03606].

[76] LIGO Scientific, KAGRA, VIRGO collaboration, *Observation of Gravitational Waves from Two Neutron Star–Black Hole Coalescences*, *Astrophys. J. Lett.* **915** (2021) L5 [2106.15163].

[77] L.L. Smarr and R. Blandford, *The binary pulsar: physical processes, possible companions, and evolutionary histories.*, ApJ **207** (1976) 574.

[78] S.F. Portegies Zwart and S. McMillan, *Black hole mergers in the universe*, *Astrophys. J. Lett.* **528** (2000) L17 [astro-ph/9910061].

[79] D. Clausen, S. Sigurdsson and D.F. Chernoff, *Black Hole-Neutron Star Mergers in Globular Clusters*, *Mon. Not. Roy. Astron. Soc.* **428** (2013) 3618 [1210.8153].

[80] J.M.B. Downing, M.J. Benacquista, M. Giersz and R. Spurzem, *Compact Binaries in Star Clusters I - Black Hole Binaries Inside Globular Clusters*, *Mon. Not. Roy. Astron. Soc.* **407** (2010) 1946 [0910.0546].

[81] F. Santoliquido, M. Mapelli, Y. Bouffanais, N. Giacobbo, U.N. Di Carlo, S. Rastello et al., *The cosmic merger rate density evolution of compact binaries formed in young star clusters and in isolated binaries*, *Astrophys. J.* **898** (2020) 152 [2004.09533].

[82] S. Rastello, M. Mapelli, U.N. Di Carlo, N. Giacobbo, F. Santoliquido, M. Spera et al., *Dynamics of black hole–neutron star binaries in young star clusters*, *Mon. Not. Roy. Astron. Soc.* **497** (2020) 1563 [2003.02277].

[83] K. Belczynski, T. Ryu, R. Perna, E. Berti, T.L. Tanaka and T. Bulik, *On the likelihood of detecting gravitational waves from Population III compact object binaries*, *Mon. Not. Roy. Astron. Soc.* **471** (2017) 4702 [1612.01524].

[84] S. Vitale, R. Lynch, R. Sturani and P. Graff, *Use of gravitational waves to probe the formation channels of compact binaries*, *Class. Quant. Grav.* **34** (2017) 03LT01 [1503.04307].

[85] L.-X. Li and B. Paczynski, *Transient events from neutron star mergers*, *Astrophys. J. Lett.* **507** (1998) L59 [astro-ph/9807272].

[86] B.D. Metzger, *Kilonovae*, *Living Rev. Rel.* **23** (2020) 1 [1910.01617].

[87] J. Goodman, *Are gamma-ray bursts optically thick?*, *Astrophys. J. Lett.* **308** (1986) L47.

[88] D. Eichler, M. Livio, T. Piran and D.N. Schramm, *Nucleosynthesis, Neutrino Bursts and Gamma-Rays from Coalescing Neutron Stars*, *Nature* **340** (1989) 126.

[89] S. Nissanke, D.E. Holz, S.A. Hughes, N. Dalal and J.L. Sievers, *Exploring short gamma-ray bursts as gravitational-wave standard sirens*, *Astrophys. J.* **725** (2010) 496 [0904.1017].

[90] N. Sarin, P.D. Lasky, F.H. Vivanco, S.P. Stevenson, D. Chattopadhyay, R. Smith et al., *Linking the rates of neutron star binaries and short gamma-ray bursts*, *Phys. Rev. D* **105** (2022) 083004 [2201.08491].

[91] S. Vitale and H.-Y. Chen, *Measuring the Hubble constant with neutron star black hole mergers*, *Phys. Rev. Lett.* **121** (2018) 021303 [1804.07337].

[92] S.M. Feeney, H.V. Peiris, S.M. Nissanke and D.J. Mortlock, *Prospects for Measuring the Hubble Constant with Neutron-Star–Black-Hole Mergers*, *Phys. Rev. Lett.* **126** (2021) 171102 [2012.06593].

[93] B.D. Lackey, K. Kyutoku, M. Shibata, P.R. Brady and J.L. Friedman, *Extracting equation of state parameters from black hole-neutron star mergers. I. Nonspinning black holes*, *Phys. Rev. D* **85** (2012) 044061 [1109.3402].

[94] S. Ascenzi, N. De Lillo, C.-J. Haster, F. Ohme and F. Pannarale, *Constraining the Neutron Star Radius with Joint Gravitational-wave and Short Gamma-Ray Burst Observations of Neutron Star–Black Hole Coalescing Binaries*, *Astrophys. J.* **877** (2019) 94 [1808.06848].

[95] M.W. Coughlin, T. Dietrich, B. Margalit and B.D. Metzger, *Multimessenger Bayesian parameter inference of a binary neutron star merger*, *Mon. Not. Roy. Astron. Soc.* **489** (2019) L91 [1812.04803].

[96] K. Kawaguchi, M. Shibata and M. Tanaka, *Constraint on the Ejecta Mass for Black Hole–Neutron Star Merger Event Candidate S190814bv*, *Astrophys. J.* **893** (2020) 153 [2002.01662].

[97] C. Barbieri, O.S. Salafia, A. Perego, M. Colpi and G. Ghirlanda, *Light-curve models of black hole – neutron star mergers: steps towards a multi-messenger parameter estimation*, *Astron. Astrophys.* **625** (2019) A152 [1903.04543].

[98] S. Tiwari, M. Ebersold and E.Z. Hamilton, *Leveraging gravitational-wave memory to distinguish neutron star-black hole binaries from black hole binaries*, *Phys. Rev. D* **104** (2021) 123024 [2110.11171].

[99] S. Borhanian and B.S. Sathyaprakash, *Listening to the Universe with next generation ground-based gravitational-wave detectors*, *Phys. Rev. D* **110** (2024) 083040 [2202.11048].

[100] S. Ronchini, M. Branchesi, G. Oganesyan, B. Banerjee, U. Dupletsa, G. Ghirlanda et al., *Perspectives for multimessenger astronomy with the next generation of gravitational-wave detectors and high-energy satellites*, *Astron. Astrophys.* **665** (2022) A97 [2204.01746].

[101] F. Iacovelli, M. Mancarella, S. Foffa and M. Maggiore, *Forecasting the Detection Capabilities of Third-generation Gravitational-wave Detectors Using GWFAST*, *Astrophys. J.* **941** (2022) 208 [2207.02771].

[102] S. Borhanian, *GWBENCH: a novel Fisher information package for gravitational-wave benchmarking*, *Class. Quant. Grav.* **38** (2021) 175014 [2010.15202].

[103] S. Biscoveanu, P. Landry and S. Vitale, *Population properties and multimessenger prospects of neutron star–black hole mergers following GWTC-3*, *Mon. Not. Roy. Astron. Soc.* **518** (2022) 5298 [2207.01568].

[104] J.-P. Zhu, S. Wu, Y. Qin, B. Zhang, H. Gao and Z. Cao, *Population Properties of Gravitational-wave Neutron Star–Black Hole Mergers*, *Astrophys. J.* **928** (2022) 167 [2112.02605].

[105] COMPAS Team, Team COMPAS collaboration, *Rapid Stellar and Binary Population Synthesis with COMPAS*, *Astrophys. J. Supp.* **258** (2022) 34 [2109.10352].

[106] Y. Qin, T. Fragos, G. Meynet, J. Andrews, M. Sørensen and H.F. Song, *The spin of the second-born black hole in coalescing binary black holes*, *Astron. Astrophys.* **616** (2018) A28 [1802.05738].

[107] D. Chattopadhyay, S. Stevenson, J.R. Hurley, L.J. Rossi and C. Flynn, *Modelling Double Neutron Stars: Radio and Gravitational Waves*, *Mon. Not. Roy. Astron. Soc.* **494** (2020) 1587 [1912.02415].

[108] S.S. Bavera, T. Fragos, Y. Qin, E. Zapartas, C.J. Neijssel, I. Mandel et al., *The origin of spin in binary black holes: Predicting the distributions of the main observables of Advanced LIGO*, *Astron. Astrophys.* **635** (2020) A97 [1906.12257].

[109] Astropy collaboration, *Astropy: A Community Python Package for Astronomy*, *Astron. Astrophys.* **558** (2013) A33 [1307.6212].

[110] Astropy collaboration, *The Astropy Project: Building an Open-science Project and Status of the v2.0 Core Package*, *Astron. J.* **156** (2018) 123 [1801.02634].

[111] LIGO Scientific Collaboration, "LIGO Algorithm Library - LALSuite." free software (GPL), 2018. 10.7935/GT1W-FZ16.

[112] C. García-Quirós, M. Colleoni, S. Husa, H. Estellés, G. Pratten, A. Ramos-Buades et al., *Multimode frequency-domain model for the gravitational wave signal from nonprecessing black-hole binaries*, *Phys. Rev. D* **102** (2020) 064002 [2001.10914].

[113] J.E. Thompson, E. Fauchon-Jones, S. Khan, E. Nitoglia, F. Pannarale, T. Dietrich et al., *Modeling the gravitational wave signature of neutron star black hole coalescences*, *Phys. Rev. D* **101** (2020) 124059 [2002.08383].

[114] S.J. Kapadia, M.K. Singh, M.A. Shaikh, D. Chatterjee and P. Ajith, *Of Harbingers and Higher Modes: Improved gravitational-wave early-warning of compact binary mergers*, *Astrophys. J. Lett.* **898** (2020) L39 [2005.08830].

[115] H. Yuksel, M.D. Kistler, J.F. Beacom and A.M. Hopkins, *Revealing the High-Redshift Star Formation Rate with Gamma-Ray Bursts*, *Astrophys. J. Lett.* **683** (2008) L5 [0804.4008].

[116] D. Wanderman and T. Piran, *The rate, luminosity function and time delay of non-Collapsar short GRBs*, *Mon. Not. Roy. Astron. Soc.* **448** (2015) 3026 [1405.5878].

[117] F.J. Virgili, B. Zhang, P. O'Brien and E. Troja, *Are all short-hard gamma-ray bursts produced from mergers of compact stellar objects?*, *Astrophys. J.* **727** (2011) 109 [0909.1850].

[118] J.A. de Freitas Pacheco, T. Regimbau, S. Vincent and A. Spallicci, *Expected coalescence rates of ns-ns binaries for laser beam interferometers*, *Int. J. Mod. Phys. D* **15** (2006) 235 [astro-ph/0510727].

[119] J.-P. Zhu et al., *Kilonova Emission from Black Hole–Neutron Star Mergers. II. Luminosity Function and Implications for Target-of-opportunity Observations of Gravitational-wave Triggers and Blind Searches*, *Astrophys. J.* **917** (2021) 24 [2011.02717].

[120] H. Sun, B. Zhang and Z. Li, *Extragalactic High-energy Transients: Event Rate Densities and Luminosity Functions*, *Astrophys. J.* **812** (2015) 33 [1509.01592].

[121] LIGO Scientific, Virgo collaboration, *Properties of the binary neutron star merger GW170817*, *Phys. Rev. X* **9** (2019) 011001 [1805.11579].

[122] L.P. Singer et al., *Going the Distance: Mapping Host Galaxies of LIGO and Virgo Sources in Three Dimensions Using Local Cosmography and Targeted Follow-up*, *Astrophys. J. Lett.* **829** (2016) L15 [1603.07333].

[123] D.N. Burrows, J.E. Hill, J.A. Nousek, A.A. Wells, A.D. Short, R. Willingale et al., *Swift X-Ray Telescope*, in *X-Ray and Gamma-Ray Instrumentation for Astronomy XI*, K.A. Flanagan and O.H. Siegmund, eds., vol. 4140 of *Society of Photo-Optical Instrumentation Engineers (SPIE) Conference Series*, pp. 64–75, Dec., 2000, DOI.

[124] Euclid collaboration, *Euclid preparation. I. The Euclid Wide Survey*, *Astron. Astrophys.* **662** (2022) A112 [2108.01201].

[125] K. Bundy, K. Westfall, N. MacDonald, R. Kupke, M. Savage, C. Poppett et al., *Fobos: A next-generation spectroscopic facility at the wm keck observatory*, *arXiv preprint arXiv:1907.07195* (2019) .

[126] A. Rau, N. Meidinger, K. Nandra, M. Porro, D. Barret, A. Santangelo et al., *The Hot and Energetic Universe: The Wide Field Imager (WFI) for Athena+*, *arXiv e-prints* (2013) arXiv:1308.6785 [1308.6785].

[127] *Vimos - visible multiobject spectrograph*, Last accessed 3 October 2022.

[128] R. Hounsell et al., *Simulations of the WFIRST Supernova Survey and Forecasts of Cosmological Constraints*, *Astrophys. J.* **867** (2018) 23 [1702.01747].

[129] *Facts about the elt*, Last accessed 3 October 2022.

[130] *Chandra x–ray observatory: Mission characteristics*, Last accessed 3 October 2022.

[131] G.H. Jacoby, R. Bernstein, A. Bouchez, M. Colless, J. Crane, D. DePoy et al., *Instrumentation progress at the Giant Magellan Telescope project*, in *Ground-based and Airborne Instrumentation for Astronomy VI*, C.J. Evans, L. Simard and H. Takami, eds., vol. 9908 of *Society of Photo-Optical Instrumentation Engineers (SPIE) Conference Series*, p. 99081U, Aug., 2016, DOI.

[132] J.A. Gaskin, D.A. Swartz, A. Vikhlinin, F. Özel, K.E. Gelmis, J.W. Arenberg et al., *Lynx X-Ray Observatory: an overview*, *Journal of Astronomical Telescopes, Instruments, and Systems* **5** (2019) 021001.

[133] *Hubble's instruments: Wfc3 - wide field camera 3*, Last accessed 3 October 2022.

[134] P.S. Cowperthwaite, V.A. Villar, D.M. Scolnic and E. Berger, *LSST Target-of-Opportunity Observations of Gravitational Wave Events: Essential and Efficient*, *Astrophys. J.* **874** (2019) 88 [1811.03098].

[135] LSST collaboration, *Target of Opportunity Observations of Gravitational Wave Events with LSST*, [1812.04051].

[136] B.S. Sathyaprakash and S.V. Dhurandhar, *Choice of filters for the detection of gravitational waves from coalescing binaries*, *Phys. Rev. D* **44** (1991) 3819.

[137] S. Sachdev et al., *An Early-warning System for Electromagnetic Follow-up of Gravitational-wave Events*, *Astrophys. J. Lett.* **905** (2020) L25 [2008.04288].

[138] M. Nicholl et al., *The Electromagnetic Counterpart of the Binary Neutron Star Merger LIGO/VIRGO GW170817. III. Optical and UV Spectra of a Blue Kilonova From Fast Polar Ejecta*, *Astrophys. J. Lett.* **848** (2017) L18 [1710.05456].

[139] F. Pannarale and F. Ohme, *Prospects for joint gravitational-wave and electromagnetic observations of neutron-star–black-hole coalescing binaries*, *Astrophys. J. Lett.* **791** (2014) L7 [1406.6057].

[140] F. Zappa, S. Bernuzzi, F. Pannarale, M. Mapelli and N. Giacobbo, *Black-Hole Remnants from Black-Hole–Neutron-Star Mergers*, *Phys. Rev. Lett.* **123** (2019) 041102 [1903.11622].

[141] G. Fragione, *Black-hole–Neutron-star Mergers Are Unlikely Multimessenger Sources*, *Astrophys. J. Lett.* **923** (2021) L2 [2110.09604].

[142] D. Chatterjee, S. Ghosh, P.R. Brady, S.J. Kapadia, A.L. Miller, S. Nissanke et al., *A Machine Learning Based Source Property Inference for Compact Binary Mergers*, *Astrophys. J.* **896** (2020) 54 [1911.00116].

[143] C.J. Krüger and F. Foucart, *Estimates for Disk and Ejecta Masses Produced in Compact Binary Mergers*, *Phys. Rev. D* **101** (2020) 103002 [2002.07728].

[144] G. Raaijmakers et al., *The Challenges Ahead for Multimessenger Analyses of Gravitational Waves and Kilonova: A Case Study on GW190425*, *Astrophys. J.* **922** (2021) 269 [2102.11569].

[145] F. Foucart, T. Hinderer and S. Nissanke, *Remnant baryon mass in neutron star-black hole mergers: Predictions for binary neutron star mimickers and rapidly spinning black holes*, *Phys. Rev. D* **98** (2018) 081501 [1807.00011].

[146] J.M. Lattimer and M. Prakash, *Neutron star structure and the equation of state*, *Astrophys. J.* **550** (2001) 426 [astro-ph/0002232].

[147] S. De and D.M. Siegel, *Igniting Weak Interactions in Neutron Star Postmerger Accretion Disks*, *Astrophys. J.* **921** (2021) 94 [2011.07176].

[148] D.M. Siegel and B.D. Metzger, *Three-Dimensional General-Relativistic Magnetohydrodynamic Simulations of Remnant Accretion Disks from Neutron Star Mergers: Outflows and r-Process Nucleosynthesis*, *Phys. Rev. Lett.* **119** (2017) 231102 [1705.05473].

[149] O. Korobkin, S. Rosswog, A. Arcones and C. Winteler, *On the astrophysical robustness of neutron star merger r-process*, *Mon. Not. Roy. Astron. Soc.* **426** (2012) 1940 [1206.2379].

[150] A. Akmal, V.R. Pandharipande and D.G. Ravenhall, *The Equation of state of nucleon matter and neutron star structure*, *Phys. Rev. C* **58** (1998) 1804 [nucl-th/9804027].

[151] S. Typel, G. Ropke, T. Klahn, D. Blaschke and H.H. Wolter, *Composition and thermodynamics of nuclear matter with light clusters*, *Phys. Rev. C* **81** (2010) 015803 [0908.2344].

[152] M. Alford, M. Braby, M.W. Paris and S. Reddy, *Hybrid stars that masquerade as neutron stars*, *Astrophys. J.* **629** (2005) 969 [nucl-th/0411016].

[153] I. Andreoni et al., *Target-of-opportunity Observations of Gravitational-wave Events with Vera C. Rubin Observatory*, *Astrophys. J. Supp.* **260** (2022) 18 [2111.01945].

[154] E. Chabanat, P. Bonche, P. Haensel, J. Meyer and R. Schaeffer, *A Skyrme parametrization from subnuclear to neutron star densities. 2. Nuclei far from stablities*, *Nucl. Phys. A* **635** (1998) 231.

[155] F. Douchin and P. Haensel, *A unified equation of state of dense matter and neutron star structure*, *Astron. Astrophys.* **380** (2001) 151 [astro-ph/0111092].

[156] M. Hempel and J. Schaffner-Bielich, *Statistical Model for a Complete Supernova Equation of State*, *Nucl. Phys. A* **837** (2010) 210 [0911.4073].

[157] N.K. Glendenning and S.A. Moszkowski, *Reconciliation of neutron star masses and binding of the lambda in hypernuclei*, *Phys. Rev. Lett.* **67** (1991) 2414.

[158] B.D. Lackey, M. Nayyar and B.J. Owen, *Observational constraints on hyperons in neutron stars*, *Phys. Rev. D* **73** (2006) 024021 [astro-ph/0507312].

[159] J.S. Read, B.D. Lackey, B.J. Owen and J.L. Friedman, *Constraints on a phenomenologically parameterized neutron-star equation of state*, *Phys. Rev. D* **79** (2009) 124032 [0812.2163].

[160] J. Guillochon, J. Parrent, L.Z. Kelley and R. Margutti, *An Open Catalog for Supernova Data*, *Astrophys. J.* **835** (2017) 64 [1605.01054].

[161] V.A. Villar et al., *The Combined Ultraviolet, Optical, and Near-Infrared Light Curves of the Kilonova Associated with the Binary Neutron Star Merger GW170817: Unified Data Set, Analytic Models, and Physical Implications*, *Astrophys. J. Lett.* **851** (2017) L21 [1710.11576].

[162] K. Chandra, I. Gupta, R. Gamba, R. Kashyap, D. Chattopadhyay, A. Gonzalez et al., *On the Origins, Remnant, and Multimessenger Prospects of the Compact Binary Merger GW230529*, *Astrophys. J.* **977** (2024) 167 [2405.03841].

[163] A. Tutukov and L. Yungelson, *Evolution of massive close binaries*, *Nauchnye Informatsii* **27** (1973) 70.

[164] K.A. Postnov and L.R. Yungelson, *The Evolution of Compact Binary Star Systems*, *Living Rev. Rel.* **17** (2014) 3 [1403.4754].

[165] S. Sigurdsson and L. Hernquist, *Primordial black holes in globular clusters*, *Nature* **364** (1993) 423.

[166] M.J. Benacquista and J.M.B. Downing, *Relativistic Binaries in Globular Clusters*, *Living Rev. Rel.* **16** (2013) 4 [1110.4423].

[167] S. Mastrogiovanni, A. Lamberts, R. Srinivasan, T. Bruel and N. Christensen, *Inferring binary black holes stellar progenitors with gravitational wave sources*, *Mon. Not. Roy. Astron. Soc.* **517** (2022) 3432 [2207.00374].

[168] LIGO Scientific, Virgo collaboration, *Astrophysical Implications of the Binary Black-Hole Merger GW150914*, *Astrophys. J. Lett.* **818** (2016) L22 [1602.03846].

[169] D. Gerosa and E. Berti, *Are merging black holes born from stellar collapse or previous mergers?*, *Phys. Rev. D* **95** (2017) 124046 [1703.06223].

[170] I. Mandel and A. Farmer, *Merging stellar-mass binary black holes*, *Phys. Rept.* **955** (2022) 1 [1806.05820].

[171] M. Zevin, S.S. Bavera, C.P.L. Berry, V. Kalogera, T. Fragos, P. Marchant et al., *One Channel to Rule Them All? Constraining the Origins of Binary Black Holes Using Multiple Formation Pathways*, *Astrophys. J.* **910** (2021) 152 [2011.10057].

[172] N. Mennekens and D. Vanbeveren, *Massive double compact object mergers: gravitational wave sources and r-process element production sites*, A&A **564** (2014) A134 [1307.0959].

[173] K. Belczynski, V. Kalogera, F.A. Rasio, R.E. Taam and T. Bulik, *On the rarity of double black hole binaries: Consequences for gravitational-wave detection*, *Astrophys. J.* **662** (2007) 504 [astro-ph/0612032].

[174] W.M. Farr, N. Sravan, A. Cantrell, L. Kreidberg, C.D. Bailyn, I. Mandel et al., *The Mass Distribution of Stellar-Mass Black Holes*, *Astrophys. J.* **741** (2011) 103 [1011.1459].

[175] K. Belczynski, D.E. Holz, T. Bulik and R. O'Shaughnessy, *The first gravitational-wave source from the isolated evolution of two 40-100 Msun stars*, *Nature* **534** (2016) 512 [1602.04531].

[176] M. Zevin, C. Pankow, C.L. Rodriguez, L. Sampson, E. Chase, V. Kalogera et al., *Constraining Formation Models of Binary Black Holes with Gravitational-Wave Observations*, *Astrophys. J.* **846** (2017) 82 [1704.07379].

[177] V. Tiwari and S. Fairhurst, *The Emergence of Structure in the Binary Black Hole Mass Distribution*, *Astrophys. J. Lett.* **913** (2021) L19 [2011.04502].

[178] K.W.K. Wong, K. Breivik, K. Kremer and T. Callister, *Joint constraints on the field-cluster mixing fraction, common envelope efficiency, and globular cluster radii from a population of binary hole mergers via deep learning*, *Phys. Rev. D* **103** (2021) 083021 [2011.03564].

[179] V. Tiwari, *Exploring Features in the Binary Black Hole Population*, *Astrophys. J.* **928** (2022) 155 [2111.13991].

[180] A.M. Farah, B. Edelman, M. Zevin, M. Fishbach, J.M. Ezquiaga, B. Farr et al., *Things That Might Go Bump in the Night: Assessing Structure in the Binary Black Hole Mass Spectrum*, *Astrophys. J.* **955** (2023) 107 [2301.00834].

[181] W.M. Farr, S. Stevenson, M. Coleman Miller, I. Mandel, B. Farr and A. Vecchio, *Distinguishing Spin-Aligned and Isotropic Black Hole Populations With Gravitational Waves*, *Nature* **548** (2017) 426 [1706.01385].

[182] B. Farr, D.E. Holz and W.M. Farr, *Using Spin to Understand the Formation of LIGO and Virgo's Black Holes*, *Astrophys. J. Lett.* **854** (2018) L9 [1709.07896].

[183] A.V. Tutukov and L.R. YungelSon, *The merger rate of neutron star and black hole binaries*, *Mon. Not. Roy. Astron. Soc.* **260** (1993) 675.

[184] M. Zaldarriaga, D. Kushnir and J.A. Kollmeier, *The expected spins of gravitational wave sources with isolated field binary progenitors*, *Mon. Not. Roy. Astron. Soc.* **473** (2018) 4174 [1702.00885].

[185] J. Fuller and L. Ma, *Most Black Holes are Born Very Slowly Rotating*, *Astrophys. J. Lett.* **881** (2019) L1 [1907.03714].

[186] M. Zevin and S.S. Bavera, *Suspicious Siblings: The Distribution of Mass and Spin across Component Black Holes in Isolated Binary Evolution*, *Astrophys. J.* **933** (2022) 86 [2203.02515].

[187] V. Kalogera, *Spin orbit misalignment in close binaries with two compact objects*, *Astrophys. J.* **541** (2000) 319 [astro-ph/9911417].

[188] R. O'Shaughnessy, D. Gerosa and D. Wysocki, *Inferences about supernova physics from gravitational-wave measurements: GW151226 spin misalignment as an indicator of strong black-hole natal kicks*, *Phys. Rev. Lett.* **119** (2017) 011101 [1704.03879].

[189] A. Olejak and K. Belczynski, *The Implications of High BH Spins on the Origin of BH–BH Mergers*, *Astrophys. J. Lett.* **921** (2021) L2 [2109.06872].

[190] C.L. Rodriguez, M. Zevin, C. Pankow, V. Kalogera and F.A. Rasio, *Illuminating Black Hole Binary Formation Channels with Spins in Advanced LIGO*, *Astrophys. J. Lett.* **832** (2016) L2 [1609.05916].

[191] E. Berti and M. Volonteri, *Cosmological black hole spin evolution by mergers and accretion*, *Astrophys. J.* **684** (2008) 822 [0802.0025].

[192] S. Vitale, S. Biscoveanu and C. Talbot, *Spin it as you like: The (lack of a) measurement of the spin tilt distribution with LIGO-Virgo-KAGRA binary black holes*, *Astron. Astrophys.* **668** (2022) L2 [2209.06978].

[193] J. Antoniadis, T.M. Tauris, F. Ozel, E. Barr, D.J. Champion and P.C.C. Freire, *The millisecond pulsar mass distribution: Evidence for bimodality and constraints on the maximum neutron star mass*, [1605.01665].

[194] J. Alsing, H.O. Silva and E. Berti, *Evidence for a maximum mass cut-off in the neutron star mass distribution and constraints on the equation of state*, *Mon. Not. Roy. Astron. Soc.* **478** (2018) 1377 [1709.07889].

[195] W.M. Farr and K. Chatziioannou, *A Population-Informed Mass Estimate for Pulsar J0740+6620*, *Research Notes of the American Astronomical Society* **4** (2020) 65 [2005.00032].

[196] F. Ozel, D. Psaltis, R. Narayan and A.S. Villarreal, *On the Mass Distribution and Birth Masses of Neutron Stars*, *Astrophys. J.* **757** (2012) 55 [1201.1006].

[197] B. Kiziltan, A. Kottas, M. De Yoreo and S.E. Thorsett, *The Neutron Star Mass Distribution*, *Astrophys. J.* **778** (2013) 66 [1309.6635].

[198] LIGO Scientific, Virgo collaboration, *GW190425: Observation of a Compact Binary Coalescence with Total Mass* $\sim 3.4 M_\odot$, *Astrophys. J. Lett.* **892** (2020) L3 [2001.01761].

[199] P. Landry and J.S. Read, *The Mass Distribution of Neutron Stars in Gravitational-wave Binaries*, *Astrophys. J. Lett.* **921** (2021) L25 [2107.04559].

[200] P. Ajith et al., *Inspiral-merger-ringdown waveforms for black-hole binaries with non-precessing spins*, *Phys. Rev. Lett.* **106** (2011) 241101 [0909.2867].

[201] E. Baird, S. Fairhurst, M. Hannam and P. Murphy, *Degeneracy between mass and spin in black-hole-binary waveforms*, *Phys. Rev. D* **87** (2013) 024035 [1211.0546].

[202] C. Cutler and E.E. Flanagan, *Gravitational waves from merging compact binaries: How accurately can one extract the binary's parameters from the inspiral wave form?*, *Phys. Rev. D* **49** (1994) 2658 [gr-qc/9402014].

[203] D.R. Lorimer, *Binary and Millisecond Pulsars*, *Living Rev. Rel.* **11** (2008) 8 [0811.0762].

[204] J.W.T. Hessels, S.M. Ransom, I.H. Stairs, P.C.C. Freire, V.M. Kaspi and F. Camilo, *A radio pulsar spinning at 716-hz*, *Science* **311** (2006) 1901 [astro-ph/0601337].

[205] M. Burgay et al., *An Increased estimate of the merger rate of double neutron stars from observations of a highly relativistic system*, *Nature* **426** (2003) 531 [astro-ph/0312071].

[206] S. Roy, A.S. Sengupta and K.G. Arun, *Unveiling the spectrum of inspiralling binary black holes*, *Phys. Rev. D* **103** (2021) 064012 [1910.04565].

[207] Y. Suwa, T. Yoshida, M. Shibata, H. Umeda and K. Takahashi, *On the minimum mass of neutron stars*, *Mon. Not. Roy. Astron. Soc.* **481** (2018) 3305 [1808.02328].

[208] V. Doroshenko, V. Suleimanov, G. Pühlhofer and A. Santangelo, *A strangely light neutron star within a supernova remnant*, *Nature Astronomy* **6** (2022) 1444.

[209] B. Margalit and B.D. Metzger, *Constraining the Maximum Mass of Neutron Stars From Multi-Messenger Observations of GW170817*, *Astrophys. J. Lett.* **850** (2017) L19 [1710.05938].

[210] M. Ruiz, S.L. Shapiro and A. Tsokaros, *GW170817, General Relativistic Magnetohydrodynamic Simulations, and the Neutron Star Maximum Mass*, *Phys. Rev. D* **97** (2018) 021501 [1711.00473].

[211] M. Shibata, S. Fujibayashi, K. Hotokezaka, K. Kiuchi, K. Kyutoku, Y. Sekiguchi et al., *Modeling GW170817 based on numerical relativity and its implications*, *Phys. Rev. D* **96** (2017) 123012 [1710.07579].

[212] L. Rezzolla, E.R. Most and L.R. Weih, *Using gravitational-wave observations and quasi-universal relations to constrain the maximum mass of neutron stars*, *Astrophys. J. Lett.* **852** (2018) L25 [1711.00314].

[213] M. Shibata, E. Zhou, K. Kiuchi and S. Fujibayashi, *Constraint on the maximum mass of neutron stars using GW170817 event*, *Phys. Rev. D* **100** (2019) 023015 [1905.03656].

[214] LIGO Scientific, Virgo collaboration, *Model comparison from LIGO–Virgo data on GW170817's binary components and consequences for the merger remnant*, *Class. Quant. Grav.* **37** (2020) 045006 [1908.01012].

[215] M. Evans et al., *Cosmic Explorer: A Submission to the NSF MPSAC ngGW Subcommittee*, [2306.13745].

[216] N.V. Krishnendu, K.G. Arun and C.K. Mishra, *Testing the binary black hole nature of a compact binary coalescence*, *Phys. Rev. Lett.* **119** (2017) 091101 [1701.06318].

[217] A. Nagar et al., *Time-domain effective-one-body gravitational waveforms for coalescing compact binaries with nonprecessing spins, tides and self-spin effects*, *Phys. Rev. D* **98** (2018) 104052 [1806.01772].

[218] T. Dietrich, A. Samajdar, S. Khan, N.K. Johnson-McDaniel, R. Dudi and W. Tichy, *Improving the NRTidal model for binary neutron star systems*, *Phys. Rev. D* **100** (2019) 044003 [1905.06011].

[219] K.G. Arun, A. Buonanno, G. Faye and E. Ochsner, *Higher-order spin effects in the amplitude and phase of gravitational waveforms emitted by inspiraling compact binaries: Ready-to-use gravitational waveforms*, *Phys. Rev. D* **79** (2009) 104023 [0810.5336].

[220] M. Cantiello, C. Mankovich, L. Bildsten, J. Christensen-Dalsgaard and B. Paxton, *Angular momentum transport within evolved low-mass stars*, *Astrophys. J.* **788** (2014) 93 [1405.1419].

[221] M.S.B. Coleman and A. Burrows, *Kicks and induced spins of neutron stars at birth*, *Mon. Not. Roy. Astron. Soc.* **517** (2022) 3938 [2209.02711].

[222] A. Burrows, T. Wang, D. Vartanyan and M.S.B. Coleman, *A Theory for Neutron Star and Black Hole Kicks and Induced Spins*, *Astrophys. J.* **963** (2024) 63 [2311.12109].

[223] A. Burrows, D. Vartanyan and T. Wang, *Black Hole Formation Accompanied by the Supernova Explosion of a 40 $M_\odot$ Progenitor Star*, *Astrophys. J.* **957** (2023) 68 [2308.05798].

[224] G.E. Soberman, E.S. Phinney and E.P.J.v. den Heuvel, *Stability criteria for mass transfer in binary stellar evolution*, *Astron. Astrophys.* **327** (1997) 620 [astro-ph/9703016].

[225] H. Ge, M.S. Hjellming, R.F. Webbink, X. Chen and Z. Han, *Adiabatic Mass Loss in Binary Stars. I. Computational Method*, ApJ **717** (2010) 724 [1005.3099].

[226] H. Ge, R.F. Webbink, X. Chen and Z. Han, *Adiabatic Mass Loss in Binary Stars. II. From Zero-age Main Sequence to the Base of the Giant Branch*, ApJ **812** (2015) 40 [1507.04843].

[227] A. Vigna-Gómez et al., *On the formation history of Galactic double neutron stars*, *Mon. Not. Roy. Astron. Soc.* **481** (2018) 4009 [1805.07974].

[228] A.J. Delgado and H.C. Thomas, *Mass transfer in a binary system - The evolution of the mass-giving helium star*, A&A **96** (1981) 142.

[229] T.M. Tauris, N. Langer and P. Podsiadlowski, *Ultra-stripped supernovae: progenitors and fate*, *Mon. Not. Roy. Astron. Soc.* **451** (2015) 2123 [1505.00270].

[230] K.S. Thorne, *Disk accretion onto a black hole. 2. Evolution of the hole.*, *Astrophys. J.* **191** (1974) 507.

[231] Z.-H.-T. Wang, R.-C. Hu, Y. Qin, J.-P. Zhu, B. Zhang, S.-X. Yi et al., *A Channel to Form Fast-spinning Black Hole–Neutron Star Binary Mergers as Multimessenger Sources. II. Accretion-induced Spin-up*, *Astrophys. J.* **965** (2024) 177 [2401.17558].

[232] C.M. Zhang and Y. Kojima, *The bottom magnetic field and magnetosphere evolution of neutron star in low-mass X-ray binary*, MNRAS **366** (2006) 137 [astro-ph/0410248].

[233] D. Kushnir, M. Zaldarriaga, J.A. Kollmeier and R. Waldman, *Dynamical tides reexpressed*, MNRAS **467** (2017) 2146 [1605.03810].

[234] S.S. Bavera et al., *The impact of mass-transfer physics on the observable properties of field binary black hole populations*, *Astron. Astrophys.* **647** (2021) A153 [2010.16333].

[235] J. Fuller and W. Lu, *The spins of compact objects born from helium stars in binary systems*, *Mon. Not. Roy. Astron. Soc.* **511** (2022) 3951 [2201.08407].

[236] E. Thrane and C. Talbot, *An introduction to Bayesian inference in gravitational-wave astronomy: parameter estimation, model selection, and hierarchical models*, *Publ. Astron. Soc. Austral.* **36** (2019) e010 [1809.02293].

[237] N. Metropolis, A.W. Rosenbluth, M.N. Rosenbluth, A.H. Teller and E. Teller, *Equation of state calculations by fast computing machines*, *J. Chem. Phys.* **21** (1953) 1087.

[238] W.K. Hastings, *Monte carlo sampling methods using markov chains and their applications*, *Biometrika* **57** (1970) 97.

[239] J. Skilling, *Nested Sampling*, *AIP Conf. Proc.* **735** (2004) 395.

[240] P. Canizares, S.E. Field, J. Gair, V. Raymond, R. Smith and M. Tiglio, *Accelerated gravitational-wave parameter estimation with reduced order modeling*, *Phys. Rev. Lett.* **114** (2015) 071104 [1404.6284].

[241] R. Smith, S.E. Field, K. Blackburn, C.-J. Haster, M. Pürrer, V. Raymond et al., *Fast and accurate inference on gravitational waves from precessing compact binaries*, *Phys. Rev. D* **94** (2016) 044031 [1604.08253].

[242] S. Morisaki and V. Raymond, *Rapid Parameter Estimation of Gravitational Waves from Binary Neutron Star Coalescence using Focused Reduced Order Quadrature*, *Phys. Rev. D* **102** (2020) 104020 [2007.09108].

[243] S. Morisaki, R. Smith, L. Tsukada, S. Sachdev, S. Stevenson, C. Talbot et al., *Rapid localization and inference on compact binary coalescences with the Advanced LIGO-Virgo-KAGRA gravitational-wave detector network*, *Phys. Rev. D* **108** (2023) 123040 [2307.13380].

[244] S. Vinciguerra, J. Veitch and I. Mandel, *Accelerating gravitational wave parameter estimation with multi-band template interpolation*, *Class. Quant. Grav.* **34** (2017) 115006 [1703.02062].

[245] S. Morisaki, *Accelerating parameter estimation of gravitational waves from compact binary coalescence using adaptive frequency resolutions*, *Phys. Rev. D* **104** (2021) 044062 [2104.07813].

[246] L. Pathak, A. Reza and A.S. Sengupta, *Fast likelihood evaluation using meshfree approximations for reconstructing compact binary sources*, *Phys. Rev. D* **108** (2023) 064055 [2210.02706].

[247] L. Pathak, S. Munishwar, A. Reza and A.S. Sengupta, *Prompt sky localization of compact binary sources using a meshfree approximation*, *Phys. Rev. D* **109** (2024) 024053 [2309.07012].

[248] C. Pankow, P. Brady, E. Ochsner and R. O'Shaughnessy, *Novel scheme for rapid parallel parameter estimation of gravitational waves from compact binary coalescences*, *Phys. Rev. D* **92** (2015) 023002 [1502.04370].

[249] R.J.E. Smith, G. Ashton, A. Vajpeyi and C. Talbot, *Massively parallel Bayesian inference for transient gravitational-wave astronomy*, *Mon. Not. Roy. Astron. Soc.* **498** (2020) 4492 [1909.11873].

[250] C. Talbot, R. Smith, E. Thrane and G.B. Poole, *Parallelized Inference for Gravitational-Wave Astronomy*, *Phys. Rev. D* **100** (2019) 043030 [1904.02863].

[251] V. Tiwari, C. Hoy, S. Fairhurst and D. MacLeod, *Fast non-Markovian sampler for estimating gravitational-wave posteriors*, *Phys. Rev. D* **108** (2023) 023001 [2303.01463].

[252] M.J. Williams, J. Veitch and C. Messenger, *Nested sampling with normalizing flows for gravitational-wave inference*, *Phys. Rev. D* **103** (2021) 103006 [2102.11056].

[253] S.R. Green, C. Simpson and J. Gair, *Gravitational-wave parameter estimation with autoregressive neural network flows*, *Phys. Rev. D* **102** (2020) 104057 [2002.07656].

[254] T.D.P. Edwards, K.W.K. Wong, K.K.H. Lam, A. Coogan, D. Foreman-Mackey, M. Isi et al., *Differentiable and hardware-accelerated waveforms for gravitational wave data analysis*, *Phys. Rev. D* **110** (2024) 064028 [2302.05329].

[255] K.W.K. Wong, M. Isi and T.D.P. Edwards, *Fast Gravitational-wave Parameter Estimation without Compromises*, *Astrophys. J.* **958** (2023) 129 [2302.05333].

[256] N.J. Cornish, *Fast Fisher Matrices and Lazy Likelihoods*, [1007.4820].

[257] B. Zackay, L. Dai and T. Venumadhav, *Relative Binning and Fast Likelihood Evaluation for Gravitational Wave Parameter Estimation*, [1806.08792].

[258] N.J. Cornish, *Heterodyned likelihood for rapid gravitational wave parameter inference*, *Phys. Rev. D* **104** (2021) 104054 [2109.02728].

[259] G. Ashton, M. Hübner, P.D. Lasky, C. Talbot, K. Ackley, S. Biscoveanu et al., *BILBY: A User-friendly Bayesian Inference Library for Gravitational-wave Astronomy*, ApJS **241** (2019) 27 [1811.02042].

[260] I.M. Romero-Shaw, C. Talbot, S. Biscoveanu, V. D'Emilio, G. Ashton, C.P.L. Berry et al., *Bayesian inference for compact binary coalescences with BILBY: validation and application to the first LIGO-Virgo gravitational-wave transient catalogue*, MNRAS **499** (2020) 3295 [2006.00714].

[261] K. Krishna, A. Vijaykumar, A. Ganguly, C. Talbot, S. Biscoveanu, R.N. George et al., *Accelerated parameter estimation in Bilby with relative binning*, [2312.06009].

[262] N. Leslie, L. Dai and G. Pratten, *Mode-by-mode relative binning: Fast likelihood estimation for gravitational waveforms with spin-orbit precession and multiple harmonics*, *Phys. Rev. D* **104** (2021) 123030 [2109.09872].

[263] M.J. Williams, *nessai: Nested sampling with artificial intelligence*, Feb., 2021. 10.5281/zenodo.4550693.

[264] M.J. Williams, J. Veitch and C. Messenger, *Importance nested sampling with normalising flows*, *Mach. Learn. Sci. Tech.* **4** (2023) 035011 [2302.08526].

[265] J. Buchner, A. Georgakakis, K. Nandra, L. Hsu, C. Rangel, M. Brightman et al., *X-ray spectral modelling of the AGN obscuring region in the CDFS: Bayesian model selection and catalogue*, A&A **564** (2014) A125 [1402.0004].

[266] J.S. Speagle, *DYNESTY: a dynamic nested sampling package for estimating Bayesian posteriors and evidences*, MNRAS **493** (2020) 3132 [1904.02180].

[267] S. Koposov, J. Speagle, K. Barbary, G. Ashton, E. Bennett, J. Buchner et al., *joshspeagle/dynesty: v2.1.3*, Oct., 2023. 10.5281/zenodo.8408702.

[268] S. Wu and A.H. Nitz, *Mock data study for next-generation ground-based detectors: The performance loss of matched filtering due to correlated confusion noise*, *Phys. Rev. D* **107** (2023) 063022 [2209.03135].

[269] A. Samajdar, J. Janquart, C. Van Den Broeck and T. Dietrich, *Biases in parameter estimation from overlapping gravitational-wave signals in the third-generation detector era*, *Phys. Rev. D* **104** (2021) 044003 [2102.07544].

[270] M. Pürrer and C.-J. Haster, *Gravitational waveform accuracy requirements for future ground-based detectors*, *Phys. Rev. Res.* **2** (2020) 023151 [1912.10055].

[271] Q. Hu and J. Veitch, *Assessing the model waveform accuracy of gravitational waves*, *Phys. Rev. D* **106** (2022) 044042 [2205.08448].

[272] A. Dhani, S. Völkel, A. Buonanno, H. Estelles, J. Gair, H.P. Pfeiffer et al., "Systematic Biases in Estimating the Properties of Black Holes Due to Inaccurate Gravitational-Wave Models." 4, 2024.

[273] L. Sun et al., *Characterization of systematic error in Advanced LIGO calibration*, *Class. Quant. Grav.* **37** (2020) 225008 [2005.02531].

[274] L. Sun et al., "Characterization of systematic error in Advanced LIGO calibration in the second half of O3." 6, 2021.

[275] Y. Huang, H.-Y. Chen, C.-J. Haster, L. Sun, S. Vitale and J.S. Kissel, *Impact of calibration uncertainties on Hubble constant measurements from gravitational-wave sources*, *Phys. Rev. D* **111** (2025) 063034 [2204.03614].

[276] J. Janquart, T. Baka, A. Samajdar, T. Dietrich and C. Van Den Broeck, *Analyses of overlapping gravitational wave signals using hierarchical subtraction and joint parameter estimation*, *Mon. Not. Roy. Astron. Soc.* **523** (2023) 1699 [2211.01304].

[277] A.D. Johnson, K. Chatziioannou and W.M. Farr, *Source confusion from neutron star binaries in ground-based gravitational wave detectors is minimal*, *Phys. Rev. D* **109** (2024) 084015 [2402.06836].

[278] I. Gupta, K. Chandra and B.S. Sathyaprakash, "Foreground signals minimally affect inference of high-mass binary black holes in next generation gravitational-wave detectors." 10, 2024.

[279] G. Pratten, S. Husa, C. Garcia-Quiros, M. Colleoni, A. Ramos-Buades, H. Estelles et al., *Setting the cornerstone for a family of models for gravitational waves from compact binaries: The dominant harmonic for nonprecessing quasicircular black holes*, *Phys. Rev. D* **102** (2020) 064001 [2001.11412].

[280] P. Madau and M. Dickinson, *Cosmic Star Formation History*, *Ann. Rev. Astron. Astrophys.* **52** (2014) 415 [1403.0007].

[281] C. Talbot, R. Smith, E. Thrane and G.B. Poole, *Parallelized inference for gravitational-wave astronomy*, Phys. Rev. D **100** (2019) 043030 [1904.02863].

[282] W.M. Farr and K. Chatziioannou, *A population-informed mass estimate for pulsar j0740+6620*, *Research Notes of the AAS* **4** (2020) 65.

[283] E. Fonseca et al., *Refined Mass and Geometric Measurements of the High-mass PSR J0740+6620*, *Astrophys. J. Lett.* **915** (2021) L12 [2104.00880].

[284] R.W. Romani, D. Kandel, A.V. Filippenko, T.G. Brink and W. Zheng, *PSR J0952−0607: The Fastest and Heaviest Known Galactic Neutron Star*, *Astrophys. J. Lett.* **934** (2022) L17 [2207.05124].

[285] C.D. Bailyn, R.K. Jain, P. Coppi and J.A. Orosz, *The Mass distribution of stellar black holes*, *Astrophys. J.* **499** (1998) 367 [astro-ph/9708032].

[286] F. Ozel, D. Psaltis, R. Narayan and J.E. McClintock, *The Black Hole Mass Distribution in the Galaxy*, *Astrophys. J.* **725** (2010) 1918 [1006.2834].

[287] LIGO Scientific, Virgo collaboration, *GWTC-1: A Gravitational-Wave Transient Catalog of Compact Binary Mergers Observed by LIGO and Virgo during the First and Second Observing Runs*, *Phys. Rev. X* **9** (2019) 031040 [1811.12907].

[288] LIGO Scientific, Virgo collaboration, *GWTC-2: Compact Binary Coalescences Observed by LIGO and Virgo During the First Half of the Third Observing Run*, *Phys. Rev. X* **11** (2021) 021053 [2010.14527].

[289] C.L. Fryer, K. Belczynski, G. Wiktorowicz, M. Dominik, V. Kalogera and D.E. Holz, *Compact Remnant Mass Function: Dependence on the Explosion Mechanism and Metallicity*, ApJ **749** (2012) 91 [1110.1726].

[290] J. Veitch and A. Vecchio, *Bayesian coherent analysis of in-spiral gravitational wave signals with a detector network*, *Phys. Rev. D* **81** (2010) 062003 [0911.3820].

[291] M. Fishbach, R. Essick and D.E. Holz, *Does Matter Matter? Using the mass distribution to distinguish neutron stars and black holes*, *Astrophys. J. Lett.* **899** (2020) L8 [2006.13178].

[292] A.M. Farah, M. Fishbach, R. Essick, D.E. Holz and S. Galaudage, *Bridging the Gap: Categorizing Gravitational-wave Events at the Transition between Neutron Stars and Black Holes*, *Astrophys. J.* **931** (2022) 108 [2111.03498].

[293] A. Ray, I. Magaña Hernandez, S. Mohite, J. Creighton and S. Kapadia, *Nonparametric Inference of the Population of Compact Binaries from Gravitational-wave Observations Using Binned Gaussian Processes*, *Astrophys. J.* **957** (2023) 37 [2304.08046].

[294] J.-P. Zhu, R.-C. Hu, Y. Kang, B. Zhang, H. Tong, L. Shao et al., *Formation of GW230529 from Isolated Binary Evolution*, *Astrophys. J.* **974** (2024) 211 [2404.10596].

[295] I. Mandel and F.S. Broekgaarden, *Rates of compact object coalescences*, *Living Rev. Rel.* **25** (2022) 1 [2107.14239].

[296] F.S. Broekgaarden and E. Berger, *Formation of the First Two Black Hole-Neutron Star Mergers (GW200115 and GW200105) from Isolated Binary Evolution*, ApJ **920** (2021) L13 [2108.05763].

[297] D. Chattopadhyay, S. Stevenson, F. Broekgaarden, F. Antonini and K. Belczynski, *Modelling the formation of the first two neutron star-black hole mergers, GW200105 and GW200115: metallicity, chirp masses, and merger remnant spins*, MNRAS **513** (2022) 5780 [2203.05850].

[298] G. Ashton et al., *BILBY: A user-friendly Bayesian inference library for gravitational-wave astronomy*, *Astrophys. J. Suppl.* **241** (2019) 27 [1811.02042].

[299] J.S. Speagle, *dynesty: a dynamic nested sampling package for estimating Bayesian posteriors and evidences*, *Mon. Not. Roy. Astron. Soc.* **493** (2020) 3132 [1904.02180].

[300] T.B. Littenberg and N.J. Cornish, *Bayesian inference for spectral estimation of gravitational wave detector noise*, *Phys. Rev. D* **91** (2015) 084034 [1410.3852].

[301] F. Foucart, L. Buchman, M.D. Duez, M. Grudich, L.E. Kidder, I. MacDonald et al., *First direct comparison of nondisrupting neutron star-black hole and binary black hole merger simulations*, *Phys. Rev. D* **88** (2013) 064017 [1307.7685].

[302] F. Foucart, M.B. Deaton, M.D. Duez, E. O'Connor, C.D. Ott, R. Haas et al., *Neutron star-black hole mergers with a nuclear equation of state and neutrino cooling: Dependence in the binary parameters*, *Phys. Rev. D* **90** (2014) 024026 [1405.1121].

[303] S. Khan, S. Husa, M. Hannam, F. Ohme, M. Pürrer, X. Jiménez Forteza et al., *Frequency-domain gravitational waves from nonprecessing black-hole binaries. II. A phenomenological model for the advanced detector era*, *Phys. Rev. D* **93** (2016) 044007 [1508.07253].

[304] G. Ashton and T. Dietrich, *The use of hypermodels to understand binary neutron star collisions*, *Nature Astron.* **6** (2022) 961 [2111.09214].

[305] C. Barbieri, O.S. Salafia, A. Perego, M. Colpi and G. Ghirlanda, *Electromagnetic counterparts of black hole-neutron star mergers: dependence on the neutron star properties*, *Eur. Phys. J. A* **56** (2020) 8 [1908.08822].

[306] J.R. Hurley, O.R. Pols and C.A. Tout, *Comprehensive analytic formulae for stellar evolution as a function of mass and metallicity*, MNRAS **315** (2000) 543 [astro-ph/0001295].

[307] K. Belczynski, T. Bulik, C.L. Fryer, A. Ruiter, F. Valsecchi, J.S. Vink et al., *On the Maximum Mass of Stellar Black Holes*, ApJ **714** (2010) 1217 [0904.2784].

[308] I. Mandel and T. Fragos, *An alternative interpretation of GW190412 as a binary black hole merger with a rapidly spinning secondary*, *Astrophys. J. Lett.* **895** (2020) L28 [2004.09288].

[309] T. Fragos and J.E. McClintock, *The Origin of Black Hole Spin in Galactic Low-Mass X-ray Binaries*, *Astrophys. J.* **800** (2015) 17 [1408.2661].

[310] L. Ma and J. Fuller, *Angular momentum transport in massive stars and natal neutron star rotation rates*, *Mon. Not. Roy. Astron. Soc.* **488** (2019) 4338 [1907.03713].

[311] Y. Qin, T. Fragos, G. Meynet, J. Andrews, M. Sørensen and H.F. Song, *The spin of the second-born black hole in coalescing binary black holes*, A&A **616** (2018) A28 [1802.05738].

[312] S.S. Bavera, T. Fragos, Y. Qin, E. Zapartas, C.J. Neijssel, I. Mandel et al., *The origin of spin in binary black holes. Predicting the distributions of the main observables of Advanced LIGO*, A&A **635** (2020) A97 [1906.12257].

[313] N. Ivanova, S. Justham, X. Chen, O. De Marco, C.L. Fryer, E. Gaburov et al., *Common envelope evolution: where we stand and how we can move forward*, A&A Rev. **21** (2013) 59 [1209.4302].

[314] K. Belczynski, A. Romagnolo, A. Olejak, J. Klencki, D. Chattopadhyay, S. Stevenson et al., *The Uncertain Future of Massive Binaries Obscures the Origin of LIGO/Virgo Sources*, ApJ **925** (2022) 69 [2108.10885].

[315] D. Langeroodi, J. Hjorth, W. Chen, P.L. Kelly, H. Williams, Y.-H. Lin et al., *Evolution of the Mass-Metallicity Relation from Redshift $z \approx 8$ to the Local Universe*, ApJ **957** (2023) 39 [2212.02491].

[316] A.M. Garcia, P. Torrey, S. Ellison, K. Grasha, L. Hernquist, H.R.M. Zovaro et al., *Does the Fundamental Metallicity Relation Evolve with Redshift? I: The Correlation Between Offsets from the Mass-Metallicity Relation and Star Formation Rate*, *arXiv e-prints* (2024) arXiv:2403.08856 [2403.08856].

[317] C. Kalaghatgi and M. Hannam, *Investigating the effect of in-plane spin directions for precessing binary black hole systems*, *Phys. Rev. D* **103** (2021) 024024 [2008.09957].

[318] P. Kolitsidou, J.E. Thompson and M. Hannam, *Impact of antisymmetric contributions to signal multipoles in the measurement of black-hole spins*, *Phys. Rev. D* **111** (2025) 024050 [2402.00813].

[319] Planck collaboration, *Planck 2018 results. VI. Cosmological parameters*, *Astron. Astrophys.* **641** (2020) A6 [1807.06209].

[320] L. Verde, T. Treu and A.G. Riess, *Tensions between the Early and the Late Universe*, *Nature Astron.* **3** (2019) 891 [1907.10625].

[321] D.E. Holz and S.A. Hughes, *Using gravitational-wave standard sirens*, *Astrophys. J.* **629** (2005) 15 [astro-ph/0504616].

[322] S. Bera, D. Rana, S. More and S. Bose, *Incompleteness Matters Not: Inference of H_0 from Binary Black Hole–Galaxy Cross-correlations*, *Astrophys. J.* **902** (2020) 79 [2007.04271].

[323] A. Nishizawa, *Measurement of Hubble constant with stellar-mass binary black holes*, *Phys. Rev. D* **96** (2017) 101303 [1612.06060].

[324] J. Yu, Y. Wang, W. Zhao and Y. Lu, *Hunting for the host galaxy groups of binary black holes and the application in constraining Hubble constant*, *Mon. Not. Roy. Astron. Soc.* **498** (2020) 1786 [2003.06586].

[325] W. Del Pozzo, *Inference of the cosmological parameters from gravitational waves: application to second generation interferometers*, *Phys. Rev. D* **86** (2012) 043011 [1108.1317].

[326] H.-Y. Chen, M. Fishbach and D.E. Holz, *A two per cent Hubble constant measurement from standard sirens within five years*, *Nature* **562** (2018) 545 [1712.06531].

[327] A. Finke, S. Foffa, F. Iacovelli, M. Maggiore and M. Mancarella, *Cosmology with LIGO/Virgo dark sirens: Hubble parameter and modified gravitational wave propagation*, *JCAP* **08** (2021) 026 [2101.12660].

[328] LIGO Scientific, Virgo collaboration, *Estimating the Contribution of Dynamical Ejecta in the Kilonova Associated with GW170817*, *Astrophys. J. Lett.* **850** (2017) L39 [1710.05836].

[329] LIGO Scientific, Virgo, 1M2H, Dark Energy Camera GW-E, DES, DLT40, Las Cumbres Observatory, VINROUGE, MASTER collaboration, *A gravitational-wave standard siren measurement of the Hubble constant*, *Nature* **551** (2017) 85 [1710.05835].

[330] D.J. Mortlock, S.M. Feeney, H.V. Peiris, A.R. Williamson and S.M. Nissanke, *Unbiased Hubble constant estimation from binary neutron star mergers*, *Phys. Rev. D* **100** (2019) 103523 [1811.11723].

[331] C. Van Den Broeck and A.S. Sengupta, *Binary black hole spectroscopy*, *Class. Quant. Grav.* **24** (2007) 1089 [gr-qc/0610126].

[332] K.G. Arun, B.R. Iyer, B.S. Sathyaprakash, S. Sinha and C. Van Den Broeck, *Higher signal harmonics, LISA's angular resolution and dark energy*, *Phys. Rev. D* **76** (2007) 104016 [0707.3920].

[333] P.B. Graff, A. Buonanno and B.S. Sathyaprakash, *Missing Link: Bayesian detection and measurement of intermediate-mass black-hole binaries*, *Phys. Rev. D* **92** (2015) 022002 [1504.04766].

[334] P. Ajith and S. Bose, *Estimating the parameters of non-spinning binary black holes using ground-based gravitational-wave detectors: Statistical errors*, *Phys. Rev. D* **79** (2009) 084032 [0901.4936].

[335] L. Barack and C. Cutler, *LISA capture sources: Approximate waveforms, signal-to-noise ratios, and parameter estimation accuracy*, *Phys. Rev. D* **69** (2004) 082005 [gr-qc/0310125].

[336] J. Calderón Bustillo, S.H.W. Leong, T. Dietrich and P.D. Lasky, *Mapping the Universe Expansion: Enabling Percent-level Measurements of the Hubble Constant with a Single Binary Neutron-star Merger Detection*, *Astrophys. J. Lett.* **912** (2021) L10 [2006.11525].

[337] H.-Y. Chen, P.S. Cowperthwaite, B.D. Metzger and E. Berger, *A Program for Multimessenger Standard Siren Cosmology in the Era of LIGO A+, Rubin Observatory, and Beyond*, *Astrophys. J. Lett.* **908** (2021) L4 [2011.01211].

[338] S. Mukherjee, G. Lavaux, F.R. Bouchet, J. Jasche, B.D. Wandelt, S.M. Nissanke et al., *Velocity correction for Hubble constant measurements from standard sirens*, *Astron. Astrophys.* **646** (2021) A65 [1909.08627].

[339] C. Nicolaou, O. Lahav, P. Lemos, W. Hartley and J. Braden, *The Impact of Peculiar Velocities on the Estimation of the Hubble Constant from Gravitational Wave Standard Sirens*, *Mon. Not. Roy. Astron. Soc.* **495** (2020) 90 [1909.09609].

[340] C. Howlett and T.M. Davis, *Standard siren speeds: improving velocities in gravitational-wave measurements of H_0*, *Mon. Not. Roy. Astron. Soc.* **492** (2020) 3803 [1909.00587].

[341] H.-Y. Chen, *Systematic Uncertainty of Standard Sirens from the Viewing Angle of Binary Neutron Star Inspirals*, *Phys. Rev. Lett.* **125** (2020) 201301 [2006.02779].

[342] J. Roulet, S. Olsen, J. Mushkin, T. Islam, T. Venumadhav, B. Zackay et al., *Removing degeneracy and multimodality in gravitational wave source parameters*, *Phys. Rev. D* **106** (2022) 123015 [2207.03508].

[343] H.-Y. Chen, P. Landry, J.S. Read and D.M. Siegel, "Inference of multi-channel r-process element enrichment in the Milky Way using binary neutron star merger observations." 2, 2024.

[344] R. Kashyap, G. Raman and P. Ajith, *Can Kilonova Light curves be Standardized?*, *Astrophys. J. Lett.* **886** (2019) L19 [1908.02168].

[345] J.M. Ezquiaga and D.E. Holz, *Spectral Sirens: Cosmology from the Full Mass Distribution of Compact Binaries*, *Phys. Rev. Lett.* **129** (2022) 061102 [2202.08240].

[346] T. Hinderer, *Tidal Love numbers of neutron stars*, *Astrophys. J.* **677** (2008) 1216 [0711.2420].

[347] E.E. Flanagan and T. Hinderer, *Constraining neutron star tidal Love numbers with gravitational wave detectors*, *Phys. Rev. D* **77** (2008) 021502 [0709.1915].

[348] N. Sarin, H.V. Peiris, D.J. Mortlock, J. Alsing, S.M. Nissanke and S.M. Feeney, *Measuring the nuclear equation of state with neutron star-black hole mergers*, *Phys. Rev. D* **110** (2024) 024076 [2311.05689].

[349] C. Messenger and J. Read, *Measuring a cosmological distance-redshift relationship using only gravitational wave observations of binary neutron star coalescences*, *Phys. Rev. Lett.* **108** (2012) 091101 [1107.5725].

[350] T. Ghosh, B. Biswas, S. Bose and S.J. Kapadia, "Joint Inference of Population, Cosmology, and Neutron Star Equation of State from Gravitational Waves of Dark Binary Neutron Stars." 7, 2024.

Vita

Ish Gupta

Ish Gupta is a Ph.D. candidate in Physics at The Pennsylvania State University, advised by Prof. B.S. Sathyaprakash. His research focuses on gravitational-wave astronomy, including cosmology, neutron star physics, tests of general relativity, and facilitating multi-messenger astrophysics. In the Fall of 2025, he is expected to join the University of California, Berkeley, as an N3AS Postdoctoral Fellow, where he will work with Prof. André de Gouvêa and Prof. Vicky Kalogera from Northwestern University.

Selected Publications

- Inferring small neutron star spins with neutron star-black hole mergers. **Ish Gupta**. *Astrophys. J 970, 1 (2024)*
- Characterizing gravitational-wave detector networks: From A$^\sharp$ to Cosmic Explorer. **Ish Gupta** *et al. Class. Quantum Grav. 41, 245001 (2024)*
- On the origins, remnant, and multimessenger prospects of the compact binary merger GW230529. Koustav Chandra, **Ish Gupta** *et al. Astrophys. J 977, 2 (2024)*
- Cosmography with next-generation gravitational wave detectors. Hsin-Yu Chen, Jose Ezquiaga and **Ish Gupta**. Class. Quantum Grav. 41, 125004 (2024)
- Neutron star-black hole mergers in next generation gravitational-wave observatories. **Ish Gupta** *et al. Phys. Rev. D 107, 124007 (2023)*
- Using gray sirens to resolve the Hubble-Lemaître tension. **Ish Gupta**. *Mon. Not. R. Astron. Soc. 524, 3537–3558 (2023)*
- Detectability of QCD phase transitions in binary neutron star mergers: Bayesian inference with the next generation gravitational wave detectors. Aviral Prakash, **Ish Gupta** *et al. Phys. Rev. D 109, 103008 (2023)*

Selected Honors & Awards

- Alumni Association Dissertation Award — Penn State, 2025
- Mebus Graduate Fellowship — Penn State, 2024
- Peter Eklund Award for Science Communication — Penn State, 2023
- BITS Pilani Merit Scholarship — BITS Pilani, 2019–20
- G.N. Ramachandran Fellowship — IIT Madras, 2018